Glacial isostatic adjustment and relative sea level change over the last earthquake cycle in upper Cook Inlet, Alaska, USA

BARLOW, NATASHA,LOUISE,MARY

Natasha Barlow

Glacial isostatic adjustment and relative sea level change over the last earthquake cycle in upper Cook Inlet, Alaska, USA

Using observations of land surface deformation, sea level change and geophysical modelling, this thesis considers the interactions of ice mass fluctuations and tectonic deformation over the last great earthquake cycle in south central Alaska.

Reconstructions of relative sea level change over the last 900 years, based upon extensive lithological, biostratigraphical and chronological investigations of salt marsh sequences in upper Cook Inlet, Alaska, record changes in marine influence and the direction of sea level that do not fit the expected interseismic model of land level movements. Dating of the sequences suggests the changes in RSL occurred sometime through c. AD 1600 – 1900, during the middle and late phases of Little Ice Age ice mass balance changes. The chronological methods used comprise a multi-method approach: ^{210}Pb, ^{137}Cs, stable lead (^{206}Pb/^{207}Pb) ratios, pollutants associated with the history of regional gold mining and development, tephrochronology and AMS ^{14}C wiggle match dating. The research highlights some of the limitations of applying some of these dating methodologies to recent, high latitude, salt marshes.

GIA modelling identifies part of the GPS measured present day uplift in upper Cook Inlet as attributable to post Little Ice Age (AD 1200 – 1900) glacial isostatic adjustment, with a spatial signal over tens of kilometres. A set of viable Earth models, constrained by GPS data and the pattern of post-seismic displacement quantifies the relative displacement and deformation of the ocean geoid at a series of locations in south central Alaska over the past 1000 years. Modelling results show the asthenosphere viscosity and thickness to be the main rheological controls on relative displacement during the last earthquake deformation cycle.

Integration of the geological data and geophysical model results show RSL in upper Cook Inlet during the last earthquake deformation cycle is a combination of tectonic land-level changes, 'local' processes, glacial isostatic adjustment and deformation of the ocean geoid. To fully quantify the relative contribution of each mechanism requires improvements in the methods of RSL reconstruction, dating of recent salt marsh sediments and GIA modelling.

Glacial isostatic adjustment and relative sea level change over the last earthquake cycle in upper Cook Inlet, Alaska, USA

Two Volumes

Volume One: Main Text and References

Natasha Louise Mary Barlow

Thesis submitted for the degree of Doctor of Philosophy

Department of Geography
Durham University

October 2010

Table of contents

Volume 1

Volume 2

Declaration of Copyright

I confirm that no part of the material presented in this thesis has previously been submitted by me or any other person for a degree in this or any other university. In all cases, where it is relevant, material from the work of others has been acknowledged.

Acknowledgements

I would firstly like to thank my supervisors Professors Ian Shennan and Antony Long. Ian's 'daft' idea of going to Alaska to do our undergraduate dissertations provided the inspiration for a career in geography, a love for Alaska and the basis for this research. He has been of much amusement both in the field and office, and offered support, friendship and an eclectic music collection when needed over the past three and a half years. Antony provided the level head when I could not see the wood from the trees and at times made sure I was not getting too carried away, often offering an alternative perspective. Without both of their guidance and inspiration, I would not have been able to complete this work.

This research would not have been possible without fantastic field and logistical assistance from Jack Allen, Sarah Grey, Rod Combellick (Alaska State Geological Survey), Ian Shennan, Frank Davies and Smiley Shields. All of them provided incredible support, muscles and time to come and dig in the muddy, bug and bear infested marshes of Alaska. Particular thanks to Rod for bringing his pistol during an unnerving trip to Hope marsh. Thank you all for putting up with my stresses and sharing in an Alaskan Amber...or two!

I am grateful to Giorgio Spada (Universití di Urbino) for providing the open access post glacial rebound calculator TABOO and putting up with some lengthy emails. Chris Larsen (University of Alaska, Fairbanks) has been fantastic, providing his regional Alaskan ice model and answering so many questions as I initially got to grips with using TABOO. I just hope one day we finally manage to meet rather conducting everything by email! Kris Crossen (University of Alaska, Anchorage) has also been a great support. So many people have offered invaluable

discussion at conferences, in the Department and in particular at the COST Training School on GIA Modelling in Sweden in June 2009.

I particularly wish to thank Dr Matt King (Newcastle University) and Dr Robin Edwards (Trinity College, Dublin) for their insightful discussions during the viva and subsequent corrections. This thesis has benefited greatly from their input.

This research has been received generous financial support for field work, radiocarbon dating and conference attendance from the American Quaternary Association; COST; Department of Geography, Durham University; The Dudley Stamp Memorial Fund, Royal Society; IGCP Project 495; The Monica Cole Research Grant, Royal Geographical Society; my grandparents Ken and Gladys Barlow; Natural Environmental Research Council Radiocarbon Facility and the Quaternary Research Association.

So many friends have made me laugh, shared in a beer, provided technical support and insightful discussion to make the past three and a half years very enjoyable. In no order I would particularly like to mention: Steve, Beth, Oven, Tomo, Woody (who in particular has put up with a lot of sea level questions), Rob, Emma, Emma, Anne, Pippa, Milledge, Mark, my grandparents, the mountain bikers, the geography girls, the Burgess-Dennis clan, Frilly, Roxy, Pudding, Red and Archie. Many members of QEC have also been a very important part of my PhD. The laboratory staff, in particular Frank, Neil, Eddie, Merv, Amanda and Martin, have been fantastic, putting up with some strange and often very last minute requests.

Finally I would like to thank my Mum, Dad, brother GT and my partner Jack for their support, love and kindness. The past three and a half years have been a rollercoaster and you have all stood behind me through thick and thin. You have reminded me there is life beyond a PhD and had confidence in my abilities when at times I have had none. You have helped me financially and mentally and put up with extended conversations when I know at times I have gone round and round in circles, both complaining and in excitement. Thank you all so much, I will never forget it.

For Mum & Dad

Thank you

Chapter 1 : Context

1.1 Introduction

Tectonics at subduction zones produce unique signatures of past relative sea level (RSL) changes described by the earthquake deformation cycle (EDC) model (e.g. Atwater, 1987; Nelson *et al.*, 1996; Long and Shennan, 1998; Hamilton and Shennan, 2005a). The dynamics of former ice sheets and glaciers that occupy the coastal mountains common along active coastlines further modify the pattern of RSL movements (e.g. James *et al.*, 2000; Clague and James, 2002; Hetherington and Barrie, 2004; Larsen *et al.*, 2005; 2009b), resulting in a dynamic and complex RSL history. Unravelling the mechanisms of RSL change and their individual contributions at active plate boundaries helps us understand tectonic processes and crustal response to changes in ice and/or water load, define ranges of isostatic correction to apply to tide gauge and satellite data, and estimate models of future RSL change.

South central Alaska, USA, is a tectonically active region with a history of great ($M_w \geq 8$) earthquakes during the late Holocene (Figure 1.1). In upper Cook Inlet, these processes result in rapid coastal coseismic submergence and periods of interseismic land uplift (Plafker, 1969; Combellick, 1994; Hamilton and Shennan, 2005a; Hamilton *et al.*, 2005; Hamilton and Shennan, 2005b; Shennan *et al.*, 2008). Glaciers in eleven mountain ranges cover approximately 75,000 km^2, (5% of the state), with one third of the total area contained in the coastal Chugach and Kenai Mountains of south central Alaska, bordering Cook Inlet (Molnia, 2008). During the Little Ice Age (LIA), the most abrupt climate fluctuation of the Holocene (Grove, 2004a), mean annual temperatures fell to an estimated 2^{o}C below present with many glaciers reaching their maximum Holocene position c. AD 1890 (Mann *et al.*, 1998; Molnia, 2007). Subsequent mass loss in southern Alaska and British Columbia is estimated to supply over half the contribution to

global sea-level from sources outside Greenland and Antarctica during the past 50 years, and 0.12 ± 0.02 mm yr^{-1} from the mid AD 1962 to 2006 (Berthier *et al.*, 2010). The coastal margins of south-central Alaska therefore provides an excellent location in which to test models of RSL response to short-term climate fluctuations and associated ice mass change in a tectonically active location.

RSL is the elevation of the sea relative to the land at a given point in space and time, which results from a combination of non-seismic and seismic processes. Shennan and Horton (2002) express changes in RSL ($\Delta\xi_{rsl}$) at any location in space (ϕ) and time (τ) by:

$$\Delta\xi_{rsl}(\tau,\phi) = \Delta\xi_{eus}(\tau) + \Delta\xi_{iso}(\tau,\phi) + \Delta\xi_{tect}(\tau,\phi) + \Delta\xi_{local}(\tau,\phi)$$

Where $\Delta\xi_{eus}$ is the time-dependent eustatic function, $\Delta\xi_{iso}$ is the total isostatic effect of the glacial rebound process including both the ice (glacio-isostatic) and water (hydro-isostatic) load contributions, $\Delta\xi_{tect}$ is the tectonic effect and $\Delta\xi_{local}$ is the total effect of local processes at the site involved, including changes in sediment deposition/erosion and tides, which can amplify or suppress any RSL changes resulting from changes in the other three functions. Recent work modelling the fingerprint of melt of the Greenland and Antarctic ice sheets shows the eustatic function can also vary spatially due to deformation of the geoid due to the effects of self gravitation in the surface mass load (e.g. Tamisiea *et al.*, 2001).

Although previous work has been done looking at non-seismic RSL change during the EDC, there has been no evaluation and quantification of the $\Delta\xi_{iso}(\tau,\phi)$ component in Upper Cook Inlet, despite its potential importance. This thesis therefore focuses on assessing the isostatic component of RSL change during the last earthquake deformation cycle (from c. 900 yr BP to present) in upper Cook Inlet, Alaska through analyses and interpretation of field based evidence of RSL changes and geophysical modelling. Section 1.3 outlines the background of research that forms the foundation of the thesis with section 1.4 defining the resulting research hypotheses.

1.2 Definitions

Definitions of terms used in this thesis:

Little Ice Age (LIA): Grove (2004a) defines the LIA as AD 1300-1850. In Alaska, early mountain glacier advances were underway from AD 1180s to 1320s. The middle and late advances occurred in AD 1540s to 1710s and AD 1810s to 1880s respectively. This thesis considers the LIA as c. AD 1200-1900 in line with the three Alaskan advance phases.

Peat-silt couplet: The unique RSL history of south central Alaska associated with the earthquake deformation cycle model of land level change results in couplets of silt and peat, where fine-grained clastic sediment overlays peat, with a sharp stratigraphic boundary between the two due to rapid coseismic submergence. During the interseismic phase, the RSL fall results in a transition from silt back to freshwater peat (Figure 1.2).

Earthquake Deformation Cycle (EDC): Numerous EDC models describe phases of land level movement associated with plate boundary movements (Thatcher, 1984; e.g. Nelson *et al.*, 1996; Shennan *et al.*, 1999). Shennan *et al.* (1999) propose a four phase EDC model for sites in south central Alaska which experience **coseismic** submergence (rapid RSL during a great earthquake). Rapid **post-seismic** uplift (RSL fall) follows in the decades after the great earthquake, with centuries of slower **interseismic** uplift (RSL fall) and finally **pre-seismic** RSL rise prior to the next great earthquake (Figure 1.3). This EDC model applies to the sites in this thesis around upper Cook.

Mean High Higher Water (MHHW): NOAA defines MHHW as the average of the higher high water height of each tidal day observed over the National Tidal Datum Epoch. In upper Cook Inlet, the large present day diurnal tidal range (> 8 m) means it is only feasible to measure the highest tides.

Palaeo marsh surface elevation (PMSE) is the estimated elevation, relative to MHHW, which the marsh surface would have accumulated at, with an error term associated with estimating the fossil sample palaeo surface elevation.

1.3 Background

1.3.1 Washington and Oregon: Developing an Earthquake Deformation Cycle Model

Early seismological and RSL research along the Pacific Northwest coast focused on assessing the potential of great ($M_w \geq 8$) earthquakes at the subduction zone of the Juan de Fuca plate beneath the continental North American plate. Land displacements associated with the AD 1960 ($M_w = 9.5$) Chile and the AD 1964 ($M_w = 9.2$) Prince William Sound, Alaska earthquakes (Plafker, 1969) led to the hypothesis that the coastal sedimentary sequences of Washington and Oregon record similar prehistoric earthquakes. Atwater (1987) documents the presence of a series of buried peats sharply overlain by grey mud containing rhizomes of the salt marsh species *Triglochin maritima* at Willapa Bay, Washington and suggests at least six occurrences of rapid land subsidence or sea level rise >0.5 m over the past 7000 years. Lithological investigation and limited bulk radiocarbon dating confirms the lateral extent and synchroneity of many of the buried peat layers along the Cascadian coastal zone, that are now attributed to RSL changes associated with multiple EDC's (Darienzo and Peterson, 1990; Atwater *et al.*, 1991; Atwater and Yamaguchi, 1991; Atwater, 1992; Nelson, 1992; Darienzo *et al.*, 1994; Atwater *et al.*, 1995; Meyers *et al.*, 1996). This information led to the development of a simple two-stage earthquake deformation cycle (EDC) model of interseismic strain accumulation producing RSL fall, followed by rapid coseismic subsidence and RSL rise (Figure 1.3) to explain Holocene RSL changes in Cascadia (Long and Shennan, 1994).

Tide gauge data, detailed levelling and observations prior to and following great earthquakes in Japan and Alaska shows that a two-stage EDC model based on lithostratigraphy and limited radiocarbon dating is an oversimplification. Gradual deformation occurs during interseismic strain accumulation, and initially includes a rapid post-seismic recovery phase, which the lithostratigraphy does not record (Plafker, 1969; Brown *et al.*, 1977; Savage and Thatcher, 1992). Spatial variations in the pattern and direction of coseismic deformation, with the region nearest to the plate boundary uplifting, and a parallel zone, arcward of the area of uplift, subsiding (Plafker, 1972) may be difficult to discern, as lithological evidence of coseismic uplift may be hard to distinguish from local erosional processes (Nelson *et al.*, 1996). Nelson (1992) note that lithofacies assessment alone cannot distinguish peat-mud boundaries resulting from seismic processes from those due to non-seismic factors, particularly when considering a single estuarine sequence. To improve understanding of RSL changes along active coastlines, Long

and Shennan (1994) propose the application of biostratigraphic techniques and the tendency approach (Shennan *et al.*, 1983) to allow rigorous testing of EDC models and separation of seismic from non-seismic processes.

The sea level tendency approach developed through studies of UK and European coastal sequences as a means to analyse and correlate sea level data at a range of spatial scales (Shennan *et al.*, 1983). The 'tendency' of sea level refers to whether there is an increase or decrease in the proximity of marine conditions, regardless of any vertical changes. Knowledge of the ecological tolerances of biological proxies including diatoms, foraminifera and pollen in the contemporary environment applied to microfossil assemblages, allows definition of the sea level tendencies between or within stratigraphic units, in contrast to methods solely based on lithostratigraphy. Radiocarbon dating of sea level index points allows the correlation of many tendencies and identification of regional patterns of RSL changes (e.g. Tooley, 1985; Shennan, 1986; Shennan and Horton, 2002). This approach therefore has the potential to aid understanding of interseismic and coseismic RSL movements.

Combining lithological, biostratigraphical and dating methods, Nelson *et al.* (1996) outline five criteria for identifying regional coseismic subsidence, including suddenness, amount and synchroneity of submergence, lateral extent of peat-mud couplets and possible tsunami concurrence, and propose a methodology for identifying RSL changes and the recurrence intervals of multiple EDCs. Applying this approach to sequences at Johns River, Washington (Shennan *et al.*, 1996) and Netarts Bay, Oregon (Shennan *et al.*, 1998) revealed a post-seismic phase of rapid RSL fall following a great earthquake and a three stage EDC model. Moreover, diatom analysis at Netarts Bay highlighted a possible fourth EDC phase of pre-seismic RSL change (Figure 1.3), suggested to be evidence for a reduction in the rate of interseismic strain accumulation in the decades prior to a great earthquake (Long and Shennan, 1998). To have confidence in these models required rigorous testing against a well-documented great earthquake.

1.3.2 South Central Alaska: Testing and Refining the Earthquake Deformation Cycle Model

The M_w = 9.2 Prince William Sound earthquake on March 27 AD 1964 resulted from a 600 - 800 km rupture of the eastern segment of the Aleutian megathrust, producing surface

deformation over 170,000 to 200,000 km^2 of south-central Alaska (Plafker, 1969) (Figure 1.4). Uplift extended from the southeast coast of Kodiak Island north to Prince William Sound and east to Yakataga, with a maximum vertical displacement of 11.3 m at Montague Island (Plafker, 1969). Land subsidence of up to 2.5 m occurred from Kodiak Island northwards, affecting the western Prince William Sound, Kenai Peninsula and the Cook Inlet, the northern and western Chugach Mountains, southern Talkeetna Mountains and western Wrangell Mountains. Local subsidence due to coseismic land-level fall in the greater Anchorage region and Turnagain Arm ranged from >0.5 m to <1.5 m (Plafker, 1969). Plafker's (1969) measurements and associated contouring of the amount of land displacement are given as absolute changes in altitude based on comparison of pre- and post-earthquake tide gauge readings, the position of the upper growth limit of certain intertidal organisms relative to tidal datum, differences in the pre- and post-earthquake positions of the lower growth limit of terrestrial vegetation, differences in the heights of pre- and post-earthquake storm beaches, estimates or measurements of changes in the position of shoreline markers by local residents, measured changes in the height of tidal bench marks relative to tidal datum and comparison of pre and post-earthquake offshore depth soundings. Observations before and after the event provide important information on pre- and post-seismic land and sea level movements (Karlstrom, 1964; Plafker, 1965, 1969; Brown *et al.*, 1977; Savage and Plafker, 1991; Plafker *et al.*, 1992; Freymueller *et al.*, 2000; Atwater *et al.*, 2001) (Figure 1.5) which allow testing of the EDC models developed in the Pacific Northwest.

A preliminary multiproxy study at Girdwood, Alaska (Shennan *et al.*, 1999) recorded four phases of land-level change during the last earthquake cycle, including a pre-seismic stage. Changes in diatoms from freshwater assemblages below to marine assemblages above the AD 1964 earthquake peat-silt boundary at Girdwood are less than expected, compared to the 1.70 m of submergence estimated by Plafker (1969). To further quantitative reconstruction of RSL changes through the EDC and to allow for the large diurnal tidal range in upper Cook Inlet, Zong *et al.* (2003) developed a transfer function using 44 contemporary diatom samples from Kenai and Portage flats. Applying the model to the AD 1964 earthquake shows the average reconstructed value of 1.78 ± 0.23 m coseismic subsidence at Girdwood is very close to Plafker's (1965) 1.70 m estimate. Diatom reconstructions at Kenai (Hamilton and Shennan, 2005b) resulted in an estimate lower than the 0.5 m interpolated from data points at Anchorage and Seldovia, suggesting values extrapolated over long distances by Plafker (1969)

mask local scale changes. The testing of these biostratigraphic methods of RSL reconstruction against the documented AD 1964 earthquake provides confidence in being able to refine the EDC model and applying these approaches to further fossil sequences.

To improve the performance of the transfer function developed by Zong *et al.* (2003), Hamilton and Shennan (2005a) developed an upper Cook Inlet contemporary diatom training set of 154 samples from Kenai, Ocean View and Girdwood. Standardising for tidal range differences and developing a range of transfer functions to apply to different lithologies has allowed reconstruction of RSL changes through multiple peat-mud couplets at Girdwood, Ocean View, Kenai and Kasilof, providing further evidence of a four stage EDC (Hamilton, 2003; Hamilton and Shennan, 2005a; Hamilton *et al.*, 2005; Hamilton and Shennan, 2005b; Shennan and Hamilton, 2006; Shennan *et al.*, 2008). A transplant experiment to simulate the rapid submergence of coastal peat by marine silt refutes the suggestion of sediment mixing as the cause of the pre-seismic RSL signal (Hamilton *et al.*, 2005). As the number of prehistoric coseismic events showing a pre-seismic RSL signal increases (Shennan *et al.*, 2008), the alternative hypothesis of the El Niño-Southern Oscillation (ENSO) being the mechanism for pre-seismic RSL change also becomes unlikely. Shennan *et al.* (2008) identify seven earthquakes at Girdwood since 3870–3640 BP, with an average of one every 600-650 years and the longest interval 790–920 years between the penultimate and the AD 1964 earthquakes (Figure 1.3). Shennan *et al.* (2008) note that reconstructing RSL changes and recurrence intervals based only on lithology and radiocarbon dating would have resulted in incorrectly identifying nine great earthquakes over this period, highlighting the importance of the biostratigraphical approaches developed in Cascadia and Alaska.

1.3.3 Non-seismic RSL change in the upper Cook Inlet

Non-seismic controls on RSL operate on both active and passive coastal margins and include changes in tidal regime, eustasy, hydro- and glacio-isostasy and deformation of the geoid, which modify regional and local patterns of RSL. To allow the preservation of buried peat-mud couplets when there is non-seismic RSL change, the interseismic uplift must be equal to or less than the coseismic subsidence (Hamilton and Shennan, 2005a). Hamilton and Shennan (2005a) represent the changes between two peat-mud couplets at a single location by the following equation identifying the role of non-seismic controls on RSL during an earthquake deformation cycle:

$$\Delta\xi_{int}(\tau) = \Delta\xi_{rsl}(\tau) + \Delta\xi_{cos}(\tau) - \Delta\xi_{sed}(\tau) - \xi_{peat}(\tau)$$

- $\Delta\xi_{int}(\tau)$ is the post- and inter-seismic uplift during time (τ)
- $\Delta\xi_{rsl}(\tau)$ is the non-seismic RSL change during time (τ)
- $\Delta\xi_{cos}(\tau)$ is the amount of coseismic subsidence across the upper peat-mud couplet accompanying subduction zone earthquake
- $\Delta\xi_{sed}(\tau)$ is the net sedimentation (including consolidation) between the tops of two peat layers
- $\xi_{peat}(\tau)$ is the difference in the formation elevation of the top of the first buried peat layer and the formation elevation of top of the second buried peat layer.

The application of the transfer function methodology to peat-mud couplets in south central Alaska has identified periods of RSL change which do not fit the proposed four-stage EDC model, suggesting that non-seismic controls on RSL are superimposed on the seismic RSL changes. Within the peat layer of the last earthquake cycle at Girdwood and Kenai, diatom changes record RSL oscillations of a 0.16 ± 0.13 m and 0.11 ± 0.13 m rise followed by a 0.12 ± 0.13 m and 0.09 ± 0.13 m fall respectively (Hamilton and Shennan, 2005a; 2005b) (Figure 1.6). Hamilton and Shennan hypothesise the fluctuation is a consequence of glacial isostatic adjustment (GIA) during Little Ice Age (LIA) glacier advance in the nearby Kenai and Chugach Mountains (e.g. Calkin *et al.*, 2001; Molnia, 2008). Shennan *et al.* (1999) note the magnitude of GIA effects in Turnagain Arm is poorly known, as at many other active coastal locations.

1.3.4 GIA at tectonically active locations

A primary focus of GIA research is the vertical land movements following the Last Glacial Maximum (LGM) deglaciation of the Laurentide, Fennoscandinavian, Antarctic, Greenland and British-Irish ice sheets from 22,000 yr BP. Global GIA models use databases of geological RSL data, GPS measurements, tide gauge and satellite data to refine estimates of Earth rheology and global patterns of vertical and horizontal land deformation (e.g. Peltier, 1986; Wu *et al.*, 1999; Lambeck and Purcell, 2001; Peltier *et al.*, 2002; Shennan *et al.*, 2002; Peltier, 2004; Milne *et al.*, 2006; Long *et al.*, 2008; van den Berg *et al.*, 2008). Regional patterns of post-LGM RSL at plate-margin locations often do not fit global GIA model estimates; for example Argus and Peltier (2010) do evaluate post glacial rebound models such as ICE5G(VM5a) west of the

eastern edge of the Rocky Mountains because they are not on the interior of the North American plate. James *et al.* (2000) suggest present day postglacial rebound uplift rates at the Cascadia subduction zone are ten times or more smaller than the rates predicted by ICE-3G. Upper mantle viscosity and lithosphere thickness variations may account for the offset between the global GIA model estimates and geological data at seismically active coastal margins.

The mantle rheology of a plate boundary can differ from tectonically stable mid-plate locations. Studies of crustal deformation following great earthquakes infer the presence of a low viscosity upper mantle ($<10^{20}$ Pa s) at Pacific subduction zones (Thatcher *et al.*, 1980; Wahr and Wyss, 1980; Thatcher and Rundle, 1984; Wang *et al.*, 1994; Suito and Hirahara, 1999; 2001; Suito and Freymueller, 2009). Anderson (1975) shows this low viscosity zone, the asthenosphere, is fundamental in allowing plate movement. Isostatic studies from subduction zones are limited, but most show that to fit post LGM RSL data to model estimates of land displacement requires an upper mantle viscosity $<10^{20}$ Pa s (Maeda *et al.*, 1992; Bills *et al.*, 1994; James *et al.*, 2000; 2009b). The low upper mantle viscosity promotes short relaxation and response times to changes in surface load due to the relatively rapid horizontal flow of the upper mantle, resulting in sea level changes that are more rapid than at a tectonically stable coastline (for regional RSL summaries at tectonically stable coastlines see Lambeck *et al.*, 1998; Dyke and Peltier, 2000; Shennan and Horton, 2002).

Geological data constrains post LGM RSL change along the Cascadia subduction zone. Microfossil data from the Strait of Georgia, British Columbia, records RSL fall from 150 m above present to -15 m below from 14,000 yr BP to 11,500 yr BP (Hutchinson *et al.*, 2004; James *et al.*, 2005). On eastern Vancouver Island RSL fell c. 100 m in <2000 years around 12,500 yr BP, with a relaxation time (defined by Heiskanen and Vening Meinesz (1958) as approximately 63% of the ultimate isostatic uplift to be achieved) of <1000 years (Mathews *et al.*, 1970; Clague *et al.*, 1982; James *et al.*, 2009a). Hutchinson *et al.* (2004) estimate a mean rate of post-LGM rebound in southern British Columbia of 0.11 m yr^{-1} in the first millennium following deglaciation of the Cordilleran ice sheet. James *et al.* (2009a) and Hutchinson *et al.* (2004) propose present day uplift of c. 0.1 mm yr^{-1} due to Late Pleistocene collapse of the south-western sector of the Cordilleran Ice Sheet. They suggest this small present day GIA rate is a consequence of the low-viscosity of the mantle in the region. There is however some

discrepancy. While considering RSL changes associated with the EDC cycle, Long and Shennan (1998) suggest geological data from Washington and Oregon shows a late Holocene north-south trend of 0.25 ± 0.02 mm yr^{-1} 100 km^{-1} continuing isostatic uplift, 2.5 times that estimated at Vancouver Island. Additionally, Hetherington and Barrie (2004) note a second wave of crustal depression during the mid Holocene in the Queen Charlotte Basin, Canada, for which they are unable to suggest a viable mechanism, though note that complicated tectonics play a significant role in late Quaternary crustal movements. However, the potential of active plate boundary locations to experience rapid GIA means there is possibility for a rheological response to short-term smaller surface load changes.

Hemispheric cooling during the Little Ice Age (LIA) resulted in maximum Holocene advances of many mountain glaciers (Grove, 2004a, b). The associated surface load changes have the potential to invoke a viscoelastic response where the lithosphere is thin and the upper mantle viscosity low. In southeast Alaska, GPS, geological and dendrochronology records show rapid rebound following the collapse of large tidewater glaciers at the end of the LIA. Dendrochronology records at Juneau show 3.2 m of uplift since c. AD 1780 (Motyka, 2003) and raised shorelines in upper Lynn Canal record -5.7 m RSL change in the same period (Larsen *et al.*, 2005). GPS measurements demonstrate continuing rapid crustal movement of >25 mm yr^{-1} (Larsen *et al.*, 2004). Geological evidence in Icy Bay suggests the fluctuating sea level record is relatively synchronous with periods of regional glacier advance and retreat (Mann and Streveler, 2008). Similarly in Patagonia, (where the Nazca oceanic plate subducts under the South American plate north of the Chile Margin Triple Junction, and the Antarctic plate subducts under the South American plate to the south) GPS measurements show rapid crustal uplift (c. 39 mm yr^{-1}) likely in response to ice mass loss following the LIA (Rignot *et al.*, 2003; Dietrich *et al.*, 2010). In both southeast Alaska and Patagonia, regional late Holocene GIA models require a low viscosity asthenosphere (2.4-4.0 x 10^{18} Pa s and 4.0-8.0 x 10^{18} Pa s respectively) to fit field observations with model predictions (Ivins and James, 1999; Larsen *et al.*, 2005; Klemann *et al.*, 2007; Dietrich *et al.*, 2010).

The potential for a subduction zone coastal margin to experience rapid GIA in response to small changes in ice load due to the presence of a low viscosity upper mantle, means isostatic driven sea level changes may be overprinted on tectonically controlled land-level changes. My thesis therefore considers geological evidence and model estimates of how the Earth responds to

small-scale ice load changes at a tectonically active coastline. The LIA in south central Alaska provides an excellent context in which to test whether GIA has contributed to regional RSL change against the established framework of the last EDC.

1.4 Research hypotheses

The background of research outlined in section 1.3 has led to the formation of the main research hypothesis:

Glacial isostatic adjustment is an important contributor to relative sea level change in upper Cook Inlet during the last earthquake deformation cycle.

I address the main research hypothesis through RSL reconstruction and modelling to evaluate the following working hypotheses:

1. There is evidence for non-EDC RSL change during the Little Ice Age in upper Cook Inlet, Alaska.
2. The RSL change is spatially variable.
3. The RSL change occurs during periods of regional glacier advance and retreat.
4. The mechanism of RSL change is GIA.

1.5 Summary

The history of RSL research at active plate margins outlined above has produced EDC models of tectonic land and sea-level movements that provides a testable template against which to measure deviations due to other non-seismic factors. The presence of a low viscosity upper mantle at a subduction zone promotes a short relaxation time to glacio-isostatic loading. The LIA in south central Alaska provides an excellent context in which to test whether GIA has contributed to regional RSL change against the established framework of the last EDC in south central Alaska where present knowledge of GIA is limited. Chapter 2 gives an overview of south central Alaska and the field sites in upper Cook Inlet. Chapter 3 outlines the methodology used to test the research hypotheses. Chapter 4 presents the geological results and Chapter 5 the modelling data. Chapter 6 integrates the geological results and modelling data to test the

research hypotheses. Chapter 7 highlights the main conclusions and outlines the wider implications of the research.

Chapter 2 : Field Area

2.1 Introduction

This chapter introduces the study area by providing a background to upper Cook Inlet and Turnagain Arm, summarising in section 2.2 the main characteristics of its climate, tidal and coastal process, geology, tectonic setting and glacial and anthropogenic histories. Section 2.3 provides an overview of the four field sites selected for coring in Turnagain Arm in order to test the hypotheses in section 1.4.

2.2 Regional Introduction

Alaska is the largest state of the United States of America, covering over 1.4 million km^2. To the east it borders Canada with the rest of state surrounded by the Pacific and Arctic Oceans and Bering Sea. The Cook Inlet in south central Alaska stretches 350 km from Barren Islands, Gulf of Alaska to Anchorage where it divides into Turnagain Arm and Knik Arm (Figure 2.1). The Cook Inlet watershed covers 120,000 km^2, draining water from the surrounding Chugach and Kenai Mountains and Aleutian Range through rivers including the Susitna, Matanuska and Kenai.

2.2.1 Climate

The Cook Inlet region of Alaska marks the transition between the maritime climate of the southern coastal area and the continental climate of the interior (Shulski and Wendler, 2007). Girdwood is the western limit of the southern Alaska rainforest. Precipitation varies greatly due to the maritime influence of the Gulf of Alaska and local mountainous relief. Tutka Bay at the southernmost point of the Kenai Mountains records the highest average annual

precipitation of the Cook Inlet region of 1,683 mm yr^{-1}, whilst the lowest average of 352 mm yr^{-1} occurs at Mirror Lake, northeast Knik Arm (Shulski and Wendler, 2007). Average July maximum temperature for the Cook Inlet is 19°C and the average January minimum -14°C (Shulski and Wendler, 2007).

2.2.2 Tides and coastal processes

The complex interplay between glacial history (section 2.2.5) and sea level dominates upper Cook Inlet late Pleistocene and Holocene coastal history. LGM ice and a bank of moraines blocked marine waters entering Cook Inlet until c. 16 k yr BP, where marine microfossils in a coastal terrace 5 to 12 m above present sea level between Kenai and Kasilof record marine waters in Cook Inlet reaching as far north as Kenai. By 14.9 ± 0.3 k yr BP the marine transgression reached Anchorage and into Turnagain Arm, recorded by marine fauna in the Bootlegger Cove Formation near Point Woronzof, Anchorage (Schmoll et al., 1972; Schmoll, 1977; Bartsch-Winkler et al., 1983). A late Pleistocene glacial advance c. 12 k yr BP likely prevented marine waters entering Turnagain Arm, though by 10.7 k yr BP the glaciers had retreated to Hope (Reger and Pinney, 1996). By 9.5 k yr BP mountain passes became ice free (Reger and Pinney, 1996) and flood tides have been bringing mineralogical material into Turnagain Arm since at least 8.2 ± 0.1 k yr BP (Bartsch-Winkler et al., 1983).

Changes in bathymetry and coastal configuration during the late Pleistocene and Holocene alter tidal regimes. Griffiths and Peltier (2009) show that significant changes in coastal configurations and the loss of shallow marginal seas at the LGM (26 k yr BP) greatly amplified ocean tides relative to present. Tidal regimes in inlets and fjords such as the Cook Inlet began to establish following deglaciation. The base of a core at Portage, at the head of Turnagain Arm, contains abundant foraminifera indicating a normal salinity, deep water environment from c. 8.2 to 6.5 k yr BP following the retreat of the ice sheets (Bartsch-Winkler et al., 1983). Above this, the core contains sediments indicative of cyclic episodes of intertidal, subtidal and subaerial deposits suggests deposition by tidal processes (complicated by eustatic sea level changes, GIA, cosesismic sediment consolidation and tectonic land level changes (Bartsch-Winkler et al., 1983)) and likely associated with an increase in the tidal prism. There is no research to date into Holocene palaeotidal regimes in Cook Inlet. Models of other estuaries and bays, such as the Humber (Hinton, 1995; Shennan et al., 2000b; Shennan et al., 2003), Gulf of Maine and Bay of Fundy (Gehrels et al., 1995), southern North Sea (Austin, 1991), estimate

increased tidal range over the Holocene in association with global sea level rise. Williams and Robinson (1979) show, in particular diurnal tidal amplification in association with reduced water depth. Sediment infilling in Turnagain Arm during the late to mid Holocene likely resulted in shallower bathymetry and increasing tidal range, with the tidal prism forming a large proportion of the water in the Arm at high tide. During the LIA, a period of hemispherically cooler climate (Mann and Jones, 2003; Jones and Mann, 2004), potential eustatic steric sea level fall (discussed further in section 6.2.4) may have resulted in further reduced bathymetry, potentially amplifying tidal range.

Present day Upper Cook Inlet and Turnagain Arm are macrotidal, with semidiurnal tides and a mean tidal range of 7.98 m at Anchorage and a diurnal range of 8.89 m (NOAA), exposing up to 90% of the Turnagain Arm mudflats at low tide. A 1.2-1.8 m tidal bore forms in the inner Turnagain Arm and travels inland from Bird Point at up to 4 m sec^{-1} (Bartsch-Winkler and Ovenshine, 1984; Greb and Archer, 2007) deforming soft sediments along Turnagain Arm (Greb and Archer, 2007) (Figure 2.2). Many glacially fed rivers enter Turnagain Arm (including Glacier Creek, Twenty Mile River, Resurrection Creek and Sixmile Creek) discharging 2.5 million tons of sediment and resulting in seasonal salinity variations (Bartsch-Winkler and Ovenshine, 1984). Tributary discharge during spring/summer snowmelt amounts to over 5 x 10^3 m^3 s^{-1} (Oey *et al.*, 2007) resulting in salinity at Anchorage in summer of 7-15 ‰ rising to 17-22 ‰ in winter (Batten *et al.*, 1978). Outside the turbid waters of Turnagain Arm, summer upper Cook Inlet salinity at Nikiski is around 26 ‰ (Gatto, 1976). Peaks in suspended sediment in Turnagain Arm are associated with peak fluvial discharge and periods of midtidal flow, with typically fine to coarse silt transported by tidewater, with medium silt comprising an average of 35% and clay 2-4% of the suspended material (Bartsch-Winkler and Ovenshine, 1984).

During the winter, ice floes, often greater than 320 m wide with individual blocks 1 m thick, form in upper Cook Inlet (Bartsch-Winkler and Ovenshine, 1984). Ebb tides deposit blocks of ice on tidal flats and marshes (Figure 2.3), often restricting tidal inundation inland. Repeated refreeze of the blocks over the winter incorporates tidal silt and sand into the ice, which once melted, can leave accumulations of sediment on the marsh surface (Hamilton *et al.*, 2005).

2.2.3 Geology

The higher relief of the eastern Turnagain Arm results in exposed bedrock, with the lowland western Turnagain Arm and upper Cook Inlet dominated by Pleistocene glacial deposits (Figure 2.4). The Kenai and Chugach Mountains comprise of Cretaceous and Upper Jurassic Rocks (Beikman, 1980), with Turnagain Arm dominated by sandstones and mudstones of the Upper Cretaceous Valdez Group east of Hope and Indian Creek to Port Wells in the western Prince William Sound (Beikman, 1980; Wilson and Hults, 2008). The valley slopes and bottoms contain unconsolidated colluvium and alluvium surficial deposits, alongside Pleistocene and Holocene glacial material (Combellick, 1984a, b; Schmoll *et al.*, 1999). Rocks of the McHugh Complex separate the Kenai Peninsula and Anchorage basin at the western end of Turnagain Arm from the Valdez Group. The northern Kenai Peninsula bedrock geology comprises of Upper Tertiary Continental Deposits of the Kenai Group topped with a complex series of glaciolacustrine and Pleistocene glacial deposits (Karlstrom, 1964; Beikman, 1980; Reger *et al.*, 2008). Pleistocene deposits, including glacio-fluvial, -deltaic and -estuarine and glacial diamicton, up to 500 m thick, top Tertiary sandstone bedrock in the Anchorage basin and Knik Arm (Beikman, 1980; Combellick, 1999; Schmoll *et al.*, 1999).

2.2.4 Tectonic setting

The present day tectonics of south-central Alaska are affected by the oblique collision of the Yakutat terrane into Alaska and subduction along the Aleutian megathrust of the Pacific plate beneath the Alaskan plate (Plafker and Berg, 1994) (Figure 2.5). The Pacific plate moves northwards at 55 mm yr^{-1}. The Yakutat microplate, a fragment of the North American plate that is partially subducted beneath and partially accreted to the continental margin of North America, moves northwest at 40-50 mm yr^{-1}, 10-20^{o} counter-clockwise to the direction of the Pacific-Alaska convergence (Fletcher and Freymueller, 1999; Bruhn *et al.*, 2004). Within the upper Cook Inlet region, the Pacific plate and Yakutat terrane subduct together with the resulting thicker lithosphere (estimated in places >100 km) reducing volcanism (Fuis *et al.*, 2008). Upper Cook Inlet also contains subsidiary faults, including the Border Range and Castle Mountain Faults, that have the potential to propagate seismic activity (Bruhn and Haeussler, 2006).

Sudden deformation of any part the active tectonic boundaries results in large to great (M_w > 8) magnitude earthquakes (Figure 1.1). The largest historical earthquake in upper Cook Inlet (M_w

= 9.2) occurred in AD 1964. A 600-800 km rupture of the eastern segment of the Aleutian megathrust produced surface deformation over 170,000-200,000 km^2 of south-central Alaska (Plafker, 1969) (Figure 2.5) with upper Cook Inlet experiencing up to 2.5 m of subsidence and a zone uplift seaward of the subsidence region. Palaeoseismic investigations record six other great earthquakes in upper Cook Inlet over the past 4000 yrs (Shennan and Hamilton, 2006; Shennan *et al.*, 2008) as a likely consequence of a rupture of one or multi segments of the Aleutian megathrust and/or Yakutat microplate (Shennan *et al.*, 2009). Alaska also experiences intraplate earthquakes with ruptures along interior faults, including the M_w = 7.9 AD 2002 Denali Fault earthquake (Figure 1.1).

Ruptures along any part of the Alaskan offshore plate boundaries have the potential to cause tsunamis (Shennan *et al.*, 2009). Tsunami waves affected the coastline bordering the Gulf of Alaska during the AD 1964 earthquake, though the geography of the upper Cook Inlet prevented any tsunami waves reaching north of Kenai (Plafker *et al.*, 1969). Tsunamis also occur in association with volcanic debris avalanches, for example the eruption of Augustine in AD 1883 which resulted in detailed written accounts of large waves around southern Cook Inlet (Begét and Kowalik, 2006; Begét *et al.*, 2008; Waitt and Begét, 2009). Begét and Kowalik (2006) model the portion of the Augustine volcano which collapsed into the Cook Inlet and show that a less than 50 cm of tsunami wave would have reached upper Cook Inlet, largely due to the event occurring during low tide. Kowalik and Proshutinsky (2010) model tidal and tsunami interactions in Cook Inlet and suggest the a potential tsunami at Anchorage can be damped if the tsunami occurs at high or low tide or be slightly amplified if the tsunami occurs when the tide is in transition between high and low tide at Anchorage. Coastal sediments around southern Cook Inlet record at least four tsunami events around upper Cook Inlet in the last 4000 years, the largest of which occurred c. 1600 yr BP and deposited sediments up to 7 m high along the southern Kenai Peninsula (Begét *et al.*, 2008). Similarly to the AD 1964 earthquake, there is no record of tsunami deposits in 4000 years of sediment at Girdwood (Shennan et al., 2008), likely due to the orientation of Turnagain Arm c. 90^o to Cook Inlet.

2.2.5 Glacial history

Molnia (2008) divides Alaska into fourteen glaciated regions. Surrounding the upper Cook Inlet, around Turnagain Arm, are the western Chugach Mountains and the Kenai Mountains, and to the west, the southern Alaska Range (Figure 2.1). Geomorphological and lacustrine

records provide evidence of late Quaternary glacier advance and retreat, dated by dendrochronology, lichenometry, radiocarbon, cosmogenic exposure ages and tephra layers. The following section provides a brief overview of Last Glacial Maximum (LGM) and Holocene glacial history of the upper Cook Inlet.

Late Wisconsinan (LGM) glaciation

The western extension of the North American Cordilleran Ice Sheet covered south central Alaska and the adjacent continental shelf during the LGM (Late Wisconsinan) (Manley and Kaufman, 2002). Ice, fed by moisture from the North Pacific, covered 727,800 km^2 (compared to 74,700 km^2 at present) (Figure 2.6), with equilibrium line altitudes 200-700 m below present (Kaufman and Manley, 2004; Barclay *et al.*, 2009). In southern Alaska, glaciers retreated from their terminal position c. 22-19 k yr BP (Briner and Kaufman, 2008) with four phases of post-LGM glacial readvance occurring in the Cook Inlet region (Reger and Pinney, 1996, 1997; Reger *et al.*, 2008). By the start of the Holocene, ice margins were at or behind their modern position (Barclay *et al.*, 2009).

Holocene glacial history

Early to middle Holocene glacier termini were at or retracted from their present positions, with only limited evidence from interior Alaska of any periods of advance (Calkin, 1988; Barclay *et al.*, 2009). Mann *et al.* (1998) suggest the Holocene climate c. 10-6 k yr BP in Alaska was warmer than today with mean July summer temperatures 14-16 ^{o}C. From c. 6-3.5 k yr BP climate began to cool and precipitation increased around the Gulf of Alaska, with climate deterioration during the height of the Neoglacial after c. 4-3.5 k yr BP. Major advances of land-based glaciers in Alaska in Saint Elias, Chugach and Coast Mountains occurred between c. 3.3-2.9 k yr BP, though subsequent, larger glaciations removed much of the geomorphological evidence of any possible early Neoglacial ice advance in southern Alaska (Wiles and Calkin, 1994; Calkin *et al.*, 2001; Barclay *et al.*, 2003; 2009).

A further phase of glacier advance occurred during the First Millennium AD with the main interval in the Chugach and Kenai Mountains c. AD 430-720 (Wiles and Calkin, 1994; Reyes *et al.*, 2006; Wiles *et al.*, 2008). During the Medieval Warm Period (c. AD 900-1240) glacier recession led to renewed forefield forests at many glaciers termini (Barclay *et al.*, 2009). Late Holocene glacial advance culminated in the second millennium during the LIA. Grove (2004a) defines the LIA as AD 1300-1850, though early advances were underway in Alaska from AD

1180s to 1320s. The middle and late advances (AD 1540s to 1710s and AD 1810s to 1880s respectively) (Figure 2.7) resulted in Holocene maxima for many land-terminating glaciers in the Chugach and Kenai Mountains (Wiles and Calkin, 1994; Wiles *et al.*, 1999; Calkin *et al.*, 2001; Molnia, 2008; 2008; Barclay *et al.*, 2009). Portage Glacier, at the head of Turnagain Arm, advanced 5 km from its present position c. AD 1890 (Mayo *et al.*, 1977; Crossen, 1992). No tidewater glaciers enter upper Cook Inlet, though several occur in the western Chugach Mountains, terminating in Prince William Sound (e.g. Columbia, Harvard and Yale Glaciers). These tidewater glaciers have fluctuated greatly throughout the Holocene and appear to be significantly controlled by non-climatic factors, with advances spanning multi-decadal and century length warm and cold periods (Molnia, 2008; Barclay *et al.*, 2009).

Recent glacier changes

The majority of Alaskan mountain glaciers have retreated and/or thinned from their maximum LIA positions. Molina (2007; 2008) documents changes in Alaskan glaciers from photographs, satellite data and glaciological records and suggests nearly every glacier that descends below an elevation of c. 1500 m is currently thinning and/or retreating. Exceptions in the Chugach Mountains are the tidewater Meares and Havard Glaciers, which advanced during the latter part of the twentieth and early part of the twenty-first centuries, and Bryn Mawr, Harriman and Columbia Glaciers that advanced during the early part of the Landsat baseline decade (AD 1972-1981). The recent changes in Columbia Glacier are an example of the dynamic nature of Prince William Sound tidewater glaciers. During c. AD 1900-1950, the glacier exhibited a series of advance and retreat phases, but following its unpinning from a submarine moraine and Heather Island in AD 1979 the glacier began retreating by c. 15 km and thinning by as much as 400 m (Meier *et al.*, 1980; Molnia, 2007; 2008). Portage Glacier, a terrestrial terminating glacier during the nineteenth century began retreating from the early AD 1900's, changing to an unstable lacustrine calving glacier, which initiated rapid retreat of c. 5 km from its LIA maximum in AD 1890 (Crossen, 1992; Kennedy *et al.*, 2006).

Recent satellite and airborne altimetry measurements of Alaskan glacier changes, aim to quantify the magnitude of ice loss and contribution to global sea level change. Ardent *et al.* (2006) use airborne altimetry measurements to determine volume changes of 23 glaciers in western Chugach Mountains, with average net balance rates of -3.1 to 0.16 m yr^{-1} for tidewater glaciers and -1.5 to -0.02 m yr^{-1} for the non-tidewater glaciers. They extrapolate this to

estimate a total regional sea level equivalent rise of 0.020 ± 0.003 mm yr^{-1} between AD 1950/1957 and 2001/2004. Berthier *et al.* (2010) revise the estimate with updated analysis and suggest that between AD 1962 and 2006 Alaskan glaciers lost 41.9 ± 8.6 km^3 yr^{-1} of water and contributed 0.12 ± 0.02 mm yr^{-1} to sea-level rise, 34% less than estimated by Ardent *et al.* (2006) (further discussion in section 3.7.2). Larsen *et al.* (2007) estimate a net average rate of ice loss in south east Alaska from the 2000 Shuttle Radar Topography Mission (SRTM) data of 16.7 ± 4.4 km^3 yr^{-1}, equivalent to a global sea level rise contribution of 0.04 ± 0.01 mm yr^{-1}. Chen *et al.* (2006) and Luthcke *et al.* (2008) use data from the Gravity Recovery and Climate Experiment (GRACE) to compute mass changes of the Gulf of Alaska glaciers of c. -101 ± 22 km^3 yr^{-1} (April 2002 – November 2005) and -102 ± 5 Gt yr^{-1} (April 2003 – March 2006) respectively. These models are reliant on global GIA models, such as ICE5G(VM2) (Peltier, 2002). Despite disagreement in absolute values and differing regional analysis, recent research indicates the general trend of recent changes in Alaskan glaciers is largely one of mass balance loss.

2.2.6 Anthropogenic history

The anthropogenic history of Alaska is relatively short, with rapid population expansion only occurring in the last 130 years. Prior to the expeditions of Bering (AD 1725-1730 and AD 1733-1745) and Cook (AD 1776-1779) occupation of Alaska was solely by Native Peoples with the Tanaina and Dena'ian Indians (Athapaskan tribe) living in the Cook Inlet-Susitna River basin and Kenai Peninsula respectively (Gibson, 1976). From c. AD 1750, Russian fur hunters began to explore the southern and western coasts for sea-otter pelts, setting up permanent establishments in the Cook Inlet from AD 1787 (Naske and Slotnick, 1987). In AD 1867, Russia sold Alaska to the USA and rapid development and population growth (Table 2.1) occurred as a consequence of gold discovery, initially in southeast Alaska from AD 1870 (Naske and Slotnick, 1987). Gold mining in Turnagain Arm started in AD 1888 at Sunrise, resulting in 3,000 people in Hope by AD 1896. In AD 1897, due to the Klondike gold rush in the Canadian Yukon, the population at Sunrise fell to 150. However, the easier conditions of Turnagain Arm, compared to interior Alaska-Canada, attracted around 10,000 people to the area in a second gold rush in AD 1898 (Hope and Sunrise Historical and Mining Museum, 2005). Mining continued around Turnagain Arm until c. AD 1940 when activity dramatically reduced due to the Second World War, though some mining continues to the present day (Lampright, 2008).

Population growth led to the building of railways to connect the coast to interior Alaska. In AD 1903, railroad construction started at Seward reaching the head of Turnagain Arm in AD 1910. Rail building started again from Ship Creek (now part of Anchorage) in AD 1915, and in AD 1923, Seward and Fairbanks connected. The establishment of Ship Creek as the headquarters of the Alaska Railroad resulted in the expansion of, the initially tent city of, Anchorage, and population (Table 2.1) and infrastructure in upper Cook Inlet rapidly developed from AD 1915 (Naske and Slotnick, 1987). In AD 1950, the Anchorage-Seward Highway opened.

Oil and gas exploration in Cook Inlet started with the first discovery on the Kenai Peninsula in the 1850's, though it was not until the opening of the Swanson River field in AD 1957 that it became commercially viable. In AD 1964, Shell installed the first Cook Inlet offshore platform and oil and gas mining continues in the Cook Inlet to present (Naske and Slotnick, 1987).

2.3 Field sites along Turnagain Arm transect

Coastal salt marshes regularly inundated by the tides provide archives of past sea level change; therefore a series of salt marshes along a transect in Turnagain Arm were selected to test the hypotheses defined in section 1.4. A transect of sites away from the main ice load centres of the Chugach and Kenai Mountains will allow identification of any spatial pattern of GIA land surface deformation. Coastal marshes along Turnagain Arm exist at Portage, Girdwood, Bird Point, Hope, Chickaloon Bay and Ocean View. Coring by Combellick (1991) at Portage shows the top 4 m of the sequence dominated by glaciofluvial sands and silts with no pre-AD 1964 peat layer or coastal sediments from which to reconstruct RSL changes over the past earthquake deformation cycle. Chickaloon Bay has no road access and is not a feasible field site due to restrictive costs in terms of access. The following sections outline the geography of the remaining four marshes selected for core sampling.

2.3.1 Girdwood

Girdwood is located at the eastern end of Turnagain Arm (Figures 2.1) and is divided into three marshes by Glacier and Virgin Creeks (Figure 2.8). A small cliff (<1 m) along much of the marsh front separates the salt marsh from the tidal flats and snags from the AD 1964 forest are still present in many areas (Figure 2.9). Ponded water and small creeks dissect the marsh and its landward limit is c. 500 m north of the Seward Highway. Previous work at Girdwood records a

series of peat silt couplets representing c. 4000 yrs of sediment accumulation over multiple earthquake cycles (Shennan *et al.*, 2008) (Figure 2.10). This site is central to this thesis as a core by Hamilton and Shennan (2005a) reveals evidence for an oscillation in RSL which does not fit the expect model of EDC land level changes (Figure 1.5) (section 1.3.4).

2.3.2 Bird Point

Bird Point is a bedrock outcrop on the northern shore of Turnagain Arm (Figures 2.1) where salt marsh has colonised the lower relief (Figures 2.11 and 2.12). The contemporary marsh is constrained landward by the Alaska Railroad and steep topography. Small areas of AD 1964 snags occur towards the back of the marsh (Figure 2.12). Ponded water occurs in the central landward section of the salt marsh and a few small creeks dissect the tidal flats entering the subtidal channel. A previous field investigation reveals the presence of peat-silt couplets (Dugdale, 2006).

2.3.3 Hope

Hope is a small delta located approximately half way along the southern shore of Turnagain Arm (Figures 2.1 and 2.13). Prior to the AD 1964 earthquake, buildings, subsequently submerged during the earthquake, covered the present tidal marsh (Hope and Sunrise Historical and Mining Museum, 2005). Exploratory coring at Hope by Quinn (2006) and again in 2008, shows that in many locations less than one meter of silt lies beneath the vegetated surface which overlies glacio-fluvial gravels and building remnants on the marsh east of Resurrection Creek. Bear Creek and its tributaries dissect a large proportion of the eastern marsh, some of which is presently used for grazing. The marsh west of Resurrection Creek is constrained landwards by a steep wooded bluff (Figure 2.14). At the western most extent a small cliff (<1 m) separates the salt marsh from the tidal flats and there are remains of a few pre-AD 1964 snags (Figure 2.14).

2.3.4 Ocean View

Ocean View forms part of the Anchorage Coastal Wildlife Refuge. The marsh borders southern Anchorage and it is constrained landwards by a steep coastal bluff c. 20 m high (Figures 2.1 and 2.15). Significant areas of pre-AD 1964 forest snags cover the tidal marsh, particularly at the Coral Lane transect (Hamilton *et al.*, 2005) (Figure 2.16). Seaward of the AD 1964 snags are

extensive shallow graded tidal flats (Figure 2.16). Coring along three transects by Hamilton *et al.* (2005) reveal up to five peat-silt couplets at Ocean View (Figure 2.17).

2.4 Summary

The study area for this thesis is upper Cook Inlet, in particular Turnagain Arm. The system is macrotidal and experiences strong mixing and changes in salinity. South central Alaska is tectonically active with the subduction of the Pacific plate underneath the North American plate resulting in repeated great earthquakes along the Aleutian megathrust. The North American Cordilleran Ice Sheet covered the area during the LGM. By the start of the Holocene glacier limits were up valley or near to their present position. During the Neoglacial there have been several episodes of glacier advance and retreat, with the most recent being the height of the LIA in which many mountain glaciers advanced to their late Holocene maxima. This chapter introduces the four field sites that are the focus of this thesis. They form a transect away from the centre of former ice loading to more peripheral areas. Previous work at Ocean View and Girdwood provides a regional tectonic framework in which to test the hypotheses outline in section 1.4. Chapter 3 outlines the methods used to test the hypotheses.

Chapter 3 : Research Design

3.1 Introduction

This chapter outlines the methodologies used to address the research hypotheses set out in section 1.4. Firstly, it outlines the methods of field sampling undertaken at Girdwood, Bird Point, Hope and Ocean View, followed by the subsequent laboratory lithological, chronological and biostratigraphical analysis of the sample sediments. It then details the numerical techniques used to quantify the rate and magnitude of RSL change over the last earthquake cycle in upper Cook Inlet using these data. Finally, it outlines the modelling methodology used to assess the spatial pattern of possible LIA-associated GIA and RSL change.

3.2 Field methods

3.2.1 Sediment sampling

I sampled sediment at one or more sites in Turnagain Arm in August 2006 (Girdwood), August 2007 (all) and August 2008 (all). Any sample collected in the field for further analysis, by either monolith or coring, was wrapped in plastic for transportation and stored in a fridge on arrival at Durham. Fossil sediment cores extend from the present surface to the penultimate peat-silt boundary, thought to represent the c.900 cal. yr BP great earthquake as dated at Girdwood, Ocean View and Kenai (Shennan and Hamilton, 2006).

Girdwood

Shennan *et al.* (2008) present a detailed record of the lithostratigraphy at Girdwood (Figure 2.10) that formed the basis for further sampling in this thesis. A small cliff at the marsh edge

present in 2006 and 2008 allowed access for stratigraphic description and sample collection from three areas of the marsh (Figure 3.1) using the Troels-Smith scheme (Troels-Smith, 1955; Long *et al.*, 1999). Samples were collected with either 50 cm or 25 cm monolith tins driven horizontally into the sediment face and then dug out with a spade and knife.

Bird Point

Initial coring with a 25 mm diameter gouge and description of stratigraphy along a marsh front transect at Bird Point in 2007 identified the area with sediments most likely to record RSL change over the past earthquake cycle, away from potential disturbance associated with the construction and operation of the railway. BP-07-3 provides material for initial diatom analysis (Figure 3.2). Gouge coring in 2008, along a landward transect and selected areas of the marsh front transect, provide a fuller record of the stratigraphy, and allowing the two recorded peat-silt couplets to be placed in the wider regional tectonic context. I collected a sample core from the location of BP-08-6, with the aim of collecting a core with sediments unaffected by marsh front processes, and equally far enough away from the railway to avoid any sediment disturbance which may have occurred during its construction (Figure 3.2). The uppermost 50 cm was collected in a monolith tin, the deeper sediments by multiple 50 cm diameter piston cores across the peat-silt boundary through to the base of the peat. Sampling with the piston corer compacts the peat layer, though a simple correction based on the ratio between the known depth sampled and extruded sample length allows approximate correction of samples for compaction during sampling and extrusion. A gouge core provided non-compacted sediment for diatom analysis. The gouge core also sampled the penultimate peat silt boundary, as the overlying silt is too compact to use a Russian or piston corer

Hope

Exploratory coring with a gouge in 2007 at Hope showed that peat-silt couplets, visually similar to those recorded elsewhere through upper Cook Inlet, only exist at the western extent of the marsh, away from the glacio-fluvial deposits of Resurrection Creek and former foundations of the town of Hope. Gouge core HP-07-11 provided material for initial diatom analysis (Figure 3.3). Bear activity on the marsh in 2008 prevented further detailed recording of the stratigraphy although marsh front exposures cleaned using a spade and a landward transect of gouge cores provides a general overview of the site lithostratigraphy (Figure 3.3). A piston core

(HP-08-1) sampled sediment from just below the present marsh surface to 18 cm below the penultimate peat-silt boundary.

Ocean View

Previous sampling at Ocean View by Hamilton *et al.* (2005) provides a detailed record of the lithostratigraphy along two transects at Ocean View (Figure 3.4) and material for diatom analysis from a previously unanalysed core (OV-02-4) (Figure 2.17). New gouge coring in 2008 extends the stratigraphic record along the Coral Lane transect seaward of the ghost forest and identified a location (OV-08-2) for collecting multiple cores to provide the volume of sediment required for dating (Figure 3.4). A 162 cm long piston core extends from the surface, with multiple samples collected over the peat-silt boundary. A gouge core sampled next to the piston core samples from the peat-silt boundary through to the base of the peat provides non-compacted sediment for diatom analysis.

3.2.2 Tidal measurements

The upper Cook Inlet has a large tidal range (section 2.2.2) and the funnel shape of Turnagain Arm results in significant spatial variations in tidal levels between sites (Oey et al., 2007). Tide gauges are present only at Anchorage and Kenai in upper Cook Inlet, and to be able to relate levelled core and modern sample elevations to a reference tidal frame requires repeated measurements of high tides at each field site. Still water high tide measurements at Girdwood and Ocean View were completed by Hamilton and Shennan (2005a), and I took similar high tide measurements at Hope and Bird Point in 2007 and 2008, each time levelled to a local bench mark on the marsh. I use MHHW, defined as the average of the higher high water height of each tidal day, averaged over the United States National Tidal Datum Epoch (Pugh, 1996), as the reference tidal level. This is because 90% of Turnagain Arm becomes tidal flats at low tide, preventing the measurement of the complete tidal cycle relative to Chart Datum. Measurements of local high tides of differing elevations allows comparison with the same high tides on the same day measured at the tide gauge at Anchorage, the recordings of which are verified by NOAA and corrected for atmospheric pressure. This allows relation of local samples to a standardised tidal level, and determines patterns of tidal amplification or dampening within Turnagain Arm.

3.2.3 Modern diatom sampling

Hamilton and Shennan (2005a) present a modern diatom assemblage training set of 154 samples from upper Cook Inlet that I revise to calibrate fossil RSL changes over the last earthquake deformation cycle. The Modern Analogue Technique (MAT) shows some previous fossil diatom assemblages have a poor modern analogue (Hamilton and Shennan, 2005a) and new modern samples aim to address some of these gaps. At Hope, there is gradual succession from tidal flat to high marsh providing a suitable landward transect (Figure 3.3) along which to collect additional surface samples with the aim of improving the transfer function models performance, whilst also providing new modern analogues from the central part of Turnagain Arm, in particular from the waterlogged high marsh. Two new samples from a Girdwood back marsh pond (Figure 3.1) also have the potential to provide a modern analogue not included in the existing upper Cook Inlet training set. I collected samples from the top 1 cm of sediment in order to allow for variations in assemblage due to seasonal diatom blooms and winter freezing, sealed them in a plastic bag and levelled each to MHHW. Closing levelling errors showed greater than 0.5 cm precision.

3.3 Lithological laboratory methods

3.3.1 Bulk density

Bulk density of a sample is required in the calculation of sediment accumulation rates and age-depths models by AMS radiocarbon and gamma dating. Bulk density of sediment varies due to mineral composition, degree of compaction and porosity. Bulk density measurements follow the *Standard Test Methods for Bulk Density of Peat and Peat Products* (ASTM D 4531-86), yielding the wet (ρ) and dry (ρ_d) bulk density of 1 cm slices of fossil sediment.

Bulk density is calculated by:

$$\rho = (M/AL)\ \text{g cm}^{-3}$$

Where:

M is the mass of the wet sample, or if calculating dry bulk density, the dry sample mass after drying the sample overnight at 105^{o}C

A is the cross-sectional area of the sample as measured with electronic callipers

L is the length of the sample.

3.3.2 Organic content

Organic content of coastal sediment, as expressed by percentage loss on ignition (%LOI), varies with position in the tidal frame, with sediment accumulating in the tidal flats having low organic content compared to material accumulating near or above MHHW where vegetation coverage is greater (Woodroffe and Long, 2009). Measuring percentage LOI through a fossil sequence helps determine changes in palaeoenvironment, which, in conjunction with other microfossil and sedimentary data, enables identification of marsh surface elevation change.

Percentage LOI is calculated by weighing dry sediment, burning it at 550^{o}C for four hours and then weighing the remaining ash using the following equation:

$$\text{LOI (\%)} = \frac{(\text{weight of dry sediment - weight of ash})}{\text{weight of dry sediment}} \times 100$$

3.4 Chronological methods

A well constrained chronology is required to quantity the rate of any RSL change over the last earthquake cycle and correlate with the regional late Holocene glacial history. I use a multi-method dating approach that combines AMS radiocarbon dating of terrestrial plant macrofossils, gamma dating (^{210}Pb and ^{137}Cs), tephrochronology, lead isotopes ^{206}Pb/^{207}Pb and for the first time in Alaska, the pollutant history associated with gold mining. To allow the most effective use of resources, two master cores, one from Girdwood (GW-08-3) and one from Bird Point (BP-08-6), provide two detailed age-depth profiles over the last earthquake cycle. Larsen *et al.* (2005) show the largest magnitude Earth displacement occurs closest to the area of greatest post-LIA ice mass loss in south east Alaska. Choosing cores from the two sites closest to the Kenai and western Chugach Mountains, where any LIA associated GIA signal may be greatest, will allow correlation of RSL history with the established regional late Holocene glacial chronology (section 2.2.5). I develop a less detailed chronological framework and lithological correlation for the sequences from Ocean View and Hope.

3.4.1 AMS Radiocarbon dating

Accelerator mass spectrometry (AMS) radiocarbon dating makes use of the three natural isotopes of carbon: stable ^{12}C and ^{13}C and radioactive ^{14}C. Following its production in the lower stratosphere and troposphere ^{14}C is oxidised to $^{14}CO_2$, allowing transfer of ^{14}C into the biosphere and oceans. The supply of ^{14}C to living organisms compensates for the decay of existing ^{14}C in the organism and results in equilibrium in the concentration of ^{14}C in the living organism and the atmosphere. When an organism dies, the supply is cut off and the ^{14}C concentration decreases by radioactive decay at a rate of the radiocarbon half-life (5730 years). AMS counts the ^{14}C atoms relative to the stable ^{12}C and ^{13}C isotopes in a sample, against a material of known ^{14}C, producing a sample/modern ratio which allows calculation of a radiocarbon age (Hua, 2009).

Solar variability, in particular solar winds, controls the atmospheric production rate ^{14}C, resulting in non-constant atmospheric ^{14}C in the past (Reimer *et al.*, 2004). Calibration of radiocarbon ages to calendar years uses the variations in atmospheric ^{14}C measured in independently dated materials, including tree-rings and corals, and is summarised by calibration curves such as the Northern Hemisphere terrestrial dataset: IntCal04 (Reimer *et al.*, 2004). Large fluctuations in atmospheric ^{14}C characterise the last 500 years, largely driven by the Spörer, Maunder and Dalton solar minima and changes in the carbon cycle associated with LIA climate changes as well as human industrial activity (Stuiver and Quay, 1980; Bard *et al.*, 1997). As a result, a plateau exists in the relationship between radiocarbon ages and calendar years from AD 1650 to 1950 (Reimer *et al.*, 2004), complicated further by the effect of nuclear weapons from AD 1950 (Hua and Barbetti, 2004). This potentially limits the use of radiocarbon dating in recent sediments as several possible calibrations solutions can exists for one date, reducing the precision of a single radiocarbon sample. To improve the precision and accuracy of the individual dates and age-depth model I apply two forms of wiggle match dating.

Wiggle match dating (WMD) of AMS radiocarbon dates provides a means of using the details of the radiocarbon calibration curve to provide a detailed chronology from samples collected in stratigraphic sequence (Bronk Ramsey *et al.*, 2001). The approach has previously been successfully applied to several tidal marsh sequences to provide detailed age-depth models (van de Plassche *et al.*, 2001; e.g. Gehrels *et al.*, 2006; Marshall *et al.*, 2007). WMD uses a set of radiocarbon samples to form a block of wiggles to compare to those in the calibration curve.

WDM requires a series of closely spaced ^{14}C dates combined with measurements of bulk density to identify changes in sedimentation, and if necessary define sample boundaries (Yeloff *et al.*, 2006). The first method in this thesis follows the approach presented by Marshall *et al.* (2007) of dating salt marsh sediments by maintaining the inter-sample stratigraphic relationship and including *a priori* knowledge of the stratigraphy and independent age markers to reduce dating uncertainties. This allows selection of the most appropriate calibration in the 2σ range with the option of plotting data manually on the IntCal04 ^{14}C curve (Reimer *et al.*, 2004) where there continues to be a range of possible dates. The second approach uses Bayesian analysis, Markov Chain Monte Carlo sampling and appropriate depositional models in OxCal 4.1 with calibration by IntCal04 (Bronk Ramsey, 1995; 2001; Blockley *et al.*, 2007; 2008; 2008, 2009). Steier and Rom (2000) suggest that the assumptions used to transform additional information into probability distributions to refine Bayesian age models may create results with higher precision of dates, but lower accuracy (i.e. reduced agreement with the true ages of samples). To ensure confidence in the models Bronk Ramsey (2000) highlights the need to trial several models allowing result comparison. Using a multifaceted approach, I am able to compare the results of different Bayesian age models, the results of the OxCal depositional models and results of the age models developed using visual WMD, and subsequently choose the most appropriate solution.

Several factors complicate radiocarbon dating of salt marsh sediments. Coastal marshes receive both inorganic and organic carbon from a range sources resulting in contamination by both younger and older carbon, with reworking of older material into recent sediments. Downward root penetration can produce erroneously young dates (Marshall *et al.*, 2007; Hua, 2009). Collection and careful washing of fragile salt marsh macrofossils helps target autochthonous samples and reduce contamination.

Methodology

Radiocarbon dating of the Bird Point core (BP-08-6) and Girdwood core (GW-08-3) is restricted to the mid to lower section of the pre-1964 peat to avoid complications of the bomb spike period and provide an overlap with ^{210}Pb profiles (see section 3.4). A radiocarbon allocation of 22 dates from the Natural Environment Research Council (NERC) (allocation number 1339.1008) provides 10 closely spaced dates in the most recent peat layer at Bird Point and Girdwood. Two additional dates from the penultimate peat-silt boundary at Bird Point (BP-08-

6) provides a maximum age to constrain the chronology and correlation with previously dated tectonic events in upper Cook Inlet, providing for the first time, a model of tectonic RSL change at Bird Point.

Samples for radiocarbon dating are obtained from 1 cm thick slices of peat at depths selected for dating (±0.5 cm the named depth) which are washed with distilled water through a 63 µm sieve. Above ground macrofossils >63 µm are collected under an optical microscope. Wherever possible, samples consist of seeds of the same species, and where there is not enough for a sample, identifiable plant remains, mainly leaves and small stems are included. The picked samples are dried, weighed and sealed in sterilised glass vials and taken to the NERC Radiocarbon Laboratory (NERC RCL) at East Kilbride.

Samples at NERC RCL were digested in 1M hydrochloric acid (80^{o}C, 8 hours), washed free from mineral acid with deionised water, then dried and homogenised. The total carbon in a known weight of the pre-treated sample is recovered as CO_2 by heating with copper oxide in a sealed quartz tube. The gas is converted to graphite by iron-zinc reduction (NERC RCL report). NERC RCL report the dates as conventional radiocarbon ages (years BP ± 1σ). Data calibration uses CALIB 5.0 (Stuiver *et al.*, 2005), OxCal 4.1 (Bronk Ramsey, 1995) and calibration curve IntCal04 (Reimer *et al.*, 2004). Reporting selected ages as the 2σ calibrated range in calendar years AD allows correlation with glacial and anthropogenic histories.

3.4.2 Gamma dating

Gamma dating by radioactive isotopes caesium-137 (^{137}Cs) and lead-210 (^{210}Pb) provides an alternative dating method for salt marsh sediments deposited over the last 100 to 150 years. Shennan *et al.* (1999), Hamilton (2003) and Zong *et al.* (2003) previously use radionuclide dating in upper Cook Inlet, but improved laboratory methods and analytical techniques at Durham Geography's new gamma laboratory means it is sensible to apply the approach again at Girdwood and Bird Point with the aim of developing an age-depth profile for the most recent sediments.

Caesium-137 is an artificially generated radionuclide artefact of atmospheric testing of nuclear weapons post AD 1950 with a half-life of 30 years. The radionuclide disperses globally by atmospheric circulation. The shape of the ^{137}Cs curve of concentration over depth identifies marked maxima in accordance with peak atmospheric deposition of ^{137}Cs in AD 1958 and 1963

from above ground testing of nuclear weapons and accidental discharge in AD 1985 during the Chernobyl accident (Pennington *et al.*, 1973; Cundy and Croudace, 1995; Higgitt, 1995; Milan *et al.*, 1995; Cundy *et al.*, 2003).

Lead-210 is a naturally occurring radionuclide that is part of the ^{238}U decay series (see equation below) and has a half-life of 22.3 years.

$$^{238}U \rightarrow {}^{226}Ra \rightarrow {}^{222}Rn \rightarrow {}^{214}Pb \rightarrow {}^{210}Pb \rightarrow {}^{206}Pb$$

A fraction of the ^{222}Rn atoms formed by the in soil decay of ^{226}Ra escape into the atmosphere where they decay to ^{210}Pb. ^{210}Pb reaches the sediment through precipitation or dry deposition and is buried by subsequent sediment accumulations. The flux of material from the atmosphere into the sediment provides excess or unsupported ^{210}Pb over and above that in equilibrium with the in-situ ^{226}Ra. Its subsequent decay can be used to date the sequence up to five half lives (c. AD 1880 to present) (Appleby and Oldfield, 1992).

Radionuclide dating of salt marsh sediments relies on the following assumptions (Milan *et al.*, 1995; Cundy *et al.*, 2003; Wolfe *et al.*, 2004):

1. The marsh sediments are rapid accreting (ideally at >3 mm yr^{-1} to avoid averaging of several years radionuclide deposition). In south central Alaska, where there is a short growing season, the accumulation rate in the pre-1964 earthquake peat has the potential to be lower than 3 mm yr^{-1} resulting in the possibility of averaging several years of sediment accumulation in a single sample.
2. There is no input or export of ^{137}Cs other than from atmospheric fallout. This is a fair assumption in upper Cook Inlet where there is no notable local or regional source of ^{137}Cs.
3. ^{210}Pb and ^{137}Cs remain immobile in the sediment column following deposition. This assumption varies with sedimentary and environmental conditions and is explored further below.
4. There is no reworking or erosion of the sediment. Careful selection of cores to avoid any sedimentary hiatuses prevents complications of erosion.

Site location and physical processes may influence presence and distribution of ^{210}Pb and ^{137}Cs in the sediment column. The strongest age models combine both ^{137}Cs and ^{210}Pb profiles

(Cundy *et al.*, 2003), though the difference in post-depositional mobility in salt marsh sediments can result in misfit between the two chronologies, placing assumption 3 (above) into question. ^{210}Pb is largely immobile in organic sediments, whereas ^{137}Cs, which preferentially binds to ions on clays and fine silts, may be remobilised with decomposition of organics, accelerated by a lowering of the water table (Davis *et al.*, 1984; Cooper *et al.*, 1995). In Alaska where the lithology is typically silt overlying highly organic peat; both processes may be in operation, affecting different parts of any age model developed by radionuclide dating. Turner *et al.* (2006) advise that some age models based on ^{137}Cs can suggest higher accretion rates than ^{210}Pb age models because the former applies to younger sediments, whereas the effects of root penetration and decomposition are greater in the latter. Dissolved ^{137}Cs can demonstrate a low absorption coefficient in saline conditions, resulting in low levels of ^{137}Cs in some coastal environments (Milan *et al.*, 1995). Levels of ^{210}Pb are often low to undetectable in high latitude environments as the release of ^{222}Rn from the soil decreases with increased influence of permafrost impeding its diffusion into the atmosphere (Wolfe *et al.*, 2004) and increased latitude can result in reduced precipitation (Outridge *et al.*, 2002). The presence of annual sea ice can further reduce polar sediment absorption capacity. The complications of post-depositional process, particularly in coastal environments, require being mindful that sometimes radionuclide data can only provide a coarse resolution age-depth model (Appleby and Oldfield, 1992; Cundy *et al.*, 2003; Harvey *et al.*, 2007).

As profiles of ^{210}Pb activity can vary significantly, different approaches are required to producing an age-depth model. 'Ideal' profiles of excess ^{210}Pb activity approximates to an exponential curve with depth, providing there is constant sediment accumulation over time (Cundy *et al.*, 2003). This is possible in laminated lacustrine sediments sequences where there is minimal sediment mixing, with annual varves often providing independent correlation (e.g. Cundy *et al.*, 1997; Plater *et al.*, 1998; Loso *et al.*, 2004). Two alternative dating models can allow for changes in sediment accumulation rate and deviations away from the 'ideal' ^{210}Pb curve: constant rate of supply (CRS) (Appleby and Oldfield, 1978) or constant initial sedimentation (CIC) (Krishnaswami *et al.*, 1971) models. The CIC model assumes there is a constant initial unsupported ^{210}Pb concentration, irrespective of changes which may have taken place in the net accumulation rate, and is particularly applicable in environments with appreciable reworking and mixing of sediment, for example intertidal sediments (Appleby and Oldfield, 1992). The CRS model assumes a constant rate of ^{210}Pb supply, with the initial

unsupported ^{210}Pb activity varying inversely with the rate of mass accumulation. The CRS model usually applies where there is a reduction in activity with depth or large inflections in the profile due to the in wash of sediments (Appleby and Oldfield, 1992). Where ^{210}Pb profiles deviate from an exponential curve, it is prudent to apply both the CRS and CIC models and compare results, allowing assessment of variation in predicted accumulation rates.

Methodology

The Ortec p-type Series Germanium gamma ray spectrometers at Durham University measure both ^{210}Pb and ^{137}Cs. Samples are prepared by placing 1 cm thick slices of fossil sediment in petri-dishes in the -80^{o}C freezer overnight. The samples are then freeze-dried and ball-milled to produce a fine-grained homogenised powder. The sediment is compacted into a standardised plastic gamma tube to 4 cm deep with the sample sediment mass recorded. A rubber cap and wax seals the gamma tube. The samples stand undisturbed for a minimum of 21 days to allow ^{226}Ra and ^{214}Pb to achieve equilibrium prior to gamma analysis. This means that the recorded ^{214}Pb emissions from the sample are from the supported decay of ^{226}Ra decay and not that due to atmospheric fallout. The samples are then are placed in a well detector for one week with the unique gamma ray energies of each isotope (^{210}Pb: 46.5 KeV and ^{137}Cs: 661.66 and 32 KeV) measured. The excess ^{210}Pb is calculated by subtracting ^{226}Ra concentration from the total ^{210}Pb. The activity of ^{137}Cs and ^{210}Pb is reported in Becquerels (Bq), defined as one nuclear disintegration per second (dps), with appropriate analysis of peaks in ^{137}Cs and age modelling of ^{210}Pb (see above) providing estimates of accumulation rate.

3.4.3 Pollutant history

Salt marshes and estuarine environments act as very effective sinks for heavy metals and are widely used, particularly in northern Europe, to reconstruct local and regional histories of contamination and define independent chronological horizons (1997; e.g. Berry and Plater, 1998; Callaway *et al.*, 1998; Cundy *et al.*, 2003; Gehrels *et al.*, 2005; 2007; Hwang *et al.*, 2009; Marshall *et al.*, 2009). LaPerriere *et al.* (1985) identifies heavy metal increases in placer gold mined streams in Circle Quadrangle, north of Fairbanks, Alaska with elevated levels of arsenic, lead, zinc and copper. Detection of these and with additional elements shown to have elevated levels in the contemporary streambed sediments of the Cook Inlet Basin (Franzel, 2002), including gold, magnesium, selenium, aluminium, iron and lithium, have the potential to provide an independent chronological control on the fossil sequences from the study area

marshes as a result of local and regional historical gold mining and industrial development in the upper Cook Inlet from AD 1895 ± 5 (section 2.2.6).

Ratios of stable isotopes $^{206}Pb/^{207}Pb$ also have the potential to identify regional and global sources of pollution and provide an alternative independent pollutant derived chronology. Mining and industrial development has deposited lead over the last 3000 years, with atmospheric flow pathways transporting compounds to the Arctic from Eurasia and North America (e.g. Bindler *et al.*, 2001; Outridge *et al.*, 2002; Klaminder *et al.*, 2003; Kylander *et al.*, 2009; Marshall *et al.*, 2009). Each Pb source has its own specific $^{206}Pb/^{207}Pb$ composition providing some identification of the source(s) of pollution (Komarek *et al.*, 2008). Sturges *et al.* (1993) suggest two thirds of the atmospheric particulate lead measured at Barrow, Alaska in AD 1990, with mean $^{206}Pb/^{207}Pb$ ratio of 1.161 ± 0.014, was derived from Russia and eastern Europe, with pollution from western Europe contributing to the majority of the remaining third. Notable falls in $^{206}Pb/^{207}Pb$ ratios around AD 0 due to lead production by the Romans', AD 1000-1200 from Medieval smelting, and AD 1970 associated with peak use of alkyl-lead additives in gasoline, provide chronological markers in sediment deposits, particularly at sites in Europe and around the North Atlantic (2000; Renberg *et al.*, 2001; Outridge *et al.*, 2002; Klaminder *et al.*, 2003; Gehrels *et al.*, 2005; Bindler *et al.*, 2009; Kylander *et al.*, 2009). Since the reduction and in some countries ban of lead additives to gasoline, levels of $^{206}Pb/^{207}Pb$ have begun to increase since the late 1970's (Renberg *et al.*, 2001; Komarek *et al.*, 2008). Measuring ratios of $^{206}Pb/^{207}Pb$ in cores from the four Turnagain Arm field sites has the potential to enhance the gold mining pollutant and radionuclide derived chronologies.

Similar to radionuclide isotopes, pollutant element deposition in the sediment column can vary by location and due to physical processes. Cundy *et al.* (2005) note in the Medway estuary there is no clear relationship between salt marsh elevation and heavy metal distribution though at the Seine estuary there is clear increase towards the more elevated, interior marsh areas. The strength of current, resulting in net erosion or accumulation of sediment, also controls deposition of heavy metals (Cundy *et al.*, 2007), with the uptake of elements by salt marsh vegetation greatest during the summer maximum growth season, or autumn decay (Hwang *et al.*, 2009). Remobilisation of pollutants in the sediment column can occur in association with organic decomposition and sediment oxidation (Berry and Plater, 1998; Spencer *et al.*, 2003), though the process varies by element, for example root-sediment

interactions modifies profiles of $^{206}Pb/^{207}Pb$ in salt marsh sediments (Sundby *et al.*, 2005; Caetano *et al.*, 2007), whereas iron cycling drives the redistribution of copper and zinc (Spencer *et al.*, 2003). To determine whether the pattern of element deposition in a sediment column is a consequence of natural causes or anthropogenic pollution, and therefore define a chronology, requires normalisation for grain size and provenance. Loring (1991) suggests that geochemical normalisation is superior to granulometric methods as it compensates for the mineralogy as well as the natural granular variability of trace-metal concentrations in estuarine and coastal-sediments. There is no universal methodology, so I use the ratios of element concentration to aluminium and lithium to provide comparison. Lithium is superior for normalising of sediments from glacial erosion of crystalline rocks, whereas aluminium is a major constitute of fine-grained aluminosilicates with which many trace elements associate (Loring, 1990, 1991).

Methodology

The Inductively Coupled Plasma Mass Spectrometer (ICP-MS) in Department of Geography, Durham University allows the measurements of a wide variety of elements at very low detection limits, down to 1-10 ppt for many of elements of interest. Sample preparation for detection of elements by ICP-MS follows standard laboratory methods where 1 cm thick slices of fossil sediment are placed in petri-dishes in the -80^{o}C freezer overnight. The samples are freeze-dried and ball-milled to produce a fine-grained homogenised powder. 5M water and 2M hydrogen peroxide is added in increments to a known mass of the sample and this digests any organic material until any reaction is complete. The sample then undergoes microwave digestion with 9M nitric acid and 3M hydrofluoric acid. It is then decanted and diluted to volume (typical 100 or 50 ml) for analysis by the ICP-MS. The reported element concentration in ppb by the ICP-MS converts to ppm by the following equation, with ^{206}Pb and ^{207}Pb reported as isotopic ratios.

$$\text{ppm (or kg mg}^{-1}) = \frac{\text{ICP-MS reading (ppb)}}{1000} \times \frac{\text{final volume}}{\text{sample mass}} \times \text{dilution factor}$$

3.4.4 Tephrochronology

A history of volcanic events in Cook Inlet, including eruptions of Augustine, Redoubt, Illiamna and Mount Spur, provides chronostratigraphic markers in sediment sequences around south central Alaska (Riehle, 1985). At Girdwood, a visible tephra at the base of the pre-1964 peat is

attributed to the Augustine tephra deposited c. 500 cal yr BP (Combellick, personal communication, unpublished geochemical and radiocarbon data). Micro-tephra or cryptotephra horizons are present in lake sediments and upland peats on the Kenai Peninsula (e.g. Beget *et al.*, 1994; de Fontaine *et al.*, 2007; Payne and Blackford, 2008). To allow correlation with known eruptions it is necessary to identify peaks in cryptotephras and extract shards for 'geochemical fingerprinting' (Turney and Lowe, 2001). Due to the tectonically active nature of southern Alaska, volcanic eruptions are common and distal tephra shards abundant throughout fossil sequences, therefore requiring detailed systematic sampling to identify tephra peaks.

Magnetic susceptibility measurements of two cores from Girdwood using a GEOTEK multisensor core scanner at Durham University do not show any peaks by which to identify distinct cryptotephras. Tests of extraction by floatation and ashing techniques and counting shards under a light microscope from Girdwood cores GW-NB-06-2 and GW-05-7 (Turney and Lowe, 2001; Blockley *et al.*, 2005) indicated that identifying cryptotephras and the required geochemical fingerprinting was too time consuming under the limitations of this thesis and would not greatly enhance the ability to test the research hypotheses. Further analyses were therefore not completed.

3.5 Biostratigraphical laboratory methods

3.5.1 Diatom preparation and counting

Diatom analysis of coastal sequences along Turnagain Arm is the most suitable method to reconstruct RSL change, since foraminifera preservation is poor in some fossil sequences and unable to reconstruct RSL change in freshwater peat (Shennan *et al.*, 1999; Zong *et al.*, 2003; Hamilton and Shennan, 2005a). Previous radiocarbon and ^{137}Cs dating at Girdwood and Ocean View, and the presence of a tephra dated to c. 500 cal. yr BP at Girdwood (Combellick, personal communication, unpublished geochemical and radiocarbon data) suggests that the peat layer below the most recent peat-silt boundary covers the duration of the peak in LIA glacial activity (Zong *et al.*, 2003; Hamilton and Shennan, 2005a; Hamilton *et al.*, 2005; Hamilton and Shennan, 2005b). The sampling interval for fossil diatoms varies from 1-8 cm, with a higher resolution

across sections though the peat layer thought to cover the interval of middle and late LIA and across peat-silt boundaries in order to quantify the magnitude of any coseismic subsidence.

Sampling and investigation focuses on the RSL changes during the middle and late LIA ice advances. The early advance occurs at a similar time to the c. 850 yr BP coseismic event (summarised by Carver and Plafker (2008) and Shennan *et al.* (2009)). Rapid coseismic submergence and post seismic uplift dominates the RSL history at this time, which may mask smaller scale RSL changes. In addition, the lack of datable material in the silt and the large error terms associated with reconstructing RSL through tidal flat sediments in upper Cook Inlet means it is not possible to develop a high precision RSL history during the early LIA advance.

Preparation of modern and fossil diatom samples follows standard laboratory techniques (Palmer and Abbott, 1986). Addition of 20% hydrochloric acid to a 1 cm^3 sample of sediment and warming overnight digests any organic material. The remaining material is centrifuged, decanted and distilled water added with the desired amount of residue dried on a cover-slip. Samples are mounted using the Naphrax refractive mountant that allows identification of diatoms under a light microscope at x1000 magnification. A minimum count of 250 diatom valves for each sample provides a statistically robust sample, though preservation of diatoms in some organic samples is poor and requires counting multiple slides to attain this minimum count. Identification of diatoms used Hartley *et al.* (1996), Hemphill-Haley (1993), Patrick and Reimer (1966, 1975) and van der Werff and Huls (1958-1974) with the results plotted in C2 (Juggins, 2003) and classified by the halobian classification system into five categories of salt tolerance (Table 3.1) (Hemphill-Haley, 1993). Changes in the summary salinity classes provide a qualitative indication of changes in marine influence; as the marine influence increases, brackish and marine mesohalobous and polyhalobous diatoms, usually dominant in tidal flats, will replace freshwater halobian and oligohalobous diatoms, characteristic of fresh and saltwater marsh.

3.6 Numerical Techniques and RSL Reconstruction

Numerical techniques establish the relationship between modern and fossil diatom samples to calibrate fossil RSL changes.

3.6.1 Transfer function

Transfer functions use regression to quantify the relationship between modern microfossil assemblages and an associated environmental variable (Imbrie and Kipp, 1971). Studies from numerous coastal marshes around the world identify a strong relationship between elevation and therefore salinity in controlling diatom distribution (Sherrod, 1999; Patterson *et al.*, 2000; Szkornik *et al.*, 2004; Hamilton and Shennan, 2005a; Horton *et al.*, 2006; Roe *et al.*, 2009), and I therefore use elevation as the environmental variable in the upper Cook Inlet transfer function. Calibration of the fossil diatom assemblages uses the transfer function modelled relationship between diatom assemblage and elevation to reconstruct palaeo marsh surface elevations (Birks, 1995) with the method successfully applied to the reconstruction of former sea levels from salt marshes in North America (Hamilton and Shennan, 2005a; Horton *et al.*, 2006; Shennan *et al.*, 2008), Greenland (Woodroffe and Long, 2009), Japan (Sawai *et al.*, 2004) and Europe (Zong and Horton, 1999; Plater *et al.*, 2000; Szkornik *et al.*, 2008).

Selection of the appropriate statistical method to develop the transfer function depends on whether the training set is linear or unimodal in relation to the environmental variable of interest (Birks, 1995). Using Detrended Canonical Correspondence Analysis (DCCA) within CANOCO (version 4.5, ter Braak and Smilauer, 2002) Hamilton and Shennan (2005a) show the upper Cook Inlet training set covers a long ecological gradient (> 2 SD units) in relation to elevation. CANOCO identifies several taxa having their environmental optimum within the ecological gradient and therefore unimodal methods of regression and calibration are most appropriate (Birks, 1995). Consequently, I apply the unimodal weighted averaging partial least squares (WA-PLS) technique in C2 (version 1.5.0, Juggins, 2003). WA-PLS is based on the idea of weighed averaging, in that particular species occupy specific environment niches characterised by species optima and species tolerance ranges, similar to a Gaussian distribution (Birks, 1995). WA-PLS updates this to species coefficients with associated standard errors, and takes into account any residual correlations in the biological data to improve the fit between the training set and environmental variable (ter Braak and Juggins, 1993; ter Braak *et al.*, 1993; Birks, 1995). However, WA-PLS with many components can fit data perfectly, but have little predictive value, and the optimum number of components must be determined on the predictive errors in a test set (RMSEP) (ter Braak and Juggins, 1993). In section 6.2.1, I consider the implications of selecting different components for the calibration of fossil data and resulting RSL reconstructions.

Statistical parameters produced in C2 provide a measure of the model performance and predictive ability of the training set. The coefficient of determination (r^2) measures the relationship between observed and inferred values (Birks, 1995). The root mean squared error of prediction (RMSEP) is one measure of the predictive abilities of the training set and is calculated by the cross validation technique bootstrapping where the environmental variable is reconstructed for each sample in the modern training set by random sampling and is then compared against the observed values. Bootstrapping also produces sample specific standard errors for individual fossil samples. I analyse the sample specific coefficients and performance statistics to assess the revised upper Cook Inlet transfer functions, and validity of the RSL reconstructions.

Removing samples from a training set can improve predictive ability, particularly if there is a poor relationship with the environmental variable. Misfit is often common of a few samples in a large training set covering a long environmental range and can be a result of additional variables controlling species distribution. For example, Roe *et al.* (2009) note that caution should be exercised when using diatoms as sea level indicators, as they can respond to grain size, organic content and pH as well as elevation in coastal locations. There are differing approaches to improving predictive ability. Gasse *et al.* (1995) remove samples that have a difference between the predicted and observed environmental variable of greater than one-quarter of the total range. Hamilton and Shennan (2005a) exclude samples below given elevations producing three transfer functions: one for all modern environments, one for vegetated intertidal flats to freshwater marsh, and one just for freshwater conditions. Woodroffe and Long (2009) use the WA-PLS species coefficient errors to remove taxa with high errors until the transfer function gains no more significant precision, producing a optimal 'small tolerances' model including only those species with error estimates <0.30 m. I test both the Hamilton and Shennan (2005a) and Woodroffe and Long (2009) approaches. Due to a poor relationship between the observed elevation of the samples from the lower elevations of the modern upper Cook Inlet and the environmental variable, removing taxa based on species coefficient errors results in relatively consistent r^2 values of c. 0.6 and does not produce model predictive ability to the level of the Hamilton and Shennan (2005a) models (RMSEP of 20-30 for 'small tolerance' transfer functions versus RMSEP of 2-4 for the restricted elevation models). Observations of the modern environment shows that freshwater peat does not form below an elevation of 5 m above MSL (relative to the Anchorage tide gauge), and vegetation does not

colonise the tidal flats below 3 m above MSL (Hamilton and Shennan, 2005a). Hamilton and Shennan (2005a) therefore suggest if peat is present in a core, it is appropriate to apply a transfer function with only those samples from 5 m above MSL, whereas if a fossil sample contains silt with rootlets requires a transfer function with all those samples from 3 m above MSL. Woodroffe and Long (2009) note that presence of rootlets within a fossil sample may not be a viable diagnostic of sediment originally accumulating on the vegetated part of the marsh due to the downwards penetration of rootlets from the current marsh surface into fossil sediments which may have formed in tidal flat environments. Modern root penetration is observed at the marsh front at Girdwood, however as the focus of this thesis is the upper most peat layer, it is possible to remove modern samples from the lower elevations and calibrate the fossil samples whilst being confident they did not form in a tidal flat. I rigorously test the predicted elevation of every fossil sample from the peat by applying both transfer functions to check for misfit and highlight any over prediction of elevation based on calibration using the freshwater training set (section 4.2.3).

Standardising elevations relative to MHHW and the difference in elevation between MHHW and mean sea level (MSL), using the equation below, accommodates for local tidal range differences in upper Cook Inlet (Hamilton and Shennan, 2005a).

$$SWLI_n = \frac{100(h_n - h_{MSL})}{h_{MHHW} - h_{MSL}} + 100$$

Where $SWLI_n$ is the standardised water level index for sample *n*, h_n the elevation of sample *n (m)*, h_{MSL} the mean sea level elevation (m) and h_{MHHW} the mean higher high water elevation (m). MSL = 100 and MHHW = 200 SWLI units. The freshwater transfer function contains all those samples with a SWLI >225 and the silt with rootlets transfer function all those modern samples with a SWLI >180. Calibration of fossil samples occurs as SWLI values with all predicted elevations then converted to local elevation relative to MHHW. Woodroffe and Long (2010) note the limitations of using SWLI when developing a regional training set. The SWLI method linearly standardises the height between two reference water levels so that, in this instance, MSL and MHHW, have the same SWLI at each site. When standardising data from sites with very different tidal ranges may distort the data in a different part of tidal range, which the transfer function may be very sensitive too.

The change in elevation between two fossil samples is the difference between the two reconstructed values with an error term calculated by the following formula (Preuss, 1979):

$$\sqrt{\text{elevation error } 1^2 + \text{ elevation error } 2^2}$$

3.6.2 Modern Analogue Technique

The minimum dissimilarity coefficient (MinDC) in the modern analogue technique (MAT) function in C2 has been used in past to test the performance and reliability of transfer function based RSL reconstructions. The squared chord distance dissimilarity method compares the fossil sample and the weighted mean of the 10 most similar modern samples, producing a dissimilarity coefficient for each fossil sample allowing identification of which samples have a 'poor' modern analogue compared to the modern training set (Birks, 1995; Edwards and Horton, 2000; Hamilton and Shennan, 2005a; Woodroffe, 2009). There is no convention for defining the threshold for the minimum dissimilarity coefficient to separate those samples considered to have a poor or good modern analogue. Some authors take a dissimilarity coefficient below the extreme 10^{th} percentile of the dissimilarities calculated between all modern samples as the upper threshold of a good modern analogue between fossil and modern samples (Birks, 1995; Edwards *et al.*, 2004; Horton and Edwards, 2005). Hamilton and Shennan (2005a) define a good modern analogue having a dissimilarity coefficient less than the extreme 5^{th} percentile, a close analogue within the 5-2.5^{th} percentile range and a poor modern analogue with the dissimilarity coefficient greater than the extreme 2.5^{th} percentile. Woodroffe (2006) and Jackson and Williams (2004) note that defining a single threshold value is incorrect, as the values vary depending on the distance metric used, the characteristics of the modern and fossil datasets and the ecological scale of analysis, as if all the modern samples are from very different environments no single sample will represent each other. I adopt the approach of Woodroffe (2006, 2009) using the largest minimum dissimilarity coefficient as a general indicator of whether a fossil samples is similar to samples in the modern training set. Woodroffe (2009) shows that the use of MAT does require some caution as fossil samples identified as having a 'good' modern analogue can have differing predicted elevations with different transfer functions. It is therefore important to consider the results of both transfer functions in association with the MAT results for each fossil sample to identify any misfit and provide confidence in the precision of the reconstructions.

3.7 GIA Modelling

The aim of GIA modelling in this thesis is to provide a sensible range for the spatial pattern, rate and magnitude of any GIA in upper Cook Inlet throughout the last earthquake cycle with Earth model solutions constrained by GPS measurements from (Freymueller *et al.*, 2008). Existing global GIA models (Peltier, 2004) are unable to account for small-scale load changes over short distances, so this project uses the simple postglacial rebound calculator, TABOO (Spada, 2003; Spada *et al.*, 2003, 2004), which has been used effectively in previous studies of GIA in Alaska (Larsen *et al.*, 2005).

3.7.1 TABOO

TABOO is a FORTRAN 90 modifiable code freely available for download from http://samizdat.mines.edu/taboo. TABOO is based on a number of assumptions regarding the Earth's structure. The model uses a layered, non-rotating, incompressible, self-gravitating, Maxwell viscoelastic, spherical symmetric Earth model where the density, shear modulus and Maxwell viscosity of each layer is constant (Spada, 2003; Spada *et al.*, 2003). Larger scale GIA models (e.g. Lambeck, 1993; Peltier, 2004; Milne *et al.*, 2006) cannot predict isostatic adjustment for small loads over a small spatial scale (Milne, personal communication, 2007) and are computationally very intensive. I apply TABOO in this thesis as a means for calculating first order estimates of Earth displacement to ice loading. The open source nature of TABOO means it can be adapted for use, in regards to both the ice and Earth models, and run on a personal computer. Homogenous flat Earth approximation is sufficient to evaluate the effects of variations in regional ice loads that cover less than 20^{o} of the Earth's surface (Ivins and James, 1999) and is therefore appropriate for the spatial scale of upper Cook Inlet. A limitation of TABOO is it ignores the gravitationally self consistent ocean load, which has the potential to modify the magnitude, direction and spatial pattern of Earth displacement across continental shelves as ocean loading changes over time (Walcott, 1972; Lambeck and Nakada, 1990; Mitrovica and Milne, 2002). For this thesis I use TABOO to calculate the radial displacement and rate of uplift for a number of points on the Earth's surface in response to various types of ice loads, both predefined, for example the ICE-3G model (Tushingham and Peltier, 1991), or user defined, such as Larsen *et al.* (2004; 2005) reconstruction of southern Alaska LIA glaciers. TABOO can also compute load deformation coefficients, relaxation spectra, tidal love numbers and changes in geoid height.

3.7.2 Ice Model

TABOO can handle ice loads characterised by various geometries and time histories (Spada *et al.*, 2003). Larsen *et al.* (2004; 2005) develop a regional ice load model by extrapolating recent ice volume changes of 67 glaciers measured by Arendt *et al.* (2002) using airborne laser altimetry, over 531 spherical symmetrical disks each of 20 km diameter (Figures 3.5 and 3.6) to estimate LIA ice thickness in southern Alaska in AD 1900. A piecewise load history for each disk over the last 2000 years, divided into 20 time intervals, provides differential load thickness (m) changes through the Neoglacial (Figure 3.7 and 3.8), with earlier mass changes estimated from the relative strength of advance and retreat cycles and terminal moraine positions. There is very little geological data constraining ice thickness changes in Alaska so extrapolating Arendt *et al.*'s (2002) values of glacier volume changes and taking account of terminal moraine positions provides the best model presently available. Comparing the Larsen *et al.* (2004; 2005) ice load history for disks surrounding upper Cook Inlet with newly published (e.g. Molnia, 2008) and unpublished LIA glaciological data (Crossen, 1997), suggests the Larsen *et al.* (2004; 2005) ice model as a reasonable estimate of ice load changes during the Neoglacial in south central Alaska. However, recent work by Berthier *et al.* (2010) does provide some basis for caution. Using digital elevation model (DEM) analysis Berthier *et al.* (2010) suggest ice wastage between AD 1962-2006 is 34% less than estimated by Arendt *et al.* (2002). This difference is potentially explained by the lower resolution of the Arendt *et al.* (2002) measurements, and that Berthier *et al.*'s (2010) estimate of the ice-covered area of Alaska is 2% less than Arendt *et al.*'s (2002). Therefore, the Larsen *et al.* (2004; 2005) ice model, and any subsequent solid Earth response, is potentially an upper estimate of regional GIA. It is also necessary to be aware of the stepped nature of the ice model when drawing any conclusions from the TABOO output, as any calculated Earth response will partially be a consequence of the stepped period of ice loading which may result in unnatural jumps in solid Earth response.

The 531 disk ice load model uses the 'Task #3' option in TABOO to calculate Earth response to complex loads, allowing one or more ice centres that may change at the same time (Spada, 2003; Spada *et al.*, 2003). TABOO outputs the predicted Earth response as radial displacement (m) and rate of land uplift (mm yr^{-1}) relative to the centre of the Earth (CE) (section 5.3) in response to the ice load history at a set of observer locations for a given time interval (generally every 100 years in this case). This thesis does not consider horizontal movements. Full assessment of the spatial pattern of Earth response uses multiple observer locations across

Alaska (Figure 3.9), though 8 selected locations around south central Alaska allows initial testing of the model output limiting the computational requirements (Figure 3.10).

3.7.3 Earth Model

The ice model allows Larsen *et al.* (2005) to estimate a best-fit Earth model when compared to GPS, tide gauge and raised shoreline data for south-east Alaska of a 60-70 km thick lithosphere, a 110 km thick asthenosphere of viscosity 2.5-4.0 x 10^{18} Pa s, over an upper mantle with viscosity 4 x10^{20} Pa s. Larsen *et al.*'s (2005) rheological model tuned to southeast Alaska may not be appropriate for upper Cook Inlet due to the proximity of the Alaska-Aleutian subduction zone and the presence of the subducted Yakutat terrane (section 2.2.4). In Chapter 5 I test a range of Earth models to assess the dominant geophysical response to relatively small ice load changes during the last earthquake cycle and provide a range for the rate and magnitude of possible GIA in upper Cook Inlet.

The initial Earth models comprise a simple one viscoelastic layer overlaying a homogenous core, with effective model lithospheric thickness (EMLT) values ranging from 50-150 km and mantle viscosity from 10^{18}-10^{23} Pa s (Figure 3.11). Density and elastic properties of the Earth models follow the seismic Preliminary Reference Earth Model (PREM) (Dziewonski and Anderson, 1981) which is defined using seismic data. I do not include a lower mantle to simplify the potential variables. Initial model runs showed that due the relatively small ice load changes the presence or absence of a lower mantle made no difference on the outputted rates or magnitudes of relative displacement. I expand the spherical harmonic degrees to degree and order 1024 as per Larsen *et al.* (2005) in order to resolve and understand the effects of small ice load changes. The half wavelength of a spherical harmonic (of degree '*l*') serves as an approximate representation of the spatial scale and is roughly 20,000/*l* km. Therefore the higher the degree (*l*), the finer the spatial resolution and 1024 spherical harmonic degrees approximates to 19.5 km allowing for the 20 km diameter of the ice load disks. Seismic observations from subduction margins identify the presence of an asthenospheric low viscosity zone (ALVZ) between the lithosphere and upper mantle, with the lithosphere-asthenosphere boundary being fundamental in allowing plate movement (Anderson, 1975). Therefore, a second set of more realistic and complex Earth models incorporate an ALVZ, similar to Larsen *et al.* (2005) and James *et al.* (2009b) (Figure 3.11) with the aim of providing a sensible range for

the spatial pattern, rate and magnitude of any GIA in upper Cook Inlet through the last earthquake cycle.

The limitation of TABOO in this region is it is unable to integrate the seismic structure of the Earth's rheology in south central Alaska (as issue with all existing published GIA models). There is potential that the subducting Pacific plate may modify any solid Earth response to load changes and the presence of a mantle wedge between the two plates cause solid Earth phenomena unable to be modelled by TABOO.

3.8 Summary

Coring of four sites along Turnagain Arm provides sediment for laboratory analysis and new modern samples from Hope and Girdwood creates a revised upper Cook Inlet modern diatom training set. New tidal measurements at Hope and Bird Point relate core and modern sediment samples to MHHW. Lithological, biostratigraphical and chronological analysis and subsequent numerical techniques allow the reconstruction and quantification of the rate of RSL change over the last earthquake cycle. GIA modelling, modified from Larsen *et al.* (2005) using the TABOO postglacial rebound calculator assesses the spatial extent of possible LIA associated GIA. The combined methodologies allow assessment of the research hypothesis. Chapter 4 presents the subsequent geological results and Chapter 5 the geophysical modelling results.

Chapter 4 : Geological Results

4.1 Introduction

This chapter presents the geological results from the four field sites along Turnagain Arm studied in this thesis. Section 4.2 presents the transfer function models used to reconstruct palaeo marsh surface elevation changes from fossil sediment cores. Section 4.3 describes the lithology, chronology and biostratigraphy for Girdwood, Bird Point, Hope and Ocean View, then presents the palaeo marsh surface elevation at each of these sites. Finally, section 4.4 considers the reliability of the different datasets and presents the reconstructions of RSL at each site during the last EDC.

4.2 Revised transfer function models

A quantitative diatom transfer function model provides the basis for the new RSL reconstructions. New tidal observations from Hope and Bird Point (section 4.2.1) and modern diatom samples from Hope and Girdwood (section 4.2.2) allow development of revised transfer function models (section 4.2.3) to calibrate fossil RSL changes over the last EDC (section 4.4). Revised transfer function models, with additional sampling focused on modern environments poorly represented in the Hamilton and Shennan (2005a) upper Cook Inlet model, has the potential to increase precision and accuracy of reconstructions of past sea level changes in the upper Cook Inlet.

4.2.1 Tidal observations

I surveyed the high tide on eleven occasions at Hope and ten at Bird Point in 2007 and 2008 to calculate mean higher high water (MHHW) at each site (Figure 4.1). Taking the highest point of the same high tide at both the field site and from the pressure corrected Anchorage tide gauge data on the same day, negates the complication of the cyclic nature of tides. Both field site results achieve good fit with the verified Anchorage tide gauge data and show an amplification of the tides from Hope to Bird Point as Turnagain Arm narrows, and dampening in amplitude at Girdwood (Hamilton and Shennan, 2005a). These data allow calculation of the SWLI value of the new Hope modern samples and the reconstructed water levels at each fossil core location at Hope and Bird Point (section 3.2) where MHHW = 200 SWLI units and MSL = 100 SWLI units.

4.2.2 A revised upper Cook Inlet modern diatom database

Sixteen new samples from Girdwood (Figure 3.1) and Hope (Figure 3.3) aim to provide modern diatom analogues for fossil assemblages that the Hamilton and Shennan (2005a) upper Cook Inlet contemporary dataset poorly represents (Figure 4.2). Fourteen samples from across a transect at Hope from intertidal mudflat to within high marsh vegetation over 1.64 m vertical range, record broadly alike assemblages to existing samples at similar elevations elsewhere in upper Cook Inlet. *Fragilaria vaucheria* dominate two samples from ponded back marsh environments at Hope (0.70 and 0.84 m MHHW); these assemblages are not represented in the Hamilton and Shennan (2005a) dataset. *Navicula salinarum* dominates the two new samples from standing water at the back of Girdwood marsh (at 0.82 and 0.97 m MHHW), though the elevation of the new samples fits with the occurrence of *Navicula salinarium* in previous samples. Overall, the new modern samples are consistent with the published upper Cook Inlet dataset (Hamilton and Shennan, 2005a), with the advantage of providing some new modern analogues.

4.2.3 Development of revised transfer function models

The new contemporary samples allow development of a revised set of transfer function models for upper Cook Inlet. Figure 4.3 show the results and performance of the revised upper Cook Inlet transfer function models for those contemporary samples with standardised water level index (SWLI) values greater than 180 (from here termed silt with rootlets model), to calibrate fossil samples from silt with herbaceous rootlets, and those with SWLI greater than 225 (from

here termed the peat model) to calibrate fossil samples from well developed peat (details in section 3.6). Model performance is not significantly different to those in Hamilton and Shennan (2005a), measured by both the spread of residuals and root mean squared error of prediction (RMSEP) (Figure 4.3). I do not remove residual outliers, as the spread of the data is a result of the wide range of environments captured in the training set, which is required to reconstruct past environmental change. Application of these revised transfer functions to appropriate fossil assemblages allows calibration fossil RSL changes.

To be confident in the reconstructed elevation for samples from fossil peat, where it is possible to apply either the silt with rootlets model or peat model, I calibrate the sample PMSE using both models to check for discrepancy (Figures 4.4 and 4.5). In BP-07-3 (Figure 4.4) and HP-07-11 (Figure 4.5) where the lithology is a silty peat compared to the highly organic peats found in other cores (Figures 4.7, 4.13, 4.22 and 4.26, discussed below), the peat model potentially over estimates the PMSE and is inappropriate, and therefore I calibrate the samples with the silt with rootlets transfer function. For all other fossil peat samples, with the exception of three specific samples (one in HP-08-1 and two in OV-02-4 as shown in Figure 4.5), the transfer function PMSE estimated by the peat transfer function falls within the error terms of silt with rootlets transfer function, providing confidence in the more precise peat model reconstructed elevations (in section 6.2.1 I discuss the implications of reconstruction precision and accuracy when selecting particular models). I examine the full core reconstructions and stratigraphic context in section 4.3 below.

4.3 Palaeo marsh surface elevation changes

The sections below follow the east-west Turnagain Arm transect, with increasing distance from the centre of LIA ice loading.

4.3.1 Girdwood

Lithology

Extensive previous coring at Girdwood provides a detailed picture of the lateral continuity of sediment horizons (Figure 2.10). The new cores for this thesis (Figures 3.1 and 4.6) corroborate the stratigraphy of the pre-1964 peat layer and the sharp upper peat-silt boundary and identify the widespread presence of the Augustine tephra (Combellick, personal communication,

unpublished geochemical and radiocarbon data) at the base of the peat layer. A silty-peat, with a transitional upper and lower boundary, occurs within the well developed pre-1964 peat at GW-NB-06-7 c. 65 cm from the surface, traceable to core GW-1 (Hamilton and Shennan, 2005a) to the west. Figure 4.7 summarises the loss on ignition, moisture content and bulk density of GW-08-3, which confirms decreasing bulk density and increasing organic content from the base of core towards to the top of the peat, with a slight reversal in the final 5 cm to the peat-silt contact, which ties in the with observations of Karlstrom (1964) of increased tidal inundation at Girdwood in the decade prior to the AD 1964 earthquake, and little variation in the post AD 1964 silt.

Chronology

Radionuclide data for GW-08-3 shows the expected peak in ^{137}Cs, at the peat-silt boundary (Figure 4.8) which corroborates the AD 1964 age for this contact. It is not possible to be sure of a minimum age at the tail of the curve. Measured levels of ^{210}Pb do not show an exponential decline (section 3.4.2) and fall below the measurable limit at 24 cm (Figure 4.8), too low to construct an age model. The peak in ^{210}Pb at 64 cm corresponds with a peak in stable lead (Figure 4.9). Overall, the gamma dating results add no additional chronological control beyond confidence in the age of the peat-silt boundary.

Figure 4.9 summarises pollutant data from Girdwood, showing a broad peak at 72-56 cm in normalised levels of all metals in the peat layer. It is likely the base represents the onset of gold mining in Turnagain Arm, and on this basis provides a tentative minimum age of AD 1895 ± 5 yrs at the base of the peak. The ratio of $^{206}Pb/^{207}Pb$ fluctuates around an average of 1.215 with a minimum of 1.193 at 56 cm and maximum of 1.230 at 51 cm, providing no clear chronological marker. However, the lower values in the upper most peat layer corroborate the heavy metal data, suggesting deposition of stable lead from gasoline in association with the development of Girdwood town next to the marsh from c. AD 1910 following the discovery of gold at Crow Creek.

At the base of the pre-1964 peat layer, a <1 cm thick tephra layer, correlated to the Augustine eruption c. 550 yr BP (Combellick, personal communication, unpublished geochemical and radiocarbon data) is visible in all cores at Girdwood (Figure 4.6). This, alongside radiocarbon dates from the preceding peat-silt boundary of the penultimate great earthquake (ca. 850 yr

BP, Hamilton and Shennan, 2005a; Shennan *et al.*, 2008), provide maximum ages on the Girdwood sediments considered in this thesis.

At time of writing (August 2010) new AMS radiocarbon dates for Girdwood are not available, though I expect 10 closely-spaced dates from the base to the middle of the peat at GW-08-3 in due course (samples are with the NERC Radiocarbon Laboratory).

Biostratigraphy

Data from two cores (GW-NB-06-2 and GW-08-3) show a gradual decrease in marine influence up core as the lithology changes from silty-peat to a well developed peat, prior to the 1964 coseismic submergence (Figures 4.10 and 4.11). In GW-NB-06-2 (Figure 4.10) the peat layer is characterised by freshwater *Eunotia exigua* and *Tabellaria flocculosa* which fluctuate slightly. GW-08-3 (Figure 4.11) shows a similar pattern with a slight increase in more salt tolerant species including *Diploneis surirella* and *Eunotia pectinalis* at 68-60 cm, suggesting a slight increase in marine influence. This is important since it demonstrates that the reconstructions of Hamilton and Shennan (2005a) core GW-1, are replicable in other parts of Girdwood marsh, and therefore not of purely local origin.

Reconstruction of palaeo marsh surface elevation

Quantitative reconstruction of the palaeo marsh surface elevation of each fossil diatom sample through the upper peat of GW-NB-06-2 and GW-08-3 shows a gradually rising marsh surface from c. 1.0 m above MHHW (Figures 4.10 and 4.11). At the top of the peat layer, both cores record a slight marsh surface elevation fall, in line with the pre-seismic phase of the EDC model, before rapid fall in elevation of 1.08 ± 0.29 m and 1.44 ± 0.37 m respectively, associated with AD 1964 coseismic submergence. Within the overall trend the reconstructions potentially estimate a slight marsh surface elevation fall of 0.12 ± 0.15 m in GW-NB-06-2 and 0.20 ± 0.14 m in GW-08-3, and a subsequent rise of 0.07 ± 0.14 m and 0.16 ± 0.14 respectively at 60-70 cm, from AD 1895. Hamilton and Shennan (2005a) quantify a similar fluctuation (0.16 ± 0.13 m fall followed by a 0.12 ± 0.13 m rise) in core GW-1, also 10-20 cm from the peat-silt contact. Assemblages from 74-88 cm in GW-08-3 have a poor modern analogue, due to the occurrence of *Pinnularia stomatophora* (Figure 4.11), a species not present in the modern training set. The fossil sample at 70 cm has a large proportion of *Eunotia lunaris*, resulting in an anomalously higher reconstructed palaeo marsh surface elevation than the surrounding samples.

Both cores potentially show a slight change in palaeo marsh surface elevation during the upper peat layer, following the deviation recorded by Hamilton and Shennan (2005a) in GW-1. The fluctuation is within the model error term, but the presence of reconstructed palaeo marsh surface elevation change within three cores from different parts of Girdwood marsh provides some confidence in its occurrence.

4.3.2 Bird Point

Lithology

A transect of twelve cores at Bird Point (Figures 3.2 and 4.12) shows the presence of peat-silt couplets comparable with the lithology at Girdwood. Cores at the northern end of Bird Point show limited peat development, compared to those sites located within the bedrock outcrops where peat is able to develop in a protected environment. Cores BP-08-2 to BP-07-3 contains a silty layer within the upper most peat layer, similar to the unit observed in GW-NB-06-7 and GW-1 at Girdwood. Figure 4.13 summarises the loss on ignition, moisture content and bulk density of BP-08-6 and shows a general trend towards greater organic content and generally lower bulk density in the peat compared to overlying silt. There are fluctuations in both the bulk density of the silt and the organic content of the peat, with a decrease in organic content at 90-100 cm.

Chronology

Radionuclide data for BP-08-6 show the expected peak in ^{137}Cs, at the peat-silt boundary (Figure 4.14), which corroborates the AD 1964 age for this contact. The early part of the rising trend suggests a possible minimum date of AD 1950 or 1952 at 78 cm, though this requires closer spaced samples to be certain. Though the ^{210}Pb profile shows an exponential decline (section 3.4), the levels of ^{210}Pb fall below the measurable limit at 16 cm, too low to construct an age model (Figure 4.14). Overall, the gamma dating results add little additional chronological control beyond confidence in the age of the peat-silt boundary.

The pollutant data from Bird Point (Figure 4.15) shows no clear pattern with numerous peaks in each of the normalised elements throughout the core, and levels typically half those measured at Girdwood. Bird Point is a bedrock outcrop bounded by steep slopes with small marshes forming between rock outcrops. There is no localised pollutant source, with only a few small creeks and no history of local gold mining (section 2.3.2). The pollutant results from Bird Point

suggesting dilution of mining related elements in Turnagain Arm prior to deposition. The ratio of $^{206}Pb/^{207}Pb$ fluctuates around an average of 1.225 with a minimum of 1.209 at 79 cm and maximum of 1.241 at 80 cm, though provides no clear chronological marker.

Two AMS radiocarbon dates of c. 850 yr BP from the top of the penultimate peat-silt contact (191 and 192 cm) at BP-08-6 (Figure 4.16) corroborate existing radiocarbon dates from the penultimate contact at Girdwood (Shennan *et al.*, 2008) and provide a maximum date on the sequence.

Ten closely-spaced samples from the base to the middle of the uppermost peat at BP-08-6 provide seven viable AMS radiocarbon dates (Figure 4.16). One sample did not contain enough carbon and two samples reported modern ages, likely due to contamination with post-1964 macrofossils due to modern root penetration into the peat layer, and are not discussed further. The orginial NERC radiocarbon analytical report is in Appendix 4_1.

Multiple calibration solutions exist for each date. The first method to refine the calibration solutions to produce an age model follows the Marshall *et al.* (2007) approach by maintaining the inter-sample stratigraphic relationship and including *a priori* knowledge of the stratigraphy (Figure 4.16). The increase of ^{137}Cs at 78 cm constrains the possible solutions of BP086-R1 to AD 1951-1954. It is possible to limit the modelled age ranges of BP086-R3, BP086-R4 and BP086-R5 to two solutions each, but the lack of additional independent chronological control prevents further precision. Keeping the dates in stratigraphic order does not allow constraint of the solutions of BP086-R7 and BP086-R8 beyond the two calibrations. It is not possible to limit the range of BP086-R9 beyond AD 1306-1437 due to its location at the base of the peat unit. With the lack of independent chronological control provided by gamma, pollutant and stable lead isotope results, the WMD dating approach provides a chronological model with relatively large age ranges for each radiocarbon sample.

The second approach to developing an age model uses Bayesian modelling in OxCal (Bronk Ramsey, 2001; 2008, 2009) (Figure 4.17). Markov Chain Monte-Carlo (MCMC) methods computed by OxCal provide analysis of the models. Plotting of probability distribution functions (both posterior marginal distribution and 95% probable range, based on the highest probability density) allows visual assessment of the models. An Agreement Index (AI) assesses model accuracy by checking for inconsistencies between the model and measurements.

Blockley *et al.* (2008) and Bronk Ramsey (2009) suggest an individual (A) and model (A_{model}) threshold value of 60% is appropriate and is therefore used here to identify any poor model or individual date solutions. I tested three different depositional models in OxCal: *Sequence, U_sequence* and *P_sequence* to develop an age model. The *Sequence* is the simplest, most flexible depositional model, providing posterior marginal distributions and broadest calibration ranges, but does not consider sample depth and offers no further refinement of the calibration from the Calib5.0.1 based WMD (see above). The *U_sequence* model assumes a constant (unlikely in a coastal setting) or exponential accumulation rate. Testing numerous versions of the *U_sequence* depositional model did not produce an A_{model} solution greater than the 60% threshold, suggesting the solutions are not robust. My investigations identifies the *P_sequence* model, which allows random variation from a constant accumulation rate, to be most robust in this coastal setting providing good model agreement (Figure 4.17). The first *P_sequence* model with an A_{model} 71% uses the seven AMS radiocarbon dates and marker of the AD 1964 silt-peat boundary (Figure 4.17A). However, this model shows poor agreement with radiocarbon date BP086R5, identifying a possible change in sedimentation rate. This fits with the reduction in organic content at 90-100 cm (Figure 4.13), though it is not enough to justify adding a 'boundary' to the age model. The median radiocarbon solution suggests an average accumulation rate of 0.8 mm yr^{-1} from AD 1400-1964 at BP-08-6. A second model includes an AD 1952 ^{137}Cs chronological marker at 78 cm reducing the A_{model} to 33%, below the 60% threshold, suggesting disagreement between the AMS dates and possible AD 1952 ^{137}Cs horizon (Figure 4.17B).

I choose to use the first *P_sequence* depositional age model (Figure 4.17A), without the gamma horizon, as the chronological framework for BP-08-6 as it offers the higher precision compared to the WMD solutions due to the lack of independent chronological control provided by the metal and isotope data. However, some caution must be exercised as Steier and Rom (2000) warn, as the assumptions used to transform additional information into probability distributions in Bayesian modelling may create results of higher precision, but reduced accuracy (i.e. reduced agreement with the true ages of the samples). The agreement index value does go some way in identifying where this may be an issue, for example with date BP086R5.

Biostratigraphy

The biostratigraphic data from the two cores at Bird Point (BP-07-3 and BP-08-6) varies (Figures 4.18 and 4.19). BP-07-3 contains a silty organic poor peat and in association, the fossil diatom assemblages contain a low percentage of halophobe species (Figure 4.18), compared to more developed peats at Girdwood. The diatoms show fluctuations in marine and brackish species. Through the silt unit at 79-93 cm, below the AD 1964 peat-silt boundary, *Navicula brockmanii* and *Stauroneis anceps* decrease slightly, with an associated increase in marine species including *Cocconeis peltoides* and *Delphineis surirella.* Above this, over the peat-silt contact, the proportion of freshwater species decreases and are replaced by polyhalobian taxon including *Delphineis surirella* and *Paralia sulcata*.

BP-08-6 records a gradual fall in marine species (Figure 4.19) with a slight fall in halophobe species in the peat layer. However at 92-82 cm there is a small peak in mesohalobian *Hantzschia virgata*. Over the peat-silt contact polyhalobous diatoms and *Navicula cari var cincta* replace freshwater and brackish species. The penultimate peat-silt contact at BP-08-6 also shows rapid marsh submergence with *Delphineis surirella* and *Paralia sulcata* replacing the freshwater taxon *Eunotia exigua* (Figure 4.20).

Reconstruction of palaeo marsh surface elevation

Quantitative reconstruction through the upper most peat of BP-07-3 shows fluctuating palaeo marsh surface elevation (Figure 4.18). BP-07-3 provided the opportunity for a core more sensitive to small-scale RSL changes due to its seaward position and being located lower in the palaeo tidal frame. The high silt content in the pre AD 1964 peat layer requires the use of the silt with rootlets transfer function model to calibrate the fossil samples, resulting in larger error terms. This reduces model precision and makes identification of any potential small-scale changes recorded in the stratigraphy difficult. The sample at 96 cm has a particularly large vertical error term due to the abundance of *Eunotia praerupta*, a species poorly represented in the modern training set, though MAT does not report a dissimilarity coefficient larger than the threshold value (Figure 4.18). The quantitative results suggest there were two periods of palaeo marsh surface elevation rise of 1.04 ± 1.09 m between 122-96 cm and 0.90 ± 0.65 m between 90-80 cm followed by subsequent falls. The model estimates 0.64 ± 0.64 m RSL rise across the peat-silt contact. Overall, there is a trend of rising though potentially fluctuating RSL through the upper silty-peat layer, though it is difficult to discern within the precision of the

model. The changes are very different from the Girdwood and Ocean View model of land level change during the last earthquake cycle (Hamilton and Shennan, 2005a; Hamilton *et al.*, 2005; Shennan and Hamilton, 2006), which suggest, if the transfer function is correctly reconstructing sea level, the main control may be local, marsh front processes.

The calibration of the fossil peat samples from BP-08-6 estimates rising palaeo marsh surface elevation with increased peat development, followed by a slight fall of 0.21 ± 0.30 m at 95 cm, age modelled as c. AD 1600 (Figure 4.19). The marsh surface then stabilised at c. 2 m above MHHW after AD 1650 with a trend of surface rise until AD 1964. The top of the peat layer records a rapid elevation fall of 1.72 ± 0.51 m associated with AD 1964 coseismic submergence. Overall, the reconstruction through the upper peat layer shows a trend of rising palaeo marsh surface elevation.

Reconstruction of palaeo marsh surface elevation through the penultimate peat-silt contact (190 cm below the contemporary marsh surface) of BP-08-6 shows marsh surface development up to 2 m above MHHW (Figure 4.20). At the top of the peat layer, one data points suggest a marsh surface elevation rise, in line with the pre-seismic phase of the EDC model, though this requires more data to draw any real conclusions, before rapid fall of 1.90 ± 0.47 m associated with coseismic submergence of the c.850 yr BP earthquake, producing reconstructed submergence at the penultimate peat-silt contact similar to the overlying AD 1964 contact.

The Bird Point geological results provide a history of palaeo marsh surface elevation change from BP-08-6 dated with a OxCal *P_sequence* age model (Figure 4.19). In comparison, WMD dating of the sequence requires use of independent age markers to constrain the calibration solutions, which low levels of ^{210}Pb and pollutant data are unable to provide. The biostratigraphy of BP-07-3 potentially records local scale marsh front processes.

4.3.3 Hope

Lithological results

On the marsh east of Resurrection Creek (Figure 3.3), gravels and rocks prevent cores greater than 0.5 m in many places, and where cores are deeper, the lithology is predominantly silts and gravels with very little organic material. A complex series of laminated silt and organic layers characterise the lithology west of Resurrection Creek (Figure 3.3 and 4.21) suggesting only

short periods of organic accumulation and vegetation development. The mix of gravel and laminated silty-clay is characteristic of the sediment bought down in the glacially fed Resurrection Creek. Local residents observe flooding of the Hope delta during periods of high creek flow, particularly during spring snow melt. It appears that sediment deposition at Hope is largely controlled by the fluvial discharge of Resurrection Creek.

Chronology

The complex lithology and likely sediment disturbance, due the development on the marsh during the gold rush, prevents establishing a detailed chronology at Hope. Figure 4.22 summarises the pollutant data from HP-08-1. The measured elements levels at Hope are twice those measured at Girdwood, with notably higher levels of arsenic and gold when normalised for lithology by aluminium and lithium. This is to be expected given that 5,000 people lived in Hope and neighbouring Sunrise in AD 1898 during the Turnagain Arm gold rush, with numerous gold claims on the surround rivers and creeks. It may be possible to place a tentative date of AD 1890 ± 5 yrs at the base of the peak in normalised arsenic, gold and selenium, though the other pollutants do not show a similar pattern and all measured elements fluctuate throughout the core. The ratio of $^{206}Pb/^{207}Pb$ fluctuates around an average of 1.222 with a minimum of 1.200 at 100 cm and maximum of 1.229 at 98 cm, providing no clear chronological marker. There is no radionuclide dating of the sequence at Hope as I had to focus the resource on Bird Point and Girdwood (section 3.4).

Biostratigraphy

Data from two cores (HP-07-11 and HP-08-1), show diatom changes associated with near surface peats and muds unlike those recorded elsewhere in the upper Cook Inlet (Figures 4.23 and 4.24). *Staurosirella pinnata* dominates the humified light brown peat and at the base of the laminated silt and organics layer in HP-07-11 (Figure 4.23) suggesting a brackish-freshwater ponded environment (Vos and de Wolf, 1988). Half way up the laminated silt and organic unit the marine influence gradually increases, with the occurrence of polyhalobian species including *Delphineis surirella* and *Paralia sulcata* and a decrease in *Staurosirella pinnata* and *Fragilaria leptostauron*.

Throughout the core, the biostratigraphy of HP-08-1 shows little change, with salt intolerant species dominant and no rapid change across the upper peat contact (Figure 4.24). At the base of the core *Fragilariforma virescens* dominates, replaced by *Diploneis ovalis* from 108 cm at the

base of the humified peat layer and coincident with the increase in arsenic, gold and selenium. Frequencies of *Pinnularia borealis* increase towards the top of the peat layer and across the contact. An increase in the abundance of the mesohalobian taxon *Pinnularia cruciformis* suggests a slight saltwater increase in the top 6 cm of the peat layer.

Reconstruction of palaeo marsh surface elevation

Quantitative reconstruction of the palaeo marsh surface elevation of fossil diatom samples from HP-07-11 and HP-08-1 continues to identify a complex history of marsh development at Hope (Figure 4.23 and 4.24). The bottom eight samples in HP-07-11 have a poor modern analogue due to the dominance of *Staurosirella pinnata*. The modern training set contains a maximum abundance of 2.3% *Staurosirella pinnata* compared to 76.5% in the samples from the base of HP-07-11. The upper part of the laminated silty-peat unit records fluctuating elevation change with net fall from 0.65 to 0.30 m MHHW (Figure 4.23), explaining why there is no significant organic accumulation as the palaeo-surface was low in the tidal frame.

The base of HP-08-1 records fluctuating marsh surface elevation around 1 m above MHHW, before reaching a stable high marsh 1.50 m above MHHW (Figure 4.24). The sharp upper contact of the peat to the overlying laminated silt and organics records an elevation change of 0.40 ± 0.37 m. Several samples have a poor modern analogue, and those samples that do not cross the largest dissimilarity coefficient threshold (section 3.6), still have a high minimum dissimilarity coefficient value.

It appears pollutant levels and fluvial deposition, along with elevation, controls palaeo diatom distribution at Hope. This limits their value for palaeo marsh surface elevation reconstruction. Therefore, although Hope was originally chosen partly because of the potential for mining activity to provide chronological control, the results of these analyses indicate that the mining activity has so-overprinted the RSL history that the data from this site is of little value to testing the hypotheses in this thesis. Hope may provide a context for future testing of models of metal mobility processes in a salt marsh setting (section 3.4.3).

4.3.4 Ocean View

Lithology

A transect seaward of the extensive ghost forest at Ocean View extends the Coral Lane transect (Hamilton *et al.*, 2005) and shows the continued separation of the peats E (pre AD 1964) and D (pre c.850 yr BP) by a layer of silt, onto the present day intertidal mud flat where the organic layers become more dominated by silt (Figure 3.4 and 4.25). Hamilton *et al.* (2005) record no peat E in the most seaward core of their Coral Lane transect as it is part of a sewage channel, and the new transect shows its continuation as far as core OV-08-9 on the present intertidal mudflat. The lithology of the new Coral Lane transect is comparable to the peat-silt couplets at Bird Point and Girdwood.

Chronology

Previous AMS radiocarbon dates from the top of peat D corroborate with a model of regional coseismic submergence at c.900 yr BP with similar dates at Bird Point, Girdwood and Kenai and provide a maximum date on the sequence (Hamilton and Shennan, 2005a; Hamilton *et al.*, 2005; Hamilton and Shennan, 2005b; Shennan and Hamilton, 2006; Shennan *et al.*, 2008). There are no radiocarbon dates for the upper part of the sequence. I did not carry out radionuclide dating at Ocean View due as I had to focus the resource on Bird Point and Girdwood (section 3.4), plus local observations during the earthquake (Plafker, 1969; Plafker *et al.*, 1969) and previous work (Hamilton, 2003; Hamilton *et al.*, 2005) provides confidence in the upper most peat-silt boundary being a consequence of AD 1964 submergence. Furthermore, results from Girdwood (section 4.3.1) and Bird Point (section 4.3.2) show that ^{137}Cs and ^{210}Pb can provide no further dating precision of the sediments from Turnagain Arm.

Figure 4.26 summarises pollutant data from OV-08-2. There is some pattern in the data with a trend of higher normalised ratios of arsenic, copper, magnesium and selenium at the bottom of core. Conversely measured levels of copper, lead and zinc increase in the upper part of the core. Normalised levels of arsenic and magnesium are higher than at Girdwood, though only in the peat layer. Knowledge of the development of Anchorage and its associated infrastructure does not provide explanation of the trends of pollutant data and prevents assigning any chemostratigraphic markers to OV-08-2. The ratio of ^{206}Pb/^{207}Pb is fluctuates around an average of 1.231 with a minimum of 1.143 at 76 cm (in association with a peak in normalised zinc) and maximum of 1.225 at 8, 84 and 100 cm, and providing no clear chronological marker.

Biostratigraphy

Very poor diatom preservation in OV-08-2, between 45-47 cm and below 48 cm to the base of the peat, yields diatom counts across only the upper peat-silt contact. Salt-intolerant species, including *Fragilariforma virescens*, dominate the well developed peat, falling in the top 1 cm to be replaced by marine species, including *Delphineis surirella* and *Paralia sulcata* in the overlying silt (Figure 4.27).

Diatoms through the upper peat layer in a previously unanalysed core: OV-02-4, from Hamilton *et al.*'s (2005) Shore Drive transect, are dominated by oligohalobian species including *Navicula cari var cincta* and *Staurosirella pinnata*, the latter particularly in the upper part of the peat (Figure 4.28). The dominance by *Staurosirella pinnata* at the top of the core suggests a brackish-freshwater ponded environment (Vos and de Wolf, 1988) comparable to environments seen on the contemporary marsh (Figure 4.29).

Reconstruction of palaeo marsh surface elevation

Reconstruction of the marsh surface elevation changes over the peat-silt boundary at OV-08-2 quantifies a rapid fall of 1.08 ± 0.31 m, likely due to AD 1964 coseismic submergence (Figure 4.27). A small marsh level fall, potentially associated with the preseismic phase of the EDC, precedes the rapid marsh surface submergence.

Quantitative reconstruction of the peat layer at OV-02-4 indicates the palaeo marsh surface was 1.50 m above MHHW prior to AD 1964 (Figure 4.28). The shape of reconstruction shows little change in the palaeo marsh surface elevation at the base of a core, with a trend of slightly increasing surface elevation from c. 76 cm to the peat-silt boundary. At the top of the peat layer, the fossil samples have a poor modern analogue due to the dominance of *Staurosirella pinnata*, similar to the reconstruction from Hope (HP-07-11) and elsewhere at Ocean View (Hamilton *et al.*, 2005). This core sample does not contain the overlying silt and so I am unable to quantify the magnitude of coseismic submergence.

The lithology and biostratigraphy of Ocean View is similar to couplets at Bird Point and Girdwood. The recorded patterns in the measured metal do not fit the expected pollutant increase associated with the development of Anchorage from the start of the 20th century. It may be that pollutants in the coastal marshes in Alaska are mobile down core and do not bind to the sediment to give clear chronological horizons, or that the level of heavy metals in upper

Cook Inlet is not actually that high and therefore the record is just one of natural variation, or that the large tidal range (section 2.2.2) flushes pollutants out of the system, preventing accumulation in the coastal salt marshes. There appears to be little net marsh surface elevation change through the peat prior to the AD 1964 earthquake at Ocean View.

4.4 Geological record of RSL in upper Cook Inlet over the last EDC

The focus of this chapter to this point is on quantifying palaeo marsh surface elevation change over the last earthquake cycle in upper Cook Inlet using the geological record from Girdwood, Bird Point, Hope and Ocean View. This section summarises all the data presented above, pulling together the information to be taken forward to Chapter 6 for integration with the modelling data in Chapter 5. The geological record from Hope suggests the mining activity has so-overprinted the history of sediment deposition over the last earthquake cycle, that the data from this site are of little value for RSL reconstruction in this thesis. The remainder of the thesis therefore focuses on the datasets from the three remaining sites, with the detailed chronologies and occurrence of fossil diatom assemblages with, in most instances, good modern analogues and conversion of palaeo marsh surface elevation to RSL. Figure 4.30 summarises the reconstructed palaeo marsh surface elevation changes as changes in RSL relative to MHHW (RSL calculated as: depth of the sample (m MHHW) minus palaeo marsh surface elevation (m MHHW)) against depth relative to the peat-silt boundary, to allow cross core comparison. I also recalibrate GW-1 (Hamilton and Shennan, 2005a) using the refined transfer function models. Figure 4.30 carries forward to Chapter 6 to test the five research hypotheses, excluding BP-07-3 where the reconstructed RSL changes cannot be clearly resolved by the transfer function and there is offset between the reconstructed palaeo marsh surface elevations as estimated by the two transfer function models (section 4.3.2). The core location near to the marsh edge may also indicate that the stratigraphy is more recording marsh front processes, such as sea ice deposition, rather than RSL as originally hoped when collecting the core.

To test the main research hypothesis '*GIA is an important contributor to RSL change in upper Cook Inlet during the last earthquake deformation cycle*', the geological data focuses on the RSL changes through the LIA during phases of mountain glacier advance and retreat. Grove (2004a) defines the LIA as AD 1300-1850, though early mountain glacier advances were underway in

Alaska from AD 1180s to 1320s. The middle and late advances (AD 1540s to 1710s and AD 1810s to 1880s respectively) resulted in Holocene maxima for many land-terminating glaciers in the Chugach and Kenai Mountains (Wiles and Calkin, 1994; Wiles *et al.*, 1999; Calkin *et al.*, 2001; Molnia, 2008; Wiles *et al.*, 2008; Barclay *et al.*, 2009) (section 2.2.5). Discussion focuses on the marsh changes during the middle and late LIA ice advances. The early advance occurs at a similar time to the c. 850 yr BP coseismic event (summarised by Carver and Plafker (2008) and Shennan *et al.* (2009) and with new dates from Bird Point in this thesis) (section 2.2.4). Rapid coseismic submergence and post seismic uplift dominates the RSL history at this time, which may mask smaller scale RSL changes. In addition, the lack of datable material in the silt and the large error terms associated with reconstructing RSL through tidal flat sediments in upper Cook Inlet, it is not possible to develop a high precision RSL history during the early LIA advance.

New radiocarbon dates from Bird Point and the occurrence of the AD 1400 ± 100 Augustine tephra at Girdwood (Combellick, personal communication, unpublished geochemical and radiocarbon data) identifies the onset of peat accumulation along the Turnagain Arm from c. AD 1400. The developing intertidal marshes record changes in marine influence which potentially relate to small-scale RSL changes during the middle and late LIA. Figure 4.30 summarises the transfer function estimated RSL changes recorded in the cores from Girdwood, Bird Point and Ocean View from c. AD 1400 to AD 1964. At AD 1964, all three Girdwood cores and BP-08-6 record rapid coseismic submergence. The six cores also demonstrate some inter-site variability, for example at Bird Point, where although both cores suggest net RSL rise during the upper part of the pre AD 1964 peat, the RSL changes in BP-07-3 differs from those recorded in BP-08-6 likely due to dominance of marsh front processes at BP-07-3 (section 4.3.2). Chapter 6 discusses the possible mechanisms of these RSL changes by integration of the geological data and model results.

The challenges of dating recent sediments using traditional ^{14}C techniques, requires application of a novel multi-proxy approach to develop a chronology. The results of AMS radiocarbon dating of terrestrial plant macrofossils, gamma dating (^{210}Pb and ^{137}Cs), tephrochronology, $^{206}Pb/^{207}Pb$ ratios and the pollutant history associated with gold mining allows some chronological definition, particularly using the OxCal *P_sequence* depositional AMS age-depth model from Bird Point (Figure 4.18A). The results in this chapter highlight imitations of applying some of these techniques to dating sediments from high latitude coastal salt marshes.

Chapter 6 examines some of these factors and Chapter 7 considers the implications for dating sediments from similar settings.

4.5 Summary

New modern samples from Hope and Girdwood create a revised upper Cook Inlet modern diatom training set and combine with new tidal measurements at Hope and Bird Point to create a series of revised transfer function models. Lithological and biostratigraphical data indentify changes in sediment deposition during the last earthquake cycle at coastal salt marshes at Girdwood, Hope, Bird Point and Ocean View. Chemical overprinting and physical disturbance associated with gold mining activity on the history of sediment deposition at Hope means the data from Hope is of little value to the hypothesis testing in this thesis. Calibration of the fossil diatom samples from Girdwood, Bird Point and Ocean View potentially identifies small-scale RSL changes during the interseismic period. A chronology based on WMD dating of AMS ^{14}C dates at Bird Point suggests this occurred from c. AD 1650. Chapter 6 discusses the possible mechanisms for these RSL changes by integration of this geological data and the geophysical modelling results from Chapter 5.

Chapter 5 : Geophysical Model Results

5.1 Introduction

This chapter outlines the model development to produce a range of best-fit Earth model parameters and identify the possible range of relative displacement in south central Alaska over the last 1000 years in response to regional ice load changes. As I will demonstrate best-fit model solutions comply with estimates of current uplift rates from GPS measurements and lie within the range of Earth model parameters used in modelling studies from other locations along the Pacific Northwest.

5.1.1 Model abbreviations

Throughout the geophysical model results, a series of abbreviations simplify the terminology:

Abbreviation	**Explanation**
EMLT	Effective model lithospheric thickness (km)
AS	Asthenosphere; viscosity (Pa s) or thickness (km) as appropriate
MN	Mantle viscosity (Pa s)
ALVZ model	Earth model including asthenospheric low viscosity zone (Figure 3.11)
Relative displacement	Modelled radial displacement relative to time = 0. Time = 0 in the model is AD 4, prior to the onset of ice loading in the Larsen *et al.* (2005) regional ice model. Present is defined as AD 2004 to allow for the ice model running to AD 2005 and the GPS data collected over AD 1992 – 2007.

5.2 TABOO verification

To verify TABOO's suitability as a postglacial rebound calculator and ability to calculate rates of uplift taking into account the model assumptions, I initially modelled rates of present day uplift for Fennoscandia in response to LGM ice loading (as represented by the ICE-3G deglaciation model (Tushingham and Peltier, 1991) which is available in TABOO) to test TABOO's sensitivity to changes in Earth model parameters in a region where the present day rate of GIA uplift is well defined by the postglacial uplift model NK2005LU (Svensson *et al.*, 2006). The results of this testing can be found in the Appendix 3_2 and provide assurance that TABOO is suitably sensitive to changes in the Earth model. Furthermore, Larsen *et al.* (2005) demonstrates the successful application of TABOO when quantifying the RSL changes during the Neoglacial in south east Alaska.

5.3 Reference frame definition

Vertical motion is generally described as motion that is normal to some defined horizontal surface. Therefore, definition of a global and internally consistent terrestrial reference frame (TRF) is important to be able to compare vertical motions in geophysical data and Earth phenomena. It is generally possible to define the Earth's centre in one of three ways: as centre of mass of the solid Earth (CE) consisting of the crust, mantle and core, but not the ice sheets; as the centre of mass of the Earths system (CM) consisting of solid Earth, the ice sheets, the ocean and the atmosphere; or as centre of surface figure (CF) defined to be the mean motion of sites on Earth's surface or the mean velocity of the Earth's surface (Greff-Lefftz and Legros, 1997; Blewitt, 2003; Argus, 2007). GIA models, including ICE5G (VM2) and ICE5G (VM5) (Peltier, 2004; Argus and Peltier, 2010), generally use CE as the velocity of the Earth's centre. For the purpose of this thesis, the geocentre of TABOO is considered as CE[1]. Geodetic studies tend to use the International Terrestrial Reference Frame (ITRF) solutions where the Earth's

[1] Spada (personal communication, 2010) gives the reference frame of TABOO as CM. However, TABOO does not include degree-one deformation of the Earth. As Blewitt (2003) and Greff-Lefftz and Legros (1997) demonstrate, it is degree-one deformation, which theoretically corresponds to change in load moment, that results in geocentre motion. Without degree-one deformation, any difference between CM and CE is solely due to inter-site deformation (change in the Earth's shape) by gravitational and pressure stresses, which should have limited affect on the definition of the Earth's centre. Therefore, in line with other GIA models which also do not include the mass of the whole Earths system, I consider CE the TRF of TABOO. For the purpose of this thesis, CE in TABOO and CE as defined by Argus *et al.* (2010) are considered comparable, though being aware of the potential for a slight un-quantified offset.

centre is defined as CM in ITRF2000 (Altamimi *et al.*, 2002) and ITRF2005 (Altamimi *et al.*, 2007), whereas in ITRF1997 (Boucher *et al.*, 1999) the velocity of the Earth's centre is CF. The velocity of the Earth's centre is uncertain and therefore differs between the definitions of the Earth's centre (Figure 5.1), for example, the velocity of CM estimated by ITRF2005 is 1.8 ± 0.3 mm yr^{-1} greater in the *Z*-axis (vertical) than estimated in ITRF2000 (Altamimi *et al.*, 2007). Figure 5.1 summarise the estimates of velocity of different definitions of the Earth's centre relative to CE defined by Argus *et al.*'s (2010) GEODVEL dataset. To allow direct comparison between all GIA model data in this thesis and the GPS solutions from Freymueller *et al.* (2008) I select CE as the TRF, as defined by GEODVEL (HORI) (Argus *et al.*, 2010), as the predictions of postglacial rebound models are relative to CE. I convert all GIA model output (with the exception of output from TABOO where the difference between GEODVEL and TABOO CE is not quantified; see footnote 1 above) and GPS data to CE defined by GEODVEL (HORI) using the relevant *Z* transformation in Figure 5.1 for 60°N. Therefore, all stated values of vertical displacement, unless otherwise indicated, are relative to CE.

5.4 Earth model constraint

Present day GPS measurements for south central Alaska (Freymueller *et al.*, 2008) and observations of the spatial pattern of post AD 1964 tectonic deformation constrain the GIA model outputs (Figure 5.2). Freymueller *et al.* (2008) report vertical velocities (relative to ITRF2000) as a result of land level movements due to both tectonics and GIA. Though in their paper, Freymueller *et al.'s* (2008) analysis is converted to ITRF2005, the data in Freymueller *et al.* (2008) Appendix 2 is relative to ITRF2000 (CM) with no additional uncertainties (Freymueller, personal communication, 2010). Addition of 0.4 mm yr^{-1} (*Z* translation (Figure 5.1) for 60°N) to the stated vertical GPS values transforms the data to CE (section 5.3). I calculate the weighted mean and weighted mean vertical sigma error of present day (AD 1992-2007) land-level changes at GPS sites within 10 km of each of the 8 observer locations (Figures 5.2 and 3.10). By subtracting the TABOO estimated present day (AD 2004) GIA land uplift from the upper weighted mean GPS vertical velocity (weighted mean plus weighted mean vertical sigma error) for each location gives an upper bound on the vertical tectonic component. Observations and measurements following the AD 1964 earthquake (section 1.3.2) identify areas of present day tectonic post-seismic uplift for Whittier and sites to the west of Prince

William Sound, and subsidence at Cordova. It is therefore possible to reject GIA models where when upper weighted mean vertical velocity minus modelled present GIA uplift results in net tectonic subsidence (at present) for any of the sites from Kenai to Whittier, or uplift for Cordova.

5.5 Model development

Figure 5.3 summarises the path of model development followed in order to assess the relative control of the elastic and viscoelastic components of the Earth rheology to ice load changes over the last earthquake cycle in south central Alaska. These model outputs provide a sensible range as to the magnitude of land level changes due to GIA during this time.

A simple one viscous layer Earth model allows initial assessment of the relative contribution of the lithosphere and viscous component of the upper Earths rheology (Figure 3.11) to relatively small ice load changes over the last earthquake for eight selected model sites around south central Alaska (Figure 3.10). The model is similar to James *et al.*'s (2000) Earth model for British Columbia. The Earth model uses a PREM averaged model available in TABOO (NV=1 CODE=0; Spada *et al.*, 2003) with variable lithospheric thickness and mantle viscosity.

A second set of more realistic and complex Earth models incorporate an asthenospheric low viscosity zone (ALVZ), similar to Larsen *et al.* (2005) and James *et al.* (2009b). The asthenosphere-upper mantle boundary is set at 220 km based on PREM values for the base of the low viscosity zone with the lithosphere-asthenosphere boundary set at 220 km minus the lithospheric thickness (Figure 3.11). TABOO does not contain an inbuilt Earth model that allows for this rheological structure, so I add a new model with PREM averaged density, depth and elastic properties allowing varying lithospheric thickness and asthenosphere and mantle viscosities. I assess variations in rheological response to the ice model by varying upper mantle and asthenosphere viscosities for an Earth model with effective model lithospheric thicknesses of 60 km and 110 km. I use an effective model lithospheric thickness of 60 km in line with Larsen *et al.*'s (2005) best estimate of a 60-70 km thick lithosphere in south east Alaska and James *et al.*'s (2009) Earth model of the Cascadia subduction zone. The higher effective model lithospheric thickness of 110 km is to take into account the lithosphere thickened by the subducting Yakutat and Pacific Plates (Fuis *et al.*, 2008).

Any estimates of solid Earth displacement contain some level of uncertainty. To account for uncertainty in the GPS data I use the upper weighted mean velocity from the GPS data (Figure 5.2) as a stringent constraint on the GIA model solutions (section 5.4), though this is used as a threshold value, and does not take into account any uncertainty. The GIA model outputs in Figures 5.4 – 5.10 and Table 5.1 also do not take into account any additional uncertainty such as uncertainty in definition of the solid Earth boundaries, potential over estimation of LIA ice mass (section 3.7.2), oversimplification of the history of regional glacier advance and retreat (see additional discussion in section 3.7.2) or computational errors, and therefore the model outputs should not be taken as absolute values, but as a range of potential solid Earth response as summarised by the final Figure in the Chapter (Figure 5.10). Section 5.6 considers uncertainty regarding long wavelength and non GIA solid Earth displacement that may be overprinted on the local-regional LIA GIA.

5.5.1 Simple Model Output

The simple model, with effective model lithospheric thicknesses from 50-150 km (at 20 km intervals) over a typical mantle of 4 x 10^{20} Pa s, following Larsen *et al.*'s (2005) best fit Earth model, predicts spatial differences in relative displacement in line with theoretical expectations, with greater displacement closer to the centre of ice loading (e.g. Whittier versus Kenai) and greater displacement with a thinner effective model lithosphere (Figure 5.4). Greater effective model lithospheric thickness results in slightly higher rates of modelled present day uplift (Figure 5.4).

To consider the influence of varying mantle viscosity, Figure 5.5 shows results of an Earth model using effective model lithospheric thicknesses of 60 km, and in Figure 5.6 for a higher effective model lithospheric thickness of 110 km. As expected, lower mantle viscosity results in greater displacement and greater present day uplift, particularly for mantle viscosities less than 4 x 10^{20} Pa s, with the greatest effect with the thinner lithosphere model. The GPS observations constrain the mantle viscosity to 10^{19} to 10^{20} Pa s with both effective model lithospheric thicknesses, with mantle viscosities of ≤ 4 x 10^{18} and ≥ 4 x 10^{21} Pa s being invalid.

5.5.2 Asthenospheric Low Viscosity Zone Model Output

The initial asthenospheric low viscosity zone model, summarised in Figure 5.7, explores the effect of varying mantle viscosity, below a low viscosity zone of 4 x 10^{18} Pa s, following the

Earth structure of Larsen *et al.*'s (2005) best fit model. For both effective model lithospheric thicknesses, a lower viscosity mantle results in greater displacement, with the greatest displacement closest to the centre of ice loading and with a thinner lithosphere. For all tested mantle viscosities, the GPS data reject all Earth models with effective model lithospheric thickness of 60 km.

When considering the influence of varying viscosity in the asthenospheric low viscosity zone, a second set of models includes a low viscosity asthenosphere over an upper mantle of 4×10^{20} Pa s, following Peltier's (2004) VM2 model. These show greater relative displacement with reduced asthenosphere viscosity, furthered by a thinner effective model lithospheric thickness (Figure 5.8). The greatest displacement is, as expected, at sites closest to the centre of ice loading. The modelled magnitude of relative displacement highlights that in certain situations different combinations of input parameters can result in similar results. With a thinner (60 km) lithosphere, the GPS data rejects an asthenosphere viscosity of $\leq 4 \times 10^{18}$ Pa s.

5.5.3 Elastic response

The results so far show the viscoelastic Earth response to ice load changes. It is clear that in the ALVZ model the thickness of the lithosphere modifies any potential GIA response, and theory suggests that the lithospheric response is primarily elastic. Two Earth models with effective model lithospheric thickness of 110 km and 60 km, constant asthenosphere viscosity of 4×10^{18} Pa s and upper mantle viscosity of 4×10^{20} Pa s explore of the elastic component of the Earth response. Figure 5.9 shows the relative contribution of the elastic geophysical response to be relatively small compared to the total viscoelastic response, with little difference in elastic relative displacement between the two effective model lithospheric thicknesses. The results suggest it is the difference in asthenosphere thickness, resulting from varying the effective model lithospheric thickness, and asthenosphere viscosity which are the primary control on the magnitude of relative displacement in the study area.

It must be noted that there is potential that any elastic response will likely change in response to recent twenty first century ice mass loss (e.g. Molnia, 2008), which the Larsen *et al.* (2004; 2005) ice model does not allow for, though the GPS data (which runs to 2007) will likely include. In this thesis, where the overall purpose of the GIA modelling is testing the palaeo-environmental reconstructions (Chapters 4 and 6) of RSL changes prior to the AD 1964

earthquake, this is will have likely minimal influence on the overall outcomes. However, one must take into consideration that the elastic component estimated by TABOO may be oversimplified due to the resolution of the ice model.

5.6 Long wavelength Earth displacement

Modelling to this point has only considered local to regional GIA due to regional LIA ice mass changes. The vertical movements measured by the GPS data, likely also incorporate long wavelength regional to global signals of vertical Earth motion due to mass redistribution following the loss of the LGM ice sheets, in this region namely the Laurentide, alongside ocean loading of the continental shelf.

5.6.1 Long wavelength GIA

The presence of the large LGM Laurentide and Cordilleran ice sheets over North America causes long wavelength solid Earth displacement due to the horizontal displacement of mantle material and deglacial collapse and migration of the forebulge. Due to the nature of TABOO it is unable to include the complex nature of the Pleistocene ice sheets as summarised by more sophisticated ice models, such as ICE5G (Peltier, 2004). Global scale GIA models calculate large scale regional to global redistribution of mass following the melt of Pleistocene ice sheets (Lambeck *et al.*, 1998; Peltier, 2004; Argus and Peltier, 2010). As discussed in sections 1.3.4 and 3.7 the Earth models used in these global GIA models, such as VM2 (Peltier, 2002), are likely inappropriate for south central Alaska as they do not include a low viscosity zone between the lithosphere and upper mantle, and therefore estimated ongoing solid Earth displacement is likely to be too great (James *et al.*, 2000; 2009a; 2009b). Furthermore, some caution must be exercised when considering the outputs from ICE5G(VM2), as Argus and Peltier (2010) demonstrate, ICE5G(VM2) poorly resolves some areas of the Laurentide ice sheet, in particularly the western segment, and achieves poor fit with some of the uplift data from the North American GPS stations. As a result, they refine VM2 with a new Earth model, VM5a, and suggest improvements to ICE5G that will form part of the in-development ICE6G model. At no point do Argus and Peltier (2010) try and resolve fit with any sites in south central Alaska or the tectonically active Pacific north west coast of the USA (section 1.3.4). However, ICE5G(VM2) is at present the only openly available estimates of long wavelength

solid Earth displacement for the region so I use the 0 k yr BP outputs[2] as maximum constraints of present day post LGM GIA.

To account for long wavelength GIA, I use Peltier's (2004) estimates of present day radial displacement for the four tide gauge stations closest to the 8 model test sites (Table 5.1). The ICE5G(VM2) solutions suggests the upper Cook Inlet is experiencing up to 0.30 mm yr^{-1} subsidence due to collapse of the forebulge. Considering the ALVZ solutions from section 5.5.2 with the ICE5G(VM2) corrections means that no model solutions in Figure 5.7 (Table 5.1) are rejected. In Figure 5.8, the models where the asthenosphere viscosity is 4 x 10^{19} Pa s for both lithospheric thicknesses of 60 km and 110 km and where the asthenosphere viscosity is 1 x 10^{18} Pa s with a lithospheric thickness of 60 km are rejected (Table 5.1). Inclusion of long wavelength GIA potentially places upper bounds on the viscosity of the asthenosphere, suggesting that it must fall within 10^{18} Pa s, and that the viscosity of the upper mantle is of little importance in controlling the solid Earth response to LIA ice mass changes in south central Alaska.

5.6.2 Ocean loading

As discussed in section 3.7.1 TABOO does not include the gravitationally self consistent ocean load. Walcott (1972) originally noted ocean loading at continental margins induces a 'levering' of continents and a subsidence of offshore regions. Following the onset of deglaciation, the oceanic regions are subjected to a water load but the continental regions are not and therefore the continents flex upward at their margin and downward offshore. Due to the superimposition of jagged coastlines, sites located toward the continental interior show elevated rates of sea-level fall (and progressively higher amplitude sea-level high stands), while those located toward the ocean will exhibit lower rates of sea-level fall and even, in some cases, submergence (Mitrovica and Milne, 2002). Work along the Australian coast identifies differential mid Holocene highstand amplitudes and ongoing hydro-isostatic displacement (of 0.16 – 0.47 mm yr^{-1}) due to ocean loading following the melt of the Pleistocene ice sheets (Nakada and Lambeck, 1989; Lambeck and Nakada, 1990; Lambeck, 2002). The spatial and temporal pattern of continental levering is rheology dependant, with a thin lithosphere and low viscosity mantle resulting in greater high stand amplitudes and strong gradients across the

[2] The ICE5G(VM2) estimates of solid Earth relative displacement are available from Peltier's webpage: http://www.atmosp.physics.utoronto.ca/~peltier/datasets/psmsl/DRAD.PSMSL.ICE5G.VM2.L90.txt

continental shelf (Lambeck, 2002). At a near field location the solid Earth displacement will be largely a consequence of GIA, though as Mitrovica and Milne (2002) discuss, the intimate connection between the ice and ocean loading effect is inherent to the sea-level equation. Though the magnitude of ocean loading over the LIA will be small compared to that following the melt of the Pleistocene ice sheets, there is potential for a spatially variable present day sea level fall and Neoglacial sea level rise due to ocean loading of the continental shelf, which the modelling in this thesis is unable to account for. Therefore, one must be mindful of the influence of ocean loading somewhere in the order of 0.2 – 0.5 mm yr^{-1} (Lambeck, 2002; Mitrovica and Milne, 2002) when considering the solid Earth displacements over the LIA in upper Cook Inlet.

5.7 Best Earth model

The results of the simple model show that the viscoelastic component of the Earth's rheology controls the solid Earth response to the ice load changes in south central Alaska over the last earthquake cycle, with mantle viscosity less than 10^{21} Pa s invoking a notable geophysical response of >0.5 m at the culmination of the LIA. The GPS data rejects viscosities ≤ 4×10^{18} and ≥ 4×10^{21} Pa s. Seismic observations from subduction margins identify the presence of an asthenospheric low viscosity zone (ALVZ) between the lithosphere and upper mantle, with the lithosphere-asthenosphere boundary being fundamental in allowing plate movement (Anderson, 1975) (section 1.3.4), so it is appropriate to consider the results of the ALVZ model for a best Earth model for south central Alaska.

The GPS observations constrain a range of valid effective model lithospheric thicknesses and corresponding asthenospheric thickness and asthenosphere viscosity for an Earth model with mantle viscosity of 4×10^{20} Pa s (Figure 5.8), rejecting solutions with a lithospheric thickness of 60 km and asthenosphere viscosity ≤ 4×10^{18} Pa s. These parameters are consistent with James *et al.* (2009b) asthenosphere model fitted to deglacial RSL data in British Columbia. They find that the RSL observations fit across a wide range of asthenospheric thicknesses providing the asthenospheric viscosity is varied from 3×10^{18} Pa s for a thin (140 km) asthenosphere and 4×10^{19} Pa s for a thick (380 km) asthenosphere, though achieve a best fit with the sea level observations with a 100-200 km asthenosphere.

The ALVZ models presented here do not consider asthenospheric viscosities above 4 x 10^{19} Pa s, as the asthenosphere viscosity inferred from subduction zone earthquakes does not exceed this value (section 1.3.4). An Earth model in this way also means the asthenosphere low viscosity zone has a viscosity an order of magnitude lower than the underlying mantle. This provides an upper limit for the viscosity of the best Earth model and therefore a lower limit to the magnitude of GIA over the last earthquake cycle. One must note that magnitude of the radial displacement may be c.25% lower, considering the potential over estimation of mass in the ice model (Berthier *et al.*, 2010) (section 3.7.2) with the spatial pattern potentially modified by variable ocean loading (section 5.6.2). Addition of Peltier's (2004) estimates of long wavelength GIA (section 5.6.1) creates an upper bound on asthenosphere viscosity of < 4 x 10^{19} Pa s (section 5.6.1) (Table 5.1). The best Earth model from the modelling in this chapter therefore has an asthenospheric viscosity of 1 x 10^{18} Pa s for an asthenospheric thickness of 110 km to 8 x 10^{18} Pa s for an asthenospheric thickness of 160 km (Figure 5.8 and Table 5.1). The asthenosphere thickness is a function of the model set up where the asthenosphere thickness = 220 km (the defined base of the low viscosity zone) minus the lithospheric thickness (Figure 3.11).

Using the constraints of seismic observations, present day GPS data, long wavelength GIA and the EDC model for south central Alaska (section 5.4) as upper bounds to constrain suitable Earth model solutions, Figure 5.10 summarises the possible range of present day land uplift due to local post LIA GIA, against total tectonic and GIA land level movements measured by GPS at the eight modelled sites across south central Alaska. The proportion of the present day uplift estimated to be a result of LIA GIA, relative to ongoing tectonic deformation, is dependent on the selected Earth model (Figure 5.10).

5.8 Summary

The geophysical model results indentify the viscoelastic response of the asthenosphere as the dominant control to changes in ice load in south central Alaska over the last earthquake cycle, with up to 2 m relative displacement experienced at sites closest to the centre of ice loading during the maximum phase of LIA ice advance (Figure 5.8). Models constrained using GPS uplift data identifies a range of best Earth models for south central Alaska having thin asthenosphere (110 km) and viscosity of 1 x 10^{18} Pa s to a model with a thicker asthenosphere (160 km) and

higher viscosity of 8 x 10^{18} Pa s (Figure 5.10). These model parameters are similar to those in Earth models from British Columbia (James *et al.*, 2009b) and south east Alaska (Larsen *et al.*, 2005). The models estimate c. 1.1 to 5.8 mm yr^{-1} present day uplift due to local GIA in Turnagain Arm, with a pattern of reducing uplift east-west, modified by potentially up to c. 1 mm yr^{-1} subsidence due to long wavelength forebulge collapse and ocean loading. Chapter 6 integrates the best Earth model geophysical results and related geoid changes, with the geological results from the upper Cook Inlet.

Chapter 6 : Integrating the Geological Data and Model Results

6.1 Introduction

Integration of the geological data from Girdwood, Bird Point and Ocean View (Chapter 4) with the geophysical modelling results (Chapter 5) allows testing of the original research hypotheses in section 6.2.

6.2 Testing the Research Hypotheses

This section follows the four working research hypotheses (below), ultimately working towards testing the main research hypothesis: '*Glacial isostatic adjustment is an important contributor to relative sea level change in upper Cook Inlet during the last earthquake deformation cycle*'.

1. There is evidence for non-EDC RSL change during the Little Ice Age in upper Cook Inlet, Alaska.
2. The RSL change is spatially variable.
3. The RSL change occurs during periods of regional glacier advance and retreat.
4. The mechanism of RSL change is GIA.

Figure 6.1 summarises, in a conceptual model, the potential impact of the four working research hypotheses on the last earthquake cycle in upper Cook Inlet. The chapter will test each part of the conceptual model in turn, with discussion of additional points that have arisen during the research. All results assume no significant changes in tidal regime or prism (section

2.2.2) over the past earthquake cycle. This assumption is based on aerial photographs of Turnagain Arm prior to the AD 1964 earthquake that shows similar coastal geography to today (Figure 6.2). As discussed in Chapter 4, the remainder of this thesis will focus on the geological data from Girdwood, Bird Point and Ocean View, as the overprinting of mining activity on the RSL history at Hope means that in this thesis it is of little value to testing the research hypotheses.

6.2.1 There is evidence for non-EDC RSL change during the Little Ice Age in upper Cook Inlet, Alaska.

RSL change at subduction zone margins is a complex interplay between seismic and non-seismic mechanisms. Previous research focuses on evidence of RSL change in upper Cook Inlet predominately associated with tectonically driven land level changes over the past 4000 years (Hamilton and Shennan, 2005a; Hamilton *et al.*, 2005; Hamilton and Shennan, 2005b; Shennan and Hamilton, 2006; Shennan *et al.*, 2008) (section 1.3.2). The EDC model of land level changes predicts net RSL fall during the phase of interseismic land uplift for upper Cook Inlet, followed by a period of pre-seismic RSL rise prior to the AD 1964 coseismic submergence (section 1.3 and Figure 1.3) (Hamilton and Shennan, 2005a; Shennan and Hamilton, 2006).

The evidence for any RSL changes, which differ from the EDC predicted model of land level changes (Figure 6.1), is the lithological, biostratigraphical and chronological data in Chapter 4. In general in many locations at Girdwood, Bird Point and Ocean View, the upper peat becomes more organic towards the peat-silt boundary, though local variations do occur, for example at GW-NB-06-7 where a slight increase in silt occurs with the organic layer at c. 10 cm from the peat-silt boundary (section 4.3.1 and Figure 4.7). The biostratigraphy of cores from Girdwood (GW-08-3, GW-NB-06-2), Bird Point (BP-08-6) and Ocean View (OV-02-4) suggests that over the period of the LIA (dated by AMS ^{14}C, tephrochronology, radionuclide and pollutant data) there are small-scale fluctuations in marine and brackish diatoms that provide evidence for changes in marine influence (Figures 4.10, 4.11, 4.19 and 4.28). To examine whether these changes may be due to RSL requires calibrating the fossil assemblages with a modern diatom training set and associated transfer function (section 3.6.1).

Reconstruction of RSL to test working hypothesis one requires a robust and comprehensive modern training set relating elevation to diatom distribution (Imbrie and Kipp, 1971; Birks,

1995; Hamilton and Shennan, 2005a) (section 3.6.1). Edwards and Horton (2005) advocate the use of a regional over local modern training set to potentially increase accuracy and produce more reliable reconstruction,s which is the approach used in this thesis (sections 3.6.1 and 4.2.2). Woodroffe and Long (2010) however suggest that a local training set over a regional training set is better suited to RSL reconstruction of marshes in western Greenland due to: different diatom assemblages at different marshes; the same species having different optima at separate marshes, particularly species from the uppermost part of the intertidal frame; differing local wind, wave and tidal processes; and the implications of SWLI as means for standardising tidal range differences (discussed in section 3.6.1). In upper Cook Inlet, it is not possible to capture the full range of fossil environments using a single-marsh training set (Hamilton, 2003). The results of the revised upper Cook Inlet training set (section 4.2.2 and Figure 4.2) show consistency between the new modern samples from Hope and Girdwood and the existing training set (Hamilton and Shennan, 2005a), suggesting differing species optima at different marshes, as encountered by Woodroffe and Long (2010), is not an issue within upper Cook Inlet. The impact of the SWLI method as means for standardising tidal range differences in upper Cook Inlet however has potential implications, particularly when new tidal observations at Hope and Bird Point identify present day tidal differences along Turnagain Arm (section 4.2.1). Use of SWLI in the regional training set may potentially amplify reconstructed RSL changes at Bird Point and dampen changes at Ocean View and Girdwood. The large tidal range and bathymetry of the Cook Inlet (section 2.2.2) means it is not possible to install a pressure transducer at any of the sites so the SWLI method is the best approach presently available, however, one must be mindful of this potential error.

To enhance the regional training set I collected additional modern samples from Hope and Girdwood (section 3.2.3). These new modern samples do not improve transfer function model performance, though provide additional modern analogues of species including *Fragilaria vaucheriae*, previously poorly represented in the Hamilton and Shennan (2005a) training set (section 4.2). MAT goes some way to identify those fossil samples with a poor modern analogue (section 3.6.2) and highlights that in a few instances the revised upper Cook Inlet training set still poorly represents some fossil assemblages. The lack of suitable modern analogues for four fossil samples in OV-02-4 and eight samples in GW-08-3 is due to the dominance of two species: S*taurosirella pinnata* and *Pinnularia stomatophora* respectively (Figures 4.28 and 4.11). Previous research records the presence of both species in freshwater

lacustrine settings with S*taurosirella pinnata* found in lakes in Canada (Finkelstein and Gajewski, 2008; Paull *et al.*, 2008; Watchorn *et al.*, 2008), Greenland (Cremer *et al.*, 2001) and Argentina (Hassan *et al.*, 2006) and *Pinnularia stomatophora* in Ukraine (Vodop'Yan, 1976) and Poland (Skalska and Kaczmarczyk, 1980). Though the training set does not contain a good modern analogue for these twelve fossil samples, one can be confident that the samples are likely to be from a high marsh to freshwater environment. Knowledge of diatom ecology is as valuable as the quantitative relationship between diatom assemblages and elevation when reconstructing past coastal environments.

To calibrate any fossil RSL changes requires use of a statistical model, in this instance the unimodal regression technique WA-PLS, to quantify the relationship between the modern diatom assemblages and elevation (section 3.6.1). WA-PLS updates the weighted averaging (WA) method by using further components to utilize the residual structure in the species data to improve the fit between the training set and environmental variable (ter Braak and Juggins, 1993; ter Braak *et al.*, 1993). The first component (equivalent to WA) is a two-way weighted average for the original environmental variable. Further components are two-way weighted averages for the residual of the environmental variable with updated species optima (ter Braak and Juggins, 1993). Using simulated data, ter Braak and Juggins (1993) show for both long and short environmental gradients, further components of WA-PLS achieve a substantial decrease in the error estimating the optima, similarly to the model performance statistics that suggest using component 3 over component 2 with the upper Cook Inlet training set in this thesis (Figure 4.3 and Hamilton and Shennan (2005a)). However, ter Braak and Juggins (1993) also note that further components of WA-PLS are seen to 'stretch out the ends' of the environmental variable. Figure 6.3 plots the C2 WA estimated species optima and tolerance against the WA-PLS species coefficients for components 2 and 3 of all species greater than 10% total valves counted in modern samples included in the silt with rootlets (SWLI >180) transfer function. It is clear that updating the component significantly shifts the species optima in nearly all instances, with the greatest shifts relative to the WA estimated optima, by component 3. In general, further components lower the optima for those species with WA optima less than 210 SWLI units, and raise the estimated optima for species with WA optima greater than 210 SWLI units, 'stretching out the ends' of the environmental variable. For example, the species optima of *Frustulia rhomboids* is estimated at 239 SWLI units by WA, updated to 260 units by WA-PLS component 3, which is beyond the upper limit of sampling of

the modern training set (Figure 4.2). By comparison, the WA optima of *Delphineis surirella* is 208 SWLI units by WA, updated to 187 SWLI units by component 3. Both these species (plus those species in red in Figure 6.3) account for greater than 10% total valves counted in the fossil samples from the four sites and have a significant influence on the outcome of the transfer function. Therefore, the estimated elevation of assemblages high in the intertidal zone may be overestimated and the elevation of assemblages from low in the intertidal underestimated, resulting in potentially exaggerated changes between high and low PMSE and therefore reconstructing greater RSL changes than actually recorded by the biostratigraphy.

Austin (2002) raises a further question regarding modelling of the relationship between species response to environmental variables. Should a species whose response curves are clearly truncated, i.e. their range extends beyond the limits of the gradient samples, be used in theoretical studies of response shape? Species position along an environmental gradient can influence the shape of the response detected (Rydgren *et al.*, 2003), and conclusions about the response curve of species can only be unambiguously determined if the sampled environmental gradients clearly exceeds the upper and lower limits of the species occurrence (Austin, 2007). Woodroffe and Long (2010) develop a 'pruned' diatom transfer function which excludes samples which have an absolute residual greater than one quarter of the elevation of the training set to avoid including species whose environmental range is greater than the upper and/or lower limits of the environmental gradient. By comparison, I included all species and samples in the transfer functions whose elevation exceeds 180 or 225 SWLI units as appropriate (section 3.6.1 and Figures 4.2 and 4.3). Excluding samples from the upper Cook Inlet training set, following the approach of Woodroffe and Long (2010), would leave too few samples from which to develop a model for calibrating the palaeo elevation of assemblages from the fossil peat (>225 SWLI units model, see section 3.6.1). However, one must be mindful that the transfer function and resulting reconstructions may suffer from including species such as *Achnanthes minutissima, Eunotia exigua, Tabellaria fenestrata et al.* whose environmental range clearly extends beyond the upper limit of the environmental gradient and therefore causing the transfer function to potentially misinterpret their optima and response curves (Figure 6.3). As a result, these species might only be considered as limiting species rather than providing clear markers of PMSE.

The model selected to calibrate the PMSE of a sample also influences the RSL reconstruction, potentially improving precision but reducing accuracy. Figures 4.4 and 4.5 show the estimated elevation of fossil samples from pre AD 1964 layer. In BP-07-3 (Figure 4.4) and HP-07-11 (Figure 4.5), where the lithology is clearly a silty peat (Figures 4.12 and 4.21), the peat model understandably over estimates the elevation of the samples compared to the silt with rootlets model (section 4.2.3). In GW-08-6 (Figure 4.4) where a highly organic peat (Figures 4.6 and 4.7) suggests either the peat or silt with rootlet models may be used, the elevation of the samples estimated by the peat model fall within the error terms of the silt with rootlets model (Figure 4.4), resulting preferential selection of the peat model to calibrate these samples. The resulting RSL reconstruction has much great precision; however, this may be at cost of reconstruction accuracy.

To fully test the first working hypothesis one requires the ability to quantify any changes in PMSE and therefore potentially RSL. The geological data suggests there is an increase in marine influence prior the AD 1964 earthquake, during the interseismic phase, whereas the conceptual model of the EDC predicts RSL fall (Figures 1.3 and 6.1) and therefore reduction in marine influence. It is unlikely the increase in brackish diatoms is due to the pre-seismic phase of the EDC, as shown by the biostratigraphy at Girdwood (Figures 4.10 and 4.11), where the diatoms return to a freshwater assemblage, prior the onset of the pre-seismic marked by a second increase in brackish diatoms in the decade or so prior the AD 1964 earthquake. The increase in marine influence may be a result of increased tidal amplification due to reduced water depth during the LIA (section 2.2.2). It is not possible to quantify tidal amplification within this thesis, but it seems unlikely that the potential tidal amplification (particularly taking into account the already large diurnal tidal range (section 2.2.2)) would exceed the potential steric sea level fall (further discussed in section 6.2.4), or regional GIA driven subsidence (Chapter 5).

Figure 6.4 summarises the transfer function based estimates of RSL changes at Girdwood, Bird Point and Ocean View from c. AD 1400 to AD 1964, which one may consider relative to the theoretical tectonic RSL model summarised in Figures 1.3 and 6.1. However, critical evaluation of the upper Cook Inlet training set and associated transfer functions highlights the limitations of the approach to calibrating subtle changes in the fossil diatoms, potentially masking or exaggerating the magnitude of small scale RSL changes. For example, to reduce the RSMEP and

sample specific errors and therefore determine presence of any small scale RSL changes greater than the model error terms, requires use of further components of WA-PLS (ter Braak and Juggins, 1993). Figure 6.3 shows this can result in updated species optima, which have implications for the calibration of fossil diatom assemblages, potentially magnifying changes in PMSE. Furthermore, by including species with truncated response curves can cause misinterpretation of species optima and therefore the calibrated PMSE. The reconstructed RSL changes in upper Cook Inlet summarised in Figure 6.4, may be an artefact of the training set and transfer function method, and must be interpreted with caution. However, even taking into account these limitations, the geological data and transfer functions do provide a record the direction of sea level change, which is not a random signal. Within the pre-AD 1964, a net RSL rise (or at least stable sea level) provides some evidence for non-EDC RSL change during the Little Ice Age in upper Cook Inlet, Alaska compared to the expected EDC driven RSL fall (Figure 6.1). Though it is not possible to fully test working hypothesis one, it is also not possible to reject the hypothesis and consequently I consider the further working hypotheses in the remainder of this Chapter.

6.2.2 The RSL change is spatially variable.

RSL changes vary both temporally and spatially, on global, regional and local scales (Mitrovica and Milne, 2003) (section 1.3.3). Testing hypothesis two is achieved by determining any spatial difference in the possible RSL deviation from that predicted by the EDC model, both between and within the three sites, but taking into consideration the limitations of the transfer function method when reconstructing small scale RSL changes as discussed in section 6.2.1.

Intra-site variation

Initially studying any intra-site variation helps determine the threshold above which to consider inter-site variability. The poor diatom preservation in OV-08-2 means there is only one RSL reconstruction through the upper peat layer at Ocean View. At Bird Point, BP-07-3, the fossil diatom changes are very different from the Girdwood and Ocean View model of land level change during the last earthquake cycle (Hamilton and Shennan, 2005a; Hamilton *et al.*, 2005; Shennan and Hamilton, 2006), suggesting, if the transfer function is correctly reconstructing sea level, the main control may be local, marsh front processes, particularly when taking in to consideration the position of BP-07-3 near to the marsh edge (sections 2.3.2 and 4.3.2 and Figure 3.2). Due to the potential for marsh front processes (erosion and silt entrained sea ice

deposition on the marsh surface) to complicate the signal at Bird Point and create differences between seaward BP-07-3 core compared to the landward BP-08-6 core which are potentially unrelated to RSL (Figure 4.30), this section focuses on the multiple cores from Girdwood (Figure 6.4).

Figure 6.4 shows the reconstructed RSL change in the three cores from Girdwood to be very similar with any deviation between cores within the model error terms. The reconstructed sample elevations through the GW-1 peat layer are c. 0.75 m higher than in GW-NB-06-2 and GW-08-3 (Figure 6.4) and the lithology varies between the three cores, with a layer of silt found within the pre AD 1964 peat at GW-1, compared to a consistently highly organic unit at GW-NB-06-2 and GW-08-3 (Figure 4.6). Intra-site processes may account for some of this variation.

Tidal creeks transport sediment into and onto the marsh, and migration of channels or the presence of palaeochannels may explain intra-site variation. In eastern Canada, Chmura and Hung (2004) found distance from a creek to be significant influence on salt marsh sediment accretion rates. Allen (1997) suggests that through an earthquake cycle the network of tidal marsh creeks will increase following coseismic submergence. As the marsh builds up during the inter-seismic phase of the EDC infilling and simplification replaces channel expansion and elaboration, until the marsh platform reaches a high intertidal peat when most creeks disappear. I carefully chose coring sites to avoid contemporary intertidal creeks, banks of glacial-fluvial rivers and eroded or slumped marsh fronts, however palaeo creeks processes may cause some intra-site variation. At Girdwood, GW-1 (Hamilton and Shennan, 2005a) is relatively proximal to Glacier Creek and changes in its former course may account for the band of silty-peat that punctuates the upper peat layer. It is therefore not possible to reject the hypothesis that palaeochannels or creek migration accounts for some intra-site variability, although the LOI and bulk density data from GW-08-3 (Figure 4.7) suggests it likely to be minimal.

Post depositional autocompaction of underlying silts, peats and clays lowers the elevation of the majority of fossil samples used as RSL indicators, resulting in over estimation of the rate and magnitude of RSL rise (Shennan et al., 2000a) (Figure 6.5). In addition, Long *et al.* (2006) attributes compaction of peat at Romney Marsh, UK, as a key driving mechanism behind rapid late Holocene coastal change. Calculation of sediment compaction to correct for these effects requires either a suite of base of basal SLIPs unaffected by compaction (Edwards, 2006; Horton

and Shennan, 2009) (to date there are none for upper Cook Inlet) or a quantitative model of autocompaction behaviour (for example the Brain (2006) model, though not applicable to the sediments in this thesis due to their high organic content). On the east coast of England and in the Mississippi Delta there is a strong correlation between sample elevation and depth of overburden for numerous intercalated peats (Tornqvist *et al.*, 2008; Horton and Shennan, 2009) and similar patterns exist at Romney Marsh, UK (Long *et al.*, 2007). The thickness of overburden silt at Girdwood varies across the marsh, with the thickest silt overlying the upper peat at GW-1 (68 cm, compared to 51 cm and 54 cm at GW-NB-06-2 and GW-08-3 respectively) where the reconstructed elevation of the fossil peat samples is lower than at the other core locations.

Compaction of sediments may also be associated with tectonic processes. Ground shaking compaction associated with a large earthquake may result in lowering of coastal wetlands. In AD 1964 there was c. 0.9 m localised surface lowering at Girdwood due to sediment compaction (Plafker *et al.*, 1969) and c. 2m site-specific ground shaking accompanied the AD 1899 M_w 8.2 Yakutat earthquake (Plafker and Thatcher, 2008). It is unlikely that coseismic ground shaking can account for the increase in brackish-marine diatoms within the pre AD 1964 peat at the three sites at Girdwood (sections 1.3.3 and 4.3.1 and Figures 4.10 and 4.11). Many of the fossil diatoms bind to substrate on the palaeo marsh surface, and though ground shaking may alter the RSL reconstruction, it cannot account for the fossil diatom assemblages within the pre AD 1964 peat. However, spatially variable coseismic liquefaction may account for some intra-site variation. It is not possible to reject the hypotheses that the compaction of the upper most peat by the overlying silt and coseismic ground shaking may have lowered the reconstructed fossil sample elevation, explaining some of the observed intra-site variability.

Inter-site variation

Despite some intra-site variation, the presence a possible (though unquantifiable (section 6.2.1)) deviation away from the EDC model prediction of land level change at all sites in Turnagain Arm (in this thesis) and Kenai (Hamilton and Shennan, 2005b) means there is potential for inter-site spatial variation. Definition of an inter-site spatial signal depends on the difference between the EDC model predicted rate of inter-seismic land-uplift and the reconstructed RSL change (Figure 6.1). The qualitative diatom data suggest the magnitude of change is greatest at Girdwood, with a reduced marine influence recorded at Bird Point and

Ocean View (sections 4.3.1, 4.3.2 and 4.3.4). The geological data records a direction of net sea level rise (Figure 6.4 and section 6.2.1). The magnitude of the possible deviation is co-dependent on the selected model of the rate of interseismic uplift at each site. This is discussed further in sections 6.2.3 and 6.2.4.

It is not possible at this stage to reject the second working hypothesis that non EDC RSL change in upper Cook Inlet is spatially variable with the available geological evidence. A combination of mechanisms may account for intra- and inter-site variation as discussed above, though it is not possible at present to quantify any regional spatial pattern. The next section considers the timing of the changes in fossil diatoms in relation to regional glacier advance and retreat.

6.2.3 The RSL change occurs during periods of regional glacier advance and retreat.

Dating of the sediments from Girdwood, Bird Point and Ocean View defines a chronology by which to test working hypothesis three. The dating methods used comprise a multi-method approach using AMS radiocarbon dating of terrestrial plant macrofossils, gamma dating (^{210}Pb and ^{137}Cs), tephrochronology, lead isotopes ^{206}Pb/^{207}Pb and for the first time in Alaska, the pollutant history. This section reviews the chronological evidence in depth and identifies the limitations of some of these methods in dating high latitude salt marsh sediments.

The focus of this research is the RSL changes during the middle and late LIA glacier advances. Grove (2004a) defines the LIA in the northern hemisphere as AD 1300-1850, though early mountain glacier advances were underway in Alaska from AD 1180s to 1320s. The middle and late advances (AD 1540s to 1710s and AD 1810s to 1880s respectively) resulted in Holocene maxima for many land-terminating glaciers in the Chugach and Kenai Mountains (Wiles and Calkin, 1994; Crossen, 1997; Wiles *et al.*, 1999; Calkin *et al.*, 2001; Molnia, 2008; Wiles *et al.*, 2008; Barclay *et al.*, 2009) (section 2.2.5). The early advance occurs at a similar time to the c. 850 yr BP earthquake event (summarised by Carver and Plafker (2008) and Shennan *et al.* (2009) and with new dates from BP-08-6 in this thesis). Rapid coseismic submergence and post seismic uplift dominates the RSL history at this time, which may mask smaller scale RSL changes. In addition, the lack of datable material in the silt and the large error terms associated with reconstructing RSL through tidal flat sediments in upper Cook Inlet (section 3.6.1) it is not possible to develop a high precision RSL history during the early LIA advance. Peat accumulation from AD 1400 ± 100 (based on the Augustine tephra at the base of the peat

at Girdwood) provides material suitable for AMS ^{14}C dating of RSL changes during the LIA, providing a foundation for developing an age-depth model. As a result, I focus on testing hypothesis three from this period onwards in relation to the middle and late LIA glacier advances.

Gamma dating

The natural decay of the radionuclide ^{210}Pb and the deposition of the ^{137}Cs have the potential to date sediments deposited over the last 100 to 150 years (section 3.4.2). Gamma dating relies on several assumptions including that there is no reworking or erosion of sediment and the radionuclides remain immobile in the sediment column following deposition (Milan *et al.*, 1995; Cundy *et al.*, 2003; Wolfe *et al.*, 2004) (section 3.4.2). In Alaska, ^{210}Pb and ^{137}Cs has previously been used successfully to date recent lacustrine sequences (Schiff *et al.*, 2008; Chipman *et al.*, 2009).

Profiles of ^{137}Cs show increased concentration over the peat-silt contact at both Girdwood (Figure 4.8) and Bird Point (Figure 4.14), corroborating that this lithological change is a consequence of the AD 1964 coseismic submergence and are in line with Zong *et al.*'s (2003) initial ^{137}Cs results from Girdwood (section 4.3.1). The profile from BP-08-6 (Figure 4.14) has the potential to be able to define the onset of nuclear weapon testing with the increase in concentration possibly attributable to AD 1952, though this really requires a greater amount of material than is available to provide very closely spaced samples. The return to background levels in BP-08-6 is c. 12 cm from the AD 1964 boundary (Figure 4.14), whereas Zong *et al.* (2003) record background levels c. 3-6 cm from the peat-silt boundary at Girdwood. This difference either highlights variable recent sediment rates, or raises questions regarding down core mobility of ^{137}Cs in association with decomposition of organics, redox reactions and lowering of the water table (Davis *et al.*, 1984; Cooper *et al.*, 1995). Testing these hypotheses requires additional gamma samples than presently available. The ^{137}Cs data indicates that the fallout from the AD 1985 Chenobyl accident is not apparent in the upper Cook Inlet coastal sediments. This may be due to either saline conditions resulting in a low ^{137}Cs absorption coefficient (Milan *et al.*, 1995) or atmospheric circulation not dispersing the radionuclide to south central Alaska. However, although unable to provide detailed chronological markers, the ^{137}Cs data does provide confidence in the AD 1964 lithological boundary.

'Ideal' profiles of excess ^{210}Pb activity approximate to an exponential curve with depth, of up to 5 half lives before reaching background levels. Both GW-08-3 and BP-08-6 show very low levels of ^{210}Pb activity with measured levels falling below the measurable limit in the silt prior to the AD 1964 boundary (Figure 4.8 and 4.14). Though the CRS and CIC dating models can allow for changes in sediment accumulation rate and deviations away from the 'ideal' ^{210}Pb curve (Krishnaswami *et al.*, 1971; Appleby and Oldfield, 1978), the low activity levels in the two cores cannot provide control on the rate of peat deposition prior to AD 1964 and are of little chronological value. Outridge *et al.* (2002) suggest increased latitude can result in reduced precipitation and therefore lower levels of ^{210}Pb, but Girdwood marks the west edge of the Alaskan temperate coastal rainforest where annual precipitation is up to 2000 mm (Spatial Climate Analysis Service, Oregon State University). The low ^{210}Pb activity at Bird Point and Girdwood is instead likely due to permafrost impeding diffusion of ^{222}Rn into the atmosphere (Wolfe *et al.*, 2004), the presence of annual sea ice reducing sediment absorption capacity, decomposition of the organic matrix (Davis *et al.*, 1984; Cooper *et al.*, 1995) or high rates of sediment accumulation in the post AD 1964 period.

Pollutant history

Salt marsh and estuarine environments can act as very effective heavy metal sinks, and therefore have the potential to record chronological pollutant markers of historical local and regional anthropogenic activity (Berry and Plater, 1998; Callaway *et al.*, 1998; Cundy *et al.*, 2003; Gehrels *et al.*, 2005; 2007; Hwang *et al.*, 2009; Marshall *et al.*, 2009) (section 3.4.3). This thesis aimed to make use of the history of gold mining in Turnagain Arm (section 2.2.6) as a possible chronological horizon in the coastal sediment sequences. In addition, ratios of stable isotopes ^{206}Pb/^{207}Pb have the potential to identify regional and global sources of pollution and provide an alternative independent pollutant derived chronology (section 3.4.3).

The occurrence of gold mining activity around Turnagain Arm from AD 1890 led to forming the hypothesis that the pollutants from mine tailings and increased human activity in the region will present as a clear heavy metal horizon in the salt marsh sequences of upper Cook Inlet. Analysis of a suite of heavy metals from all four sites shows limited clear trends and in general no obvious pollutant marker horizons (Figures 4.9, 4.15, 4.22 and 4.26). The GW-08-3 sequence shows a broad peak in normalised levels of all measured metals, to which I ascribe a tentative minimum age of AD 1895 ± 5 yrs at its base (Figure 4.9). No other site shows a similar

clear signal. It is reasonable to expect a broad correlation between measured pollutant concentration and proximity to pollutant source. At Hope, the geographical focus of Turnagain Arm gold mining activity, the sediments record the highest pollutant concentration (Figure 4.22), followed by Girdwood (Figure 4.9), where local mining occurred on Glacier Creek. The sediments record the lowest levels in the Bird Point sequence (Figure 4.15), where there was no local mining source and therefore the signal may be too weak to provide at clear chronological marker. At Ocean View, the concentration varies by metal with higher normalised ratios of arsenic, copper, magnesium and selenium at the bottom of core (Figure 4.26). Conversely measured levels of copper, lead and zinc increase up core. Normalised levels of arsenic and magnesium are higher at Ocean View than at Girdwood, though only in the peat layer. Knowledge of the development of Anchorage and its associated infrastructure does not provide explanation of the trends of pollutant data and prevents assigning any chemostratigraphic markers to OV-08-2 (section 4.3.4). It is not possible to reject the hypothesis that the pollutants from mine tailings and increased human activity can occur locally as clear heavy metal horizons, however the signal is spatially variable and dependant on the local pollutant source.

Changes in the ratio of $^{206}Pb/^{207}Pb$ have the potential to provide chronological markers associated with the peak use of alkyl-lead additives in gasoline and regional industrial development. Stable lead ratios date sedimentary sequences around the North Atlantic (2000; Renberg *et al.*, 2001; Outridge *et al.*, 2002; Klaminder *et al.*, 2003; Gehrels *et al.*, 2005; Bindler *et al.*, 2009; Kylander *et al.*, 2009). In all four cores, there are no clear trends in lead ratios (Figures 4.9, 4.15, 4.22 and 4.26). Figure 6.6 summarises the lead ratios from the four field sites, overlaying a schematic plot of the isotopic composition of different lead sources (adapted from Komarek *et al.* (2008) Figure 1). This suggests much of the deposited fossil stable lead is natural lead from the weathering of bedrock. At Ocean View, several samples have lower $^{206}Pb/^{207}Pb$ ratios and higher $^{208}Pb/^{206}Pb$ ratios, indicating deposition of stable lead from U.S. gasoline and anthropogenic burning of waste and fossil fuels, explained by proximity to the development of Anchorage from the start of c. AD 1900. The lowest $^{206}Pb/^{207}Pb$ ratio corresponds with a peak in normalised Zn, suggesting this may indicate onset of industrial development from the start of c. AD 1900. However, the $^{206}Pb/^{207}Pb$ ratios quickly return to higher levels, so it is not possible to be certain of a date (Figure 4.26). Similarly, the low $^{206}Pb/^{207}Pb$ values in the upper most peat at Girdwood marsh (section 4.3.1) may be associated

with development of Girdwood on the old town site next to the marsh from the c. AD 1910, prior to the town's submergence and subsequent relocation following the 1964 earthquake. This is in agreement with the Girdwood heavy metal data. The high stable $^{206}Pb/^{207}Pb$ ratios are a likely consequence of the lack anthropogenic activity around AD 1900 in south central Alaska (section 2.2.6), with still relatively little heavy industry in the region. Recent salt marsh sequences in Greenland show similarly high $^{206}Pb/^{207}Pb$ ratios (Woodroffe, personal communication). High latitude salt marshes covered by seasonal sea ice with a short growing season may not have the uptake potential for low levels of stable lead from distal pollutant sources. Stable lead ratios do not provide independent chronological control on Turnagain Arm salt marsh sequences, but at Girdwood they do corroborate heavy metal pollutant data.

In summary, although salt marsh and estuarine environments can act as effective heavy metal sinks, in upper Cook Inlet the contamination history is localised with only a clear gold mining derived heavy metal horizon at Girdwood. Stable lead ratios appear to be entirely a consequence of local site pollutant and sedimentary histories, rather than global and regional shifts in industry and gasoline usage.

Tephrochronology

A history of volcanic events in Cook Inlet, including eruptions of Augustine, Redoubt, Illiamna and Mount Spur, provides chronostratigraphic markers in sediment sequences around south central Alaska (Riehle, 1985). As a result, fossil sequences in south central Alaska contain both visible tephra horizons and abundant cryptotephras (Beget *et al.*, 1994; de Fontaine *et al.*, 2007; Payne *et al.*, 2008). Trialled extraction techniques on two Girdwood cores showed that without detailed counting and geochemical fingerprinting of a large number of shards, which was too time-consuming under the limitations of this thesis, tephrochronology would not greatly enhance the ability to test the research hypotheses (section 3.4.4). The Augustine tephra deposited c. 500 cal yr BP (Combellick, personal communication, unpublished geochemical and radiocarbon data) is visible at the base of the peat in all cores at Girdwood providing a minimum age of AD 1400 ± 100. The tephra is not visible at any other field site, preventing cross-site correlation.

AMS Radiocarbon dating

The plateau in the relationship between radiocarbon ages and calander years from AD 1650 to 1950 means several possible calibration solutions exist for dates from this time interval (Reimer

et al., 2004). To improve the precision and accuracy of the individual dates and produce an age-depth model from sediments of this age I apply two forms of WMD for radiocarbon dates from BP-08-6 (section 4.3.2) which use the details of the radiocarbon calibration curve to provide a detailed chronology from samples collected in stratigraphic sequence (Bronk Ramsey *et al.*, 2001) (section 3.4.1). The first approach follows Marshall *et al.* (2007), who advocates the selection of the most appropriate calibration in the 2σ range by maintaining the inter-sample stratigraphic relationship and including *a priori* knowledge of the stratigraphy and independent age markers to reduce dating uncertainties. The inability to define a range of independent age markers in the Turnagain Arm salt marsh sediments (as discussed above in this section) means two calibration solutions still exist for six of the seven BP-08-6 samples, resulting in a chronology with limited precision (Figure 4.16).

The second approach uses Bayesian analysis, Markov Chain Monte Carlo sampling and the *P_sequence* depositional model in OxCal 4.1 with calibration by IntCal04 (Bronk Ramsey, 1995; 2001; Blockley *et al.*, 2007; 2008; 2008, 2009) (section 4.3.2 and Figure 4.17). Repeated testing of the depositional models produces a good fit for six of the seven samples, estimating an average accumulation rate of 0.8 mm yr^{-1} (Figure 4.17A). Date BP086-R5 at 92 cm has a low agreement value, below the 60% threshold (Blockley *et al.*, 2008; Bronk Ramsey, 2009), highlighting poor fit with the depositional model and identifying a possible change in accumulation rate c. AD 1600-1650. The LOI data shows a slight decrease in organic content at 95-100 cm (Figure 4.13) suggesting a slight change in sediment deposition around this time.

Both WMD dating methods have the potential to provide a chronology for recent high latitude salt marsh sediments, though the Marshall *et al.* (2007) approach requires a greater number of independent age markers than possible from these sequences. Where a suite of suitable AMS ^{14}C dates are available, Bayesian modelling, with inclusion of additional independent age markers where appropriate and careful assessment of the model agreement with the true ages of the samples (section 4.3.2), can produce an age-depth model for recent salt marsh sequences, so it is possible to use this age-depth model from BP-08-6 (Figure 4.17A) to test working hypothesis three.

Testing the hypothesis

To test working hypothesis three that the RSL change is time synchronous with periods of regional glacier advance and retreat I use the broad chronology from the five cores, and in

particular the BP-08-6 age-depth model (Figures 4.17A and 6.4). In a coastal setting, it is not possible to assume a constant sediment rate across all the cores. However, comparison of the transfer function based estimates of RSL shows the possible deviation away from that predicted by the EDC model of land level change occurs consistently c. 30 cm from the peat-silt boundary (Figure 6.4), suggesting the basic framework of the BP-08-6 age-depth model may be loosely applied to the RSL changes in the other four cores. The addition of future AMS ^{14}C dates from GW-08-3 will help refine these chronologies further.

To test working hypothesis three requires definition of the timing of any deviation away from the pattern of EDC predicted land uplift, and this in turn requires establishing a rate of interseismic RSL fall. Hamilton and Shennan (2005a) represent the changes between two earthquakes at a single location as:

$$\Delta\xi_{int}(\tau) = \Delta\xi_{rsl}(\tau) + \Delta\xi_{cos}(\tau) - \Delta\xi_{sed}(\tau) - \xi_{peat}(\tau)$$

$\Delta\xi_{int}(\tau)$ represents post- and inter-seismic uplift, $\Delta\xi_{rsl}(\tau)$ is non-seismic relative sea-level change over the time period in question (including tidal range changes), $\Delta\xi_{cos}(\tau)$ equals co-seismic subsidence accompanying a subduction zone earthquake, $\Delta\xi_{sed}(\tau)$ is net sedimentation (including consolidation) between the tops of two peat layers and $\xi_{peat}(\tau)$ is the difference in the formation elevation of the top of the first buried peat ($\xi_{peat1}(\tau)$) and the formation elevation of the top of the second buried peat ($\xi_{peat2}(\tau)$).

At BP-08-6 the $\Delta\xi_{sed}(\tau)$ between the top of the upper most (AD 1964) peat and top of the underlying (c. 850 yr BP) peat is 1.25 m. The transfer function reconstruction of elevation provides estimates of 1.72 m and 0.14 m for $\Delta\xi_{cos}(\tau)$ and $\xi_{peat}(\tau)$ respectively. As discussed in section 6.2.1 the training set, the components of the transfer function and the impact of the SWLI method may exaggerate the magnitude of RSL change across the peat-silt boundary at Bird Point and therefore $\Delta\xi_{cos}(\tau)$. However, 1.72 m is within the magnitude of displacement mapped by Plafker (1969) (Figure 1.4) for Turnagain Arm.

The value of $\Delta\xi_{rsl}(\tau)$ is dependent on the selected models of isostasy and eustasy. Hamilton and Shennan (2005a) quote a regional estimate of RSL rise of 0.5 ± 0.5 mm yr^{-1} which they derive from Peltier (2002) ICE4G(VM2) model. In comparison, the most recent ICE5G(VM2) model (Peltier, 2004) estimates the rate of $\Delta\xi_{rsl}(\tau)$ at Anchorage 100 yr BP of -0.27 mm yr^{-1} and -0.19 mm yr^{-1} at present. Increased thickness of ice over the Laurentide region in ICE5G, to fit with

measurements of uplift in Yellowknife, and collapse of the forebulge and ocean loading, explains the estimated RSL fall over the last 100 years predicted by ICE5G(VM2) compared to the RSL rise estimated by ICE4G(VM2).

Peltier tunes the VM2 Earth model for a mid continental rheology largely using RSL data from passive coastal margins, as well as GPS data from tectonically stable regions (Peltier, 2002, 2004). Sella *et al.* (2007) highlights for a GIA model to reproduce the horizontal motions measured by North American GPS data requires horizontally variable mantle viscosities. Peltier and Drummond (2008) and Argus and Peliter (2010) suggest that the developing VM5a Earth model accounts for these horizontal motions by including rheological stratification of the lithosphere (section 5.6.1). In both instances, the authors do not attempt to resolve the large horizontal motions from the seismically active west coast of the USA. Reviewing the literature of isostatic modelling at tectonically active locations (section 1.3.4), identifies the need for laterally heterogeneous rheology which allows plate movement at tectonically active locations (Anderson, 1975).

GIA modelling and tectonic observations corroborate the need for variable Earth rheology (section 1.3.4). Modelling and field measurements at the Cascadia subduction zone suggests a rapid relaxation time (defined by Heiskanen and Vening Meinesz (1958) as the time for about 63% of the ultimate isostatic uplift to be achieved) of probably less than 1000 years following retreat of the Cordilleran Ice Sheet, with much of the post LGM uplift complete by 8000 ^{14}C years ago (Mathews *et al.*, 1970; Clague *et al.*, 1982; Clague and James, 2002; Hutchinson *et al.*, 2004; James *et al.*, 2009a). James *et al.* (2009a) estimate only 0.1 mm yr^{-1} of present crustal uplift at southern Vancouver Island in response to the collapse of the south west sector of the Cordilleran Ice Sheet. They attribute this small GIA rate as a consequence of the low mantle viscosity of the subduction zone.

The use of Peltier's estimates of $\Delta\xi_{rsl}(\tau)$ are, for the reasons outlined above and further in sections 1.3.4 and 5.6.1, probably unrealistic for the south central Alaska subduction zone rheology. Therefore, to calculate reasonable minimum and maximum rates of $\Delta\xi_{rsl}(\tau)$ I consider estimates of global sea level change and regional isostasy over the last 2000 years. Comparison of archaeological, geological and historical records (after correcting for land motion) suggests there has been little net change in global sea level from 2000 yr BP until c. AD 1800 (Lambeck *et al.*, 2004). The 4th IPCC assessment quotes a mean value of 0.0 – 0.2 mm yr^{-1} global sea level

rise during the last 2000 years (Bindoff *et al.*, 2007) with the rate of sea level rise generally less than 1 mm yr^{-1} prior to AD 1930 (Church *et al.*, 2008). Estimates of the timing and magnitude of c. AD 1800-2000 sea level accelerations from tide gauges, geological and geodetic data, and modelling results vary from c.1.0 – 2.5 mm yr^{-1} (Table 6.1). In this thesis, the period of interest to is c. 850 yr BP to AD 1964, which includes a phase of marked sea level acceleration from c. AD 1930-1950 (Woodworth *et al.*, 2009). Assuming no ongoing post LGM GIA in south central Alaska, a maximum value of 1 mm yr^{-1} $\Delta\xi_{rsl}(\tau)$ provides a sensible average of relatively stable sea level from 2000 yr BP to AD 1800 and global sea level rise from AD 1800 to AD 1964.

For the minimum estimate of $\Delta\xi_{rsl}(\tau)$, I assume some ongoing post LGM GIA (for example the c. 0.1 mm yr^{-1} suggested by James *et al.* (2009a) in British Columbia (section 1.3.4) and by Peltier (2004) for south central Alaska, which exceeds any global sea level rise. To account for any error in the estimate by James *et al.* (2009a) I use an minimum $\Delta\xi_{rsl}(\tau)$ estimate of -0.2 mm yr^{-1}.

Table 6.2 provides solutions to the $\Delta\xi_{int}(\tau)$ equation using these minimum (-0.2 mm yr^{-1}) and maximum (1 mm yr^{-1}) $\Delta\xi_{rsl}(\tau)$ values with the geological data from BP-08-6 (summarised above) and GW-1 (Hamilton and Shennan, 2005a) over a period of 860 years from the penultimate great earthquake to AD 1964. The solutions to the equation estimates minimum and maximum $\Delta\xi_{int}(\tau)$ rates of 0.1 mm yr^{-1} and 1.4 mm yr^{-1} respectively.

To test hypothesis three, Figure 6.7 shows the RSL change (m MHHW) (though being mindful of the limitations of the method as discussed in section 6.2.1) against modelled age for each BP-08-6 fossil diatom sample covered by the Bayesian age-depth model, plotted against the minimum and maximum $\Delta\xi_{int}(\tau)$ rates. I estimate the interseismic land uplift from the median age and mean elevation of the oldest radiocarbon dated fossil sample. The timing of the deviation away from the expected EDC model of land level change varies with the selected interseismic rate. Using the maximum interseismic rate (1.4 mm yr^{-1}) the BP-08-6 RSL deviates from the interseismic land uplift from c. AD 1580. Based on the minimum interseismic rate (0.1 mm yr^{-1}) the BP-08-6 RSL deviates from the interseismic land uplift some time from c. AD 1780. The rate of interseismic land uplift likely sits within this upper and lower limit suggesting that possible change in the direction of RSL (section 6.2.1) at BP-08-6 (Figure 6.7) and the other 5 cores (Figure 6.4) occurred sometime in c. AD 1600 - 1900. Definition of the timing of the

deviation using this approach allows testing of the working hypothesis that RSL change in upper Cook Inlet occurs during periods of regional glacier advance and retreat.

Regional glacier advance and retreat of Alaskan mountain glaciers occurred in three phases during the LIA, with the culmination of the LIA hemispheric cooling resulting in Holocene maxima for many land-terminating glaciers in the Chugach and Kenai Mountains (Wiles and Calkin, 1994; Wiles *et al.*, 1999; Calkin *et al.*, 2001; Molnia, 2008; 2008; Barclay *et al.*, 2009). Early advances were underway in Alaska from AD 1180s to 1320s, with the two maximum advance phases during the 1540s to 1710s and 1810s to 1880s (section 2.2.5 and Figure 2.7). The exact advance-retreat chronology is glacier specific, but within the error terms of dating terminal moraine positions and Turnagain Arm salt marsh sequences, it appears that some RSL change in upper Cook Inlet during c. AD 1600-1900 occurred in phase with the regional middle and late LIA advances. It is not possible with the present dating control and limitations of the RSL reconstruction method (section 6.2.1) to determine if there is any lag in RSL response to the regional glacier mass balance changes.

The geological data from upper Cook Inlet means it is not possible to reject the hypothesis that some change in the direction of RSL occurred during periods of regional glacier advance and retreat. The next section considers the possible mechanisms of the change during the last EDC in upper Cook Inlet.

6.2.4 The mechanism of RSL change is GIA.

Integration of the geological data and modelling estimates allows testing of working hypothesis four that the mechanism of increase in marine influence recorded by the fossil diatoms and the net RSL estimated by calibration of the fossil diatom assemblages (section 6.2.1) is GIA. Testing this hypothesis is structured around solving the components of the equation that express changes in RSL ($\Delta\xi_{rsl}$) at any location in space (ϕ) and time (τ) by:

$$\Delta\xi_{rsl}(\tau,\phi) = \Delta\xi_{eus}(\tau) + \Delta\xi_{iso}(\tau,\phi) + \Delta\xi_{tect}(\tau,\phi) + \Delta\xi_{local}(\tau,\phi)$$

Where $\Delta\xi_{eus}$ is the time-dependent eustatic function, $\Delta\xi_{iso}$ is the total isostatic effect of the glacial rebound process including both the ice (glacio-isostatic) and water (hydro-isostatic) load contributions, $\Delta\xi_{tect}$ is the tectonic effect and $\Delta\xi_{local}$ is total effect of local processes at the site involved, including changes in sediment and tides. As the geological data suggests it is not

possible to reject working hypothesis one and therefore there is potentially evidence, within the limitations of the reconstruction methodologies, for non-EDC RSL change during the LIA in upper Cook Inlet (section 6.2.1), there must be changes in one or more components of the RSL equation over the last earthquake cycle. I consider each component in turn to assess its possible contribution towards any potential RSL change in the upper Cook Inlet during the middle and late LIA.

Tectonic mechanism

Subduction zone dynamics result in unique RSL histories that record the interplay of global, regional and local processes. Extensive work in Cascadia, southern Alaska and Japan defines different EDC models of land/sea-level changes associated with tectonic deformation of the coast (Long and Shennan, 1994; Nelson *et al.*, 1996; Sawai, 2001; e.g. Hamilton and Shennan, 2005a) (section 1.3.2). Fossil diatoms preserved in the upper peat layer of the Turnagain Arm salt marsh sediments record a subtle increase in marine influence, which the transfer function based estimates as rise in RSL (Figure 6.4), counter to the RSL fall predicted by EDC model of land-level change in this region (Figure 1.3). It is worth noting that the EDC model described in Figure 1.3 developed from analysis of RSL motions associated with the cycle of M_w 8 or greater earthquakes. Earthquakes less than M_w 8 (Figure 1.1) may result in smaller scale RSL changes and/or ground shaking compaction of coastal salt marsh sediments that may differ from the great (M_w >8) earthquake model. It is however possible to reject the hypothesis that the change in the direction of RSL is a result of an M_w 6-8 earthquake due to the duration of the RSL rise over several centuries (section 6.2.3) and no coseismic RSL fall. Geological data in this thesis showing a potential RSL deviation away from the expected EDC model of land level changes (section 6.2.1) suggests that the driver of RSL change is a non-seismic process.

Local mechanism

The 'local' component of the RSL equation above includes changes in sediment and tidal regime, autocompaction of sediments, creek migration and, in a tectonically active location, liquefaction (section 6.2.2). When testing the hypothesis whether RSL changes in upper Cook Inlet over the earthquake cycle are spatially variable I assessed the possible contribution of these mechanisms. Section 6.2.2 concludes that local processes may account for some intra-site variability with spatially variable erosional processes and coseismic liquefaction responsible for the variable magnitude of the RSL change recorded in the six cores. It is likely that these

processes, in particular coseismic liquefaction, would occur at all sites, possibly driving what could appear to be larger scale RSL changes. There is also potential that the increase in marine influence could be due to increased tidal amplification due to reduced water depth during the LIA (section 2.2.2). It is not possible to quantify tidal amplification within this thesis, but it seems unlikely that the potential tidal amplification would exceed the potential steric sea level fall (further discussed below), or land level displacement due to regional GIA (Chapter 5). Within the limitations of the RSL reconstruction methodology (section 6.2.1) and age model (section 6.2.3), it is not possible to define the timing and magnitude of small scale RSL changes and therefore difficult to separate the contribution of 'local-regional' processes from larger scale 'regional-global' processes. Examination of the 'local' marsh specific processes in section 6.2.2 eliminates some as mechanisms for the increase in marine influence and drivers of the net RSL rise within the interseismic peat as they relatively short lived processes. Despite not being able to isolate separate mechanisms, the potentially for a consistent RSL deviation away from the expected EDC model of land-level change and a net RSL rise in five cores (Figure 6.4) from three salt marshes over c. 50 km (Figure 2.1), suggests possible operation of longer term 'regional-global' mechanism(s) of RSL change overprinting 'local-regional' mechanisms.

Eustatic mechanism

Milne and Mitrovica (2008) define eustasy as a spatially uniform height shift of the ocean surface to accommodate any mass gained/lost from grounded ice but show there are significant deviations from the eustatic sea level curve due to GIA, hydro-isostasy (section 5.6.2), the influence of the Earth's rotation, melt source and ocean syphoning. Any LIA expansion of mountain glaciers and ice sheets (Grove, 2004a, b) will lock up water and result in a fall in eustatic sea level. Few studies quantify eustatic change over the LIA. Indeed many show no change over the last few millennia (Peltier, 2002; Lambeck *et al.*, 2004; 2004; Bassett *et al.*, 2005) (section 6.2.3).

In contrast, Grinsted *et al.* (2009) link modelled changes in sea level to temperature by combining knowledge from instrumental and proxy climate records, to produce a reconstruction of eustasy over the past 2000 years. They show decimetre-scale variability within the timeframe considered here, with minimum sea level, around AD 1730, although the exact values depend on the climate reconstruction used (Figure 6.8) and the relative contributions of eustatic sea level and steric volume change are unspecified. Hemispheric

temperature reconstructions of the past 1000 years demonstrate a period of cooling c. AD 1200-1900 (Jones and Mann, 2004; Moberg *et al.*, 2005) suggesting likely global thermo-steric lowering of sea level during this time. Modelling of steric sea-level changes, for future sea-level rise scenarios, shows a highly model-dependent spatial variability (Bindoff *et al.*, 2007). Figure 6.9 illustrates a global eustatic plus steric trend against the RSL change suggested by fossil daitoms in the Turnagain Arm salt marsh sediments over the last 600 years, demonstrating that the projected fall of global sea level during c. AD 1600-1800 is the inverse of the trends in RSL reconstructed in upper Cook Inlet in this thesis over the same period. Given the uncertainty over both the magnitude of a global LIA eustatic signal and the spatial variability of steric changes this is not considered further other than to note that they cannot explain the potential RSL trend recorded in the Turnagain Arm salt marshes during the middle and late LIA.

Isostatic mechanism

Depression of the Earth's crust by surface loading from small regional ice sheets and mountain glaciers has the potential to cause regional RSL changes. The total isostatic component of RSL is the net effect of ocean geoid height deformation and vertical land displacement, both of which are considered in this section. Modelling, GPS results and geological data in Patagonia (Ivins and James, 2004; Klemann *et al.*, 2007; 2008; Dietrich *et al.*, 2010) and south east Alaska (Motyka, 2003; 2005; Larsen *et al.*, 2007; Mann and Streveler, 2008) show recent mountain glacier retreat results in rapid crustal uplift. Modelling in this thesis (Chapter 5), using the Larsen *et al.* (2005) ice model of ice thickness change over the LIA and a series of realistic Earth models, show that the mass balance changes over the past 1000 years have the potential to cause vertical land displacement.

Figure 6.10 displays the maximum and minimum uplift predictions of the spatial pattern and magnitude of vertical land displacement, and rates of land displacement at AD 1890 and AD 2005, in south central Alaska in response to local-regional LIA ice loading as estimated by the acceptable ALVZ models from section 5.5.2. The maximum LIA radial displacement model has a 60 km thick lithosphere and an 8 x 10^{18} Pa s asthenosphere, and the minimum radial displacement model has a 110 km thick lithosphere and a 4 x 10^{19} Pa s asthenosphere. Other solutions fall within these ranges (section 5.7 and Figure 5.8), though the Earth model with a 110 km thick lithosphere and 1 x 10^{18} Pa s asthenosphere viscosity results in the greatest AD

2005 uplift (Figure 5.8). Inclusion of long wavelength solid Earth displacement caused by the LGM ice sheets (section 5.6.1), potentially further constrains the best Earth model as having an asthenospheric viscosity of 1 x 10^{18} Pa s for an asthenospheric thickness of 110 km (110 km thick lithosphere) to 8 x 10^{18} Pa s for an asthenospheric thickness of 160 km (60 km thick lithosphere) (section 5.7 and Table 5.1), which are the solutions I use from here onwards, though there are limitations of applying global GIA models to upper Cook Inlet (sections 1.3.4, 3.7.3, 5.6.1 and 6.2.3). The model results suggest the main control on the rheological response is asthenosphere thickness (defined as 220 km minus effective model lithosphere thickness (Figure 3.11)) and viscosity. These findings are in line with similar, independent models, of the Cascadia and Peru-Chile subduction zones, which also include a low viscosity (< 10^{20} Pa s) asthenosphere (James *et al.*, 2009b; Dietrich *et al.*, 2010).

Changes in ice load can also cause deformation of the ocean geoid, due to the effects of self-gravitation in the surface mass load (Farrell and Clark, 1976), resulting in regional and local sea level changes (Figure 6.11). Modelling predictions and satellite altimetry measurements of geoid changes arising from present day mass variations from the Antarctic and Greenland ice sheets and mountain glaciers, show notable sea level changes due to differential gravitational effects over time (2001; Tamisiea *et al.*, 2003; Fleming *et al.*, 2004; Lombard *et al.*, 2007; Milne and Mitrovica, 2008). Tamisiea *et al.* (2001) predict melting of Alaskan glaciers can cause a non-uniform changes in sea level height, with RSL rise experienced along the Washington and Oregon coasts and RSL fall in the areas closest to the Alaskan glaciers, including upper Cook Inlet. Tamisiea *et al.* (2003) note the non-uniform deformation of the ocean geoid becomes more localised, and reaches higher amplitudes, close to a glacier system, as viscous effects become more active. Their results suggest the weakening of the gravitational pull as the mountain glaciers retreat exceeds the increased gravitational pull due to ongoing glacio-isostatic uplift, though the latter becomes more important for viscosities below 10^{20} Pa s, the value which is considered to be the upper threshold value for asthenosphere viscosity at a subduction zone (section 3.7.3).

TABOO (section 3.7) can also provides estimates of ocean geoid height deformation in response to the input Earth and ice models. Figure 6.12 shows the model estimated geoid height deformation over the last 1000 years for the four best Earth models (constrained using GPS data and the model estimates of long wavelength GIA (Chapter 5, Figure 5.8 and Table 5.1) for

Girdwood, Bird Point and Ocean View (section 5.7). The models predict decreased deformation of the ocean geoid with distance from ice load and increased asthenosphere viscosity (following the pattern predicted by Tamisiea *et al.* (2001), and similar to that estimated for the solid Earth displacement (Figure 5.8)), with maximum ocean geoid height during the early and middle LIA advances and present day (AD 2005) geoid height fall in response to mountain glacier retreat from their LIA maximum positions.

As mentioned above, the total isostatic component of RSL is the net effect of ocean geoid height deformation (Figure 6.12) and vertical land displacement (Figure 5.8). Figure 6.13 shows the model predicted rate of RSL at Girdwood, Bird Point and Ocean View over the last 1000 years in response to change in ice thickness over the LIA. Low asthenosphere viscosities result in the greatest rates of modelled RSL change.

Figure 6.13 highlights that the model predicts the greatest rates of RSL change during the early LIA advance phase. This is a result of the mantle material not being in a recovery phase, as during the latter two LIA advances. It is not possible to use the geological data to test GIA RSL during this phase of the LIA, as the early advance occurs at a similar time to the c. 850 yr BP earthquake event. Rapid coseismic submergence and post seismic uplift dominates the RSL history at this time, which may mask smaller scale RSL changes. In addition, the lack of datable material in the silt and the large error terms associated with reconstructing RSL through tidal flat sediments in upper Cook Inlet it is not possible to develop a high precision RSL history during the early LIA advance.

For GIA to cause net RSL rise during the middle and late LIA, over the expected tectonically driven interseismic RSL fall (Figures 1.3 and 6.1), the isostatically driven RSL rise must exceed the rate of interseismic land uplift. In section 6.2.3 I define a maximum (1.4 mm yr^{-1}) and minimum (0.1 mm yr^{-1}) rate of interseismic land uplift over the last earthquake cycle. To test whether the GIA displacement exceeds the interseismic rate, Figure 6.13 shows these interseismic rates on the best Earth model graphs of RSL over the last 1000 years for Girdwood, Bird Point and Ocean View. During the middle and late LIA ice advances, all model solutions exceed the minimum (0.1 mm yr^{-1}) rate of interseismic uplift, and between two and four Earth model solutions exceed the maximum (1.4 mm yr^{-1}) interseismic rate. This shows it is possible to model a potential RSL rise during the middle and late LIA that exceeds the rate of interseismic land uplift, using a range of Earth model parameters (sections 5.5.2 and 5.7)

consistent with those used in modelling studies in southeast Alaska, Cascadia and Patagonia (Larsen *et al.*, 2005; James *et al.*, 2009b; Dietrich *et al.*, 2010). It must be noted that the probable over estimation of present day ice by Ardent et al. (2002) (Berthier et al., 2010) and therefore over estimation of LIA ice mass by the Larsen et al . (2005) ice model means that the TABOO estimates of GIA must be considered as upper bounds as the magnitude of isostasy and geoid deformation (section 3.7.2), and therefore, there is potential for the modelled GIA to not exceed the estimated rate of interseismic land uplift and not cause a rise in RSL in Turnagain Arm.

Unlike the coseismic RSL changes accompanying a great earthquake, isostatically driven RSL changes have a smooth pattern due to the viscoelastic response of the Earth's rheology (Figure 6.1), which I show by converting the GIA model predictions in Figure 6.13 to rates of RSL change in Figure 6.14. It is reasonable therefore to expect that any GIA related RSL deviation away from the predicted EDC model to comprise a gradual trend of rising and then falling RSL.

Testing the hypothesis that the mechanism of RSL change is GIA

Assessing each component of the sea level equation in turn determines which process or combination of processes may be a responsible for the fossil diatom changes and changes in the direction of sea level reconstructed in the geological data. Figure 6.15 integrates the modelling results and geological data based on the assumptions set out below.

To standardise the modelling results and geological data to the same period (AD 1400-1964), rather than the top of the peat-silt boundary as per Figure 6.4, I develop a linear age-depth model for GW-08-3 and OV-02-4 due to the absence of suitable chronological control at Girdwood and Ocean View (sections 4.3.1, 4.3.4 and 6.2.3). I decide a linear model is potentially applicable in the absence of any other suitable dating control based upon the more comprehensive AMS ^{14}C Bayesian modelled age-depth profile for BP-08-6 which suggests a near linear accumulation rate of c. 0.8 mm yr^{-1} through the upper peat at Bird Point (section 4.3.2). Using the Augustine (AD 1400 ± 100) tephra horizon at the base of the peat at Girdwood and the AD 1964 lithological horizon, I develop a linear age-depth model for GW-08-3, which suggests a c. 0.9 mm yr^{-1} accumulation rate. I chose too not include the tentative AD 1895 ± 5 data based on the pollutant data (section 4.3.1 and Figure 4.9), as the increase in pollutant concentration is a broad peak and the exact timing of the onset of gold mining within this peak remains unknown. There is no basal chronological horizon at OV-02-4, but a date at the

preceding peat silt boundary of 929-1056 yr BP (Hamilton *et al.*, 2005) provides a minimum age for the sequence. Assuming the onset of peat development at a similar time to that at Girdwood and Bird Point, it is reasonable to place a date of AD 1400 at the base of the peat at Ocean View to develop a linear age model, which again suggests a c. 0.9 mm yr^{-1} accumulation rate. I plot all the geological data against these age models to allow direct comparison with the geophysical modelling results and testing of the hypothesis (Figure 6.15).

Diatom assemblages summarised using the halobian classification scheme, from cores at Girdwood, Bird Point and Ocean View, show an overall trend of increasing abundance of freshwater species from AD 1400 – 1600. From AD 1600 – 1800 there is a slight increase and subsequent decrease in brackish species before an increase in freshwater species from AD 1800, prior to any pre-seismic increase in brackish diatoms such as is notable at Girdwood (Figure 6.15A). Plotted as summary halobian classes the changes are much greater at Girdwood, compared to Bird Point or Ocean View.

It is not possible to satisfactorily quantify the magnitude of any small scale RSL change due to the limitations of the transfer function approach. The RSL changes estimated by the transfer function often fall within the sample specific errors and may be a consequence of: truncated species in the training set; the impact of the SWLI method; WA-PLS component 3 causing over estimation of species optima (Figure 6.3); and poor modern analogues for some fossil species, and therefore not truly represent changes in RSL, and consequently should viewed with some caution (sections 4.4 and 6.2.1). Calibrating fossil diatom assemblages using a set of refined upper Cook Inlet transfer function models (section 4.2.3) however goes some way in quantifying the direction of any RSL change (relative to AD 1400) which is not random in nature (Figure 6.15B). The base of the sequence at Girdwood is complicated by the sample specific error terms making it hard to distinguish the direction of any RSL change. The transfer function results suggest from c. AD 1600 – 1800 RSL falls at Girdwood and then stabilises. AD 1800 – 1900 there is potentially a slight RSL fall, and then rise again, prior to the AD 1964 submergence. At Bird Point the transfer function estimates a RSL fall c. AD 1400 – 1550, followed by a trend of rising RSL prior the AD 1964. At Ocean View, RSL appears to similarly fall from c. AD 1400 – 1550, rise from c. AD 1550 – 1750 and then fall again from AD 1750 prior to AD 1964.

The GIA model predictions (Figure 16.5C) show RSL rise from c. AD 1500 for all three sites until c. AD 1850, after which RSL begins to fall. They show a spatial pattern of decreased RSL change with increased distance from ice load.

Best estimates of interseismic land uplift through the last earthquake cycle range from 0.1 mm yr^{-1} to 1.4 mm yr^{-1} (section 6.2.3). Figure 6.15D shows two scenarios; a spatially constant interseismic rate, using a mean value, 0.75 mm yr^{-1}; and a spatially variable rate. Based on simple model of the EDC (Nelson *et al.,* 1996, Hamilton & Shennan 2005) (Figure 1.3), the interseismic rate should decline from Girdwood to Ocean View. There are no constraints from which to define a spatial variable rate to the three sites so I subscribe the mean value of 0.75 mm yr^{-1} to the central site, Bird Point, and simply added 0.25 mm yr^{-1} for Girdwood, c. 10 km to the east, and minus 0.35 mm yr^{-1} for Ocean View, c. 30 km to the west, giving 1.0 and 0.4 mm yr^{-1} for Girdwood and Ocean View respectively. Without comprehensive seismic modelling these values serves as simple, logical, first order estimates within the upper and lower range for interseismic land uplift estimated in section 6.2.3. The EDC model includes a period of RSL rise prior to the AD 1964 earthquake (Figure 1.3). There is no consensus as to the timing of the pre-seismic phase of the EDC, however, Karlstrom (1964) notes increased frequency of tidal inundation of Girdwood marsh from AD 1952, which I therefore take as the start of the pre-seismic RSL rise. I calculate a mean rate (15.5 mm yr^{-1}) of pre-seismic RSL rise simply by averaging the pre-seismic rates gained from geological data around upper Cook Inlet, as summarised by Shennan and Hamilton (2006) Table 1, for AD 1952-1964.

Theory suggests the RSL changes recorded in the geological data in upper Cook Inlet are a combination of EDC land-level movement and GIA RSL change. Combining the model estimates of GIA sea level change during the middle and late LIA and the rates of interseismic and pre-seismic sea level change produces model estimates of RSL relative to AD 1400 for Girdwood, Bird Point and Ocean View (Figure 6.15E and 6.15F). The modelled GIA plus EDC RSL curves shows a stable or slightly falling RSL at the three field-sites from AD 1400 to c. 1550, following by a period of RSL rise in response to LIA mountain glacier advance until c. AD 1850. From c. AD 1850 to 1952 RSL falls as mountain glaciers retreat resulting in isostatic uplift and reduced ocean geoid deformation, until the onset of pre-seismic RSL rise from AD 1952-1964 prior to the AD 1964 great earthquake.

To test whether the changes in fossil diatom assemblages recorded in sequences at Girdwood, Bird Point and Ocean View (Figure 6.15A) and associated RSL changes suggested by the transfer function (Figure 6.15B) are a consequence of the combination of EDC land-level changes and LIA GIA as predicted by the models, I overlay the geological reconstructed RSL on the modelled RSL (Figure 6.15E and 6.15F). Comparison of Figures 6.15E and 6.15F clearly show the best fit occurs with a spatially variable interseismic rate (Figure 6.15F). However, this fit must be qualified by the following the points that should form working hypotheses for future research.

1. There is one clear outlier in the Girdwood diatom-based RSL reconstruction due to a poor modern analogue for *Eunotia lunaris* (section 4.3.1). This requires further modern samples to find a contemporary analogous environment for this species.

2. While the summary diatom halobian data show some potential changes in the direction of RSL, the reconstruction error terms are mainly of the same order of magnitude as the RSL changes. Further modern samples to represent the wider range of assemblages seen in the fossil sequences may reduce sample-specific reconstruction error terms.

3. As discussed in section 6.2.1 the geological transfer function based RSL reconstruction suffers from inclusion of species in the modern training set with truncated response curves, updated species optima with each component of WA-PLS and the SWLI method, producing reconstructions that may well be an artefact of the method, rather than a true reconstruction of past sea level. To be confident in reconstructions of small scale RSL changes and disentangle the driving mechanisms requires either differing approaches to high resolution RSL reconstruction, for example potentially refining the visual assessment method advocated by Long *et al.* (2010), or improved statistical based techniques.

4. The linear age model for Girdwood and Ocean View based upon assumptions from the Bayesian age model from Bird Point, fits less well with the Girdwood data, in particular the pre-seismic phase in the decade prior to AD 1964. An exponential accumulation rate would allow for more rapid sedimentation in the decade prior to AD 1964 and stretch the lower part of age-depth model, producing better fit with the modelled

estimates of RSL. Radiocarbon samples for Girdwood, currently with NERC Radiocarbon Laboratory, will test this assumption.

5. A greater sampling resolution at the top of the peat is required to test the pre-seismic phase of the EDC which the Bird Point geological appears to not record.

6. The GIA modelling shows a spatially variable signal in response to early LIA mass balance changes which overlap with the coseismic and post-seismic phase of the penultimate great earthquake in the area (section 4.4 and Figures 5.8 and 6.15E and F). This will require further research to resolve.

7. The GIA model estimates rely upon a simple post glacial rebound calculator (section 3.7 and 5.7) that does not solve the sea level equation, does not take into account ocean loading (section 5.6.2) and does not include long wavelength GIA due the Pleistocene ice sheets (section 5.6.1). Constraining the Earth models using GPS data (section 5.4) and estimates of long wavelength GIA (section 5.6.1) still leaves multiple model solutions. To provide more realistic model estimates of RSL change and further constrain the Earth model requires development of a comprehensive GIA model with integrated short and long term ice loads, (potentially) a horizontally heterogeneous Earth model and integration of the seismic structure of south central Alaska.

Overall, integration of the modelling results and geological data in Figure 6.15F shows the fossil diatom changes and the transfer function estimated reconstructions of changes in the direction of RSL through the last earthquake cycle at Girdwood, Bird Point and Ocean View (Chapter 4) are a likely a combination of spatially variable tectonic land-level changes and GIA adjustment during the middle and late LIA ice advance phases. It is difficult within the present confines of the RSL reconstruction methodology (section 6.2.1), the limitations of dating recent high latitude sediments (section 6.2.3) and the structure of GIA models for south central Alaska (Chapter 5) to be sure of the exact timing and magnitude of any RSL change or fully assess the relative contribution of the tectonic, isostatic and 'local' mechanisms in driving any RSL change during the LIA in upper Cook Inlet.

6.2.5 Glacial isostatic adjustment is an important contributor to relative sea level change in upper Cook Inlet during the last earthquake deformation cycle.

The culmination of Little Ice Age glacier advance and retreat during the last earthquake cycle in upper Cook Inlet provides an excellent opportunity in which to test the hypothesis: *glacial isostatic adjustment is an important contributor to relative sea level change in upper Cook Inlet during the last earthquake deformation cycle*. Extensive lithological, biostratigraphical and chronological investigation at coastal salt marshes in upper Cook Inlet in this thesis (Chapter 4) shows an increase in marine influence and changes in the direction RSL that would appear to deviate away from the predicted EDC model of land-level uplift during the interseismic phase, prior to the onset of any pre-seismic RSL rise (Figure 6.4). Local processes may result in site specific modification of the RSL trend (section 6.2.2). Dating of the sediment sequences suggests that lithological and biostratigraphical changes occurred sometime through c. AD 1600 - 1900, during the middle and late phases of LIA regional glacier advance and retreat (section 6.2.3 and Figures 6.7 and 6.15). Geophysical modelling predicts LIA ice load changes during this time can result in Earth displacement and deformation of the ocean geoid (Chapter 5, section 6.2.4 and Figure 6.13). Integration of the geological data and modelling results (Figure 6.15) show there is potential for RSL changes through the last earthquake cycle at Girdwood, Bird Point and Ocean View that are a combination of tectonic land-level changes and GIA adjustment during the middle and late LIA ice advance phases. Limitations of the approaches to reconstructing past sea level, dating recent sediments and GIA modelling means it is not possible to fully test the hypothesis *glacial isostatic adjustment is an important contributor to relative sea level change in upper Cook Inlet during the last earthquake deformation cycle*. However, the data in this thesis does suggest it is not possible to reject the hypothesis and the field, laboratory and modelling work undertaken provides a framework for future work, indentifying areas which need development and refinement, to improve understanding and quantification of small scale RSL changes.

6.3 Conclusions

The results outlined above suggest the main research hypothesis cannot be rejected and that glacial isostatic adjustment is a potentially an important contributor to relative sea level change in upper Cook Inlet during the last earthquake deformation cycle. Lithological,

biostratigraphical and chronological data show a potential increase in marine influence suggest sea level changes which deviate from the expected EDC model of land level changes during the LIA in upper Cook Inlet (section 6.2.1). Chronological constraints suggest the observed changes sometime through c. AD 1600 - 1900, during the middle and late phases of LIA regional glacier advance and retreat (section 6.2.3). Modelled deformation of the regional ocean geoid and asthenosphere predicts LIA mass balance changes result in RSL change during the middle and late LIA. Integration of the geological data and modelling results shows there is potential for RSL changes at salt marsh sequences in upper Cook Inlet to be a combined function of tectonic land level changes, ocean geoid deformation and isostatic loading and unloading during the LIA (section 6.2.4). However, limitations of transfer function methodology, issues with dating high latitude recent salt marsh sediments and the state of GIA modelling in south central Alaska means it is not possible a present to quantify the magnitude or timing of small scale RSL changes or assess the relative contribution of the possible driving mechanisms. However, this thesis provides a framework from which to develop approaches to refine our understanding of small scale RSL changes. Chapter 7 outliners the wider implications of the research and indentifies areas for future work.

Chapter 7 : Wider Implications

The results and discussion in this thesis have wider implications for high latitude coastal research, disentangling the mechanisms of RSL change, our wider understanding of short term GIA, modelling of land uplift at tectonically active locations and future predictions of regional RSL change. Particular questions arise from the research that I also highlight as areas for future investigation.

Geological investigation at coastal salt marshes in this thesis show that to a limited extend it is possible to disentangle complex mechanisms of RSL change at a tectonically active high latitude coastal environment. Discussion in this thesis, particularly in section 6.2.1, highlights the limitations of the training set and transfer function approach to the reconstruction of former sea levels. When trying to quantify the magnitude of small scale changes that are a product of a change in the direction of sea level over time, the RSL signal may not be reconstructed accurately, rather becoming an artefact of the methodology. To fully understand small scale changes in sea level and disentangle the mechanisms of change is going to require differing and novel complementary approaches to constrain sea level signals, rather than just applying methods used to reconstruct much larger sea level changes where the signal is clear and not lost within the method.

The research highlights the limitations in high latitude environments of some of the chronological approaches that are applied to similar recent sequences from temperate salt marshes (Cundy *et al.*, 2003; Gehrels *et al.*, 2006; Marshall *et al.*, 2007; Kemp *et al.*, 2009). Gehrels *et al.* (2006) apply similar approaches tested in this thesis to date sequences from a similar latitude in Iceland, but the proximity of Iceland to north west Europe ensures the presence of anthropogenic chronological horizons. It is clear some of this industrial

atmospheric fall out does not reach south central Alaska, despite Sturges *et al.* (1993) recording contemporaneous fallout from Russia and Eastern Europe at Barrow in north west Alaska. The ^{137}Cs results from Girdwood and Bird Point, particularly when compared to previous results from Girdwood (Zong *et al.*, 2003), raise questions about down core migration of ^{137}Cs in salt marsh sequences, and whether it is possible to use the onset of nuclear weapon testing as a chronological horizon. Additional samples should allow development and testing of relevant hypothesis about mobility of ^{137}Cs in saline environments. Limitations of gamma and pollutant horizon dating, due to the presence of permafrost, the short growing season and seasonal sea ice identifies the need to consider alternative dating methods. Radiocarbon results from Bird Point show it is however possible to develop a depositional model using closely spaced ^{14}C AMS dates for recent sediment sequences, an approach to date largely applied to longer records (Blockley *et al.*, 2007; Bronk Ramsey, 2008). It may be applicable to apply a similar methodology to recent sequences elsewhere in the Canadian Arctic, Greenland and southern South America where chronological horizons of recent anthropogenic activity may also be sparse, although in all cases a reasonable rate of sedimentation is required, most likely associated with RSL rise. Full investigation of the crypotephras in the upper Cook Inlet salt marsh sequences, and correlating them to known events recorded in upper peat lands and lacustrine records from Kenai Peninsula (de Fontaine *et al.*, 2007; Payne and Blackford, 2008; Schiff *et al.*, 2008), may provide further dating constraint. More distally sourced tephras, especially if they have distinct geochemical fingerprints, may prove more useful than locally or regionally derived tephras which may overprint each other.

As on all coastlines, different processes interact to make it complex to identify the relative importance of individual mechanisms. The land level changes at a tectonically active location compounds this. This thesis shows it is possible to use a framework, such as the EDC model, as a theoretical basis against which to test hypotheses regarding the mechanisms of RSL change. As knowledge of particular elements of past RSL continue to develop, so it becomes ever more feasible to use known frameworks in which to disentangle the complex mechanisms of coastal change.

Integration of modelling results and geological data identifies that RSL changes in upper Cook Inlet are a combination of tectonics, GIA driven land displacement and geoid deformation and 'local' processes, which might have otherwise been misinterpreted as hitherto unidentified

elements of the EDC model. Mountain glaciers are sensitive to climate change and have the potential to impose mass changes on the Earth over a relatively short time, particularly at an active coastal margin with relatively thin lithosphere and low viscosity asthenosphere. The coastlines of Iceland and Patagonia with thin lithospheres and records of LIA ice mass balance changes may record LIA RSL changes similar that modelled in this thesis in south central Alaska (Ivins and James, 1999; Glasser *et al.*, 2004; 2005; Klemann *et al.*, 2007; Brandsdottir and Menke, 2008; Bjarnason and Schmeling, 2009; Geirsdottir *et al.*, 2009; Chenet *et al.*, 2010; Dietrich *et al.*, 2010). Alaskan glaciers will respond quickly to future climate changes, potentially resulting in a unique RSL fingerprint, both due to the deformation of the geoid and the solid Earth.

The modification of crust and mantle material has the potential to change stress fields and modify regional seismic behaviour. Klemann *et al.* (2008) and Stewart *et al.* (2000) discuss horizontal GIA motion on active plates, an area that requires further research in light of evidence of short term GIA. Initial studies in Alaska suggest tectonic activity increases with glacier surge phases and ice thinning (Sauber *et al.*, 2000; Sauber and Molnia, 2004; Doser *et al.*, 2007). Understanding the potential for perturbations to the trend of global sea level change is important for knowledge of the regional impacts of future RSL change.

To understand the complex interactions between GIA and tectonics requires integration of GIA models of the Earths' structure within seismic models. Both processes occur simultaneously with the rheology of a tectonically active location responsible for rapid GIA response. This research and similar at other subduction zones (Clague and James, 2002; Klemann *et al.*, 2007; James *et al.*, 2009b; Dietrich *et al.*, 2010) highlights the need for GIA models with lateral lithosphere and mantle heterogeneity to be able to fully model global GIA.

As well as integrating Earth model solutions it is important to improve ice models of mountain glaciers with geological data of past thickness changes and include values of changes in lateral glacier extent, ideally with improved chronological constraint. The present Larsen *et al.* (2005) regional LIA ice model needs refining to allow for surge and retreat cycles of dynamic terrestrial and water terminating glaciers and the likely over estimation of present day ice volume changes (Berthier et al., 2010). Prediction of future RSL changes requires modelling of past GIA and tectonic process over shorter time scales. Geological data and modelling results of the RSL changes during the LIA in Alaska provide a case study of the potential for short term GIA and

geoid deformation associated with changes in mountain glacier mass balance which may be applied to other locations and understanding of future RSL change. However, to fully understand and constrain past changes and predict future changes requires improvements to the sea level reconstruction methodology, dating of salt marsh sediments and GIA modelling.

References

Allen, J.R.L., 1997. Simulation models of salt-marsh morphodynamics: some implications for high-intertidal sediment couplets related to sea-level change. Sedimentary Geology 113, 211-233.

Altamimi, Z., Collilieux, X., Legrand, J., Garayt, B., Boucher, C., 2007. ITRF2005: A new release of the International Terrestrial Reference Frame based on time series of station positions and earth orientation parameters. Journal of Geophysical Research-Solid Earth 112.

Altamimi, Z., Sillard, P., Boucher, C., 2002. ITRF2000: A new release of the International Terrestrial Reference frame for earth science applications. Journal of Geophysical Research-Solid Earth 107.

Anderson, D.L., 1975. Accelerated Plate Tectonics. Science 187, 1077-1079.

Appleby, P.G., Oldfield, F., 1978. The calculation of ^{210}Pb dates assuming a constant rate of supply of unsupported ^{210}Pb to the sediment. *Catena* 5, 1-8.

Appleby, P.G., Oldfield, F., 1992. Application of lead-210 to sedimentation studies, In: Ivanovich, M., Harmon, R.S. (Eds.), Uranium-series disequilibrium: applications to earth, marine, and environmental sciences, 2nd ed ed. Clarendon Press, Oxford, pp. 731-778.

Ardent, A., Echelmeyer, K., Harrison, W., Lingle, C., Valentine, V., 2002. Rapid wastage of Alaska glaciers and their contribution to rising sea levels. Science 297, 382-386.

Arendt, A., Echelmeyer, K., Harrison, W., Lingle, C., Zirnheld, S., Valentine, V., Ritchie, B., Druckenmiller, M., 2006. Updated estimates of glacier volume changes in the western Chugach Mountains, Alaska, and a comparison of regional extrapolation methods. J. Geophys. Res.-Earth Surf. 111, 12.

Argus, D.F., 2007. Defining the translational velocity of the reference frame of Earth. Geophysical Journal International 169, 830-838.

Argus, D.F., Gordon, R.G., Heflin, M.B., Ma, C., Eanes, R.J., Willis, P., Peltier, W.R., Owen, S.E., 2010. The angular velocities of the plates and the velocity of Earth's centre from space geodesy. Geophysical Journal International 180, 913-960.

Argus, D.F., Peltier, W.R., 2010. Constraining models of postglacial rebound using space geodesy: a detailed assessment of model ICE-5G (VM2) and its relatives. Geophysical Journal International 181, 697-723.

Atwater, B.F., 1987. Evidence for great Holocene earthquakes along the outer coast of Washington State. Science 236, 942-944.

Atwater, B.F., 1992. Geologic evidence for earthquakes during the past 2000 years along the Copalis River, Southern coastal Washington. Journal of Geophysical Research 97, 1901-1919.

Atwater, B.F., Nelson, A.R., Clague, J.J., Carver, G.A., Yamaguchi, D.K., Bobrowski, P.T., Borgeois, J., Darienzo, M.E., Grant, W.C., Hemphill-Haley, E., Kelsey, H.M., Jacoby, G.C., Nishenko, S.P., Palmer, S.P., Peterson, C.D., Reinhart, M.A., 1995. Summary of coastal geologic evidence for past great earthquakes at the Cascadia subduction zone. Earthquake Spectra 11, 1-18.

Atwater, B.F., Stuiver, M., Yamaguchi, D.K., 1991. A radiocarbon test of earthquake magnitude at the Cascadia subduction zone. Nature 353, 156-158.

Atwater, B.F., Yamaguchi, D.K., 1991. Sudden, probably co-seismic submergence of Holocene trees and grass in coastal Washington State. Geology 19, 706-709.

Atwater, B.F., Yamaguchi, D.K., Bondevik, S., Barnhardt, W.A., Amidon, L.J., Benson, B.E., Skjerdal, G., Shulene, J.A., Nanayama, F., 2001. Rapid resetting of an estuarine recorder of the 1964 Alaska Earthquake. Bulletin of the Geological Society of America 113, 1193-1204.

Austin, M., 2007. Species distribution models and ecological theory: A critical assessment and some possible new approaches. Ecol. Model. 200, 1-19.

Austin, M.P., 2002. Spatial prediction of species distribution: an interface between ecological theory and statistical modelling. Ecol. Model. 157, 101-118.

Austin, R.M., 1991. Modelling Holocene tides on the NW European continental shelf. Terra Nova 3, 276-288.

Barclay, D.J., Wiles, G.C., Calkin, P.E., 2003. An 850 year record of climate and fluctuations of the iceberg-calving Nellie Juan Glacier, south central Alaska, USA, Annals Of Glaciology, Vol 36, pp. 51-56.

Barclay, D.J., Wiles, G.C., Calkin, P.E., 2009. Holocene glacier fluctations in Alaska. Quaternary Science Reviews 28, 2034-2048.

Bard, E., Raisbeck, G.M., Yiou, F., Jouzel, J., 1997. Solar modulation of cosmogenic nuclide production over the last millennium: comparison between C-14 and Be-10 records. Earth and Planetary Science Letters 150, 453-462.

Bartsch-Winkler, S., Ovenshine, A.T., 1984. Macrotidal subarctic environment of Turnagain and Knik Arms, Upper Cook Inlet, Alaska: Sedimentology of the intertidal zone. Journal of Sedimentary Petrology 54, 1221-1238.

Bartsch-Winkler, S., Ovenshine, A.T., Kachadoorian, R., 1983. Holocene history of the estuarine area surrounding Portage, Alaska as recorded in a 93 m core. Canadian Journal of Earth Sciences 20, 802-820.

Bassett, S.E., Milne, G.A., Mitrovica, J.X., Clark, P.U., 2005. Ice Sheet and Solid Earth Influences on Far-Field Sea-Level Histories. Science 309, 925-928.

Batten, A.R., Murphy, S., Murray, D.F., 1978. Definition of Alaskan coastal wetlands by floristic criteria. Corvallis Environmental Research Lab, Corvallis, Oregan.

Begét, J., Gardner, C., Davis, K., 2008. Volcanic tsunamis and prehistoric cultural transitions in Cook Inlet, Alaska. Journal of Volcanology and Geothermal Research 176, 377-386.

Begét, J.E., Kowalik, Z., 2006. Confirmation and calibration of computer modeling of tsunamis produced by Augustine Volcano, Alaska. Science of Tsunami Hazards 24, 257-266.

Beget, J.E., Stihler, S.D., Stone, D.B., 1994. A 500 year long record of tephra falls from Redoubt volcano and other volcanoes in Upper Cook Inlet, Alaska. Journal of Volcanology and Geothermal Research 62, 55-67.

Beikman, H.M., 1980. Geologic map of Alaska. U.S. Geological Survey Special Map 1:2,500,000. 2 sheets.

Berry, A., Plater, A.J., 1998. Rates of tidal sedimentation from records of industrial pollution and environmental magnetism: The Tees estuary, north-east England. Water Air and Soil Pollution 106, 463-479.

Berthier, E., Schiefer, E., Clarke, G.K.C., Menounos, B., Remy, F., 2010. Contribution of Alaskan glaciers to sea-level rise derived from satellite imagery. Nature Geoscience 3, 92-95.

Bills, B.G., Desilva, S.L., Currey, D.R., Emenger, R.S., Lillquist, K.D., Donnellan, A., Worden, B., 1994. Hydro-isostatic deflection and tectonic tilting in the Central Andes - initial results of a GPS survey of Lake Minchin shorelines. Geophysical Research Letters 21, 293-296.

Bindler, R., Renberg, I., Appleby, P.G., Anderson, N.J., Rose, N.L., 2001. Mercury accumulation rates and spatial patterns in lake sediments from west Greenland: A coast to ice margin transect. Environmental Science & Technology 35, 1736-1741.

Bindler, R., Renberg, I., Rydberg, J., Andren, T., 2009. Widespread waterborne pollution in central Swedish lakes and the Baltic Sea from pre-industrial mining and metallurgy. Environmental Pollution 157, 2132-2141.

Bindoff, N.L., Willebrand, J., Artale, V., A, C., Gregory, J., Gulev, S., Hanawa, K., Quéré, C.L., Levitus, S., Nojiri, Y., Shum, C.K., Talley, L.D., Unnikrishnan, A., 2007. Observations: Oceanic Climate Change and Sea Level., In: Solomon, S., Qin, D., Manning, M., Chen, Z., Marquis, M., Averyt, K.B., Tignor, M., Miller, H.L. (Eds.), Climate Change 2007: The Physical Science Basis. Contribution of Working Group I to the Fourth Assessment Report of the Intergovernmental Panel on Climate Change. Cambridge University Press, Cambridge, UK and New York, NY, USA.

Birks, H.J.B., 1995. Quantitative palaeoenvironmental reconstructions, In: Maddy, D., Brew, J.S. (Eds.), Statistical modelling of Quaternary Science data. Quaternary Research Association., Cambridge, pp. 161-254.

Bjarnason, I.T., Schmeling, H., 2009. The lithosphere and asthenosphere of the Iceland hotspot from surface waves. Geophysical Journal International 178, 394-418.

Blewitt, G., 2003. Self-consistency in reference frames, geocenter definition, and surface loading of the solid Earth. Journal of Geophysical Research-Solid Earth 108, 10.

Blockley, S.P.E., Blaauw, M., Bronk Ramsey, C., van der Plicht, J., 2007. Building and testing age models for radiocarbon dates in Lateglacial and Early Holocene sediments. Quaternary Science Reviews 26, 1915-1926.

Blockley, S.P.E., Bronk Ramsey, C., Lane, C.S., Lotter, A.F., 2008. Improved age modelling approaches as exemplified by the revised chronology for the Central European varved lake Soppensee. Quaternary Science Reviews 27, 61-71.

Blockley, S.P.E., Pyne-O'Donnell, S.D.F., Lowe, J.J., Matthews, I.P., Stone, A., Pollard, A.M., Turney, C.S.M., Molyneux, E.G., 2005. A new and less destructive laboratory procedure for the physical separation of distal glass tephra shards from sediments. Quaternary Science Reviews 24, 1952-1960.

Boucher, C., Altamimi, Z., Sillard, P., 1999. The International Terrestrial Reference Frame (ITRF97), IERS Technical Note 27. Central Bureau of IERS - Observatoire de Paris, Paris, p. 192.

Brain, M.J., 2006. Autocompaction of Mineralogenic Intertidal Sediments, Department of Geography. Unpublished PhD Thesis, Durham University, Durham.

Brandsdottir, B., Menke, W.H., 2008. The seismic structure of Iceland. Jokull 58, 17-34.

Briner, J.P., Kaufman, D.S., 2008. Late Pleistocene mountain glaciation in Alaska: key chronologies. Journal of Quaternary Science 23, 659-670.

Bronk Ramsey, C., 1995. Radiocarbon calibration and analysis of stratigraphy: The OxCal program. Radiocarbon 37, 425-430.

Bronk Ramsey, C., 2000. Comment on 'the use of bayesian statistics for C-14 dates of chronologically ordered samples: A critical analysis'. Radiocarbon 42, 199-202.

Bronk Ramsey, C., 2001. Development of the radiocarbon calibration program OxCal. Radiocarbon 43, 355-363.

Bronk Ramsey, C., 2008. Deposition models for chronological records. Quaternary Science Reviews 27, 42-60.

Bronk Ramsey, C., 2009. Bayesian Analysis of Radiocarbon Dates. Radiocarbon 51, 337-360.

Bronk Ramsey, C., van de Plitch, J., Weninger, B., 2001. 'Wiggle matching' radiocarbon dates. Radiocarbon 43, 381-389.

Brown, L.D., Reilinger, R.E., Holdahl, S.R., Balazs, E.I., 1977. Postseismic crustal uplift near Anchorage, Alaska. Journal of Geophysical Research 83, 3369-3378.

Bruhn, R.L., Haeussler, P.J., 2006. Deformation driven by subduction and microplate collision: Geodynamics of Cook Inlet basin, Alaska. Geological Society of America Bulletin 118, 289-303.

Bruhn, R.L., Pavlis, T.L., Plafker, G., Serpa, L., 2004. Deformation during terrane accretion in the Saint Elias orogen, Alaska. Geological Society of America Bulletin 116, 771-787.

Caetano, M., Fonseca, N., Vale, C., 2007. Mobility of Pb in salt marshes recorded by total content and stable isotopic signature. Science of the Total Environment 380, 84-92.

Calkin, P.E., 1988. Holocene glaciation of Alaska (and adjoining Yukon territory, Canada). Quaternary Science Reviews 7, 159-184.

Calkin, P.E., Wiles, G.C., Barclay, D.J., 2001. Holocene coastal glaciation of Alaska. Quaternary Science Reviews 20, 449-461.

Callaway, J.C., Delaune, R.D., Patrick, W.H., 1998. Heavy metal chronologies in selected coastal wetlands from Northern Europe. Mar. Pollut. Bull. 36, 82-96.

Carver, G., Plafker, G., 2008. Paleoseismicity and Neotectonics of The Aleutian Subduction Zone - An Overview, In: Freymueller, J.T., Haeussler, P., Wesson, R.L., Ekstrom, G. (Eds.), Active Tectonics and Seismic Potential of Alaska. AGU Geophysical Monograph Series Vol 179, Washington, DC, pp. 43-63.

Chen, J.L., Tapley, B.D., Wilson, C.R., 2006. Alaskan mountain glacial melting observed by satellite gravimetry. Earth and Planetary Science Letters 248, 368-378.

Chenet, M., Roussel, E., Jomelli, V., Grancher, D., 2010. Asynchronous Little Ice Age glacial maximum extent in southeast Iceland. Geomorphology 114, 253-260.

Chipman, M.L., Clarke, G.H., Clegg, B.F., Gregory-Eaves, I., Hu, F.S., 2009. A 2000 year record of climatic change at Ongoke Lake, southwest Alaska. Journal of Paleolimnology 41, 57-75.

Chmura, G.L., Hung, G.A., 2004. Controls on salt marsh accretion: A test in salt marshes of Eastern Canada. Estuaries 27, 70-81.

Church, J.A., White, N.J., Aarup, T., Wilson, W.S., Woodworth, P.L., Domingues, C.M., Hunter, J.R., Lambeck, K., 2008. Understanding global sea levels: past, present and future. Sustain. Sci. 3, 9-22.

Clague, J.J., Haper, J.R., Hedba, R.J., Howes, D.E., 1982. Late Quaternary sea levels and crustal movements, coastal British Columbia. Canadian Journal of Earth Science 19, 597-618.

Clague, J.J., James, T.S., 2002. History and isostatic effects of the last ice sheet in southern British Columbia. Quaternary Science Reviews 21, 71-87.

Combellick, R., 1984a. Surficial-geologic map of the Seward D-6 Quadrangle Alaska, Alaska Division of Geological and Geophysical Surveys Report of Investigations 84-15.

Combellick, R., 1984b. Surficial-geologic map of the Seward D-7 Quadrangle Alaska, Alaska Division of Geological and Geophysical Surveys Report of Investigations 84-22.

Combellick, R., 1999. Simplified geologic map and cross sections of central and east Anchorage, Alaska, Preliminary Interpretive Report 1999-1. Alaska Division of Geological and Geophysical Surveys.

Combellick, R.A., 1991. Palaeoseismicity of the Cook Inlet region, Alaska: Evidence from peat stratigraphy in Turnagain and Knik Arms., Alaska Division of Geological and Geophysical Surveys Professional Report 112, Fairbanks, Alaska.

Combellick, R.A., 1994. Paleoseismicity of the Cook Inlet region, Alaska: Evidence from peat stratigraphy in Turnagain and Knik Arms.

Cooper, L.W., Grebmeier, J.M., Larsen, I.L., Solis, C., Olsen, C.R., 1995. Evidence for the re-distribution of Cs-137 in Alaskan tundra, lake and marine sediments. Science of the Total Environment 161, 295-306.

Cremer, H., Melles, M., Wagner, B., 2001. Holocene climate changes reflected in a diatom succession from Basaltso, East Greenland. Canadian Journal of Botany-Revue Canadienne De Botanique 79, 649-656.

Crossen, K.J., 1992. Guide to the little ice age landforms and glacial dynamics of portage glacier, In: Crossen, K.J. (Ed.), Guide to the Little Ice Age Landforms and Glacial Dynamics in Portage Valley and Portage Pass. Alaska Geological Society, Anchorage, Alaska, pp. 3-15.

Crossen, K.J., 1997. Geological Fluctuations of Terrestrial, Tidewater and Calving Lacustrine Glaciers, Blackstone-Spencer Ice Complex, Kenai Mountains, Alaska. University of Washington.

Cundy, A.B., Croudace, I.W., 1995. Physical and chemical associations of radionuclides and trace metals in estuarine sediments: an example from Poole Harbour, southern England. Journal of Environmental Radioactivity 29, 191-211.

Cundy, A.B., Croudace, I.W., Cearreta, A., Irabien, M.J., 2003. Reconstructing historical trends in metal input in heavily-disturbed, contaminated estuaries: studies from Bilbao, Southampton Water and Sicily. Appl. Geochem. 18, 311-325.

Cundy, A.B., Croudace, I.W., Thomson, J., Lewis, J.T., 1997. Reliability of salt marshes as "geochemical recorders" of pollution input : a case study from contrasting estuaries in southern England. Environmental Science and Technology 31, 1093-1101.

Cundy, A.B., Hopkinson, L., Lafite, R., Spencer, K., Taylor, J.A., Ouddane, B., Heppell, C.M., Carey, P.J., Charman, R., Shell, D., Ullyott, S., 2005. Heavy metal distribution and accumulation in two Spartina sp.-dominated macrotidal salt marshes from the Seine estuary (France) and the Medway estuary (UK). Appl. Geochem. 20, 1195-1208.

Cundy, A.B., Lafite, R., Taylor, J.A., Hopkinson, L., Deloffre, J., Charman, R., Gilpin, M., Spencer, K.L., Carey, P.J., Heppell, C.M., Ouddane, B., De Wever, S., Tuckett, A., 2007. Sediment transfer and accumulation in two contrasting salt marsh/mudflat systems: the Seine estuary (France) and the Medway estuary (UK). Hydrobiologia 588, 125-134.

Darienzo, M.E., Peterson, C.D., 1990. Episodic tectonic subsidence of late Holocene salt marshes, Northern Oregon coast, central Cascadia margin, U.S.A. Tectonics 9, 1-22.

Darienzo, M.E., Peterson, C.D., Clough, C., 1994. Stratigraphic evidence for great subduction-zone earthquakes at four estuaries in Northern Oregon, USA. Journal of Coastal Research 10, 850-876.

Davis, R.B., Hess, C.T., Norton, S.A., Hanson, D.W., Hoagland, K.D., Anderson, D.S., 1984. Cs-137 and Pb-210 dating of sediments from soft-water lakes in New England (USA) and Scandinavia, a failure of Cs-137 dating. Chemical Geology 44, 151-185.

de Fontaine, C.S., Kaufman, D.S., Anderson, R.S., Werner, A., Waythomas, C.F., Brown, T.A., 2007. Late quaternary distal tephra-fall deposits in lacustrine sediments, Kenai Peninsula, Alaska. Quaternary Research 68, 64-78.

Dietrich, R., Ivins, E.R., Casassa, G., Lange, H., Wendt, J., Fritsche, M., 2010. Rapid crustal uplift in Patagonia due to enhanced ice loss. Earth and Planetary Science Letters 289, 22-29.

Doser, D.I., Wiest, K.R., Sauber, J., 2007. Seismicity of the Bering Glacier region and its relation to tectonic and glacial processes. Tectonophysics 439, 119-127.

Dugdale, S.J., 2006. Evidence for late-Holocene great earthquakes and palaeotsunamis from Bird Point, upper Cook Inlet, Alaska, Geography. Department of Geography, Durham University.

Dyke, A.S., Peltier, W.R., 2000. Forms, response times and variability of relative sea-level curves, glaciated North America. Geomorphology 32, 315-333.

Dziewonski, A.M., Anderson, D.L., 1981. Preliminary Reference Earth Model. Physics of The Earth and Planetary Interiors 25, 297-356.

Edwards, R.J., 2006. Mid- to late-Holocene relative sea-level change in southwest Britain and the influence of sediment compaction. Holocene 16, 575-587.

Edwards, R.J., Horton, B.P., 2000. Reconstructing relative sea-level change using UK salt-marsh foraminifera. Marine Geology 169, 41-56.

Edwards, R.J., Wright, A.J., van de Plassche, O., 2004. Surface distributions of salt-marsh foraminifera from Connecticut, USA: modern analogues for high-resolution sea level studies. Marine Micropaleontology 51, 1-21.

Farrell, W.E., Clark, J.A., 1976. On postglacial sea level. Geophysical Journal of the Royal Astronomical Society 46, 647-667.

Finkelstein, S.A., Gajewski, K., 2008. Responses of Fragilarioid-dominated diatom assemblages in a small Arctic lake to Holocene climatic changes, Russell Island, Nunavut, Canada. Journal of Paleolimnology 40, 1079-1095.

Fleming, K., Martinec, Z., Hagedoorn, J., 2004. Geoid displacement about Greenland resulting from past and present-day mass changes in the Greenland Ice Sheet. Geophysical Research Letters 31.

Fletcher, H.J., Freymueller, J.T., 1999. New GPS constraints on the motion of the Yakutat block. Geophysical Research Letters 26, 3029-3032.

Franzel, S.A., 2002. Priority-Pollutant Trace Elements in Streambed Sediments of the Cook Inlet Basin, Alaska, 1998-2000, Water-Resources Investigations Report 02-4163. U.S. Department of the Interior and U.S. Geological Survery, Anchorage, Alaska.

Freymueller, J.T., Cohen, S., Fletcher, H.J., 2000. Spatial variations in present-day deformation, Kenai Peninsula, Alaska, and their implications. Journal of Geophysical Research 105, 8079-8101.

Freymueller, J.T., Woodard, H., Cohen, S.C., Cross, R., Elliot, J., Larsen, C.F., Hreinsdottir, S., Zweek, C., 2008. Active Deformation Processes in Alaska, based on 15 Years of GPS Measurements, In: Freymueller, J.T., Haeussler, P.J., Wesson, R.L., Ekstrom, G. (Eds.), Active Tectonics and Seismic Potential of Alaska. AGU Geophysical Monograph 179, Washington, DC.

Fuis, G.S., Moore, T.E., Plafker, G., Brocher, T.M., Fisher, M.A., Mooney, W.D., Nokleberg, W.J., Page, R.A., Beaudoin, B.C., Christensen, N.I., Levander, A.R., Lutter, W.J., Saltus, R.W., Ruppert, N.A., 2008. Trans-Alaska Crustal Transect and continental evolution involving subduction underplating and synchronous foreland thrusting. Geology 36, 267-270.

Gasse, F., Juggins, S., Khelifa, L.B., 1995. Diatom-based transfer functions for inferring past hydrochemical characteristics of African lakes. Palaeogeography, Palaeoclimatology, Palaeoecology 117, 31-54.

Gatto, L.W., 1976. Baseline data on the oceanography of Cook Inlet, Alaska. CRREL Report 76-25. National Aeronautics and Space Administration, Hanover, N.H., p. 81.

Gehrels, W.R., Belknap, D.F., Pearce, B.R., Gong, B., 1995. Modelling the contribution of M2 tidal amplification to the Holocene rise of mean high water in the Gulf of Maine and the Bay of Fundy. Marine Geology 124, 71-85.

Gehrels, W.R., Kirby, J.R., Prokoph, A., Newnham, R.M., Achterberg, E.P., Evans, H., Black, S., Scott, D.B., 2005. Onset of recent rapid sea-level rise in the western Atlantic Ocean. Quaternary Science Reviews 24, 2083.

Gehrels, W.R., Marshall, W.A., Gehrels, M.J., Larsen, G., Kirby, J.R., Eiriksson, J., Heinemeier, J., Shimmield, T., 2006. Rapid sea-level rise in the North Atlantic Ocean since the first half of the nineteenth century. Holocene 16, 949-965.

Geirsdottir, A., Miller, G.H., Axford, Y., Olafsdottir, S., 2009. Holocene and latest Pleistocene climate and glacier fluctuations in Iceland. Quaternary Science Reviews 28, 2107-2118.

Gibson, J.R., 1976. Imperial Russia in Frontier America. Oxford University Press, New York.

Glasser, N.F., Harrison, S., Winchester, V., Aniya, M., 2004. Late Pleistocene and Holocene palaeoclimate and glacier fluctuations in Patagonia. Global and Planetary Change 43, 79-101.

Glasser, N.F., Jansson, K.N., Harrison, S., Rivera, A., 2005. Geomorphological evidence for variations of the North Patagonian Icefield during the Holocene. Geomorphology 71, 263-277.

Greb, S.F., Archer, A.W., 2007. Soft-sediment deformation produced by tides in a meizoseismic area, Turnagain Arm, Alaska. Geology 35, 435-438.

Greff-Lefftz, M., Legros, H., 1997. Some remarks about the degree-one deformation of the Earth. Geophysical Journal International 131, 699-723.

Griffiths, S.D., Peltier, W.R., 2009. Modeling of Polar Ocean Tides at the Last Glacial Maximum: Amplification, Sensitivity, and Climatological Implications. Journal of Climate 22, 2905-2924.

Grinsted, A., Moore, J.C., Jevrejeva, S., 2009. Reconstructing sea level from paleo and projected temperatures 200 to 2100AD. Climate Dynamics, doi:10.1007/s00382-00308-00507-00382.

Grove, J.M., 2004a. Little Ice Ages: Ancient and Modern - Volume 1, Second ed. Routledge, London.

Grove, J.M., 2004b. Little Ice Ages: Ancient and Modern - Volume 2, Second ed. Routledge, London.

Hamilton, S., Shennan, I., 2005a. Late Holocene relative sea-level changes and the earthquake deformation cycle around upper Cook Inlet, Alaska. Quaternary Science Reviews 24, 1479-1498.

Hamilton, S., Shennan, I., Combellick, R., Mulholland, J., Noble, C., 2005. Evidence for two great earthquakes at Anchorage, Alaska and implications for multiple great earthquakes through the Holocene. Quaternary Science Reviews 24, 2050-2068.

Hamilton, S.L., 2003. Late Holocene relative sea-level changes and earthquakes around the upper Cook Inlet, Alaska, USA. Durham University.

Hamilton, S.L., Shennan, I., 2005b. Late Holocene great earthquakes and relative sea-level change at Kenai, southern Alaska. Journal of Quaternary Science 20, 95-111.

Hartley, B., Barber, H.G., Carter, J.R., 1996. An Atlas of British Diatoms. Biopress, Bristol.

Harvey, M.M., Hansom, J.D., MacKenzie, A.B., 2007. Constraints on the use of anthropogenic radionuclide-derived chronologies for saltmarsh sediments. Journal of Environmental Radioactivity 95, 126-148.

Hassan, G.S., Espinosa, M.A., Isla, F.I., 2006. Modern diatom assemblages in surface sediments from estuarine systems in the southeastern Buenos Aires province, Argentina. Journal of Paleolimnology 35, 39-53.

Heiskanen, W.A., Vening Meinesz, F.A., 1958. The Earth and Its Gravity Field. Wiley, New York.

Hemphill-Haley, E., 1993. Taxonomy of recent and fossil (Holocene) diatoms (Bacilloriophyta) from northern Willapa Bay, Washington. US Geological Survey Open File Report 93-289, 1-151.

Hetherington, R., Barrie, J.V., 2004. Interaction between local tectonics and glacial unloading on the Pacific margin of Canada. Quaternary International 120, 65-77.

Higgitt, D.L., 1995. The development and application of Caesium-137 measurements in erosion investigations, In: Foster, I.D.L., Gurnell, A.M., Webb, B.W. (Eds.), Sediment and water quality in river catchments. Wiley, Chichester, pp. 287-305.

Hinton, A.C., 1995. Holocene tides of The Wash, U.K.: The influence of water-depth and coastline-shape changes on the record of sea-level change. Marine Geology 124, 87-111.

Horton, B., Shennan, I., 2009. Compaction of Holocene strata and the implications for relative sea level change on the east coast of England. Geology 37, 1083-1086.

Horton, B.P., Corbett, R., Culver, S.J., Edwards, R.J., Hillier, C., 2006. Modern saltmarsh diatom distributions of the Outer Banks, North Carolina, and the development of a transfer function for high resolution reconstructions of sea level. Estuar. Coast. Shelf Sci. 69, 381-394.

Horton, B.P., Edwards, R.J., 2005. The application of local and regional transfer functions to the reconstruction of Holocene sea levels, north Norfolk, England. Holocene 15, 216-228.

Hua, Q., 2009. Radiocarbon: A chronological tool for the recent past. Quaternary Geochronology 4, 378-390.

Hua, Q., Barbetti, M., 2004. Review of tropospheric bomb C-14 data for carbon cycle modeling and age calibration purposes. Radiocarbon 46, 1273-1298.

Hutchinson, I., James, T., Clague, J., Barrie, J.V., Conway, K., 2004. Reconstruction of late Quaternary sea-level change in southwestern British Columbia from sediments in isolation basins. Boreas 33, 183-194.

Hwang, H.M., Green, P.G., Young, T.M., 2009. Historical trends of trace metals in a sediment core from a contaminated tidal salt marsh in San Francisco Bay. Environmental Geochemistry and Health 31, 421-430.

Imbrie, J., Kipp, N.G., 1971. A new micropaleontological method for quantitative paleoclimatology: application to a Late Pleistocene Caribbean core, In: Turekian, K.K. (Ed.), The Late Cenozoic Glacial Ages. Yale University Press, New Haven, pp. 71-181.

Ivins, E.R., James, T.S., 1999. Simple models for late Holocene and present-day Patagonian glacier fluctuations and predictions of a geodetically detectable isostatic response. Geophysical Journal International 138, 601-624.

Ivins, E.R., James, T.S., 2004. Bedrock response to Llanquihue Holocene and present-day glaciation in southernmost South America. Geophysical Research Letters 31.

Jackson, S.T., Williams, J.W., 2004. Modern analogues in Quaternary Paleoecology: here today, gone yesterday, gone tomorrow? Annual Review of Earth and Planetary Sciences 32, 495-537.

James, T., Gowan, E.J., Hutchinson, I., Clague, J.J., Barrie, J.V., Conway, K.W., 2009a. Sea-level change and paleogeographic reconstructions, southern Vancouver Island, British Columbia, Canada. Quaternary Science Reviews 28, 1200-1216.

James, T.S., Clague, J.J., Wang, K., Hutchinson, I., 2000. Postglacial rebound at the northern Cascadia subduction zone. Quaternary Science Reviews 19, 1527-1541.

James, T.S., Gowan, E.J., Wada, I., Wang, K., 2009b. Viscosity of the asthenosphere from glacial isostatic adjustment and subduction dynamics at the northern Cascadia subduction zone, British Columbia, Canada. Journal of Geophysical Research 114, B04405.

James, T.S., Hutchinson, I., Barrie, J.V., Conway, K., Mathews, D., 2005. Relative Sea-Level Change in the Northern Strait of Georgia, British Columbia. Géographie physique et Quaternaire 59, 113-127.

Jones, P.D., Mann, M.E., 2004. Climate over past millennia. Reviews of Geophysics 42.

Juggins, S., 2003. C2: A Microsoft Windows program for developing and applying palaeoecological transfer functions and for visualising multi-proxy stratigraphic datasets, 1.4.2 ed. University of Newcastle, Newcastle upon Tyne.

Karlstrom, T.N.V., 1964. Quaternary geology of the Kenai lowland and the glacial history of the Cook Inlet region, Alaska. US Geological Survey Professional Paper 443, 1-69.

Kaufman, D.S., Manley, W.F., 2004. Pleistocene Maximum and Late Wisconsinan glacier extents across Alaska, U.S.A., In: Ehlers, J., Gibbard, P.L. (Eds.), Quaternary Glaciations - Extent and Chronology, Part II. Elsevier, Amsterdam.

Kemp, A.C., Horton, B.P., Culver, S.J., Corbett, D.R., van de Plassche, O., Gehrels, W.R., Douglas, B.C., Parnell, A.C., 2009. Timing and magnitude of recent accelerated sea-level rise (North Carolina, United States). Geology 37, 1035-1038.

Kennedy, B.W., Trabant, D.C., Mayo, L.R., 2006. A century of retreat at Portage Glacier, South-Central Alaska. USGS Fact Sheet 2006-3141.

Klaminder, J., Renberg, I., Bindler, R., Emteryd, O., 2003. Isotopic trends and background fluxes of atmospheric lead in northern Europe: Analyses of three ombrotrophic bogs from south Sweden. Global Biogeochemical Cycles 17.

Klemann, V., Ivins, E.R., Martinec, Z., Wolf, D., 2007. Models of active glacial isostasy roofing warm subduction: Case of the South Patagonian Ice Field. Journal of Geophysical Research-Solid Earth 112.

Klemann, V., Martinec, Z., Ivins, E.R., 2008. Glacial isostasy and plate motion. J. Geodyn. 46, 95-103.

Komarek, M., Ettler, V., Chrastny, V., Mihaljevic, M., 2008. Lead isotopes in environmental sciences: A review. Environment International 34, 562-577.

Kowalik, Z., Proshutinsky, A., 2010. Tsunami-tide interactions: A Cook Inlet case study. Cont. Shelf Res. 30, 633-642.

Krishnaswami, S., Lal, D., Martin, J.M., Maybeck, M., 1971. Geochronology of lake sediments. Earth and Planetary Science Letters 11, 407-414.

Kylander, M.E., Weiss, D.J., Kober, B., 2009. Two high resolution terrestrial records of atmospheric Pb deposition from New Brunswick, Canada, and Loch Laxford, Scotland. Science of the Total Environment 407, 1644-1657.

Lambeck, K., 1993. Glacial Rebound of the British Isles-II. A High-Resolution, High-Precision Model. Geophysical Journal International 115, 960-990.

Lambeck, K., 2002. Sea Level Change from Mid Holocene to Recent Time: An Australian Example with Global Implications, In: Mitrovica, J.X., Vermeersen, B. (Eds.), Ice Sheets, Sea Level and the Dynamic Earth. AGU Geodynamics Series 29, Washington, DC, pp. 33-50.

Lambeck, K., Anzidei, M., Antonioli, F., Benini, A., Esposito, A., 2004. Sea level in Roman time in the Central Mediterranean and implications for recent change. Earth and Planetary Science Letters 224, 563-575.

Lambeck, K., Nakada, M., 1990. Late Pleistocene and Holocene sea-level change along the Australian coast. Global and Planetary Change 89, 143-176.

Lambeck, K., Purcell, A.P., 2001. Sea-level change in the Irish Sea since the last glacial maximum: constraints from isostatic modelling. Journal of Quaternary Science 16, 497-506.

Lambeck, K., Smither, C., Johnston, P., 1998. Sea-level change, glacial rebound and mantle viscosity for northern Europe. Geophysical Journal International 134, 102-144.

Lampright, R.L., 2008. Gold placer deposits near Anchorage, Alaska, 2nd ed. Iron Fire Publications, Nederland, Colorado.

LaPerriere, J.D., Wagener, S.M., Bjerklie, D.M., 1985. Gold-mining effects on heavy metals in streams, Circle Quadrangle, Alaska. Journal of the American Water Resource Association 21, 245-252.

Larsen, C.F., Motyka, R.J., Arendt, A.A., Echelmeyer, K.A., Geissler, P.E., 2007. Glacier changes in southeast Alaska and northwest British Columbia and contribution to sea level rise. Journal of Geophysical Research 112, F01007.

Larsen, C.F., Motyka, R.J., Freymueller, J.T., Echelmeyer, K.A., Ivins, E.R., 2004. Rapid uplift of southern Alaska caused by recent ice loss. Geophysical Journal International 158, 1118-1133.

Larsen, C.F., Motyka, R.J., Freymueller, J.T., Echelmeyer, K.A., Ivins, E.R., 2005. Rapid viscoelastic uplift in southeast Alaska caused by post-Little Ice Age glacial retreat. Earth And Planetary Science Letters 237, 548-560.

Lombard, A., Garcia, D., Ramillien, G., Cazenave, A., Biancale, R., Lemome, J.M., Flechtner, F., Schmidt, R., Ishii, M., 2007. Estimation of steric sea level variations from combined GRACE and Jason-1 data. Earth and Planetary Science Letters 254, 194-202.

Long, A., Waller, M.P., Plater, A.J., 2007. Dungeness and Romney Marsh: Barrier Dynamics and Marshland Evolution. Oxbow Books, Oxford.

Long, A.J., Innes, J.B., Shennan, I., Tooley, M.J., 1999. Coastal stratigraphy: A case study from Johns River, Washington, U.S.A., In: Jones, A.P., Tucker, M.E., Hart, J.K. (Eds.), The description and analysis of Quaternary stratigraphic field sections. Quaternary Research Association, London, pp. 267-286.

Long, A.J., Roberts, D.H., Simpson, M.J.R., Dawson, S., Milne, G.A., Huybrechts, P., 2008. Late Weichselian relative sea-level changes and ice sheet history in southeast Greenland. Earth and Planetary Science Letters 272, 8-18.

Long, A.J., Shennan, I., 1994. Sea level changes in Washington and Oregon and the "Earthquake deformation cycle". Journal of Coastal Research 10, 825-838.

Long, A.J., Shennan, I., 1998. Models of rapid relative sea-level change in Washington and Oregon, USA. Holocene 8, 129-142.

Long, A.J., Waller, M.P., Stupples, P., 2006. Driving mechanisms of coastal change: Peat compaction and the destruction of late Holocene coastal wetlands. Marine Geology 225, 63-84.

Long, A.J., Woodroffe, S.A., Milne, G.A., Bryant, C.L., Wake, L.M., 2010. Relative sea level change in west Greenland during the last millennium. Quaternary Science Reviews 29, 367-383.

Loring, D.H., 1990. Lithium - a New Approach for the Granulometric Normalization of Trace-Metal Data. Marine Chemistry 29, 155-168.

Loring, D.H., 1991. Normalization of Heavy-Metal Data from Estuarine and Coastal Sediments. Ices Journal of Marine Science 48, 101-115.

Loso, M.G., Anderson, R.S., Anderson, S.P., 2004. Post-Little Ice Age record of coarse and fine clastic sedimentation in an Alaskan proglacial lake. Geology 32, 1065-1068.

Luthcke, S.B., Arendt, A.A., Rowlands, D.D., McCarthy, J.J., Larsen, C.F., 2008. Recent glacier mass changes in the Gulf of Alaska region from GRACE mascon solutions. Journal of Glaciology 54, 767-777.

Maeda, Y., Nakada, M., Matsumoto, E., Matsuda, I., 1992. Crustal tilting derived from Holocene sea-level observations along the east-coast of Hokkaido in Japan and upper mantle rheology. Geophysical Research Letters 19, 857-860.

Manley, W.F., Kaufman, D.S., 2002. Alaska PaleoGlacier Atlas. Institute of Arctic and Alpine Research (INSTAAR), University of Colorado.
http://instaar.colorado.edu/QGISL/ak_paleoglacier_atlas v.1.

Mann, D.H., Crowell, A.L., Hamilton, T.D., Finney, B.P., 1998. Holocene geologic and climatic history around the Gulf of Alaska. Arctic Anthropology 35, 112-131.

Mann, D.H., Streveler, G.P., 2008. Post-glacial relative sea level, isostasy, and glacial history in Icy Strait, Southeast Alaska, USA. Quaternary Research 69, 201-216.

Mann, M.E., Jones, P.D., 2003. Global surface temperatures over the past two millennia. Geophysical Research Letters 30.

Marshall, W.A., Clough, R., Gehrels, W.R., 2009. The isotopic record of atmospheric lead fall-out on an Icelandic salt marsh since AD 50. Science of the Total Environment 407, 2734-2748.

Marshall, W.A., Gehrels, W.R., Garnett, M.H., Freeman, S., Maden, C., Xu, S., 2007. The use of 'bomb spike' calibration and high-precision AMS C-14 analyses to date salt-marsh sediments deposited during the past three centuries. Quaternary Research 68, 325-337.

Mathews, W.H., Fyles, J.G., Nasmith, H.W., 1970. Postglacial crustal movements in southwestern British Columbia and adjacent Washington State. Canadian Journal of Earth Sciences 7, 690-702.

Mayo, I.R., Zenone, C., Trabant, D.C., 1977. Reconnaissance hydrology of Portage Glacier basin, Alaska. US Geological Survey Hydrologic Investigations Atlas HA-583.

Meier, M.F., Rasmussen, L.A., Post, A.S., Brown, C.S., Sikonia, W.G., Bindschadler, R.A., Mayo, L.R., Trabant, D.C., 1980. Predicted Timing of the Disintegration of the Lower Reach of Columbia Glacier, Alaska. USGS Open-File Report 80-582.

Meyers, R.A., Smith, D.G., Jol, H.M., Peterson, C.D., 1996. Evidence for eight great earthquake-subsidence events detected with ground-penetrating radar, Willapa barrier, Washington. Geology 24, 99-102.

Milan, C.S., Swenson, E.M., Turner, R.E., Lee, J.M., 1995. Assessment of the 137Cs method for estimating sediment accumulation rates: Louisiana salt marshes. Journal of Coastal Research 11, 296-307.

Milne, G., Shennan, I., Youngs, B.A.R., Waugh, A.I., Teferle, F.N., Bingley, R.M., Bassett, S.E., Cuthbert-Brown, C., Bradley, S.L., 2006. Modelling the glacial isostatic adjustment of the UK region. Philosophical Transactions of the Royal Society A - Mathematical Physical and Engineering Sciences 364, 931-948.

Milne, G.A., Mitrovica, J.X., 2008. Searching for eustasy in deglacial sea-level histories. Quaternary Science Reviews 27, 2292-2302.

Mitrovica, J.X., Milne, G.A., 2002. On the origin of late Holocene sea-level highstands within equatorial ocean basins. Quaternary Science Reviews 21, 2179-2190.

Mitrovica, J.X., Milne, G.A., 2003. On post-glacial sea level: I. General theory. Geophysical Journal International 154, 253-267.

Moberg, A., Sonechkin, D.M., Holmgren, K., Datsenko, N.M., Karlen, W., 2005. Highly variable Northern Hemisphere temperatures reconstructed from low- and high-resolution proxy data. Nature 433, 613-617.

Molnia, B.F., 2007. Late nineteenth to early twenty-first century behaviour of Alaskan glaciers as indicators of changing regional climate. Global and Planetary Change 56, 23-56.

Molnia, B.F., 2008. Glaciers of North America - Glaciers of Alaska, In: Williams, R.S., Jr., Ferrigno, J.G. (Eds.), Satellite images atlas of glaciers of the world. US Geological Survey Professional Paper 1386-K p525.

Motyka, R.J., 2003. Little Ice Age subsidence and post Little Ice Age uplift at Juneau, Alaska, inferred from dendrochronolgy and geomorphology. Quaternary Research 59, 300-309.

Nakada, M., Lambeck, K., 1989. Late Pleistocene and Holocene sea-level change in the Australian region and mantle rheology. Geophysical Journal International 96, 497-517.

Naske, C.-M., Slotnick, H.E., 1987. Alaska: A history of the 49th State. University of Oklahoma Press, Norman.

Nelson, A.R., 1992. Holocene Tidal-Marsh Stratigraphy in South-Central Oregon-Evidence for Localized Sudden Submergence in the Cascadia Subduction Zone. SEPM 48, 287-301.

Nelson, A.R., Shennan, I., Long, A.J., 1996. Identifying coseismic subsidence in tidal-wetland stratigraphic sequences at the Cascadia subduction zone of western North America. Journal Of Geophysical Research-Solid Earth 101, 6115-6135.

NOAA, http://www.co-ops.nos.noaa.gov.

Oey, L., Ezer, T., Chuanmin, H., Muller-Karger, F.E., 2007. Baroclinic tidal flows and inundation processes in Cook Inlet, Alaska: numerical modeling and satellite observations. Ocean Dynamics 57, 205-221.

Outridge, P.M., Hermanson, M.H., Lockhart, W.L., 2002. Regional variations in atmospheric deposition and sources of anthropogenic lead in lake sediments across the Canadian Arctic. Geochimica Et Cosmochimica Acta 66, 3521-3531.

Palmer, A.J., Abbott, W.H., 1986. Diatoms as indicators of sea level change, In: Van de Plassche, O. (Ed.), Sea Level Research: A manual for the collection and evaluation of data. Geobooks, Norwich, pp. 457-488.

Patrick, R., Reimer, C.W., 1966. The Diatoms of the United States. Volume 1. Monographs of The Academy of Natural Sciences of Philadelphia No 13. Academy of Natural Sciences of Philadelphia, Philadelphia.

Patrick, R., Reimer, C.W., 1975. The Diatoms of the United States. Volume 2, Part 1. Monographs of The Academy of Natural Sciences of Philadelphia No 13. The Academy of Natural Sciences of Philadelphia, Philadelphia.

Patterson, R.T., Hutchinson, I., Guilbault, J.P., Clague, J.J., 2000. A comparison of the vertical zonation of diatom, foraminifera, and macrophyte assemblages in a coastal marsh: implications for greater paleo-sea level resolution. Micropaleontology 46, 229-244.

Paull, T.M., Hamilton, P.B., Gajewski, K., LeBlanc, M., 2008. Numerical analysis of small Arctic diatoms (Bacillariophyceae) representing the Staurosira and Staurosirella species complexes. Phycologia 47, 213-224.

Payne, R., Blackford, J., 2008. Extending the late Holocene tephrochronology of the central Kenai Peninsula, Alaska. Arctic 61, 243-254.

Payne, R., Blackford, J., van der Plicht, J., 2008. Using cryptotephras to extend regional tephrochronologies: An example from southeast Alaska and implications for hazard assessment. Quaternary Research 69, 42-55.

Peltier, W.R., 1986. Deglaciation-induced vertical motion of the North American Continent. Journal of Geophysical Research 91, 900-9123.

Peltier, W.R., 2002. Global glacial isostatic adjustment: palaeogeodetic and space geodetic test of the ICE-4G (VM2) model. Journal of Quaternary Science 17, 491-510.

Peltier, W.R., 2004. Global glacial isostasy and the surface of the ice-age earth: The ICE-5G (VM2) model and GRACE. Annual Review of Earth and Planetary Sciences 32, 111-149.

Peltier, W.R., Drummond, R., 2008. Rheological stratification of the lithosphere: A direct inference based upon the geodetically observed pattern of the glacial isostatic adjustment of the North American continent. Geophysical Research Letters 35.

Peltier, W.R., Shennan, I., Drummond, R., Horton, B., 2002. On the postglacial isostatic adjustment of the British Isles and the shallow viscoelastic structure of the Earth. Geophysical Journal International 148, 443-475.

Pennington, W., Cambray, R.S., Fisher, E.H., 1973. Observations on lake sediments using fallout 137Cs as a tracer. Nature 242, 324-326.

Plafker, G., 1965. Tectonic Deformation Associated with the 1964 Alaska Earthquake. Science 148, 1675-1687.

Plafker, G., 1969. Tectonics of the March 27, 1964, Alaska earthquake. U.S. Geological Survey Professional Paper 543-I, 74.

Plafker, G., 1972. Implications for arc tectonics. Journal of Geophysical Research 77, 901-925.

Plafker, G., Berg, H.C., 1994. Overview of the geology and tectonic evolution of Alaska, In: Plafker, G., Berg, H.C. (Eds.), The Geology of Alaska. Geological Society of America, Boulder, Colorado.

Plafker, G., Kachadoorian, R., Eckel, E.B., Mayo, L.R., 1969. Effects of the earthquake of march 27, 1964 on various communities. US Geological Survey Professional Paper 542-G, 1-50.

Plafker, G., Lajoie, K.R., Rubin, M., 1992. Determining recurrence intervals of great subduction zone earthquakes in southern Alaska by radiocarbon dating, In: Taylor, R.E., Long, A., Kra, R.S. (Eds.), Radiocarbon after four decades - An Interdisiplinary Perspective. Springer-Verkag, New York, pp. 436-453.

Plafker, G., Thatcher, W., 2008. Geological and geophysical evaluation of the mechanisms of the great 1899 Yakutat Bay earthquakes, In: Freymueller, J.T., Haeussler, P., Wesson, R.L., Ekstrom, G. (Eds.), Active Tectonics and Seismic Potential of Alaska. AGU Geophysical Monograph Series Vol 179, Washington, DC, pp. 215-236.

Plater, A.J., Horton, B.P., Haworth, E.Y., Appleby, P.G., Zong, Y., Wright, M.R., Rutherford, M.M., 2000. Holocene tidal levels and sedimentation rates using a diatom-based palaeoenvironmental reconstruction: the Tees estuary, northeastern England. Holocene 10, 441-452.

Plater, A.J., Ridgway, J., Appleby, P.G., Berry, A., Wright, M.R., 1998. Historical contaminant fluxes in the Tees estuary, UK: Geochemical, magnetic and radionuclide evidence. Mar. Pollut. Bull. 37, 343-360.

Preuss, H., 1979. Progress in computer evaluation of sea level data within the IGCP Project No. 61.

Pugh, D.T., 1996. Tides, Surges and Mean Sea-Level. John Wiley & Sons, Chichester.

Quinn, R., 2006. Palaeo-seismic evidence from the marsh at Hope, Alaska, Geography. Geography Department, Durham University.

Reger, R.D., Pinney, D.S., 1996. Late Wisconsin glaciation of the Cook Inlet region with emphasis on the Kenai lowland and implications for early peopling, In: Davis, N.Y., Davis, W.E. (Eds.), Adventures through time: Readings in the anthropology of Cook Inlet, Alaska. Cook Inlet Historical Society, Anchorage, pp. 15-35.

Reger, R.D., Pinney, D.S., 1997. Last major glaciation of Kenai lowland, In: Karl, S.M., Vaughn, N.R., Ryherd, T.J. (Eds.), Guide to the geology of the Kenai Peninsula, Alaska. Alaska Geological Society, Anchorage, pp. 54-67.

Reger, R.D., Sturmann, A.G., Berg, E.E., Burns, P.A.C., 2008. A guide to the late Quaternary History of the Northern and Western Kenai Peninsula, Alaska. Guidebook 8. State of Alaska Department of Natural Resources Division of Geological and Geophysical Surveys.

Reimer, P.J., Baillie, M.G.L., Bard, E., Bayliss, A., Beck, J.W., Bertrand, C.J.H., Blackwell, P.G., Buck, C.E., Burr, G.S., Cutler, K.B., Damon, P.E., Edwards, R.L., Fairbanks, R.G., Friedrich, M., Guilderson, T.P., Hogg, A.G., Hughen, K.A., Kromer, B., McCormac, G., Manning, S., Ramsey, C.B., Reimer, R.W., Remmele, S., Southon, J.R., Stuiver, M., Talamo, S., Taylor, F.W., van der Plicht, J., Weyhenmeyer, C.E., 2004. IntCal04 terrestrial radiocarbon age calibration, 0-26 cal kyr BP. Radiocarbon 46, 1029-1058.

Renberg, I., Bindler, R., Brannval, M., 2001. Using the historical atmopsheric lead-deposition record as a chronological marker in sediment deposits in Europe. The Holocene 11, 511-516.

Renberg, I., Brannvall, M.L., Bindler, R., Emteryd, O., 2000. Atmospheric lead pollution history during four millennia (2000 BC to 2000 AD) in Sweden. Ambio 29, 150-156.

Reyes, A.V., Wiles, G.C., Smith, D.J., Barclay, D.J., Allen, S., Jackson, S., Laxton, S., Lewis, D., Calkin, P.E., Clague, J., 2006. Expansion of alpine glaciers in Pacific North America in the first millennium A.D. Geology 34, 57-60.

Riehle, J.R., 1985. A reconnaissance of the major Holocene tephra deposits in the Upper Cook Inlet region, Alaska. Journal of Volcanology and Geothermal Research 26, 37-74.

Rignot, E., Rivera, A., Casassa, G., 2003. Contribution of the Patagonia Icefields of South America to sea level rise. Science 302, 434-437.

Roe, H.M., Doherty, C.T., Patterson, R.T., Swindles, G.T., 2009. Contemporary distributions of saltmarsh diatoms in the Seymour-Belize Inlet Complex, British Columbia, Canada: Implications for studies of sea-level change. Marine Micropaleontology 70, 134-150.

Rydgren, K., Økland, R.H., Økland, T., 2003. Species response curves along environmental gradients. A case study from SE Norwegian swamp forests. Journal of Vegetation Science 14, 869-880.

Sauber, J., Plafker, G., Molnia, B.F., Bryant, M.A., 2000. Crustal deformation associated with glacial fluctuations in the eastern Chugach Mountains, Alaska. Journal of Geophysical Research-Solid Earth 105, 8055-8077.

Sauber, J.M., Molnia, B.F., 2004. Glacier ice mass fluctuations and fault instability in tectonically active Southern Alaska. Global and Planetary Change 42, 279-293.

Savage, J.C., Plafker, G., 1991. Tide gage measurements of uplift along the south coast of Alaska. Journal of Geophysical Research 96, 4325-4335.

Savage, J.C., Thatcher, W., 1992. Interseismic deformation at the Nankai Trough, Japan subdcution zone. Journal of Geophysical Research 97, 11,117-111,135.

Sawai, Y., 2001. Episodic emergence in the past 3000 years at the Akkeshi estuary, Hokkaido, northern Japan. Quaternary Research 56, 231-241.

Sawai, Y., Horton, B.P., Nagumo, T., 2004. The development of a diatom-based transfer function along the Pacific coast of eastern Hokkaido, northern Japan - An aid in paleoseismic studies of the Kuril subduction zone. Quaternary Science Reviews 23, 2467-2483.

Schiff, C.J., Kaufman, D.S., Wallace, K.L., Werner, A., Ku, T.L., Brown, T.A., 2008. Modeled tephra ages from lake sediments, base of Redoubt Volcano, Alaska. Quaternary Geochronology 3, 56-67.

Schmoll, H.R., 1977. Engineering geology of Anchorage Borough, In: Blean, K.M. (Ed.), The United States Geological Survey in Alaska: accomplishments during 1976. US Geological Survey Circular **751-B**, pp. B51-B52.

Schmoll, H.R., Szabo, B.J., Rubin, M., Dobrovolny, E., 1972. Radiometric dating of marine shells from the Bootlegger Cove clay, Anchorage area, Alaska. Geological Society of America Bulletin 83, 1107-1113.

Schmoll, H.R., Yehle, L.A., Updike, R.G., 1999. Summary of Quaternary geology of the Municipality of Anchorage, Alaska. Quaternary International 60, 3-36.

Sella, G.F., Stein, S., Dixon, T.H., Craymer, M., James, T.S., Mazzotti, S., Dokka, R.K., 2007. Observation of glacial isostatic adjustment in "stable" North America with GPS. Geophysical Research Letters 34.

Shennan, I., 1986. Flandrian sea-level changes in the Fenland II. Tendencies of sea-level movement, altitudinal changes and local and regional factors. Journal of Quaternary Science 1, 155-179.

Shennan, I., Barlow, N., Combellick, R., 2008. Palaeoseismological records of multiple great earthquakes in south-central Alaska: a 4000 year record at Girdwood, In: Freymueller, J.T., Haeussler, P.J., Wesson, R.L., Ekstrom, G. (Eds.), Active tectonics and seismic potential of Alaska. AGU Geophysical Monograph Series Vol 179, Washington, DC, pp. 185-199.

Shennan, I., Bruhn, R., Plafker, G., 2009. Multi-segment earthquakes and tsunami potential of the Aleutian megathrust. Quaternary Science Reviews 28, 7-13.

Shennan, I., Coulthard, T., Flather, R., Horton, B., Macklin, M., Rees, J., Wright, M., 2003. Integration of shelf evolution and river basin models to simulate Holocene sediment dynamics of the Humber Estuary during periods of sea-level change and variations in catchment sediment supply. The Science of the Total Environment 314-316, 737-754.

Shennan, I., Hamilton, S., 2006. Coseismic and pre-seismic subsidence associated with great earthquakes in Alaska. Quaternary Science Reviews 25, 1-8.

Shennan, I., Horton, B.P., 2002. Holocene land- and sea-level changes in Great Britain. Journal of Quaternary Science 17, 511-526.

Shennan, I., Horton, B.P., Innes, J.B., Gehrels, W.R., Lloyd, J.M., McArthur, J.J., Rutherford, M.M., 2000a. Late Quaternary sea-level changes, crustal movements and coastal evolution in Northumberland, UK. Journal of Quaternary Science 15, 215-237.

Shennan, I., Lambeck, K., Flather, R., Horton, B.P., McArthur, J.J., Innes, J.B., Lloyd, J.M., Rutherford, M.M., Wingfield, R., 2000b. Modelling western North Sea palaeogeographies and tidal changes during the Holocene, In: Shennan, I., Andrews, J. (Eds.), Holocene land-ocean interaction and environmental change around the North Sea. Geological Society, Special Publications, 166, London, pp. 299-319.

Shennan, I., Long, A.J., Rutherford, M.M., Green, F.M., Innes, J.B., Lloyd, J.M., Zong, Y., Walker, K.J., 1996. Tidal marsh stratigraphy, sea-level change and large earthquakes, I: A 5000 year record in Washington, USA. Quaternary Science Reviews 15, 1023-1059.

Shennan, I., Long, A.J., Rutherford, M.M., Kirkby, J., Green, F.M., Innes, J.B., Walker, K., 1998. Tidal marsh stratigraphy, sea level change and large earthquakes, II: Events during the last 3500 years at Netarts Bay, Oregon, USA. Quaternary Science Reviews 17, 365-393.

Shennan, I., Peltier, W.R., Drummond, R., Horton, B., 2002. Global to local scale parameters determining relative sea-level changes and the post-glacial isostatic adjustment of Great Britain. Quaternary Science Reviews 21, 397-408.

Shennan, I., Scott, D.B., Rutherford, M.M., Zong, Y., 1999. Microfossil analysis of sediments representing the 1964 earthquake, exposed at Girdwood Flats, Alaska, USA. Quaternary International 60, 55-73.

Shennan, I., Tooley, M.J., Davis, M.J., Haggart, B.A., 1983. Analysis and interpretation of Holocene sea level data. Nature 302, 404-406.

Sherrod, B.L., 1999. Gradient analysis of diatom assemblages in a Puget Sound salt marsh: can such assemblages be used for quantitative paleoecological reconstructions? Paleogeogr. Paleoclimatol. Paleoecol. 149, 213-226.

Shulski, M., Wendler, G., 2007. The Climate of Alaska. University of Alaska Press, Anchorage.

Skalska, T., Kaczmarczyk, D., 1980. Peripyton diatoms of 3 mid forest ponds in Strzybnica, upper Silesian industrial district, Poland. Prace Naukowe Uniwersytetu Slaskiego w Katowicach, 237-252.

Spada, G., 2003. The Theory Behind TABOO. Samizdat Press, Golden-White River Junction.

Spada, G., Antonioli, A., Boschi, L., Brandi, V., Cianetti, S., Galvani, G., Giunchi, C., Perniola, B., Piana Agostinetti, N., Piersanti, A., Stocchi, P., 2003. TABOO, User Guide. Samizdat Press, Golden-White River Junction.

Spada, G., Antonioli, A., Boschi, L., Brandi, V., Cianetti, S., Galvani, G., Giunchi, C., Perniola, B., Piana Agostinetti, N., Piersanti, A., Stocchi, P., 2004. Geodesy: modeling earth's post-glacial rebound. Eos Transactions. AGU 85, 62.

Spencer, K.L., Cundy, A.B., Croudace, I.W., 2003. Heavy metal distribution and early-diagenesis in salt marsh sediments from the Medway Estuary, Kent, UK. Estuarine Coastal and Shelf Science 57, 43-54.

Steier, P., Rom, W., 2000. The use of Bayesian statistics for C-14 dates of chronologically ordered samples: A critical analysis. Radiocarbon 42, 183-198.

Stewart, I.S., Sauber, J., Rose, J., 2000. Glacio-seismotectonics: ice sheets, crustal deformation and seismicity. Quaternary Science Reviews 19, 1367-1389.

Stuiver, M., Quay, P.D., 1980. Patterns of atmopsheric C-14 changes. Radiocarbon 22, 166-176.

Stuiver, M., Reimer, P.J., Reimer, R.W., 2005. CALIB 5.0 - Online documentation http://calib.qub.ac.uk/calib/.

Sturges, W.T., Hopper, J.F., Barrie, L.A., Schnell, R.C., 1993. Stable lead isotope ratios in Alaskan Arctic aerosols. Atmospheric Environment 27A, 2865-2871.

Suito, H., Freymueller, J.T., 2009. A viscoelastic and afterslip postseismic deformation model for the 1964 Alaska earthquake. Journal of Geophysical Research-Solid Earth 114.

Suito, H., Hirahara, K., 1999. Simulation of Postseismic Deformations caused by the 1896 Riku-u Earthquake, Northeast Japan: Re-evaluation of the viscosity in the upper mantle. Geophysical Research Letters 26, 2561-2564.

Sundby, B., Caetano, M., Vale, C., Gobeil, C., Luther, G.W., Nuzzio, D.B., 2005. Root-induced cycling of lead in salt marsh sediments. Environmental Science & Technology 39, 2080-2086.

Svensson, R., Agren, J., Olsson, P., Eriksson, P., Lilje, M., 2006. The New Swedish Height System RH 2000 and geoid model SWEN 05LR, Shaping the Changes, XXIII FIG Congress, Munich, Germany.

Szkornik, K., Gehrels, W.R., Kirby, J.R., 2004. Salt-marsh diatom distributions in Ho Bugt (western Denmark) and the development of a transfer function for reconstructing Holocene sea-level changes, 6th International Conference on Tidal Sedimentology. Elsevier Science Bv, Copenhagen, DENMARK, pp. 137-150.

Szkornik, K., Gehrels, W.R., Murray, A.S., 2008. Aeolian sand movement and relative sea-level rise in Ho Bugt, western Denmark, during the 'Little Ice Age'. Holocene 18, 951-965.

Tamisiea, M.E., Mitrovica, J.X., Davis, J.L., 2003. A method for detecting rapid mass flux of small glaciers using local sea level variations. Earth and Planetary Science Letters 213, 477-485.

Tamisiea, M.E., Mitrovica, J.X., Milne, G.A., Davis, J.L., 2001. Global geoid and sea level changes due to present-day ice mass fluctuations. Journal of Geophysical Research-Solid Earth 106, 30849-30863.

ter Braak, C.J.F., Juggins, S., 1993. Weighted averaging partial least squared regression (WA-PLS): an improved method for reconstructing environmental variables from species assemblages. Hydrobiologia 269/270, 485-502.

ter Braak, C.J.F., Juggins, S., Birks, H.J.B., van de Voet, H., 1993. Weighted averaging partial least squared regression (WA-PLS): definition and comparison with other methods for species-environmental calibration, In: Patil, G.P., Rac, C.R. (Eds.), Multivariate Environmental Statistics. Elsevier Science Publishers, Amsterdam, pp. 525-560.

ter Braak, C.J.F., Smilauer, P., 2002. CANOCO Reference Manual and CanoDraw for Windows User's Guide: Software for Canonical Community Ordination (version 4.5). Microcomputer Power, Ithaca, NY, USA.

Thatcher, W., 1984. The earthquake deformation cycle, recurrence and the time predictable model. Journal of Geophysical Research 89, 5674-5680.

Thatcher, W., Matsuda, T., Kato, T., Rundle, J.B., 1980. Lithospheric Loading by the 1896 Riku-U Earthquake, Northern Japan - Implications for Plate Flexure and Asthenospheric Rheology. Journal of Geophysical Research 85, 6429-6435.

Thatcher, W., Rundle, J.B., 1984. A viscoelastic coupling model for the cyclic deformation due to periodically repeated earthquakes at subduction zones. Journal of Geophysical Research 89, 7631-7640.

Tooley, M.J., 1985. Sea-level changes and coastal morphology in North-West England, In: Johnson, R.H. (Ed.), The Geomorphology of North-West England. Manchester University Press, Manchester, pp. 94-121.

Tornqvist, T.E., Wallace, D.J., Storms, J.E.A., Wallinga, J., Van Dam, R.L., Blaauw, M., Derksen, M.S., Klerks, C.J.W., Meijneken, C., Snijders, E.M.A., 2008. Mississippi Delta subsidence primarily caused by compaction of Holocene strata. Nature Geoscience 1, 173-176.

Troels-Smith, J., 1955. Characterization of unconsolidated sediments. Danmarks Geologiske Undersogelse Series IV, 38-73.

Turner, R.E., Milan, C.S., Swenson, E.M., 2006. Recent volumetric changes in salt marsh soils. Estuarine Coastal and Shelf Science 69, 352-359.

Turney, C.S.M., Lowe, J.J., 2001. Tephrochronology, In: Last, W.M., Smol, J.P. (Eds.), Tracking Environmental Change Usng Lake Sediments. Volume 1: Basin Analysis, Coring and Chronological Techniques. Kluwer Academic Press, Dordrecht, The Netherlands.

Tushingham, A.M., Peltier, W.R., 1991. Ice-3G: a new global model of late Pleistocene de-glaciation based upon geophysical predictions of post-glacial relative sea level change. Journal of Geophysical Research 96, 4497-4523.

van de Plassche, O., Edwards, R.J., van der Borg, K., de Jong, A.F.M., 2001. C-14 wiggle-match dating in high-resolution sea-level research. Radiocarbon 43, 391-402.

van den Berg, J., van de Wal, R.S.W., Milne, G.A., Oerlemans, J., 2008. Effect of isostasy on dynamical ice sheet modeling: A case study for Eurasia. Journal of Geophysical Research-Solid Earth 113.

van der Werff, A., Huls, H., 1958-1974. Diatomeeenflora van Nederland. 8 parts. Published privately, De Hoef, The Netherlands.

Vodop'Yan, N.S., 1976. Flora of diatomaceae from water bodies in the small Polesye, USSR. Ukrayins'kyi Botanichnyi Zhurnal 33, 485-489.

Vos, P.C., de Wolf, H., 1988. Methodological aspects of palaeo-ecological diatom research in coastal areas of the Netherlands. Geologie en Mijnbouw 67, 31-40.

Wahr, J., Wyss, M., 1980. Interpretation of postseismic deformation with a viscoelastic relaxation model. Journal of Geophysical Research 85, 6471-6477.

Waitt, R.B., Begét, J.E., 2009. Volcanic processes and geology of Augustine Volcano, Alaska, U.S. Geological Survey Professional Paper 1762.

Walcott, R.I., 1972. Past sea levels, eustasy and deformation of the Earth. Quaternary Research 2, 1-14.

Wang, K.L., Dragert, H., Melosh, H.J., 1994. Finite-element study of uplift and strain across Vancouver-Island. Canadian Journal of Earth Sciences 31, 1510-1522.

Wang, K.L., He, J.H., Dragert, H., James, T.S., 2001. Three-dimensional viscoelastic interseismic deformation model for the Cascadia subduction zone. Earth Planets and Space 53, 295-306.

Watchorn, M.A., Hamilton, P.B., Anderson, T.W., Roe, H.M., Patterson, R.T., 2008. Diatoms and pollen as indicators of water quality and land-use change: a case study from the Oak Ridges Moraine, Southern Ontario, Canada. Journal of Paleolimnology 39, 491-509.

Wiles, G.C., Barclay, D.J., Calkin, P.E., 1999. Tree-ring-dated 'Little ice age' histories of maritime glaciers from western Prince William Sound, Alaska. Holocene 9, 163-173.

Wiles, G.C., Barclay, D.J., Calkin, P.E., Lowell, T.V., 2008. Century to millennial-scale temperature variations for the last two thousand years indicated from glacial geologic records of southern Alaska. Global and Planetary Change 60, 115-125.

Wiles, G.C., Calkin, P.E., 1994. Late Holocene, high resolution glacial chronologies and climate, Kenai mountains, Alaska. Geological Society of America Bulletin 106, 281-303.

Williams, R.T., Robinson, E.S., 1979. Ocean tides and waves beneath the Ross Ice Shelf, Antartica. Science 203, 443-445.

Wilson, F.H., Hults, C.P., 2008. Geology of the Prince William Sound and Kenai Peninusla Region, Alaska. U.S. Geological Survey Open-File Report 2008-1002

Wolfe, A.P., Miller, G.H., Olsen, C.A., Forman, S.L., Doran, P.T., Holmgren, S.U., 2004. Geochronology of high latitude lake sediments, In: Pienitz, R., Douglas, M.S.V., Smol, J.P. (Eds.), Long-term Environmental Change in Arctic and Antarctic Lakes. Springer, The Netherlands, pp. 19-52.

Woodroffe, S.A., 2006. Holocene relative sea-level changes in Cleveland Bay, North Queensland, Australia, Department of Geography. Durham University, Unpublished PhD Thesis, Durham.

Woodroffe, S.A., 2009. Recognising subtidal foraminiferal assemblages: implications for quantitative sea-level reconstructions using a foraminifera-based transfer function. Journal of Quaternary Science 24, 215-223.

Woodroffe, S.A., Long, A., 2010. Reconstructing recent relative sea-level changes in West Greenland: Local diatom-based transfer functions are superior to regional models. Quaternary International 221, 91-103.

Woodroffe, S.A., Long, A.J., 2009. Salt marshes as archives of recent relative sea level change in West Greenland. Quaternary Science Reviews 28, 1750-1761.

Woodworth, P.L., White, N.J., Jevrejeva, S., Holgate, S.J., Church, J.A., Gehrels, W.R., 2009. Evidence for the accelerations of sea level on multi-decade and century timescales. Int. J. Climatol. 29, 777-789.

Wu, P., Johnston, P., Lambeck, K., 1999. Postglacial rebound and fault instability in Fennoscandia. Geophysical Journal International 139, 657-670.

Yeloff, D., Bennett, K.D., Blaauw, M., Mauquoy, D., Sillasoo, U., van der Plicht, J., Geel, B., 2006. High precision C-14 dating of Holocene peat deposits: A comparison of Bayesian calibration and wiggle-matching approaches. Quaternary Geochronology 1, 222-235.

Zong, Y., Shennan, I., Combellick, R.A., Hamilton, S.L., Rutherford, M.M., 2003. Microfossil evidence for land movements associated with the AD 1964 Alaska earthquake. Holocene 13, 7-20.

Zong, Y.Q., Horton, B.P., 1999. Diatom-based tidal-level transfer functions as an aid in reconstructing Quaternary history of sea-level movements in the UK. Journal of Quaternary Science 14, 153-167.

Glacial isostatic adjustment and relative sea level change over the last earthquake cycle in upper Cook Inlet, Alaska, USA

Two Volumes

Volume Two: Figures, Tables and Appendices

Natasha Louise Mary Barlow

Thesis submitted for the degree of Doctor of Philosophy

Department of Geography
Durham University

October 2010

Table of Contents

Volume 2

Table of Figures

Volume 2

Chapter 1

Chapter 2

Chapter 3

Chapter 4

Chapter 5

Chapter 6

Table of Tables

Volume 2

Contents of Appendices

Volume 2

All appendices are at the end of this volume, with the exception of A2_1 and A2_2 which are available on request from the author, or on the CD at the back of the hard copy volume.

Lithostratigraphy

A1_1 Girdwood Troels Smith.pdf	Girdwood Troels-Smith descriptions
A1_2 Bird Point Troels Smith.pdf	Bird Point Troels-Smith descriptions
A1_3 Hope Troels Smith.pdf	Hope Troels-Smith descriptions
A1_4 Ocean View Troels Smith.pdf	Ocean View Troels-Smith descriptions

Diatom data

A2_1 Fossil diatoms.xls	Fossil diatom counts from all cores
A2_2 Contemporary diatoms.xls	Contemporary diatom counts
A2_3 Species list.pdf	Name and codes of upper Cook Inlet diatoms

Modelling

A3_1 Example TABOO Task 3 file.pdf	Example of TABOO Task#3 input file
A3_2 TABOO Verification	Results of TABOO verification from section 5.2

Radiocarbon samples

A4_1 Radiocarbon report from NERC	NERC Radiocarbon Analytical Report – Bird Point dates

Chapter 1 : Figures

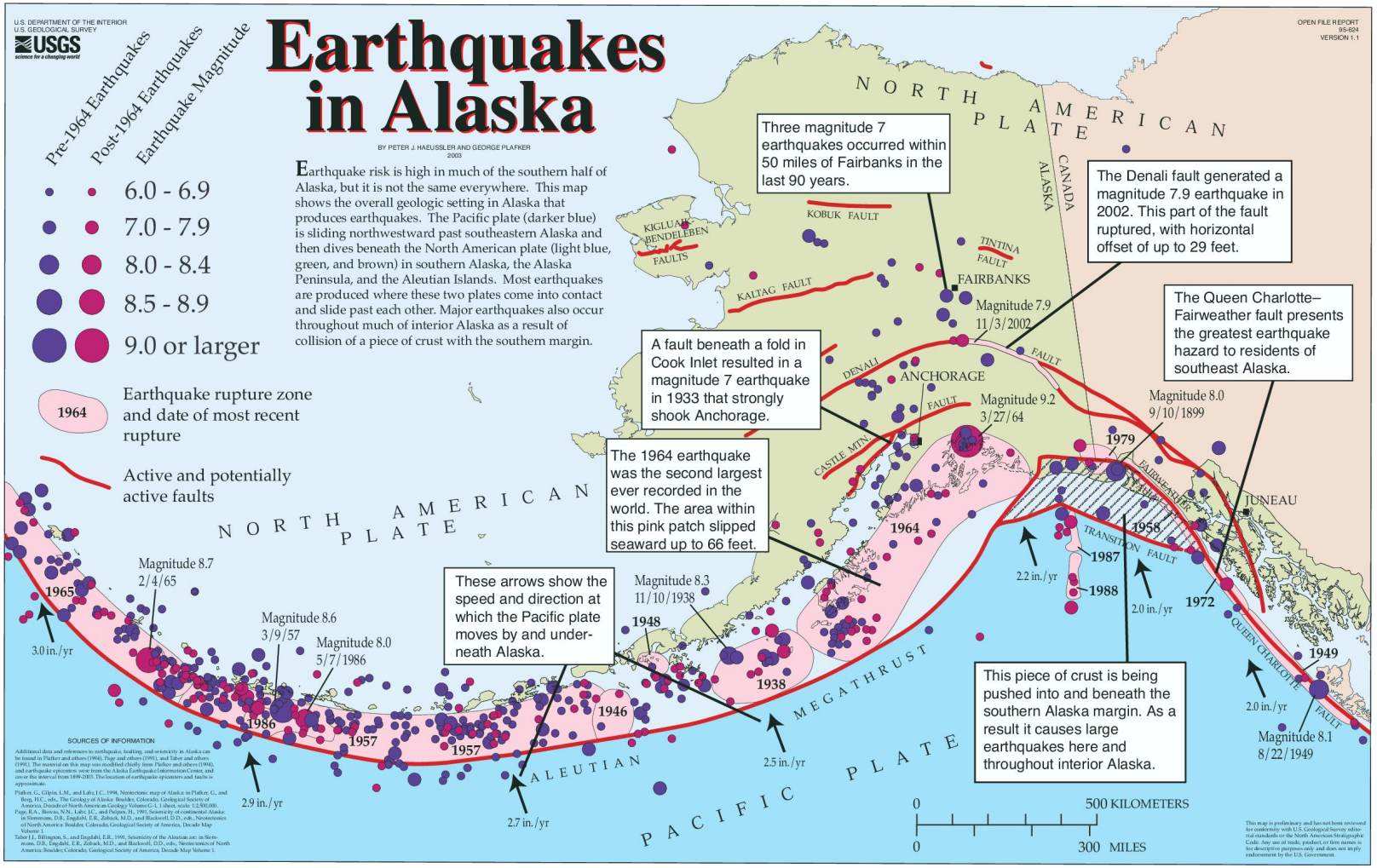

Figure 1.1 – Map of historic earthquakes, active faults and rupture zones by Haeussler and Plafker (2003). The map shows the location of known major earthquakes, active faults, in particular the Aleutian Megathrust where the Pacific Plate subducts under the North American Plate and areas of known rupture associated with recent earthquakes. (Source: http://www.aeic.alaska.edu/html_docs/historic_quakes_tectonics.html, Accessed August, 2010).

Figure 1.2 - Example of a sedimentary peat-silt couplet at a coastal salt marsh (Girdwood) which results from the land level movements during the earthquake deformation cycle in upper Cook Inlet. This stratigraphy results from land uplift during the interseismic phase of the EDC during which tidal silt is raised over time to become freshwater peat. During a great earthquake, coseismic submergence results in the deposition of intertidal silt over freshwater peat resulting in a distinct lithological horizon.

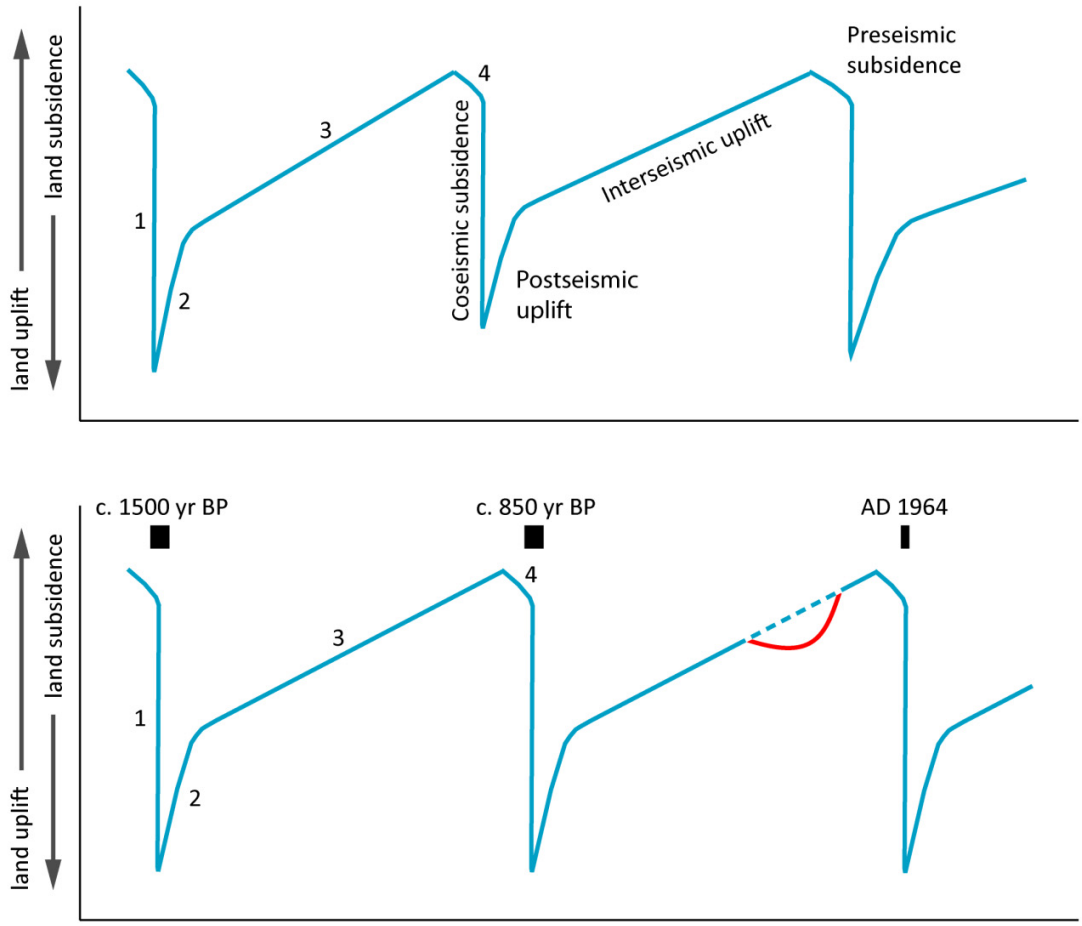

Figure 1.3 - Four phase earthquake deformation cycle (EDC) model (top figure) with the most recent three great earthquakes in south central Alaska in AD 1964, c. 850 yr BP and c.1500 yr BP (bottom figure). In upper Cook Inlet great earthquakes result in coseismic land subsidence and rapid RSL rise (1), followed by decades of rapid post-seismic uplift (2) and centuries of gradual interseismic land uplift and RSL fall (3), before pre-seismic subsidence (4) in the decades prior to the next great earthquake. Geological data from the Cascadian and Alaskan subduction zones has established this framework of tectonically driven land level changes which provides a testable model against which to measure non seismic RSL deviations from the EDC model. This thesis focuses on a possible deviation during the last earthquake deformation cycle (illustrated by red curve) hypothesised by Hamilton and Shennan (2005a) to be due to LIA associated GIA (Figure 1.6).

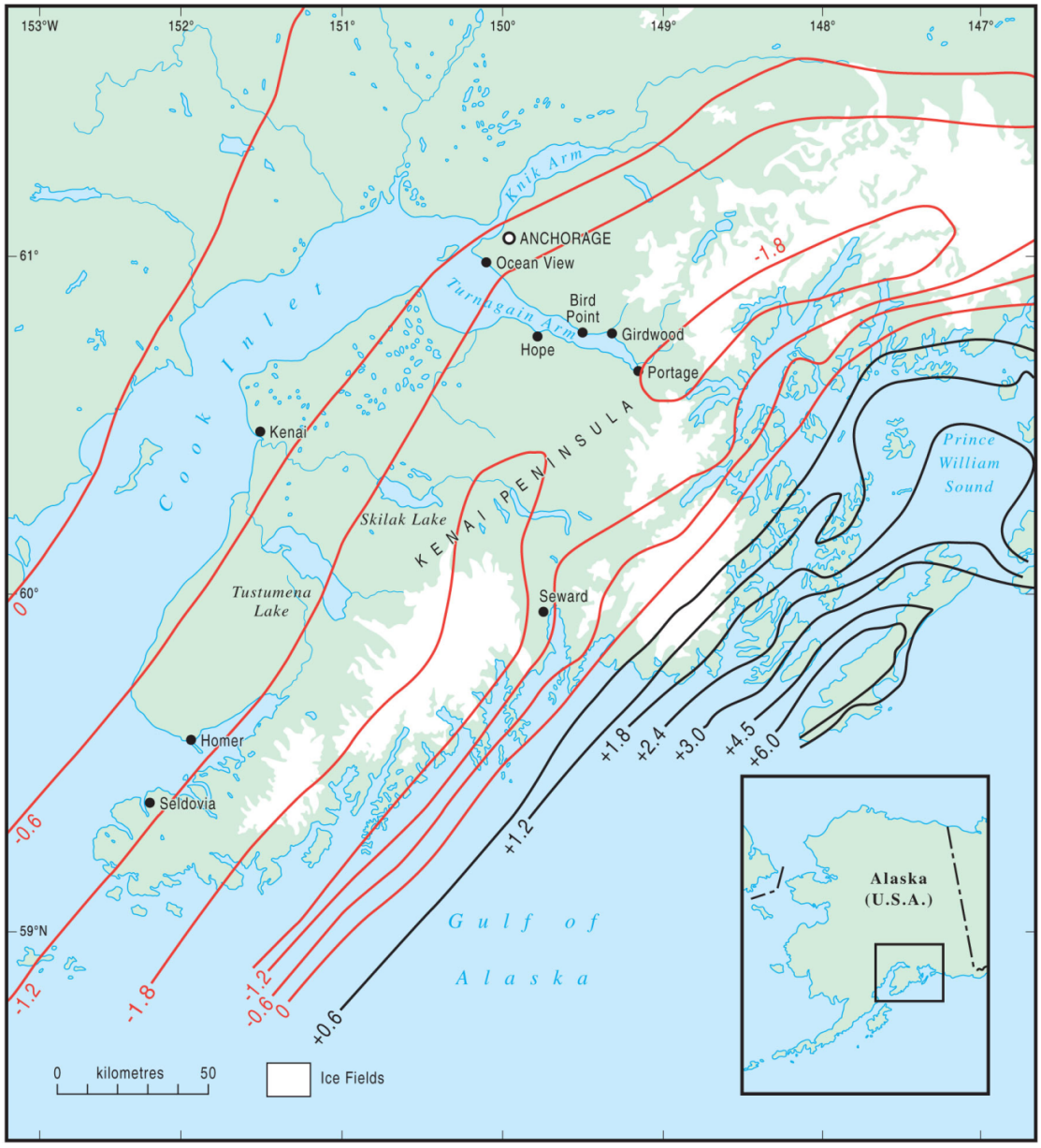

Figure 1.4 - Contour map of vertical displacement in south central Alaska caused by the AD 1964 earthquake, based upon Plafker (1969). Contours hide many local scale variations, including local subsidence caused by sediment compaction. Additionally some are based on interpolations over long distances. Figure also shows some of the key locations mentioned in the text. Adapted from Hamilton and Shennan (2005a) Figure 1.

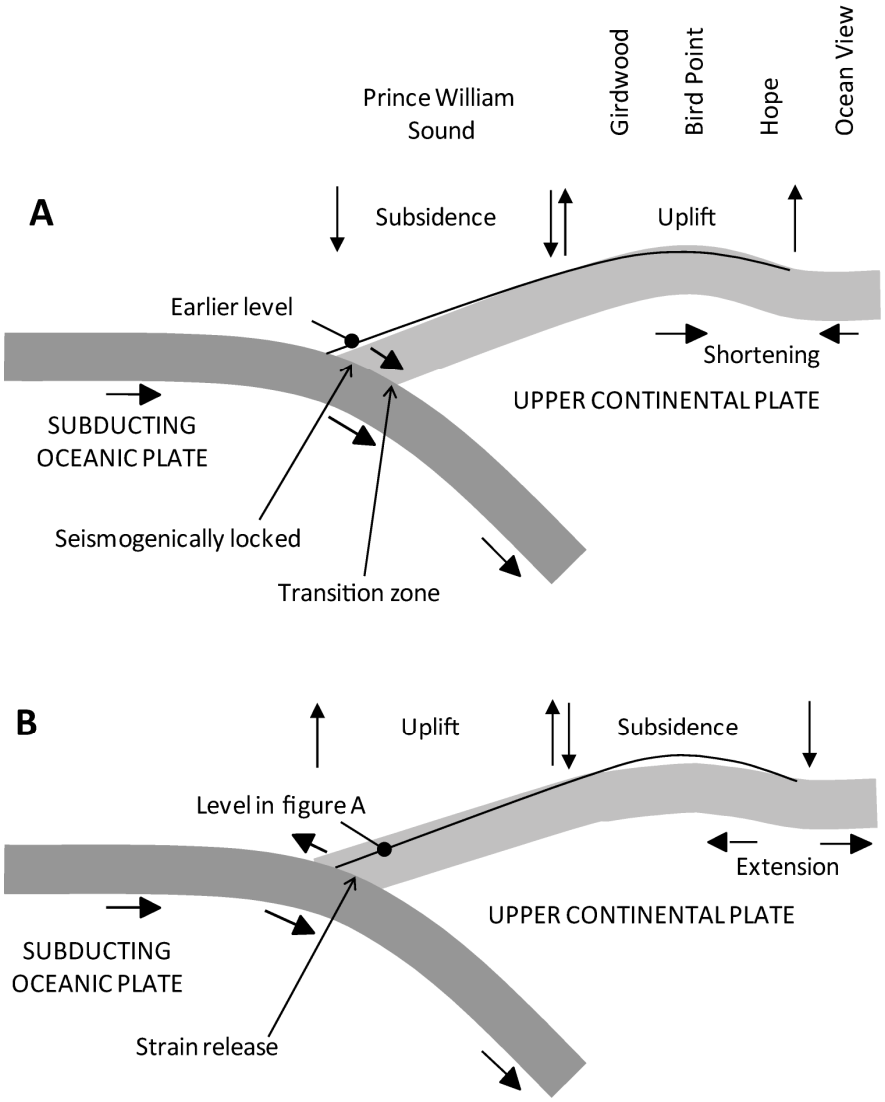

Figure 1.5 - Schematics showing the pattern of (A) interseismic and (B) coseismic deformation associated with a subduction zone earthquake during an earthquake deformation cycle. Adapted from Nelson *et al.* (1996) to reflect the spatial pattern of coseismic deformation during the AD 1964 earthquake in Alaska. Adapted from Hamilton and Shennan (2005a) (Figure 2) to include field sites along Turnagain Arm used in this thesis. Exact spatial pattern of inter-seismic uplift along Turnagain Arm is unknown, but this provides a simple model of possible displacement.

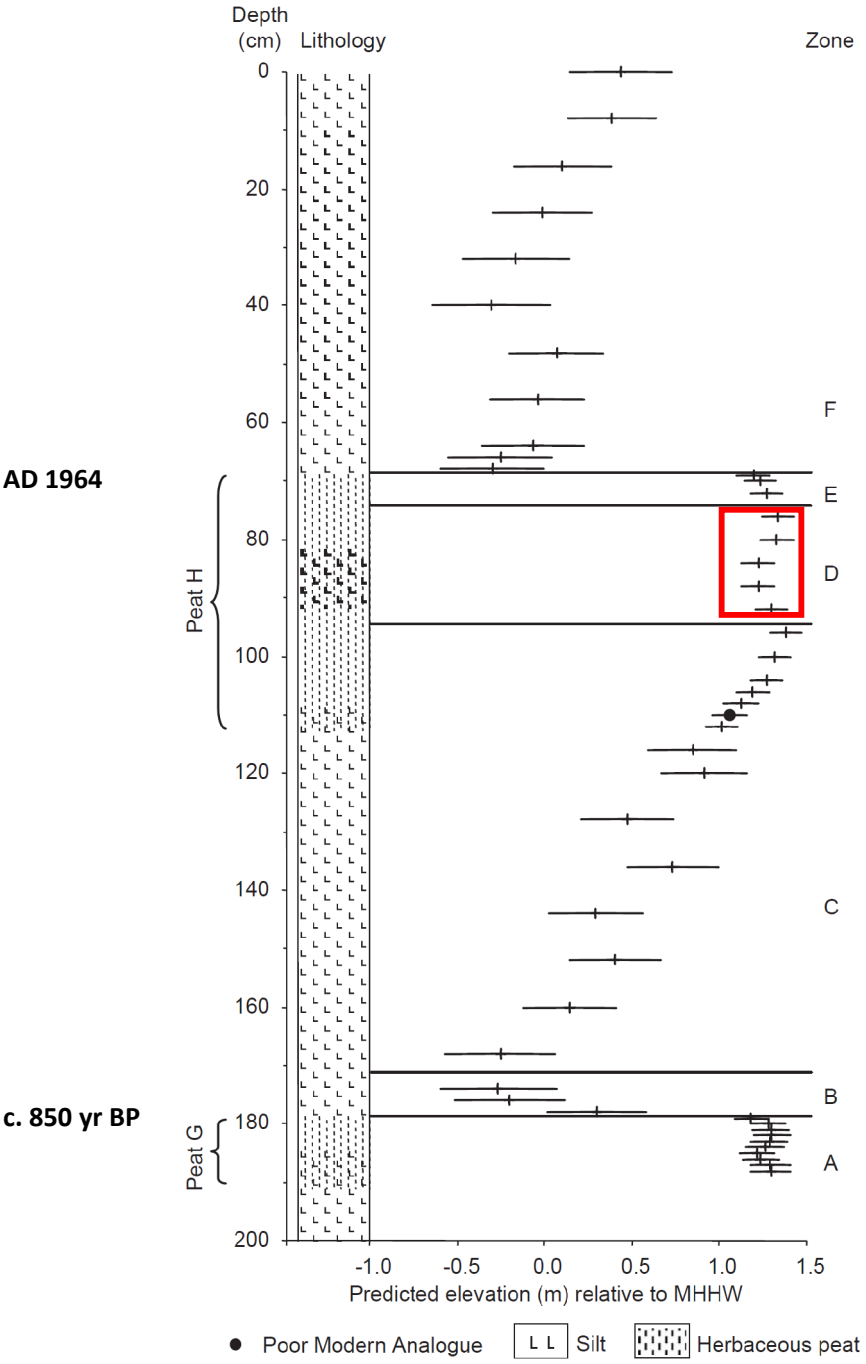

Figure 1.6 - Changes in predicted elevation (m) relative to mean higher high water (MHHW) for GW-1, at Girdwood, estimated by Hamilton and Shennan (2005a) from fossil diatom data calibrated by a series of upper Cook Inlet transfer function models. In section D (red box) Hamilton and Shennan (2005a) show a slight RSL rise followed by a slight fall (prior to the pre-seismic RSL rise in E) which they hypothesis is due to LIA GIA. Peat H is the AD 1964 peat and peat G formed prior to the preceding great earthquake (c. 850 yr BP). Adapted from Hamilton and Shennan (2005a) Figure 11.

Chapter 2 : Figures & Tables

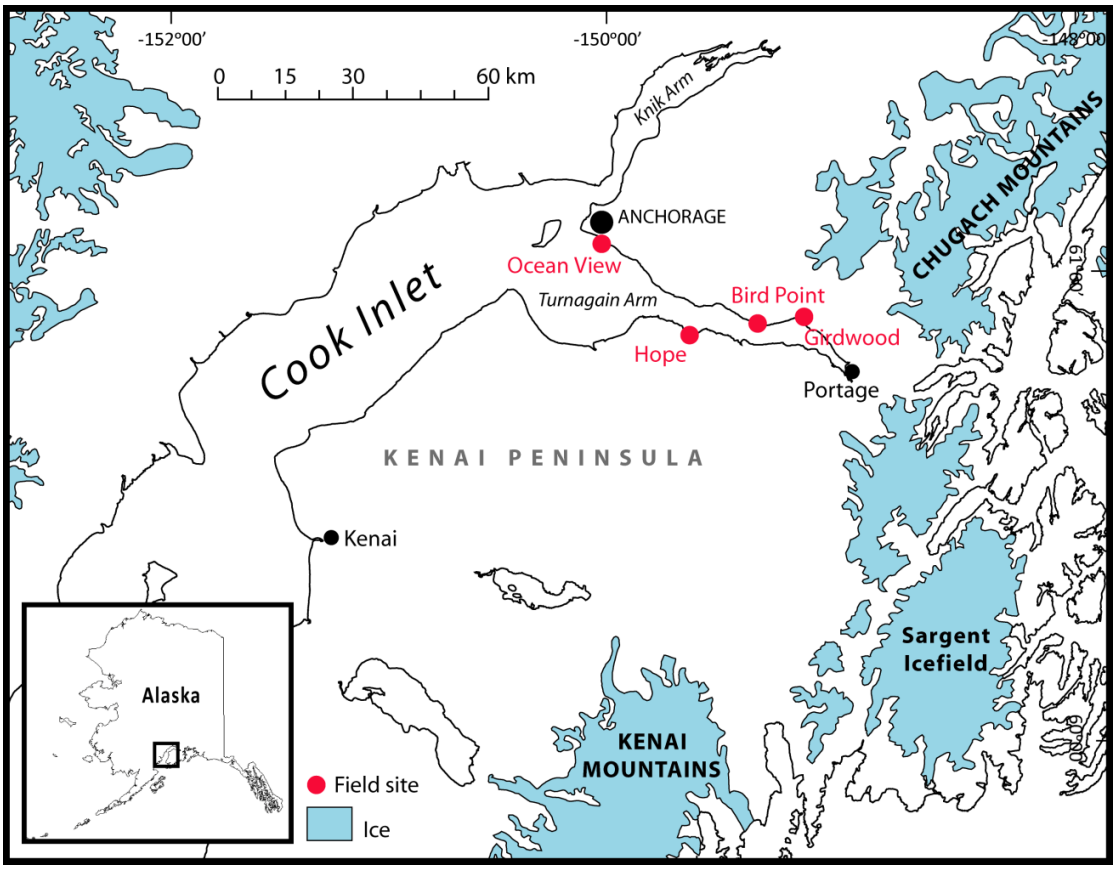

Figure 2.1 - Map of upper Cook Inlet and locations of field sites along Turnagain Arm (marked in red) and other key locations referenced in the text.

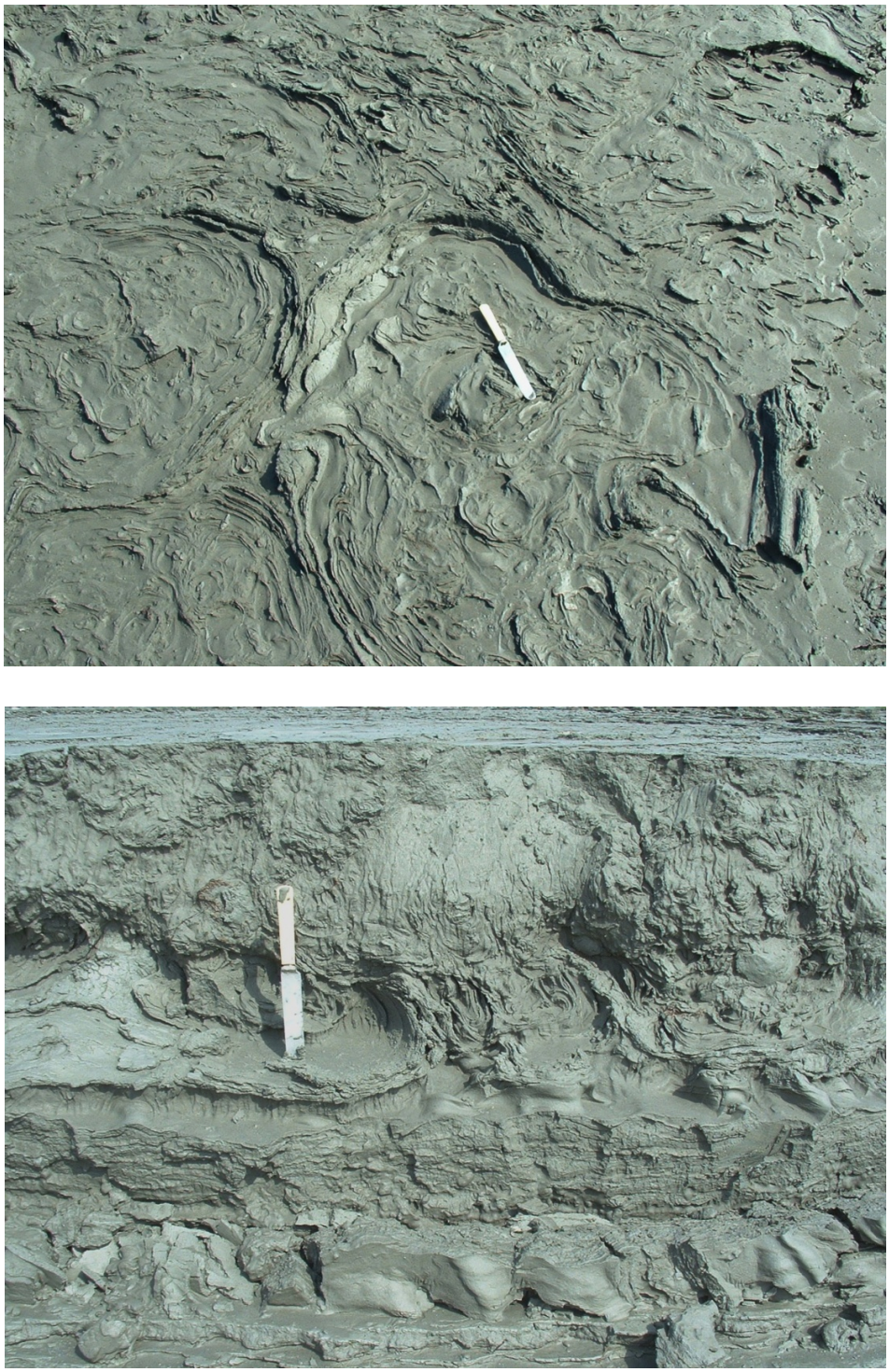

Figure 2.2 - Pictures of tidally deformed Turnagain Arm soft sediments. Top figure is a plan view of cyroturbated muds showing the roughly polygonal/circular structures of frost heave. Bottom figure shows an intercalated unit of frost heaved sediment within horizontally bedded sediments. (Images courtesy of Antony Long).

Figure 2.3 - Deposition of sea ice entrained with silt on frozen Girdwood marsh, April 2003. Photograph courtesy of Ian Shennan from Hamilton *et al.* (2005) Figure 8.

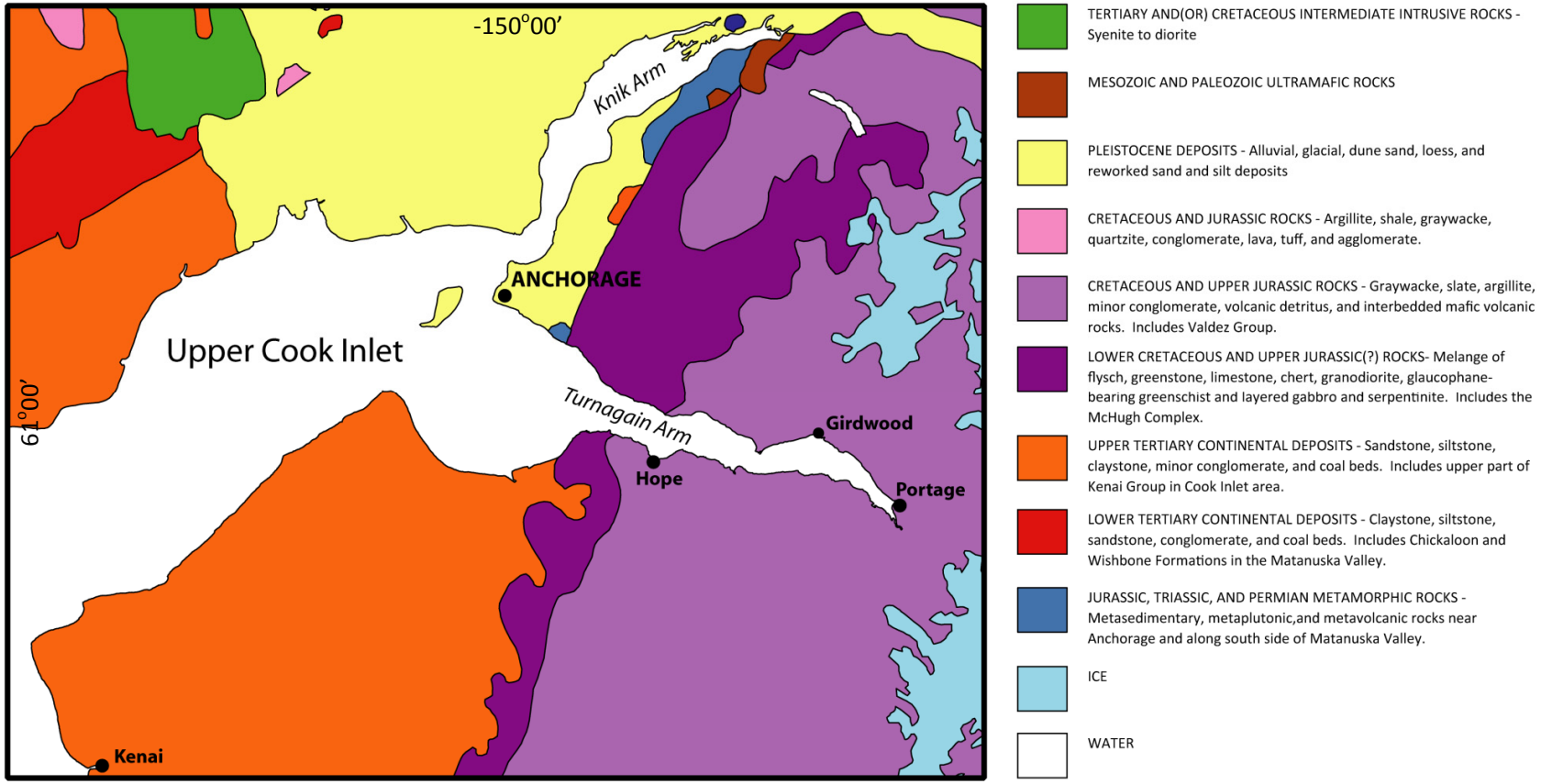

Figure 2.4 - Geologic map of Upper Cook Inlet. Map adapted from polygons and associated attribute data derived from the 1980 Geologic Map of Alaska (Beikman, 1980) published by the USGS (1997).

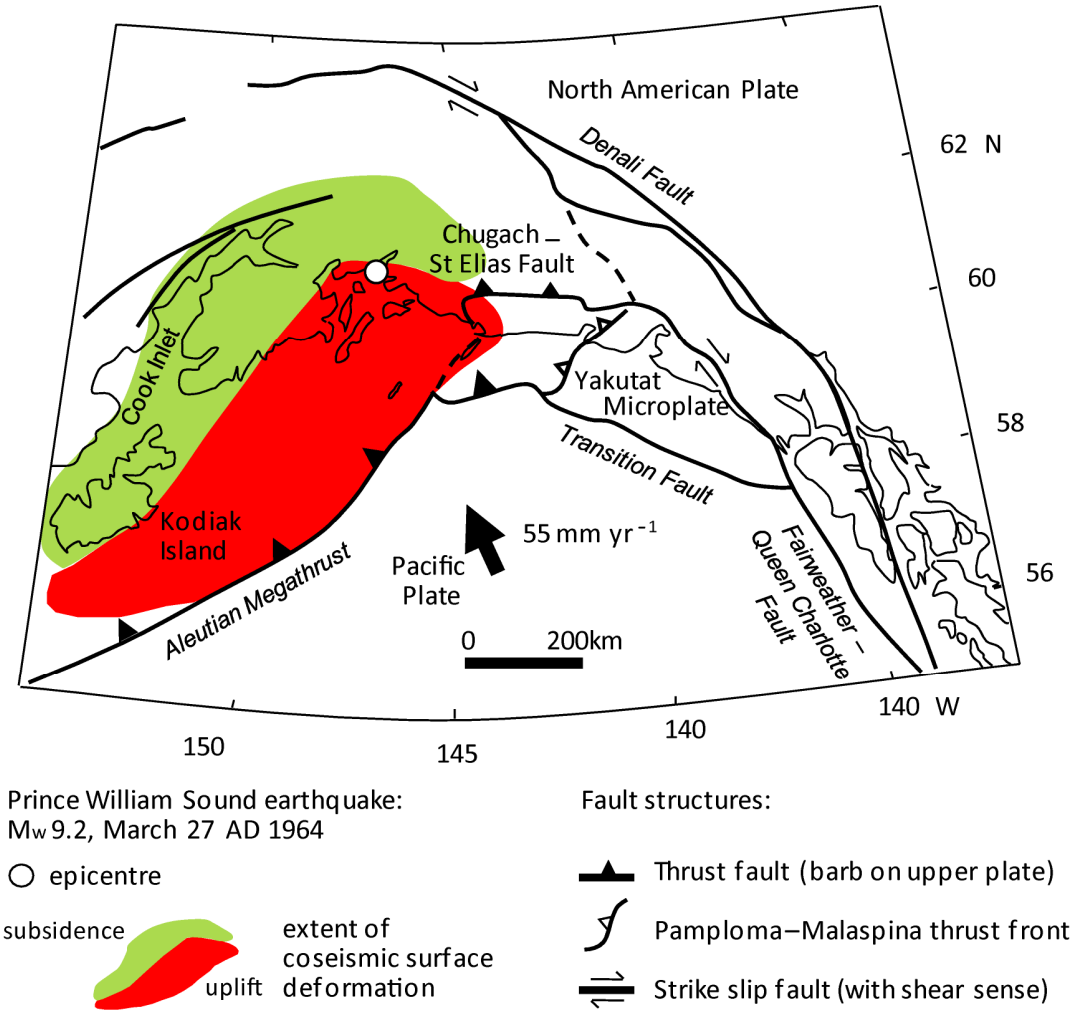

Figure 2.5 - Tectonic setting of south central Alaska showing the Aleutian Megathrust and non-subducted section of the Yakutat Microplate, as well as other major tectonic faults. Coloured segments mark extent of coseismic surface deformation during the AD 1964 earthquake. Adapted from Shennan 2009 Figure 1.

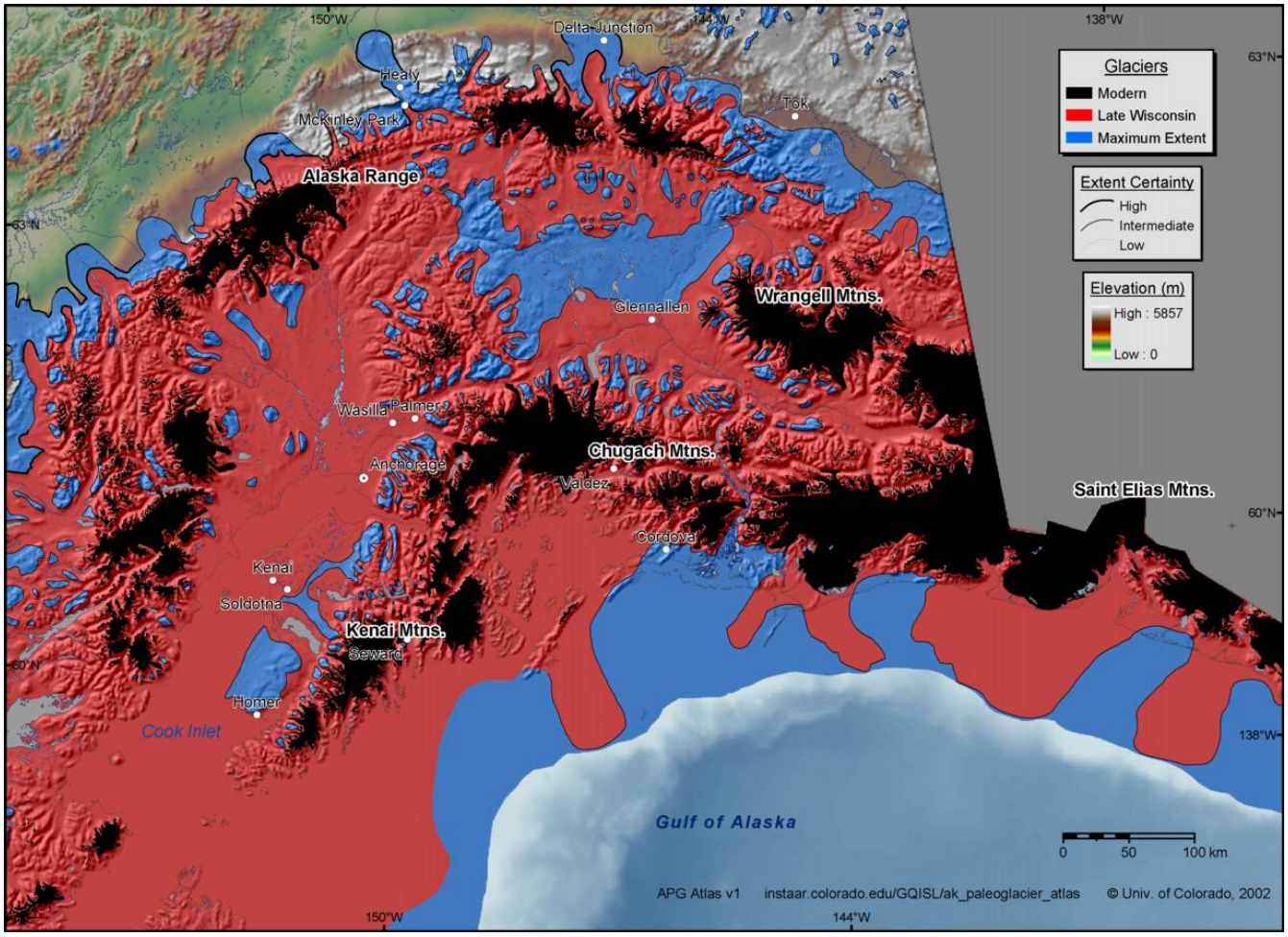

Figure 2.6 - Anchorage/south-central Alaska region of Alaska PaleoGlacier Atlas showing the maximum and Late Wisconsin extent of the western portion of the North American Cordilleran Ice Sheet and present day distribution of ice in south central Alaska (Manley and Kaufman, 2002).

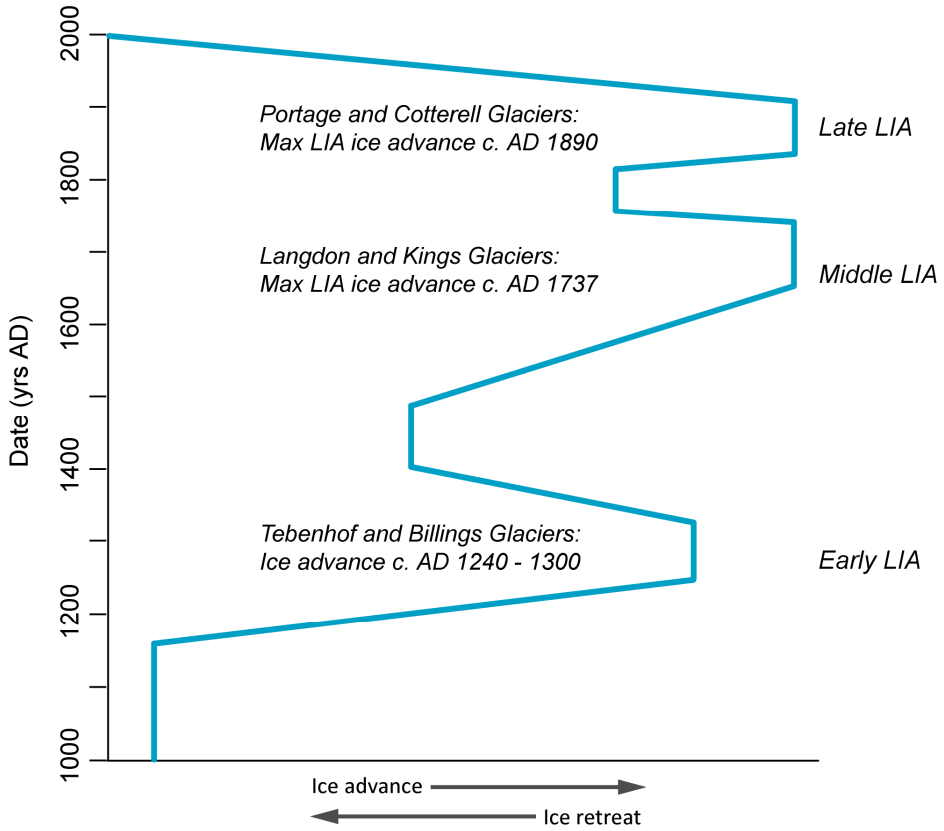

Figure 2.7 - LIA glaciation curve for mountain glaciers of western Chugach and northern Kenai Mountains. LIA ice advance and retreat shown in three phases. Dates from terminal moraines for selected glaciers demonstrate the timing of the three advance phases (Crossen, 1992; Wiles et al., 1999; Barclay et al., 2009).

Year AD	Total population	Native	Non-native	Military
1880[1]	33,426	32,996	430	-
1890[1]	32,052	25,354	4,298	-
1900[1]	63,592	29,542	30,450	-
1910[1]	64,356	25,331	36,400	-
1920[1]	55,036	26,558	28,228	250
1930[1]	59,278	29,983	29,045	250
1940[1]	72,524	32,458	39,566	500
1950[1]	128,643	33,863	74,373	20,407
1960[1]	226,167	43,081	150,394	32,692
1970[2]	302,583			
1980[2]	401,851			
1990[2]	550,043			
2000[2]	626,932			

Table 2.1: Total population of Alaska (with breakdown into Native, non-native and military where available) for each decade from AD 1880 to 2000. Information from 1: Naske and Slotnick (1987) Appendix F; 2: U.S. Census data (http://www.censusscope.org, 2009).

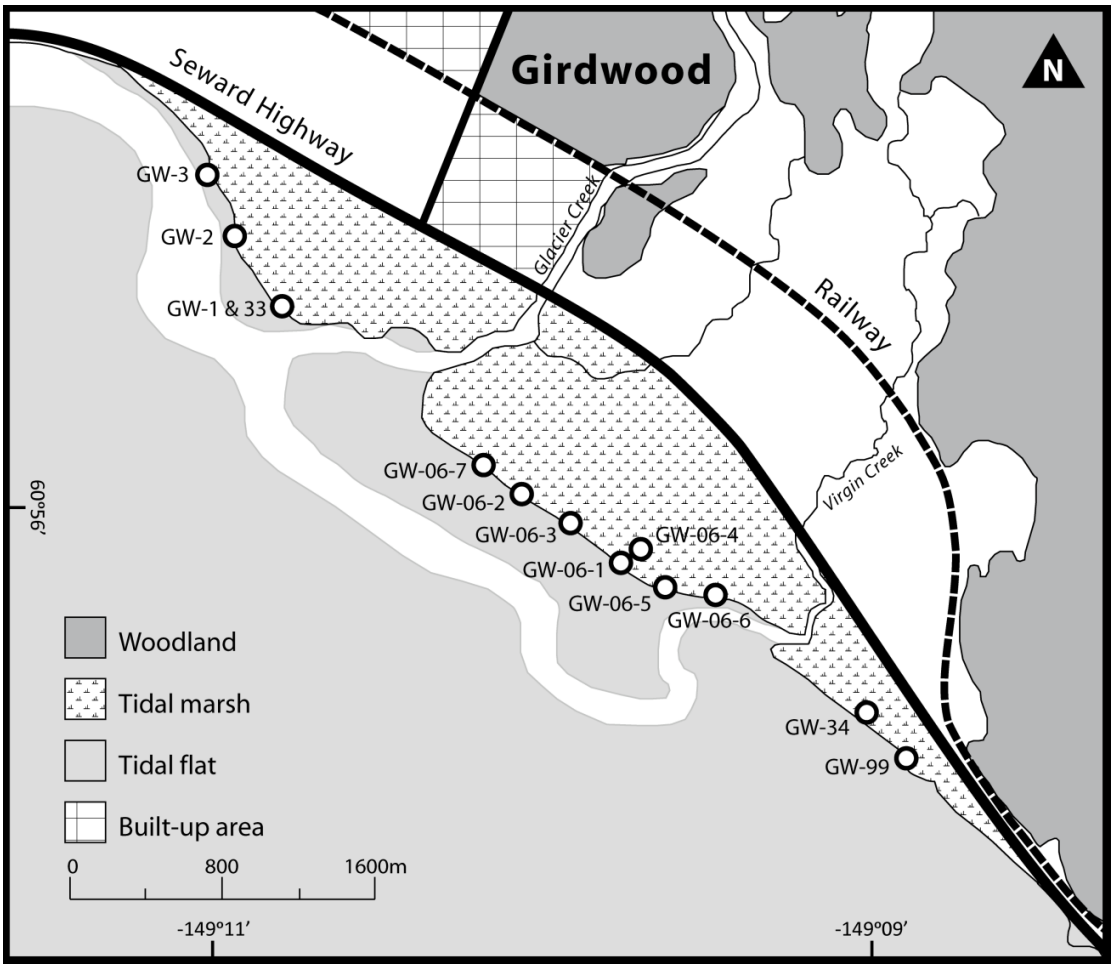

Figure 2.8 - Map of Girdwood field site showing location of previous coring as summarised in Shennan *et al.* (2008).

Figure 2.9 - Photographs of Girdwood marsh, showing (top photograph) small cliff along marsh front and (bottom photograph) ghost forest of trees which were submerged during the AD 1964 earthquake.

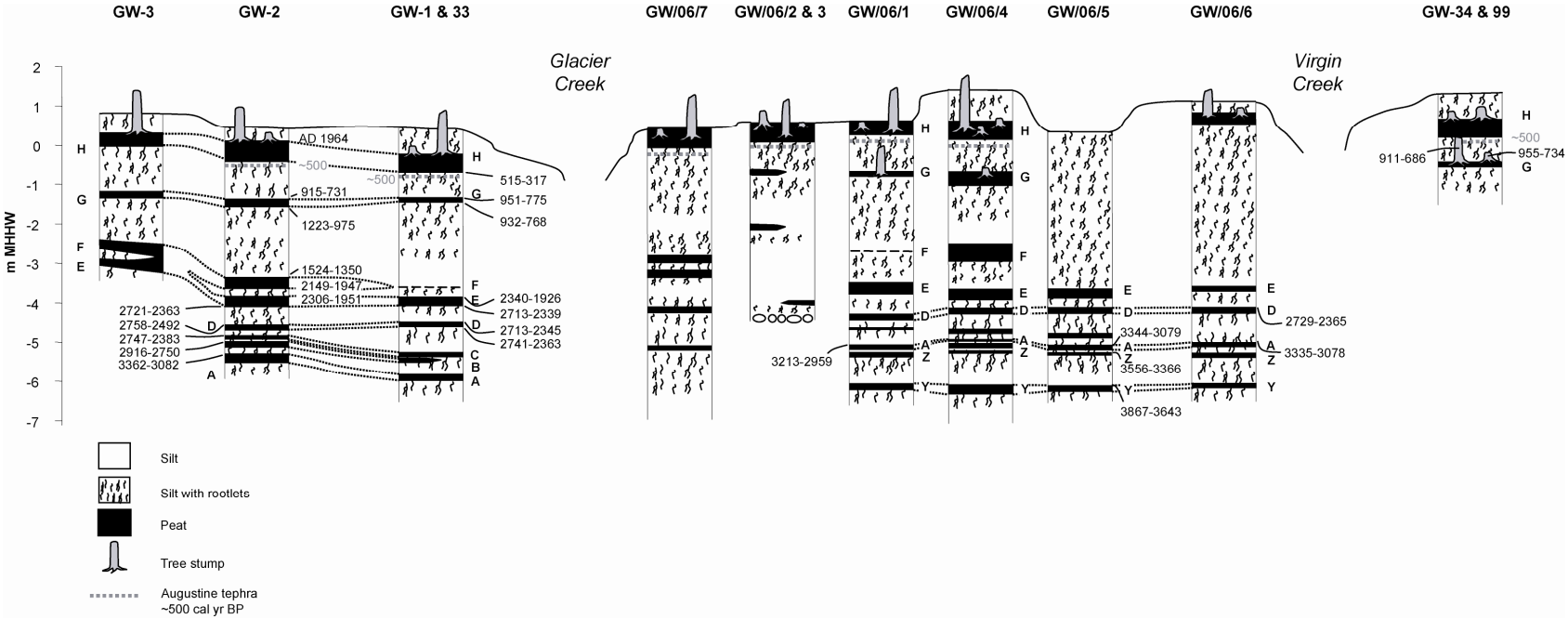

Figure 2.10 - Cross sections of cores previously sampled at Girdwood showing buried peat-silt couplets below the surface (from Shennan *et al.*, 2008 Figure 3). Peat H is the pre AD 1964 earthquake peat layer. Seven great earthquakes are recorded by the peat-silt couplets above peats H, G, F, E, D, A, Y.

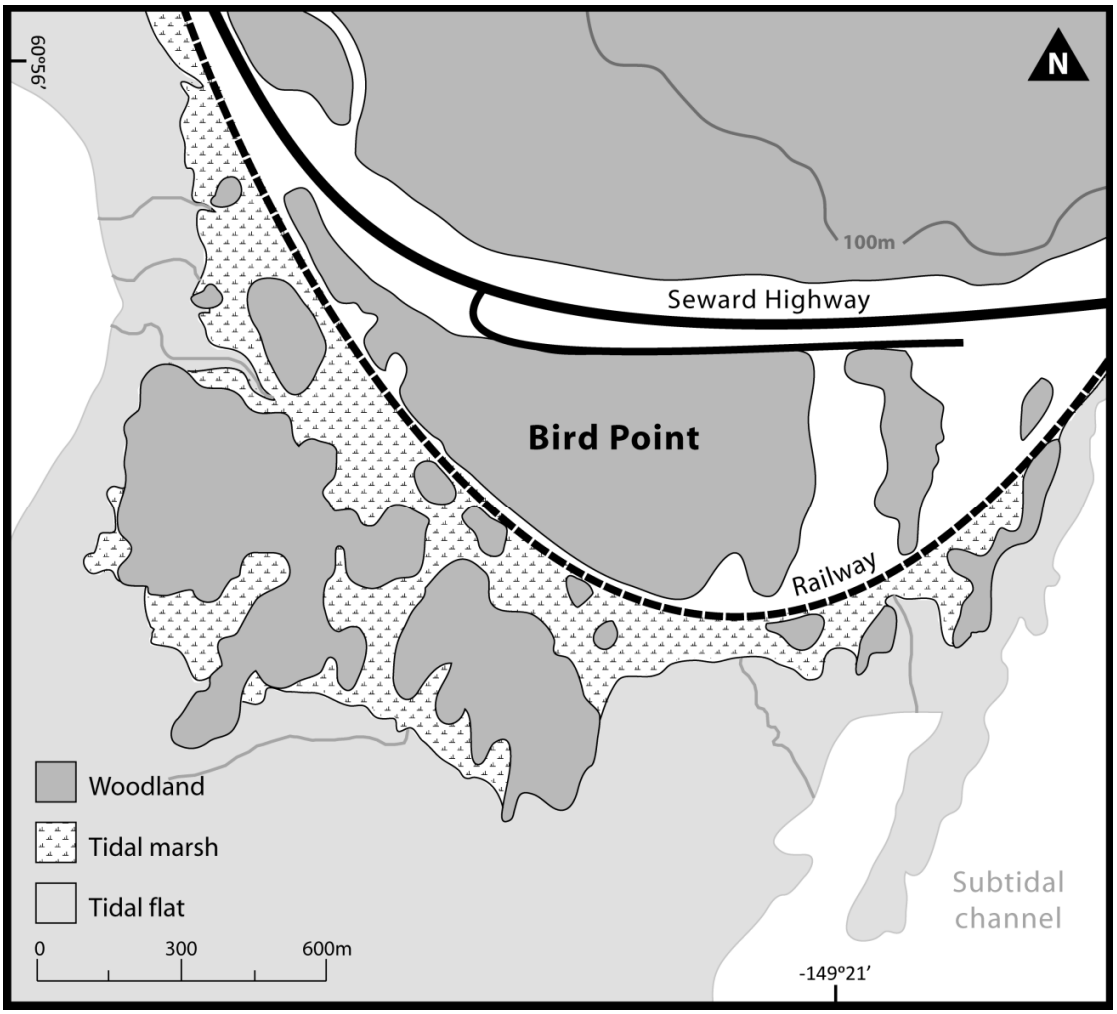

Figure 2.11 - Map of Bird Point field site.

Figure 2.12 - Photograph of western end of Bird Point marsh showing small marshes that form between bedrock outcrops and ghost forest of trees submerged during the AD 1964 earthquake.

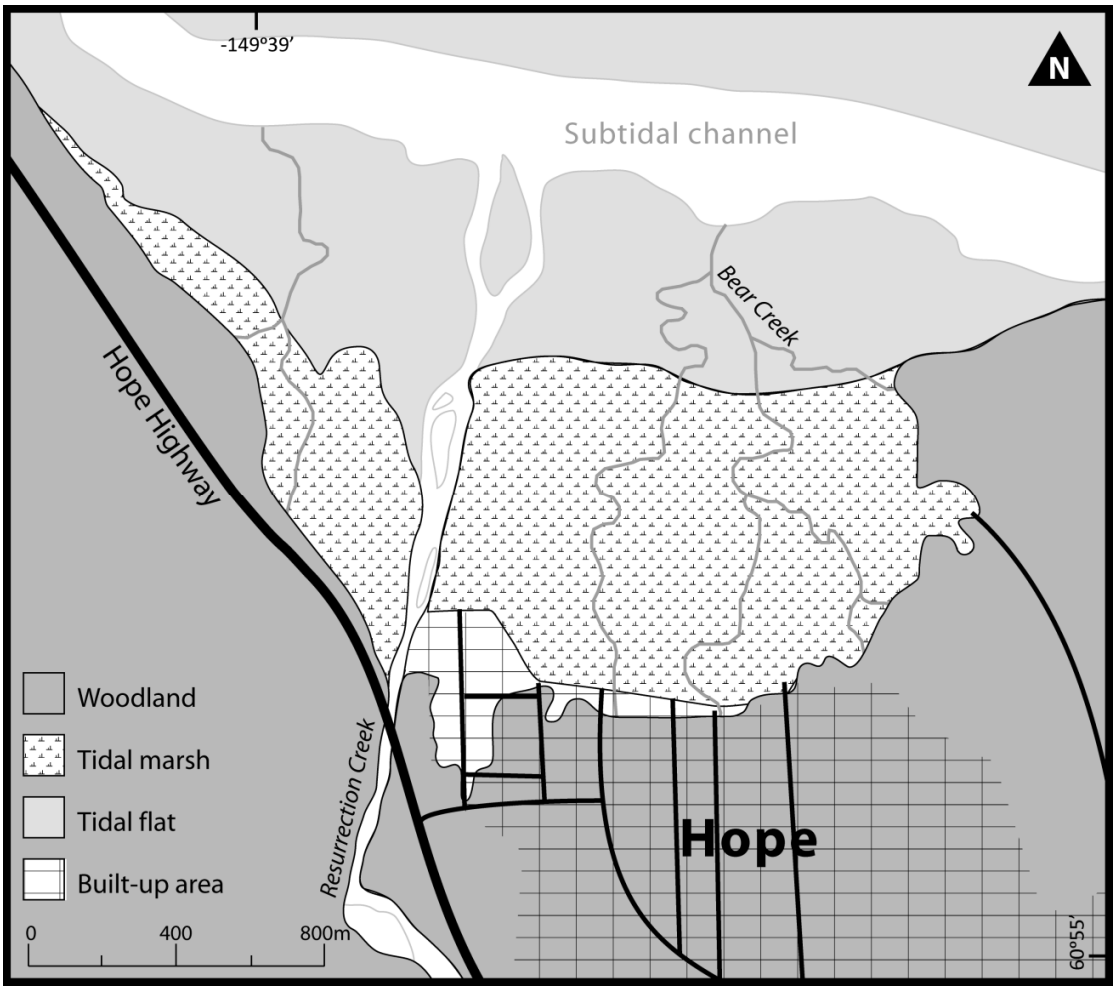

Figure 2.13 - Map of Hope field site.

Figure 2.14 - Photograph of western end of Hope marsh seaward of the steep bluff, looking west towards the small ghost forest. Areas of the marsh front have a small cliff, similar to Girdwood marsh (Figure 2.9).

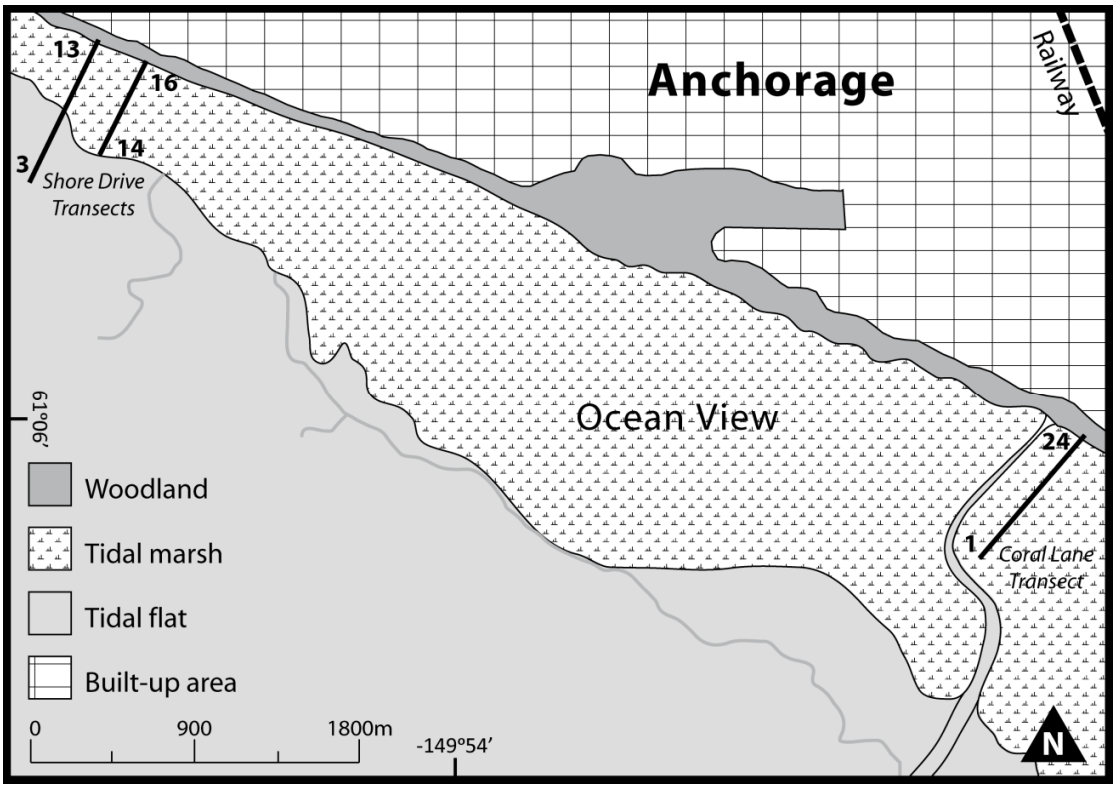

Figure 2.15 - Map of Ocean View field site showing location of Hamilton et al. (2005) transects shown in Figure 2.17.

Figure 2.16 - Photographs of Ocean View marsh showing (top photograph) ghost forest of trees submerged during the AD 1964 earthquake that divides the existing Coral Lane transect from the seaward part of the marsh (bottom photograph) which is the location of the new transect in this thesis (Figure 3.4).

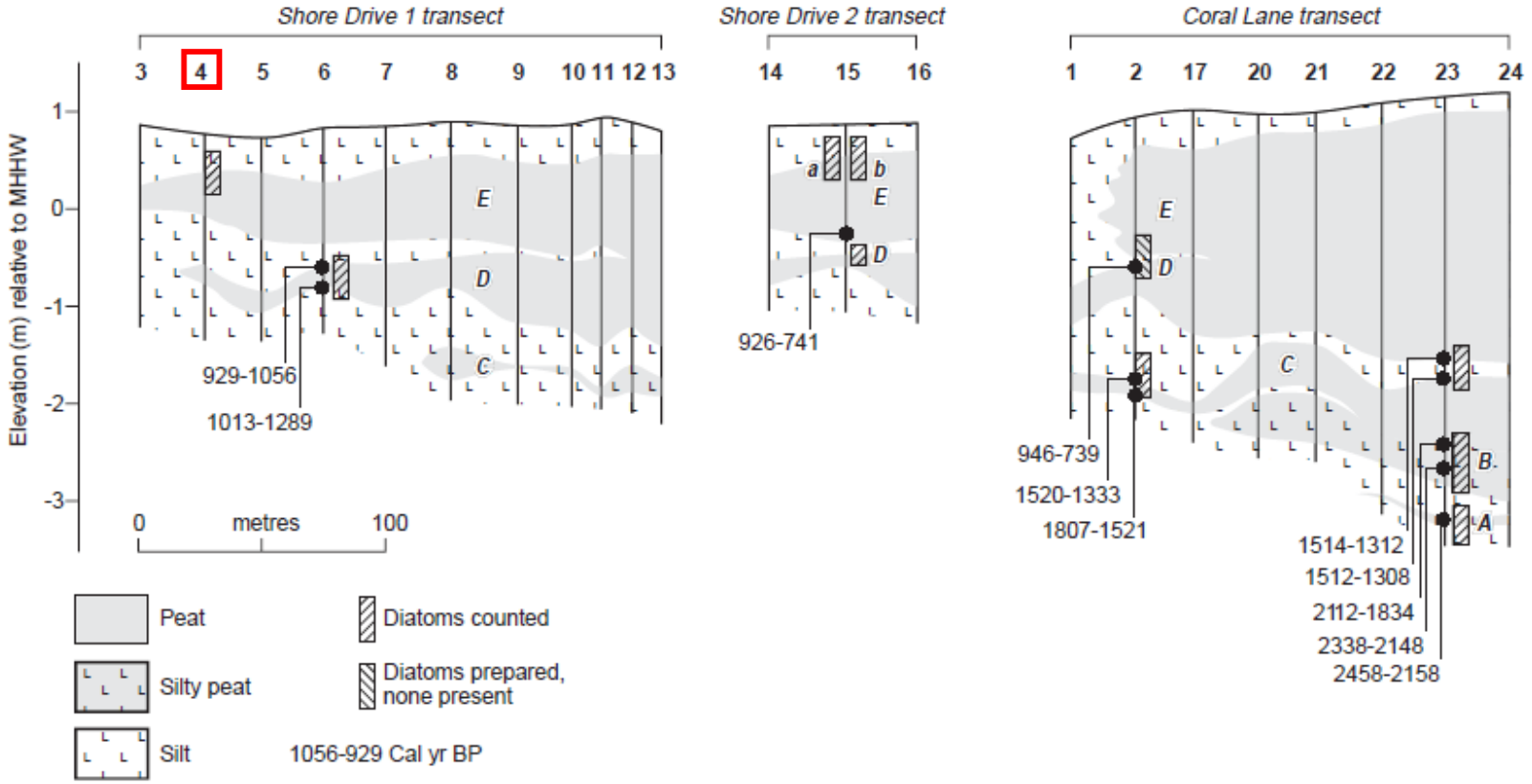

Figure 2.17 - Cross sections of transects in Figure 2.15 cored by Hamilton *et al.* (2005) at Ocean View, recording up to five peat-silt couplets. Peat E is the pre-1964 earthquake peat layer. Core OV-02-4, used later in this thesis (Chapter 4), is core 4 on Shore Drive 1 transect, marked in red. (Source: Hamilton *et al.*, 2005 Figure 2).

Chapter 3 : Figures & Tables

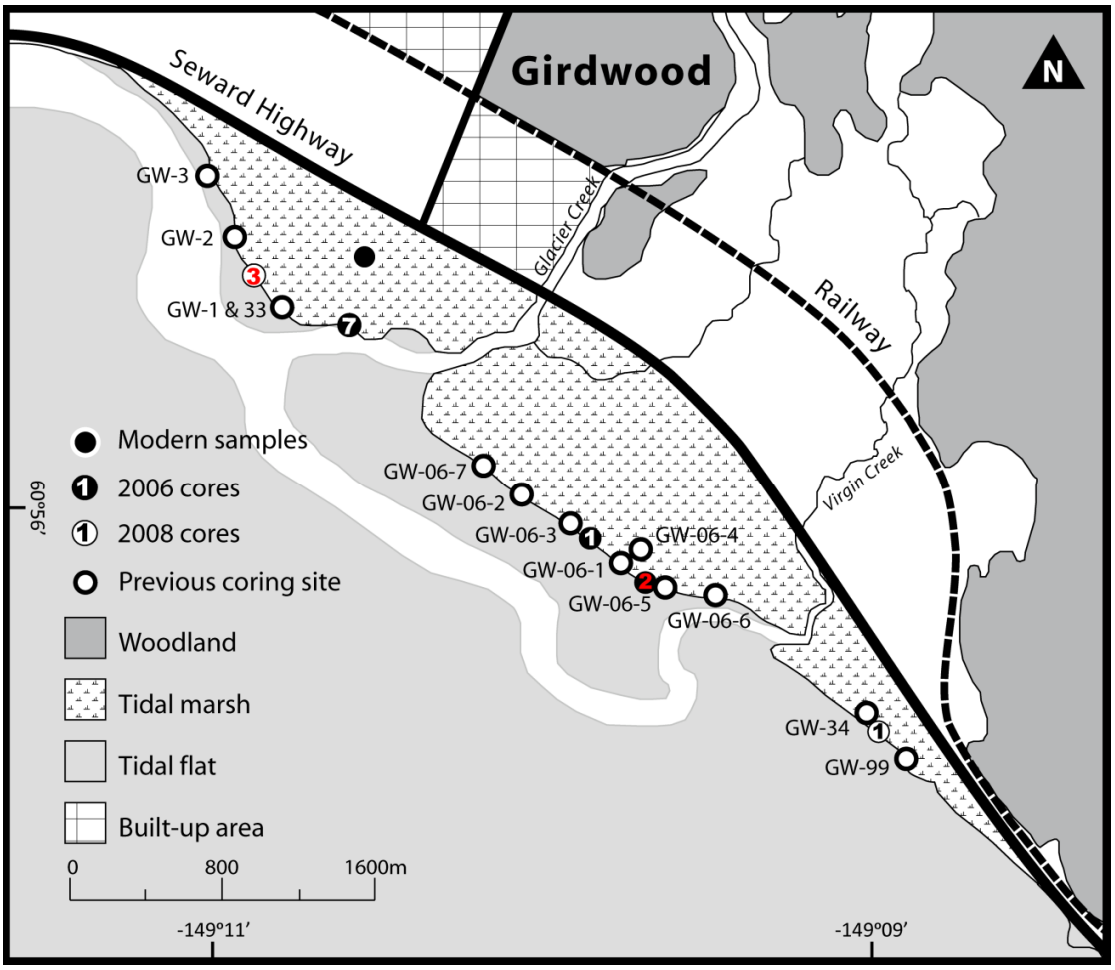

Figure 3.1 - Map of Girdwood showing location of new cores for this thesis. Note not all cores shown as replicates of previous cores. All numbers match numbers in Figure 4.6. Cores used in analysis highlighted with red numbers.

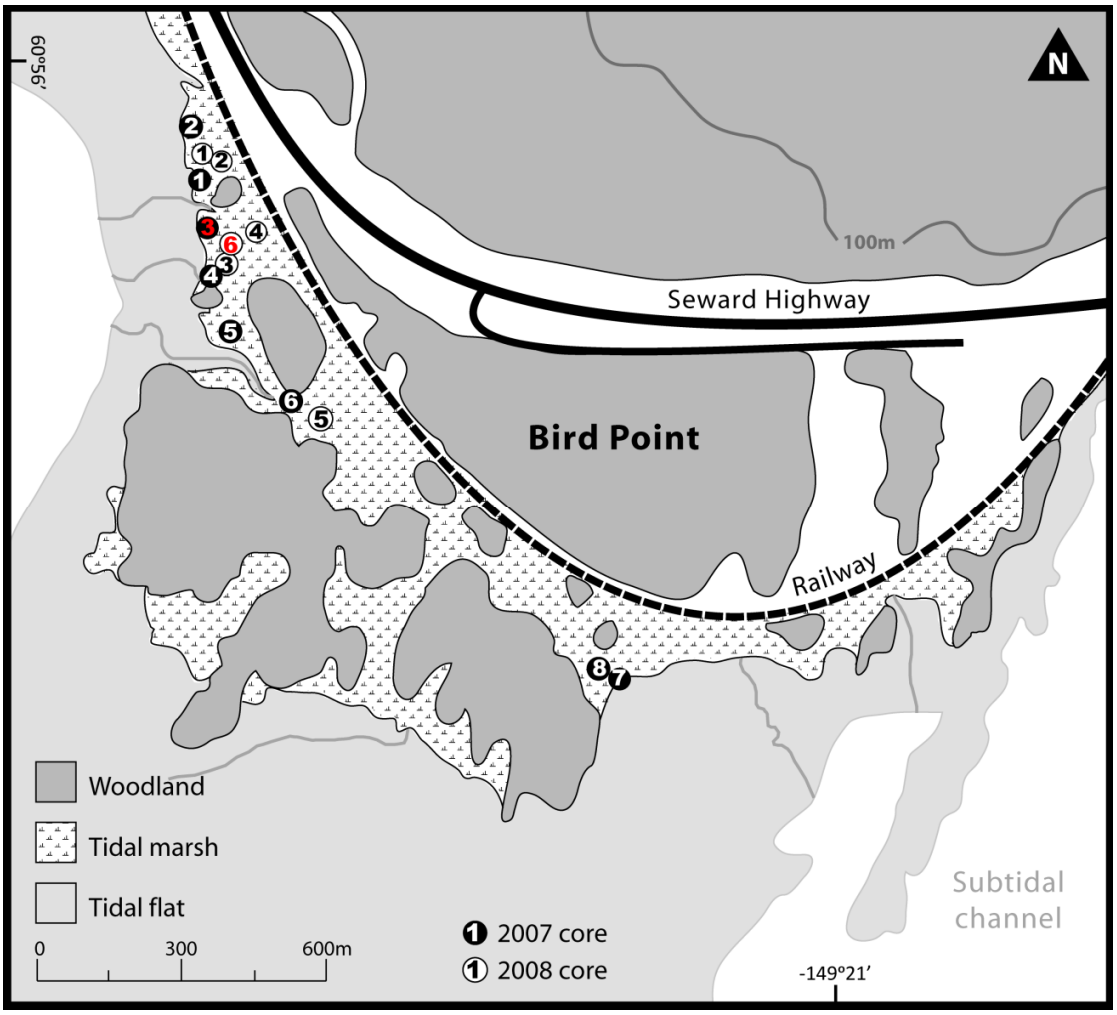

Figure 3.2 - Map of Bird Point showing location of new cores for this thesis. Cores used in analysis highlighted with red numbers.

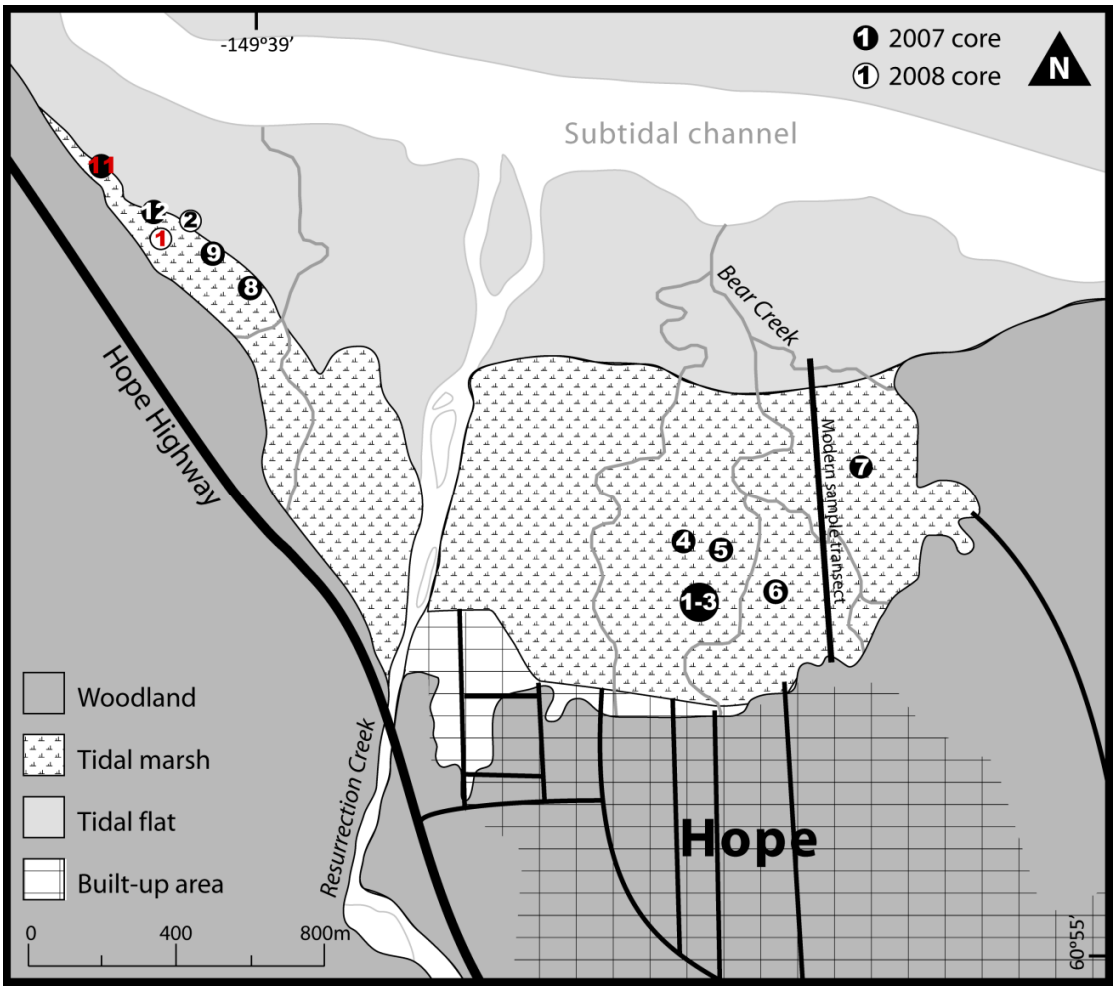

Figure 3.3 - Map of Hope showing location of new cores for this thesis. Gravels and rocks prevent coring deeper than 0.5m on much of the marsh east of Resurrection Creek, with cores predominately recording silt. These cores are not shown in the lithology diagram in Figure 4.21 (full details of the stratigraphy can be found in Appendix 1_3). Cores used in analysis highlighted with red numbers

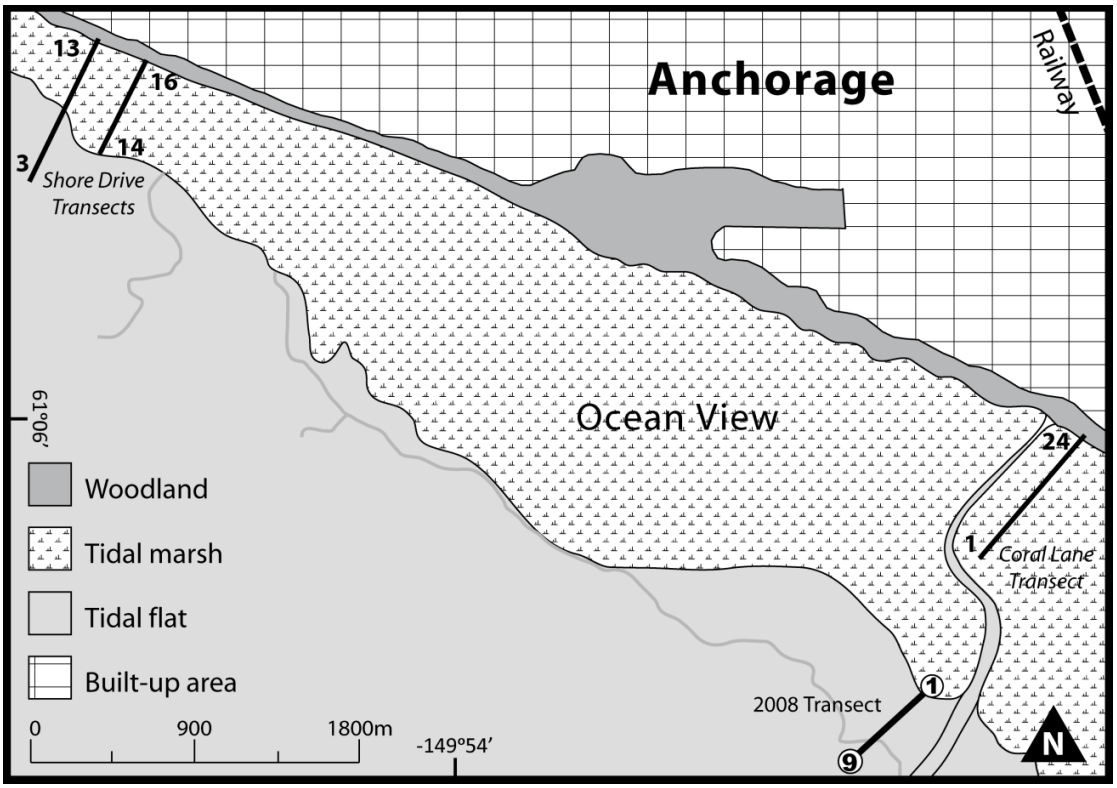

Figure 3.4 - Map of Ocean View showing location of new cores along the 2008 transect for this thesis, with additional transects reported by Hamilton *et al.* (2005) and in Figure 2.17. A large expanse of submerged ghost forest occurs between the two Coral Lane Transects.

Classification	Salinity range (‰)	Description
Polyhalobous	> 30	Marine
Mesohalobous	0.2 to 30	Brackish
Oligohalobous-halophile	< 0.2	Freshwater (stimulated at low salinity)
Oligohalobous-indifferent	< 0.2	Freshwater (tolerates low salinity)
Halophobous	0	Salt-intolerant

Table 3.1: The halobian classification scheme after Hemphill-Haley (1993).

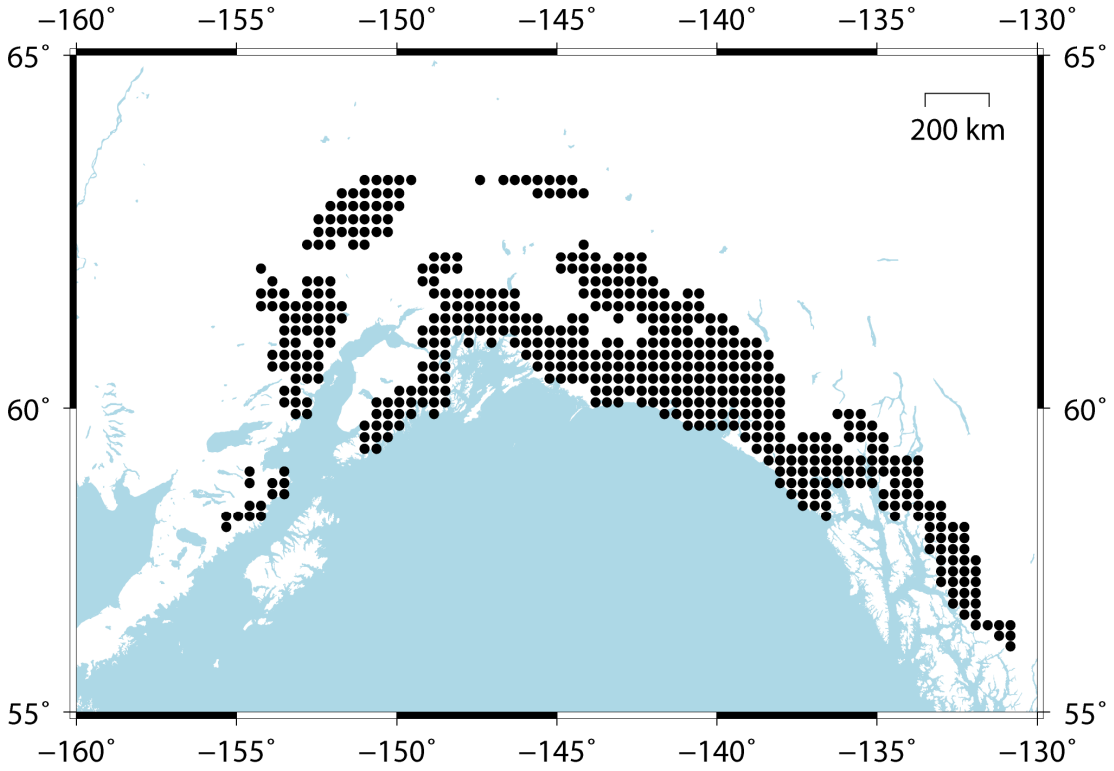

Figure 3.5 - Map of 531 spherical symmetrical disks that make the regional Alaska ice model (Larsen *et al.*, 2004; 2005). Each disk has a 20 km diameter and a 20-step time interval load history for the past 2000 years.

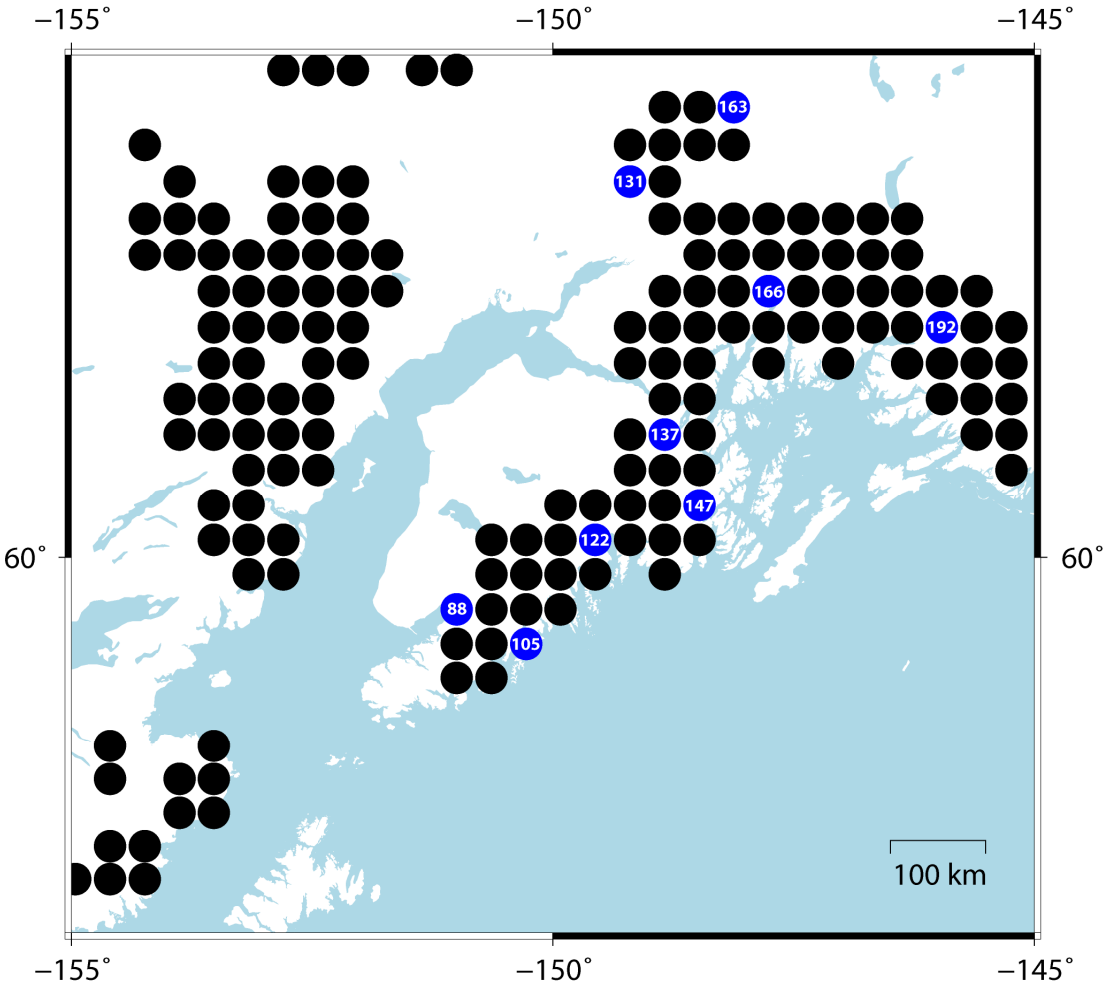

Figure 3.6 - Close up map of the regional ice model disks representing the ice covered areas of south central Alaska. The ice history of the disks highlighted in blue, as defined by the model, are shown in Figure 3.3.

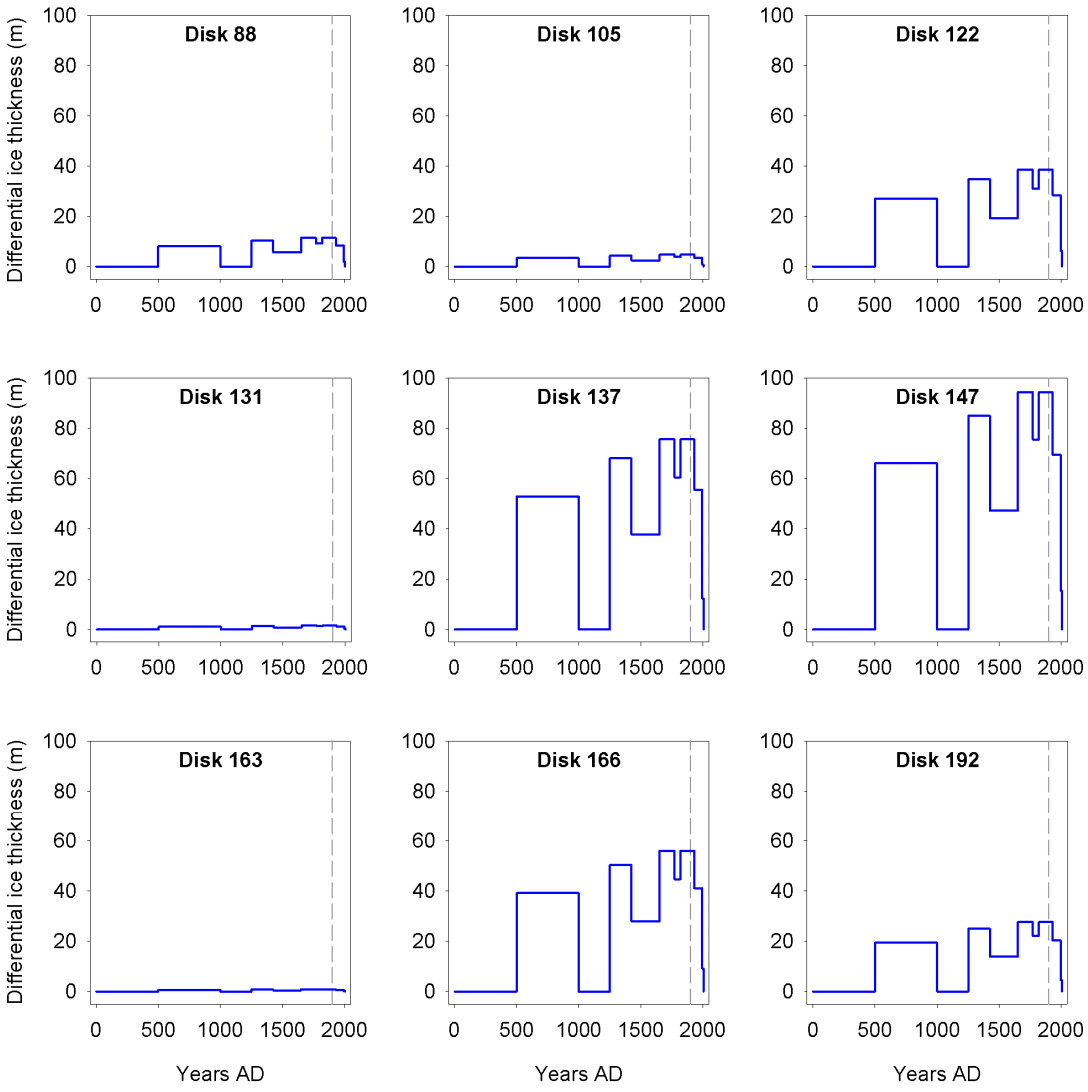

Figure 3.7 - Ice load history for 9 disks from the south central Alaska sector of the Larsen regional ice model (disk locations highlighted in Figure 3.2) to show modelled spatial ice load differences. Differential ice thickness is defined as relative to present ice mass being zero. A piecewise linear history allows for the various glacier fluctuations over the Neoglacial as defined by numerous glaciological records (e.g. Crossen, 1992; Wiles and Calkin, 1994; Crossen, 1997; Calkin et al., 2001; Barclay et al., 2003; Molnia, 2008; Wiles et al., 2008). A 20 step time interval over the past 2000 years provides the required resolution for the dynamic nature of the Alaskan mountain glaciers. Four main peaks in each model (e.g. disk 147) represents the early Neoglacial advance AD500-100, followed by the three phases of the LIA. Grey dashed line marks culmination of the LIA at AD 1900.

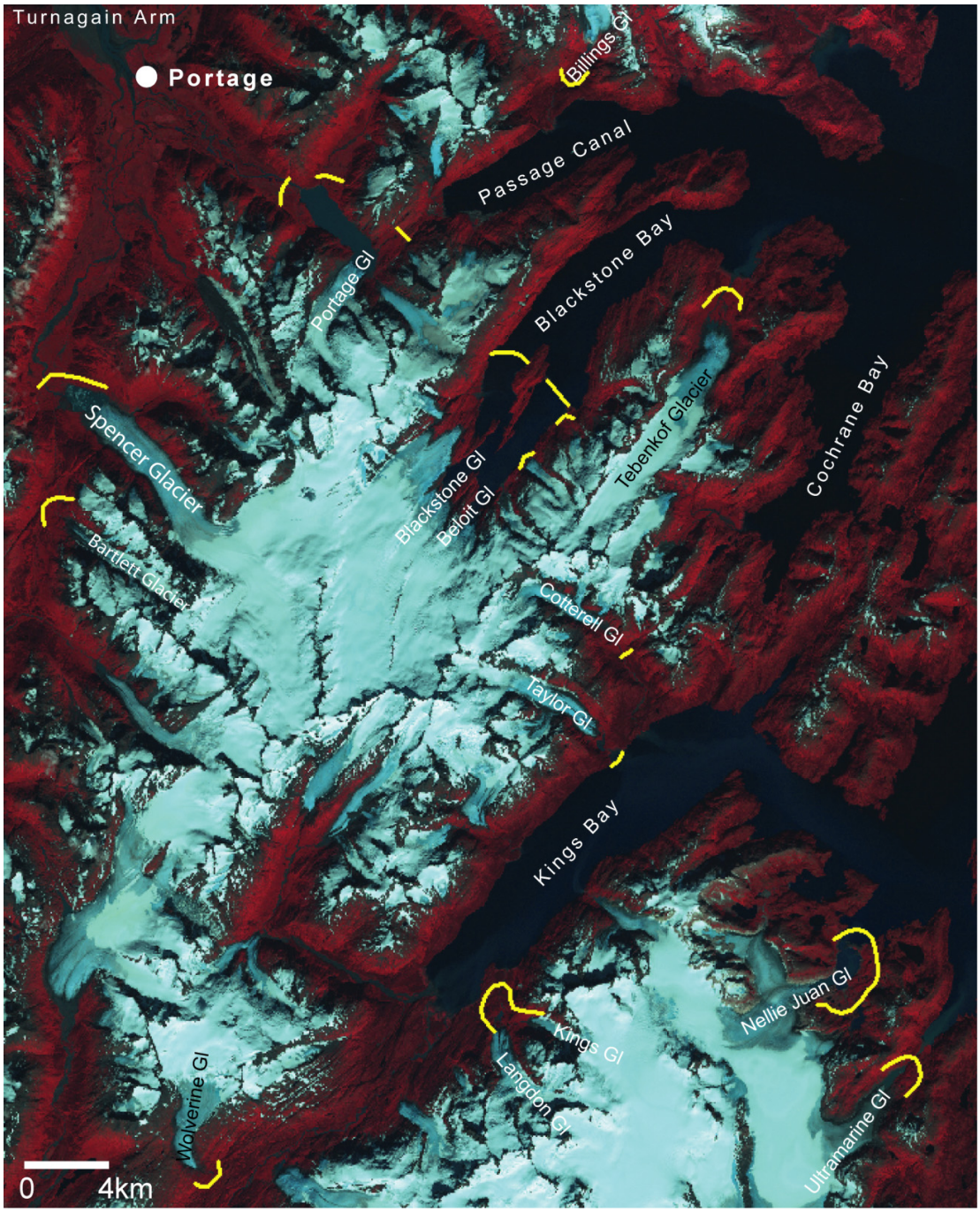

Figure 3.8 - Landsat false colour image of Blackstone-Spencer ice complex and northern sector of the Sargent icefield with Holocene terminal moraine positions marked where known (Crossen, 1992; Wiles and Calkin, 1994; 1997). All terminal moraines formed during the final two phases of the LIA, corroborating with the load history defined in the ice model (for example Figure 3.3). The area of this image is represented by approximately 8 disks in the regional ice model (Figure 3.1 and 3.2).

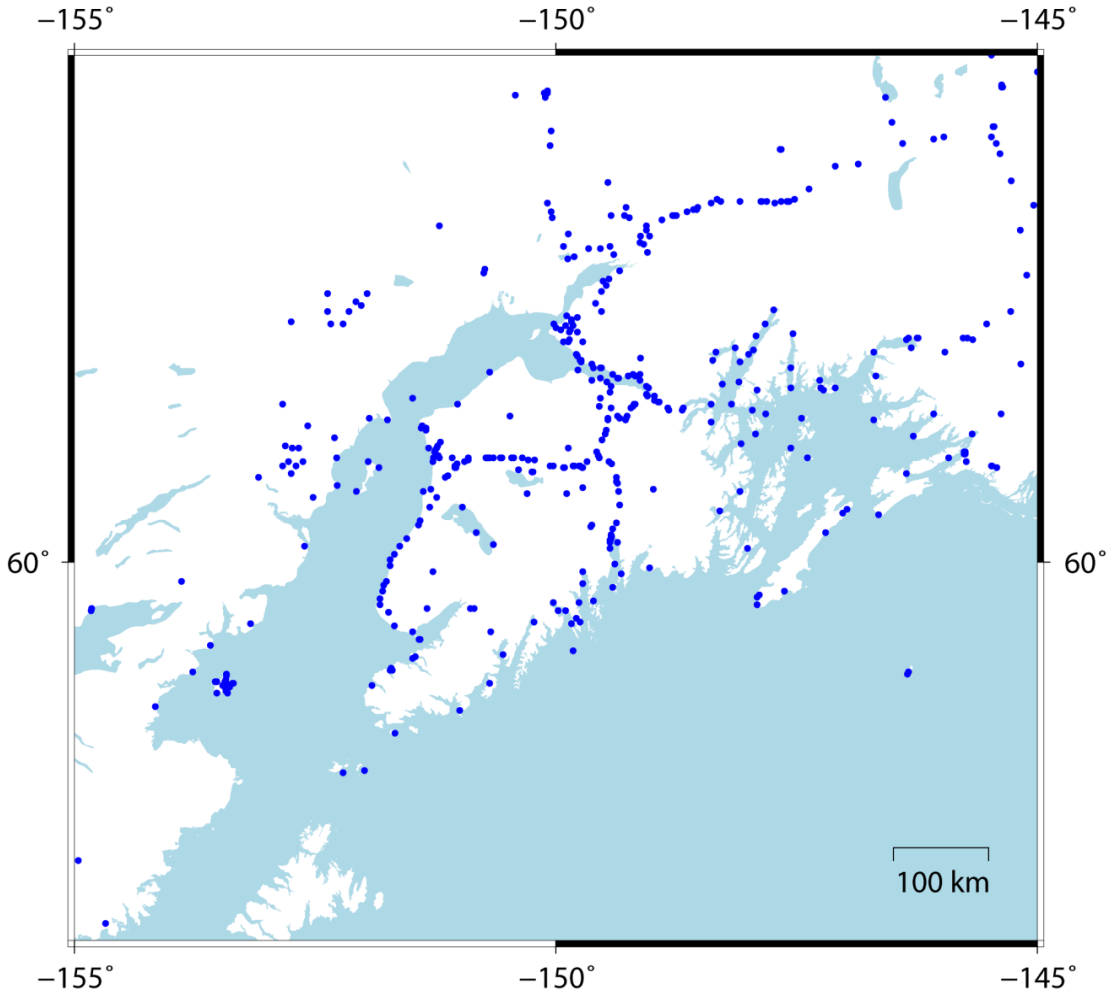

Figure 3.9 - Map of the south central Alaska portion of the 1198 observer locations that TABOO calculates geophysical response to the ice load model.

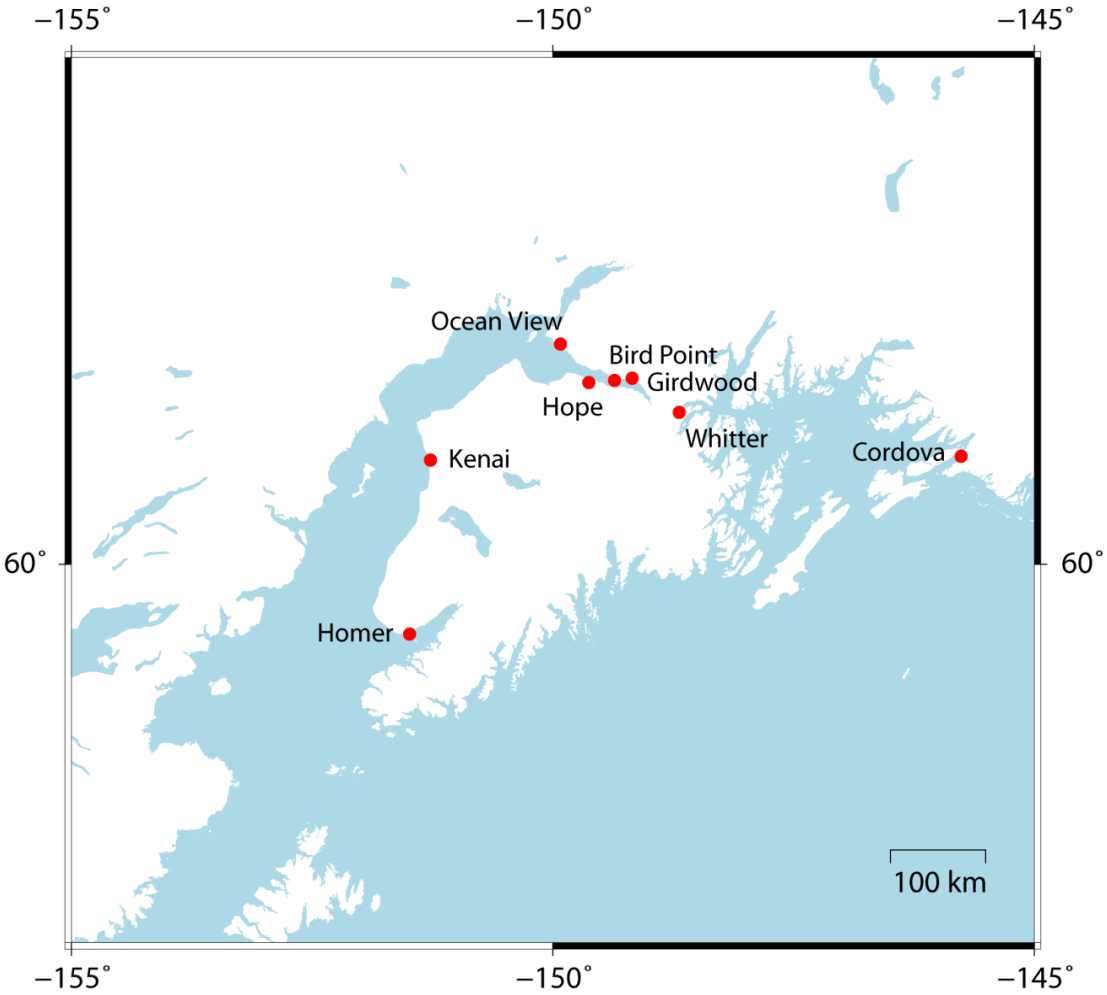

Figure 3.10 - Map of the eight selected model locations to test the TABOO model outputs.

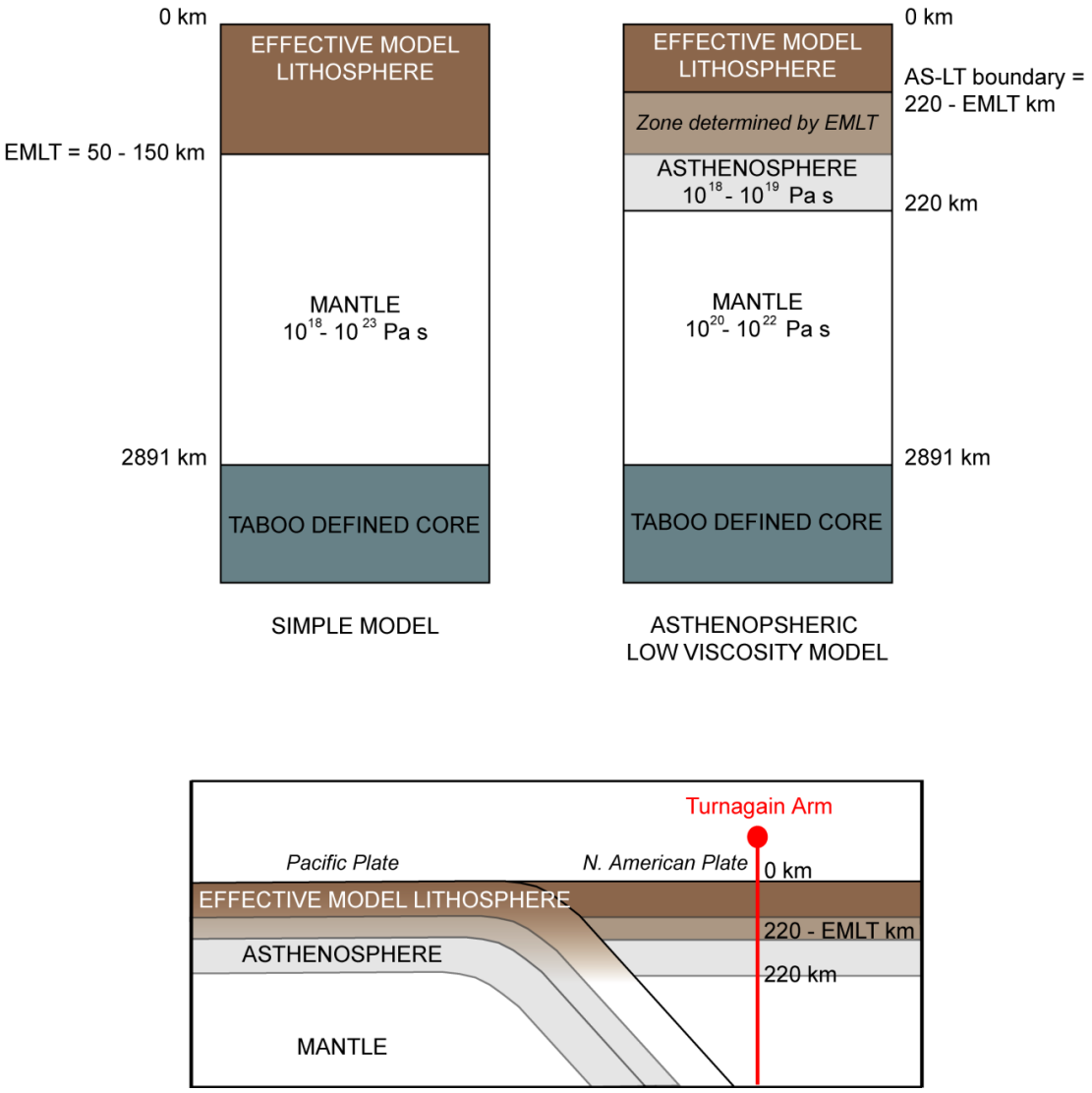

Figure 3.11 - Schematic of two earth models in TABOO developed to test earth response to changes in ice load in southern Alaska over the past earthquake cycle. The simple model follows the models of James at al. (2000) with a single viscous layer. The asthenospheric low viscosity zone model (ALVZ) model includes a low viscosity asthenosphere whose thickness is controlled by the lithospheric thickness. TABOO cannot accommodate the subducting Pacific slab in the model.

Chapter 4 : Figures & Tables

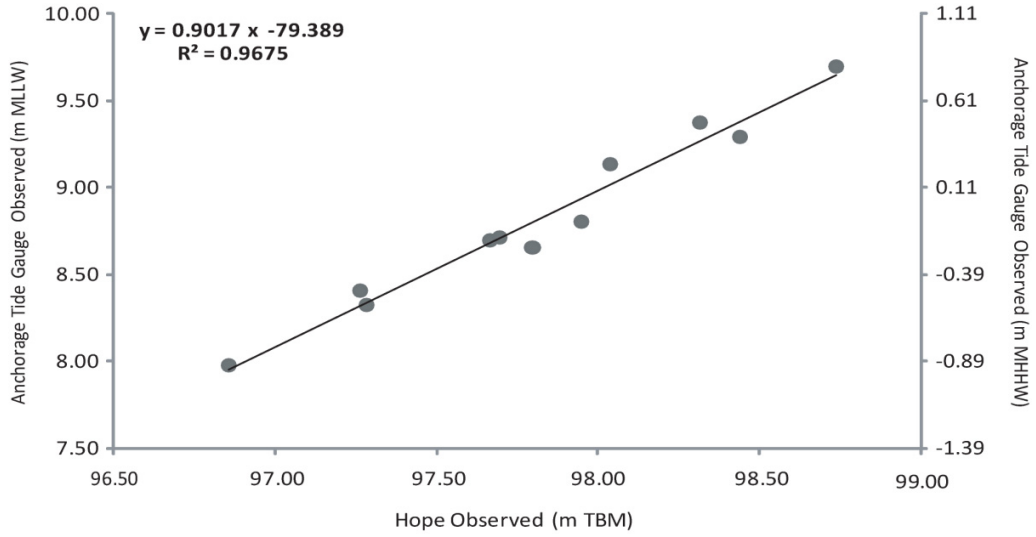

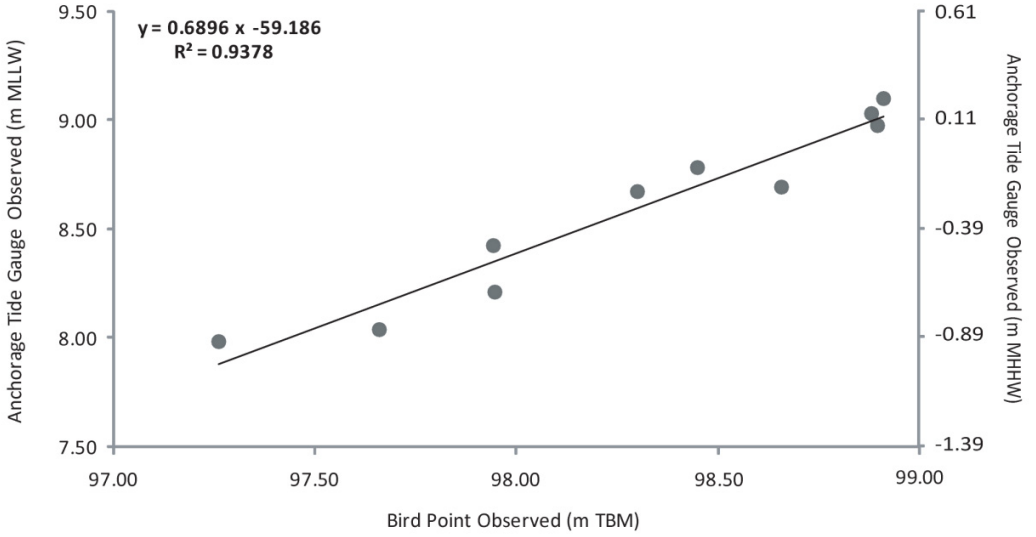

Datum	Height at Anchorage (m) relative to MLLW
Mean Higher-High Water (MHHW)	8.89
Mean Sea Level (MSL)	5.02
Mean Lower-Low Water (MLLW)	0.00

Figure 4.1 - Tidal observations at Hope and Bird Point (relative to a temporary benchmark (TBM) established on marsh) compared to validated tide gauge data at Anchorage (www.co-ops.nos.noaa.gov). Tide gauge observations for specific days at Bird Point and Hope relative to verified MLLW tide data at Anchorage allow calculation of the MHHW at Hope and Bird Point using the best fit regression equation show in each graph. Table gives tidal datum (m, relative to MLLW) at the Anchorage tide gauge.

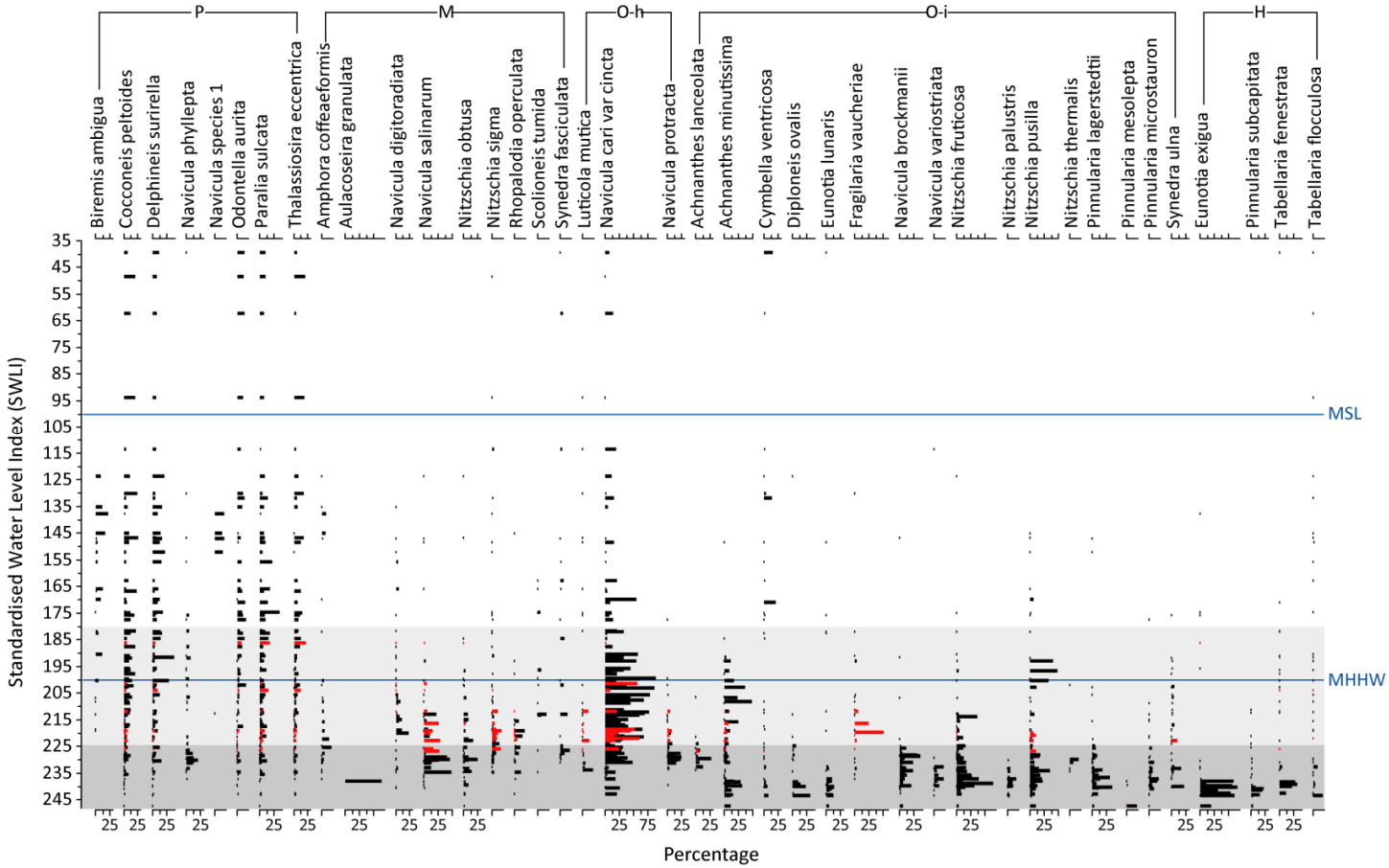

Figure 4.2 - Contemporary diatom samples (for species >15% total diatom valves counted) ordered by elevation (standardised water level index). Samples in black from Hamilton and Shennan (2005a) Upper Cook Inlet contemporary diatom database; samples in red are 16 new samples added for this thesis. Those samples in the grey box form the 'silt with rootlets SWLI > 180' transfer function, with those samples in the darker grey box forming the 'peat SWLI >225' transfer function (Hamilton and Shennan, 2005a). Mean sea level (MSL) = standardised water level index 100; mean high higher water = standardised water level index 200.

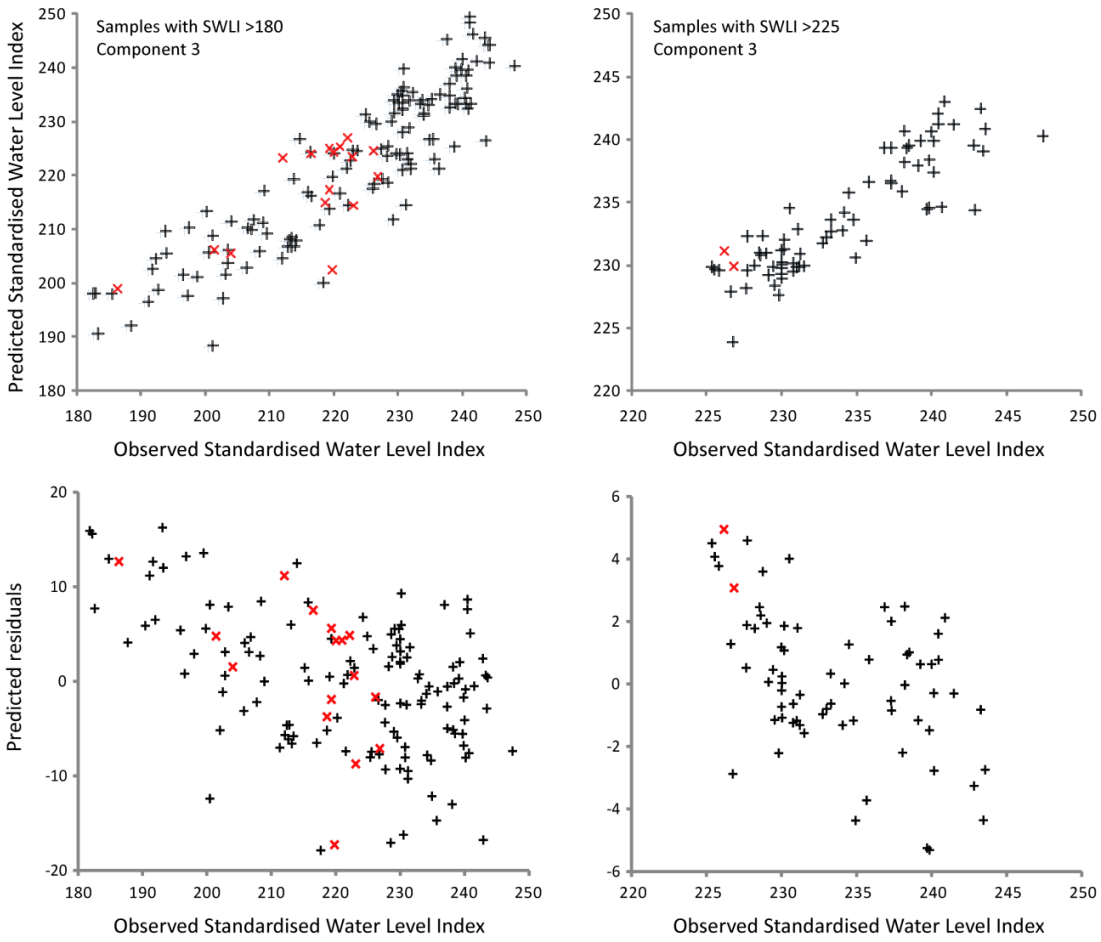

	Hamilton and Shennan (2005a) Upper Cook Inlet dataset *(154 samples)*		New Upper Cook Inlet dataset *(170 samples)*	
	Samples with SWLI >180 *(149 samples)*	**Samples with SWLI >225** *(78 samples)*	**Samples with SWLI >180** *(149 samples)*	**Samples with SWLI >225** *(78 samples)*
r^2	0.89	0.93	0.89	0.93
Boot r^2	0.81	0.77	0.79	0.77
RMSEP	7.79	2.90	7.78	2.95

Figure 4.3 - New upper Cook Inlet transfer function model regression, residuals and table of associated model performance for the two restricted sample transfer functions: the silt with rootlets (SWLI >180) and peat (SWLI >225) models (see Chapter 3 for details). The transfer function models use transfer function component 3 in C2 (Juggins, 2003). Hamilton and Shennan (2005a) upper Cook Inlet contemporary samples in black, new contemporary samples for this thesis in red.

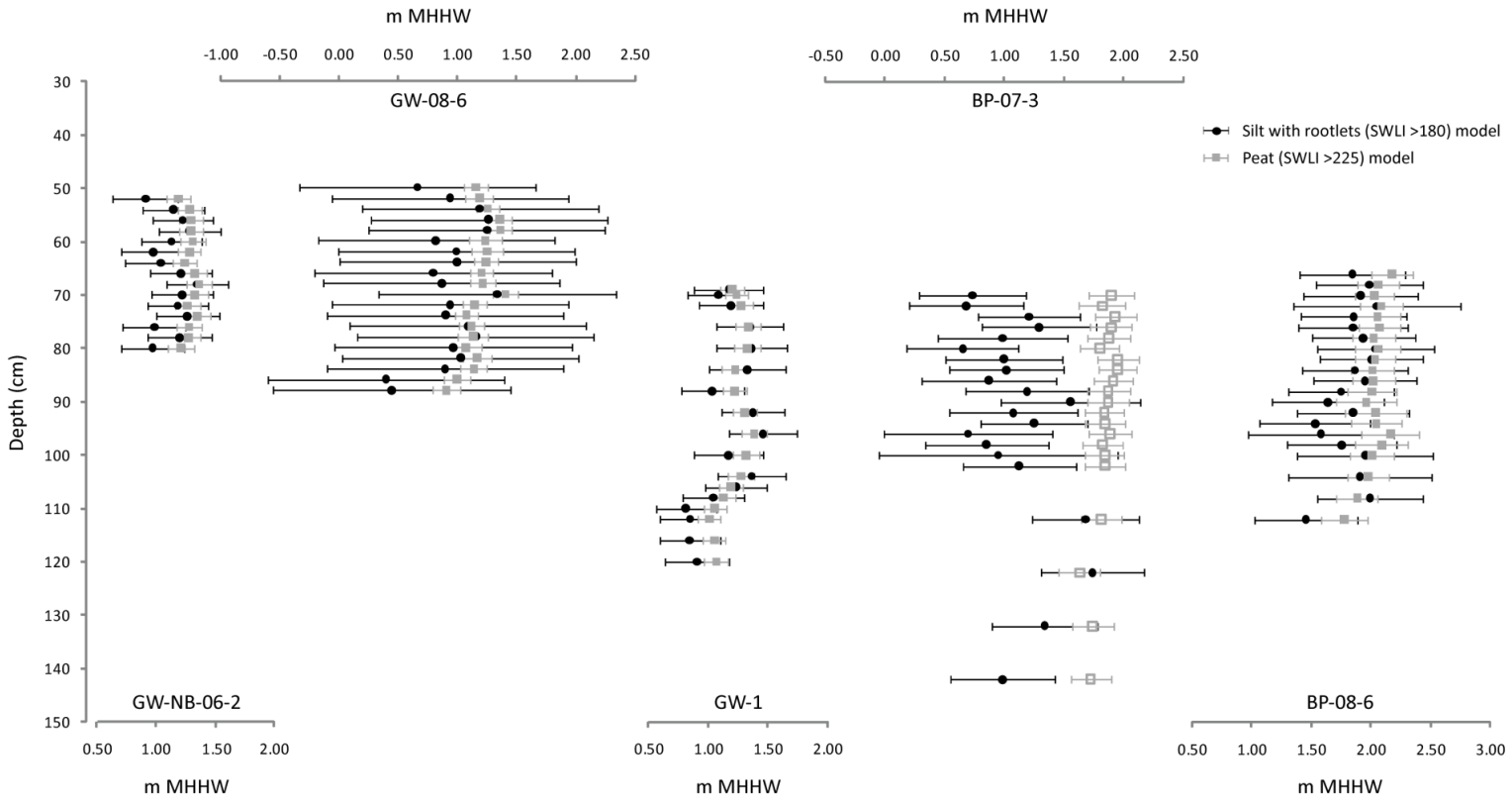

Figure 4.4 – Transfer function estimated PMSE (relative to m MHHW) of those fossil diatom samples from Girdwood and Bird Point that come from fossil peat (for lithology see Figure 4.6, Figure 4.12 and details in text), and therefore could be calibrated using either the peat or silt with rootlet transfer functions, to test for any discrepancy between the PMSE elevation estimated by the two models. The silty lithology of BP-07-3, compared to the organic layers found in the other cores, suggests calibration of the fossil samples requires the silt with rootlets transfer function. The peat transfer function produces much higher estimates and is therefore inappropriate and shown with no marker fill. In all other instances the estimated elevations by the two models fall within the sample specific error terms, therefore allowing selection of the peat transfer function, whilst being sure the PMSE of the sample is not being over estimated. For full reconstructions for each core see sections 4.3.1 and 4.3.2.

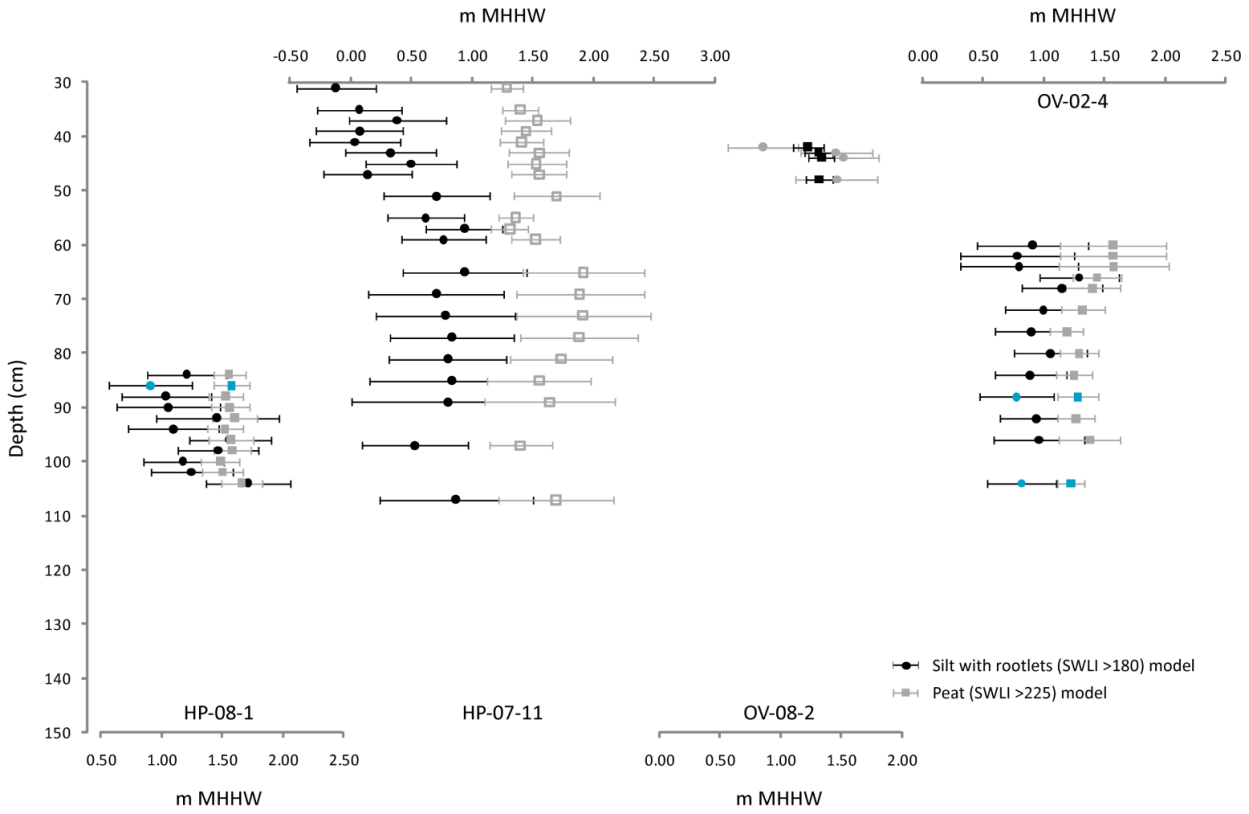

Figure 4.5 – Transfer function estimated PMSE (relative to m MHHW) of those fossil diatom samples from Hope and Ocean View (as per Figure 4.4) that come from fossil peat (for lithology see Figure 4.21, Figure 4.25 and details), and therefore could be calibrated using either the peat or silt with rootlet transfer functions, to test for any discrepancy between the PMSE elevation estimated by the two models. The silty lithology of HP-07-11, compared to the organic layers found in the other cores, suggests calibration of the fossil samples requires the silt with rootlets transfer function. The peat transfer function produces much higher estimates and is therefore inappropriate and shown with no marker fill. In all other instances, with the exception of one sample highlighted in blue in HP-08-1 and two samples highlighted in blue in OV-02-4, the estimated elevations by the two models fall within the sample specific error terms, therefore allowing selection of the peat transfer function, whilst being sure the PMSE of the sample is not being over estimated. For full reconstructions for each core see sections 4.3.3 and 4.3.4.

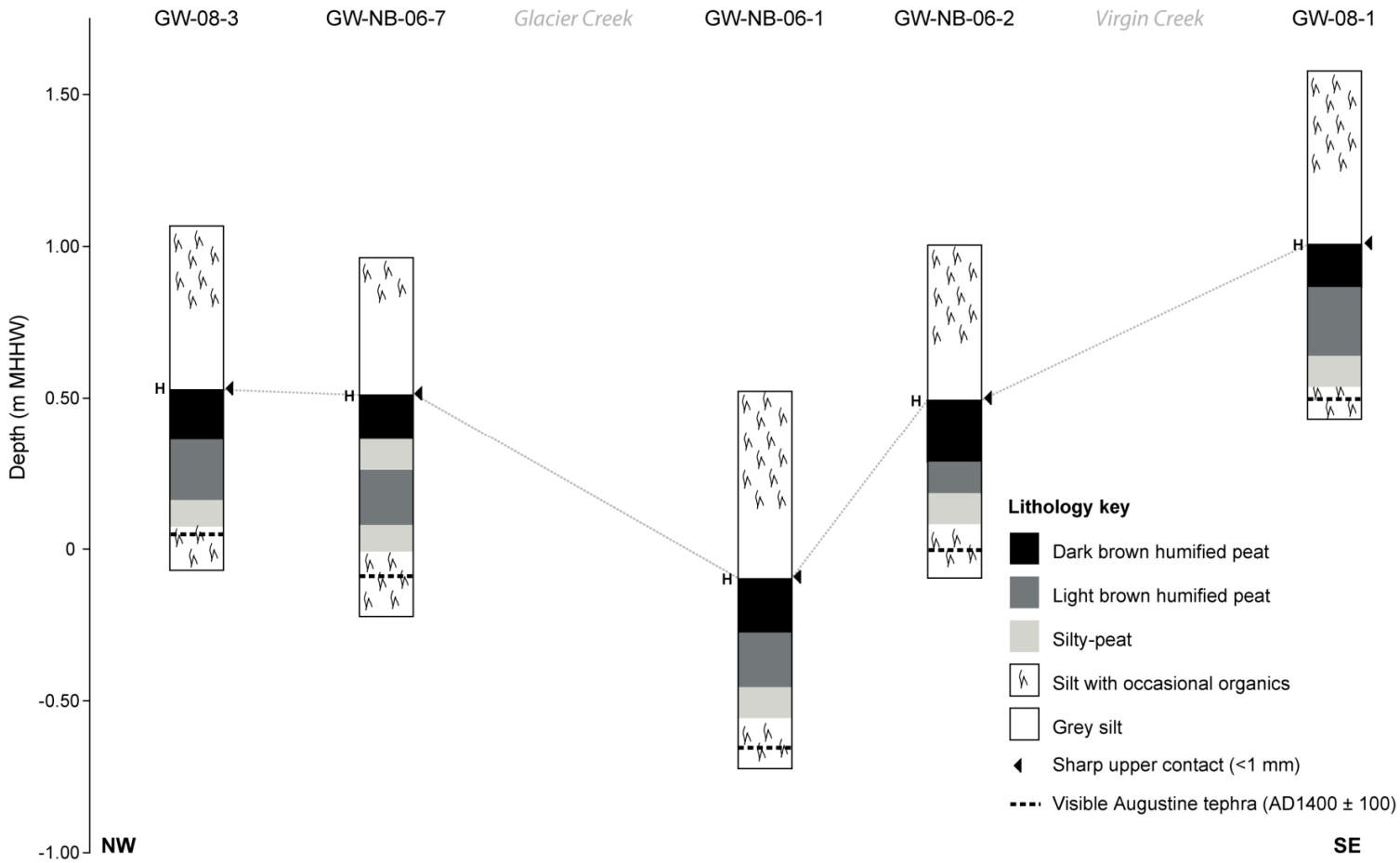

Figure 4.6 - Lithology of new cores at Girdwood. Letters suggest correlation with previously cored peat layers at Girdwood (Figure 2.10) with Augustine tephra (shown by dashed line) dated to AD1400 ± 100 (Combellick, personal communication, unpublished geochemical and radiocarbon data).

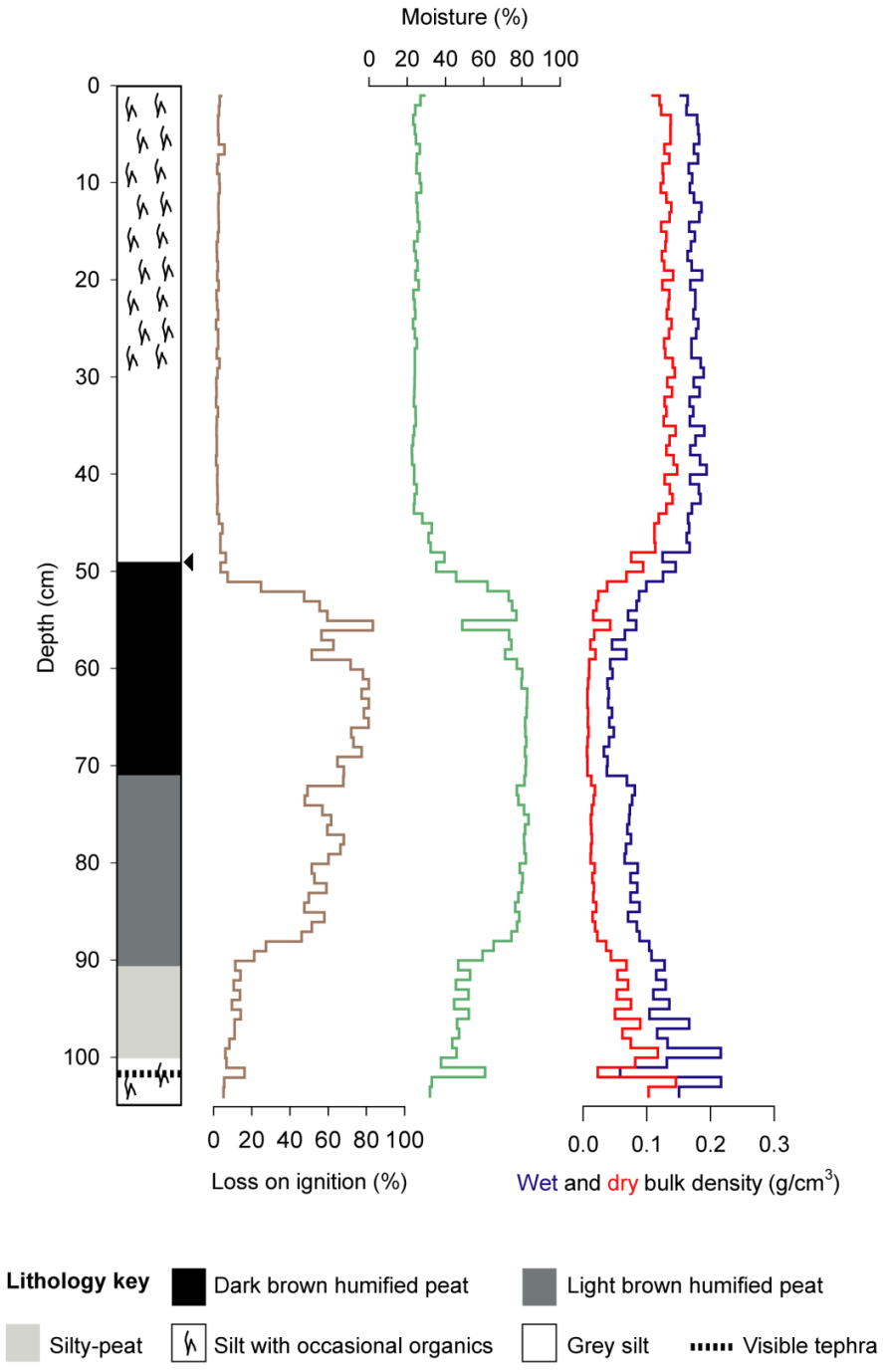

Figure 4.7 - Physical properties for GW-08-3 1 cm sampled at 1 cm contiguous slices.

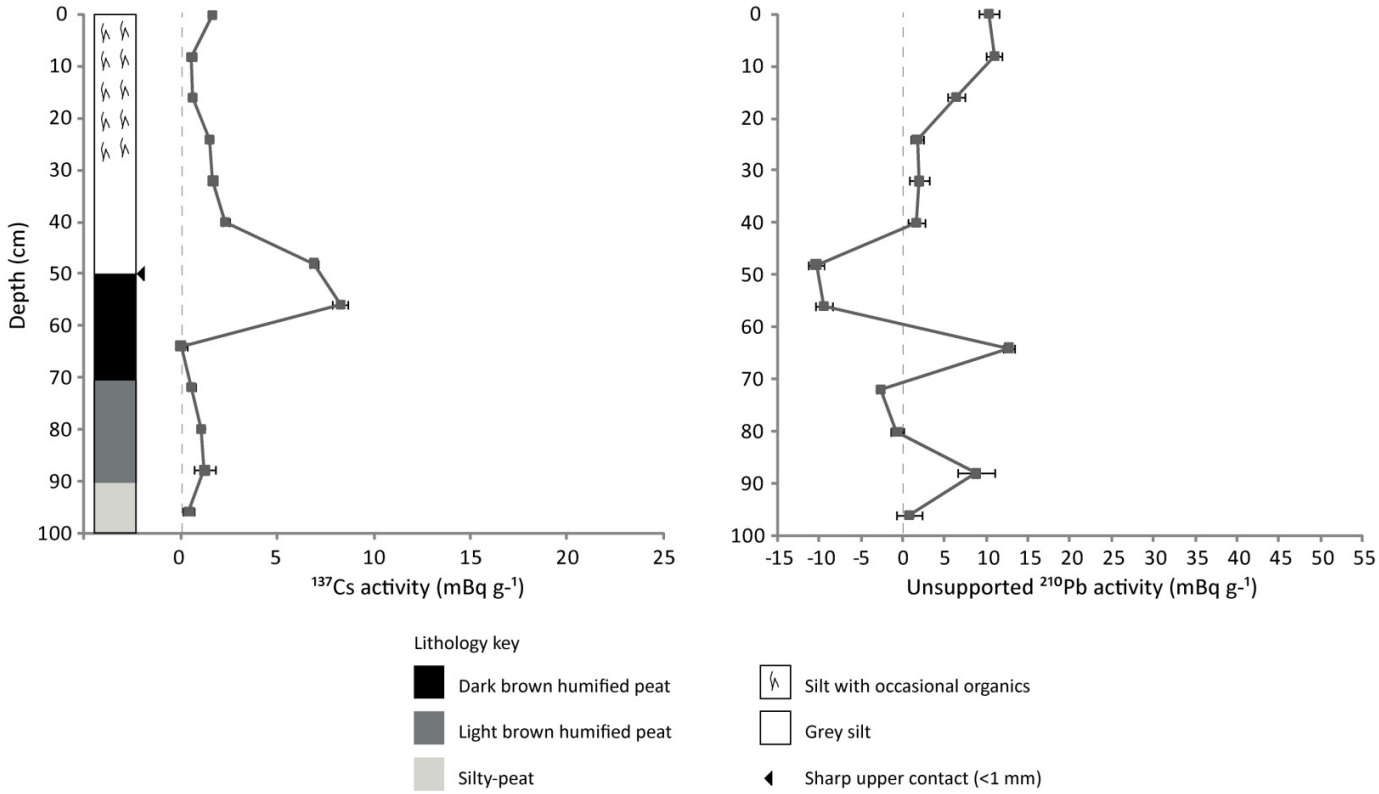

Figure 4.8 - ^{137}Cs and unsupported ^{210}Pb activity measured through GW-08-3. Peak in ^{137}Cs activity corroborates date of peat-silt boundary as AD 1964. The very low level of ^{210}Pb measured for many of the samples prevents development of a ^{210}Pb age-depth model. The peak in ^{210}Pb at 64 cm coincides with the peak in stable lead (Figure 4.9).

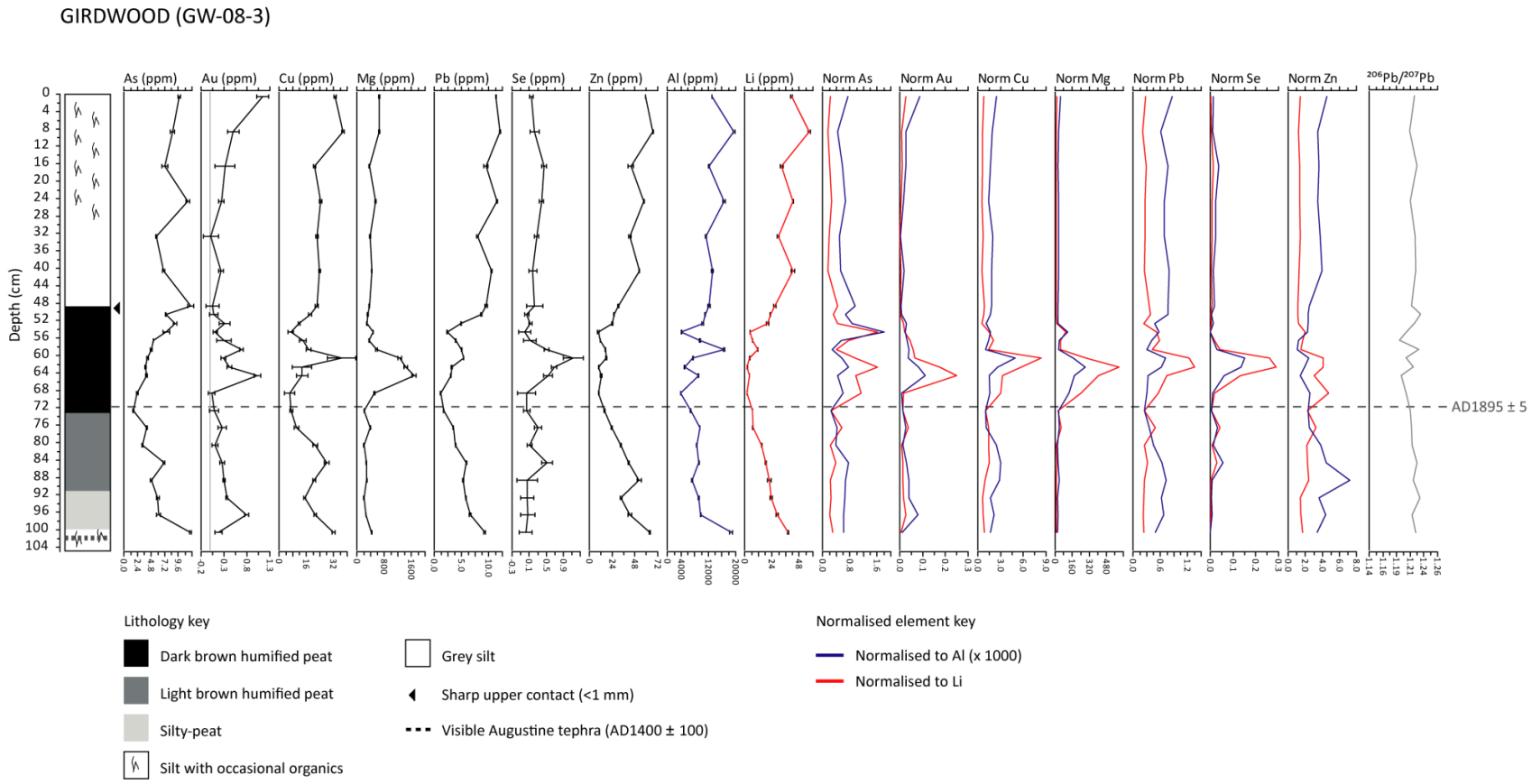

Figure 4.9 - Measured pollutant levels (ppm) through GW-08-3 and ratio of each element to aluminium (blue) and lithium (red) to account for changes in lithology. Ratios of elements to aluminium multiplied by 1000 to allow plotting on the same axis as the element ratio to lithium. The base of the peak in normalised elements at 72 cm provides a chronological marker of AD1895 ± 5 yrs, based upon the history of gold mining in upper Cook Inlet (section 2.2.6 and Lampright, 2008). Final graph (in grey) shows ratio of isotopic ^{206}Pb to ^{207}Pb.

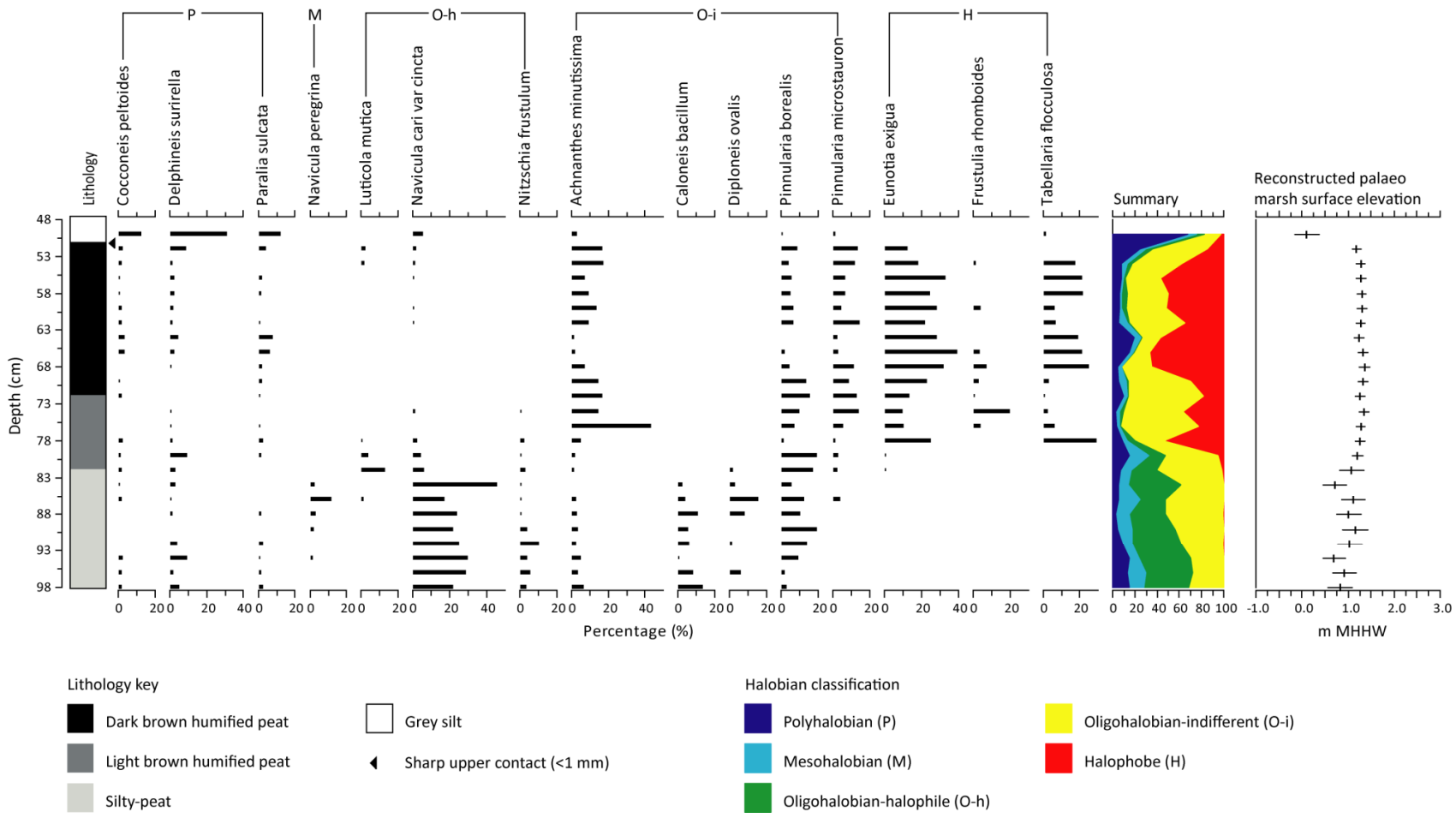

Figure 4.10 - Biostratigraphy of GW-NB-06-2 showing diatoms that account for 10% of total diatom valves counted. Final graph shows composite reconstructed palaeo marsh surface elevation of each sample relative to m MHHW with errors, using peat transfer function for samples from fossil peat (80-52 cm) and silt with rootlets transfer function for all other samples.

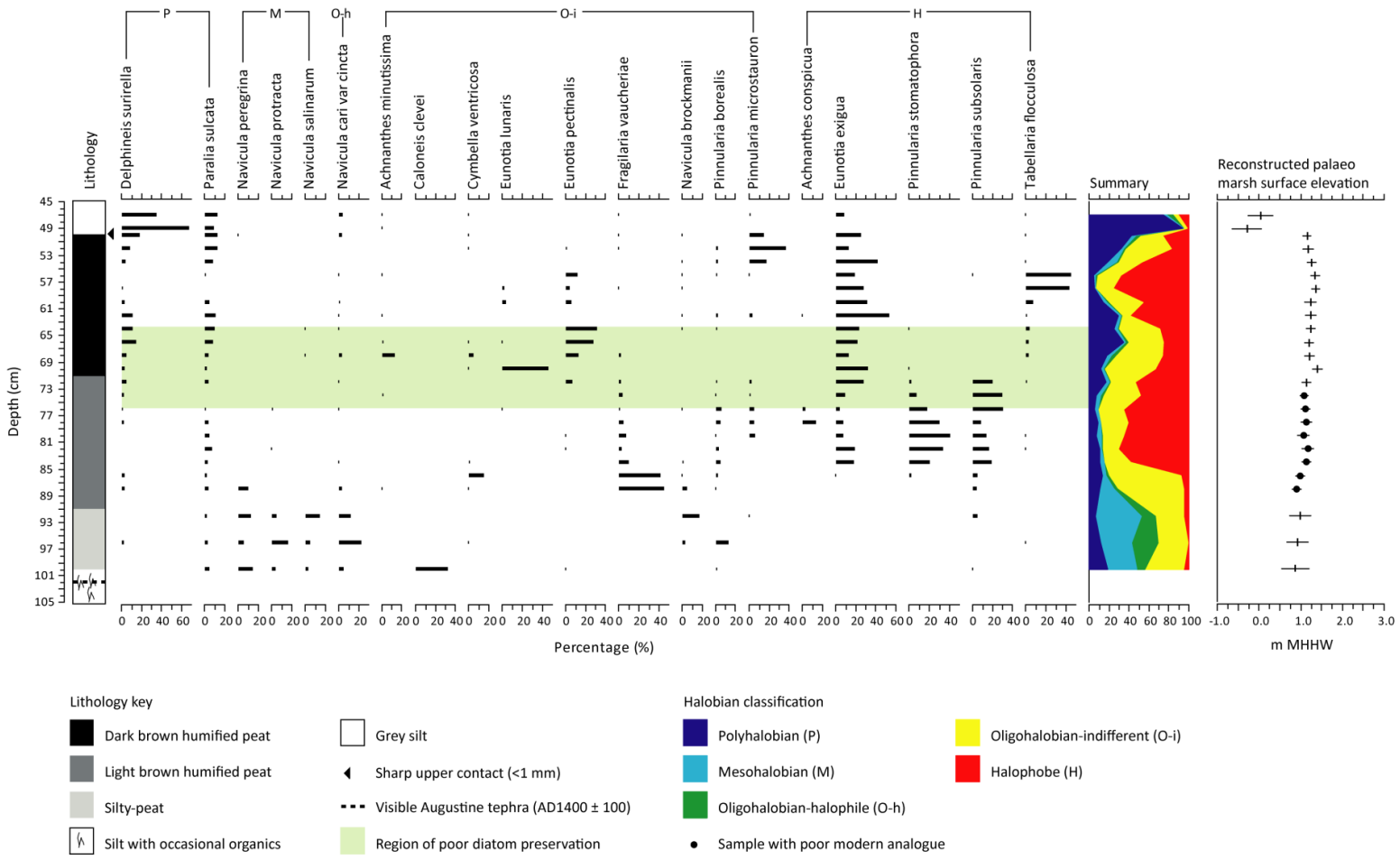

Figure 4.11 - Biostratigraphy of GW-08-3 showing diatoms that account for 10% of total diatom valves counted. 250 valves counted for samples in region of poor diatom preservation across multiple slides. Final graph shows composite reconstructed palaeo marsh surface elevation of each sample relative to m MHHW, using peat transfer function for samples from fossil peat (80-50 cm) and silt with rootlets transfer function for all other samples. Those samples considered to have a poor modern analogue shown with circle.

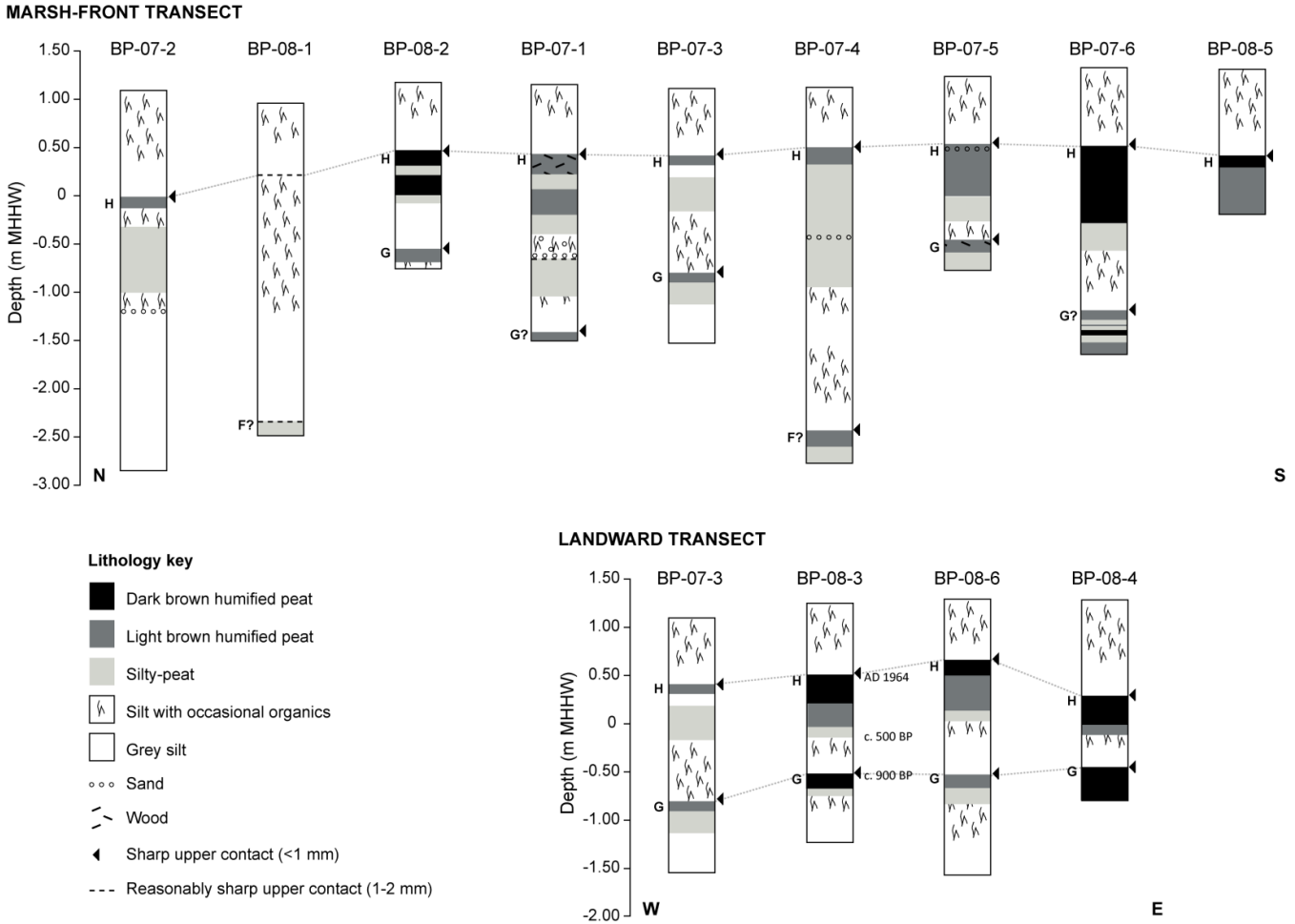

Figure 4.12 - Lithology of cores at Bird Point. Letters suggest correlation with peat layers at Girdwood (Figure 2.10): H being AD 1964 and with radiocarbon date on the penultimate peat-silt boundary at BP-08-6 of c. 900 yr BP (reported in this thesis - section 4.3.2) confirming correlation with peat G at Girdwood (Figure 2.10).

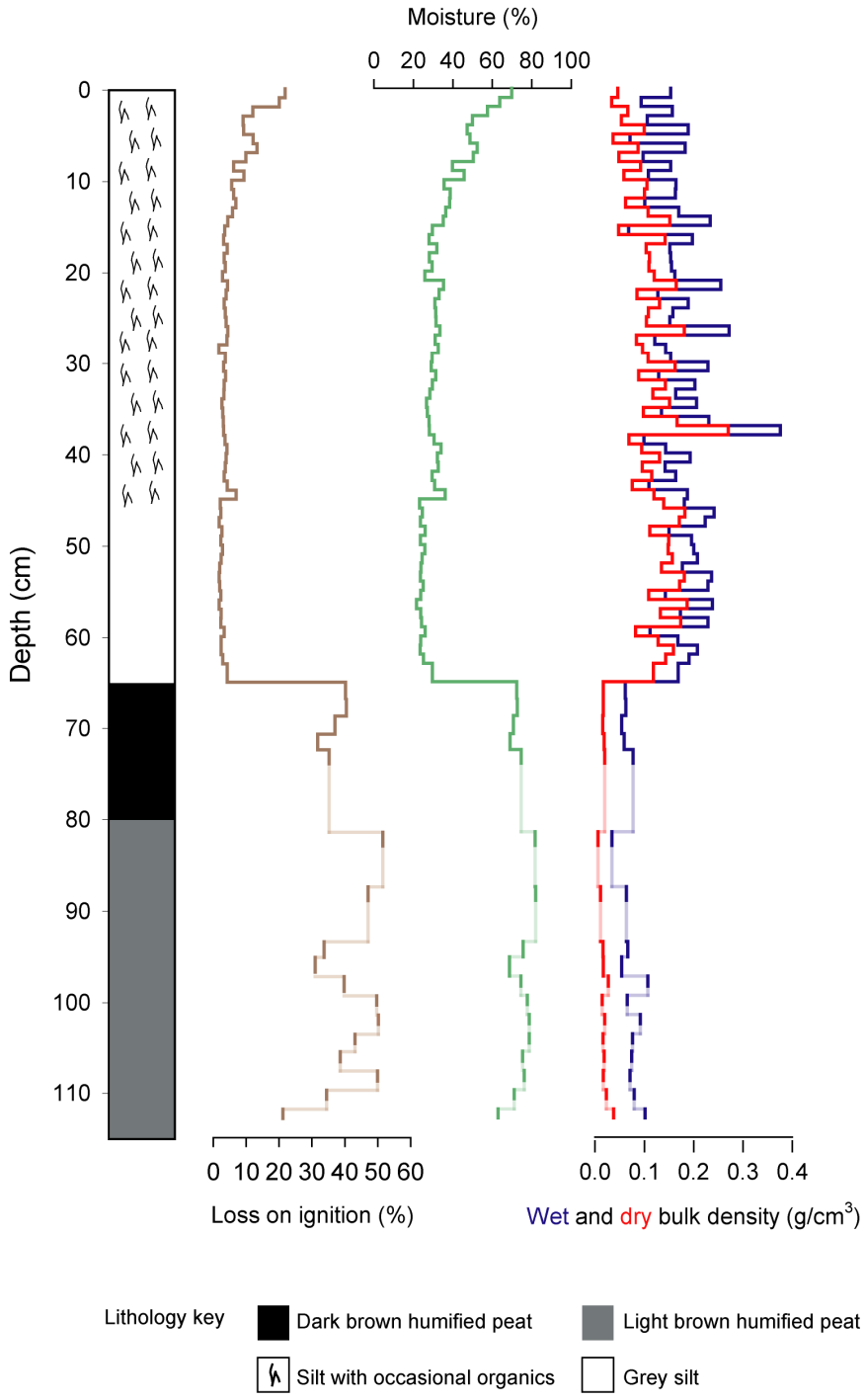

Figure 4.13 - Physical properties for BP-08-6 sampled at 1 cm contiguous slices until 74 cm. Non contiguous slices below 74 cm shown by dark lines, with light lines suggesting correlation between samples.

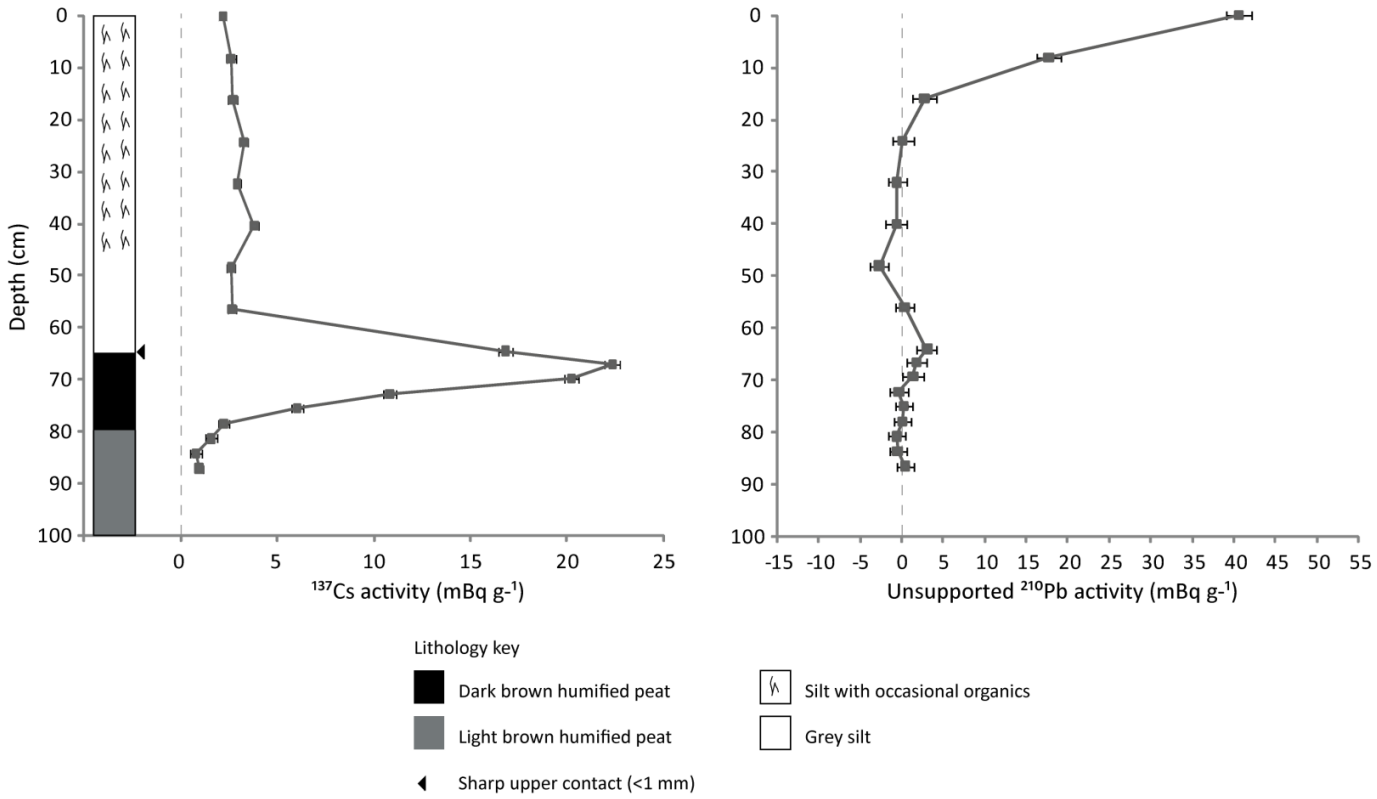

Figure 4.14 - ^{137}Cs and unsupported ^{210}Pb activity measured through BP-08-6. Peak in ^{137}Cs activity corroborates date of peat-silt boundary as AD 1964 and onset of rise in activity taken as AD 1952. The very low level of ^{210}Pb measured below 16 cm prevents development of a ^{210}Pb age-depth model.

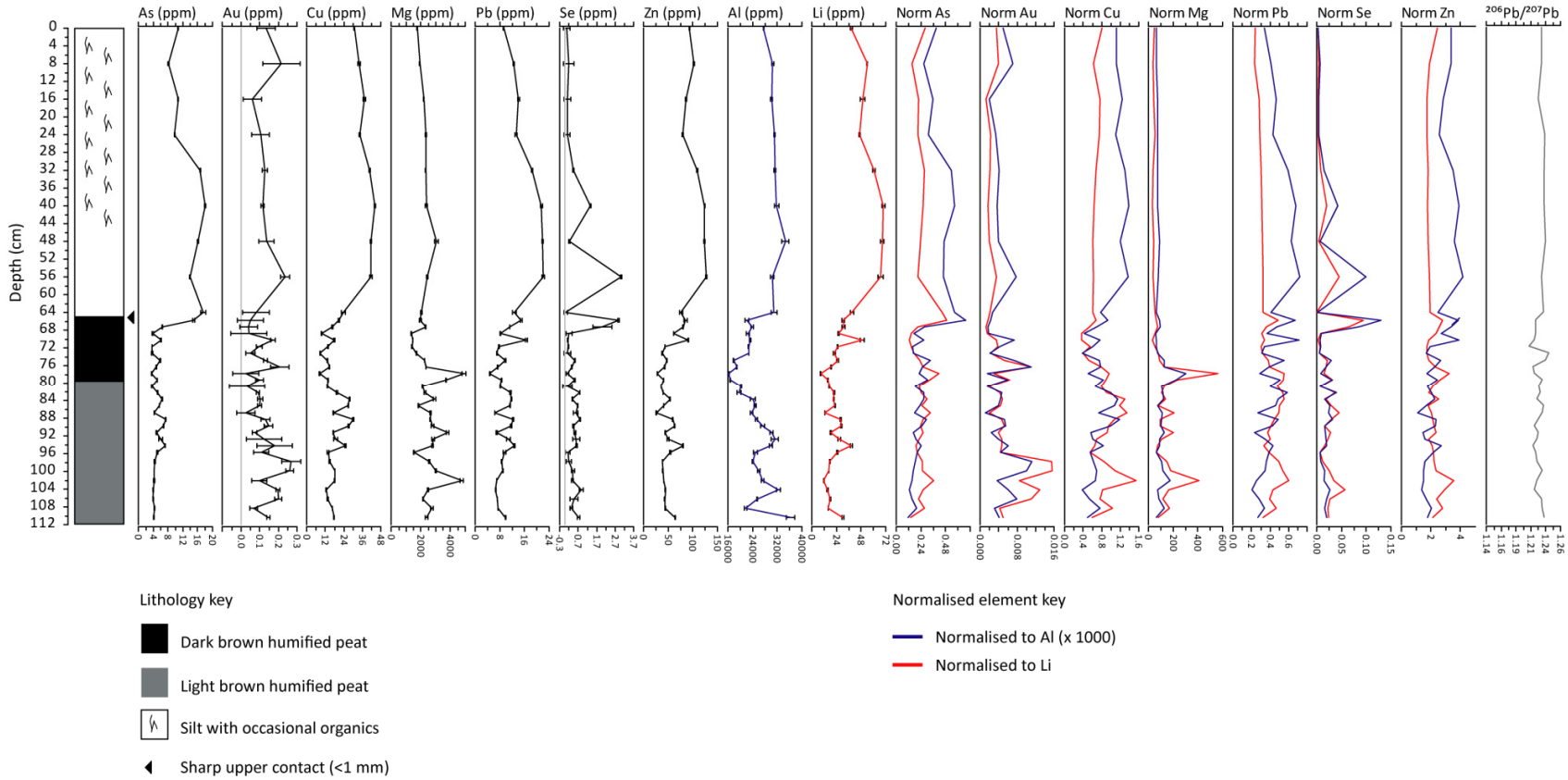

Figure 4.15 - Measured pollutant levels (ppm) through BP-08-6 and ratio of each element to aluminium (blue) and lithium (red) to account for changes in lithology. Ratios of elements to aluminium multiplied by 1000 to allow plotting on the same axis as the element ratio to lithium. Final graph (in grey) shows ratio of isotopic ^{206}Pb to ^{207}Pb.

Lab Code	Sample Code	Depth	14C yr BP ± 1σ	2σ age ranges (cal yr AD)
Dates from the upper peat layer				
SUERC-22662	BP086R1	76	110 ± 37	1680-1764; 1774-1776 1800-1939; **1951-1954**
SUERC-22666	BP086R3	84	125 ± 37	1674-1778; 1799-1898 1901-1941; 1950-1953
SUERC-22667	BP086R4	88	250 ± 37	1517-1595; 1618-1682 1737-1757; 1761-1803 1936-1951
SUERC-22668	BP086R5	92	248 ± 37	1519-1593; 1619-1682 1737-1758; 1761-1804 1936-1951
SUERC-22669	BP086R7	100	368 ± 35	1447-1529; 1542-1634
SUERC-22670	BP086R8	104	399 ± 37	1435-1524; 1558-1631
SUERC-22671	BP086R9	108	549 ± 37	1306-1363; 1385-1437
Dates from the penultimate peat-silt boundary				
SUERC-22673	BP086R11	191	991 ± 35	986-1059; 1067-1072 1075-1155
SUERC-22676	BP086R12	192	1060 ± 37	894-928; 933-1025

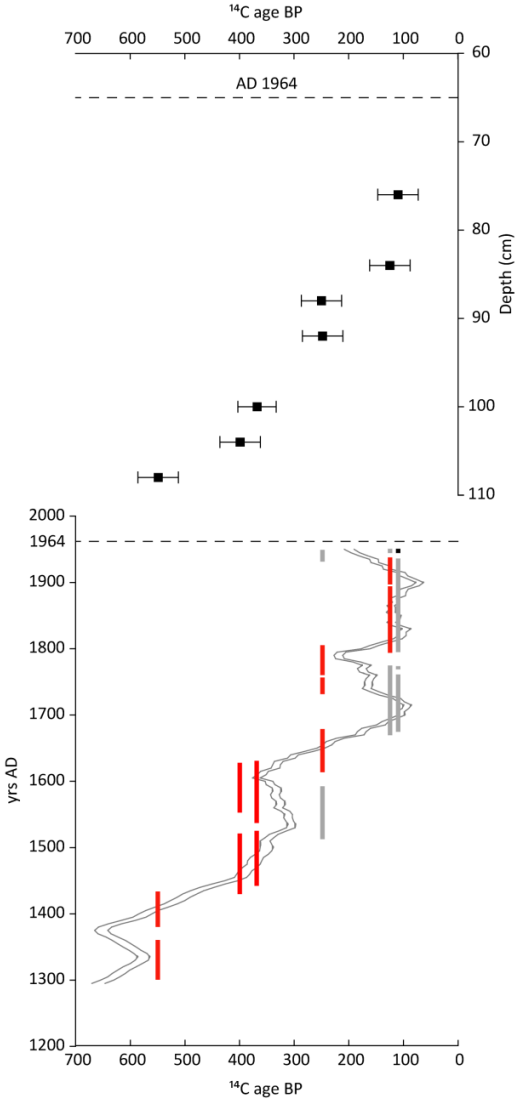

Figure 4.16 – Table: reported AMS radiocarbon dates for BP-08-6 with 2σ calibration range solutions using Calib5.0 and IntCal04 (Reimer *et al.*, 2004) in years AD. Top graph: reported radiocarbon ages from the upper peat layer plotted against depth. Lower graph: calibration solutions for each radiocarbon date from the upper peat layer, plotted over the IntCal04 calibration curve for reference. Dates BP086R4 and BP086R5 report similar ages so are shown as by one set of lines in the lower graph for clarity.

Several 2σ calibration solutions exist for each radiocarbon date from the upper most peat layer. Those solutions that can be rejected are shown in grey, acceptable solutions are shown in black and dates in red are where several solutions remain (detailed in main text section 4.3.2).

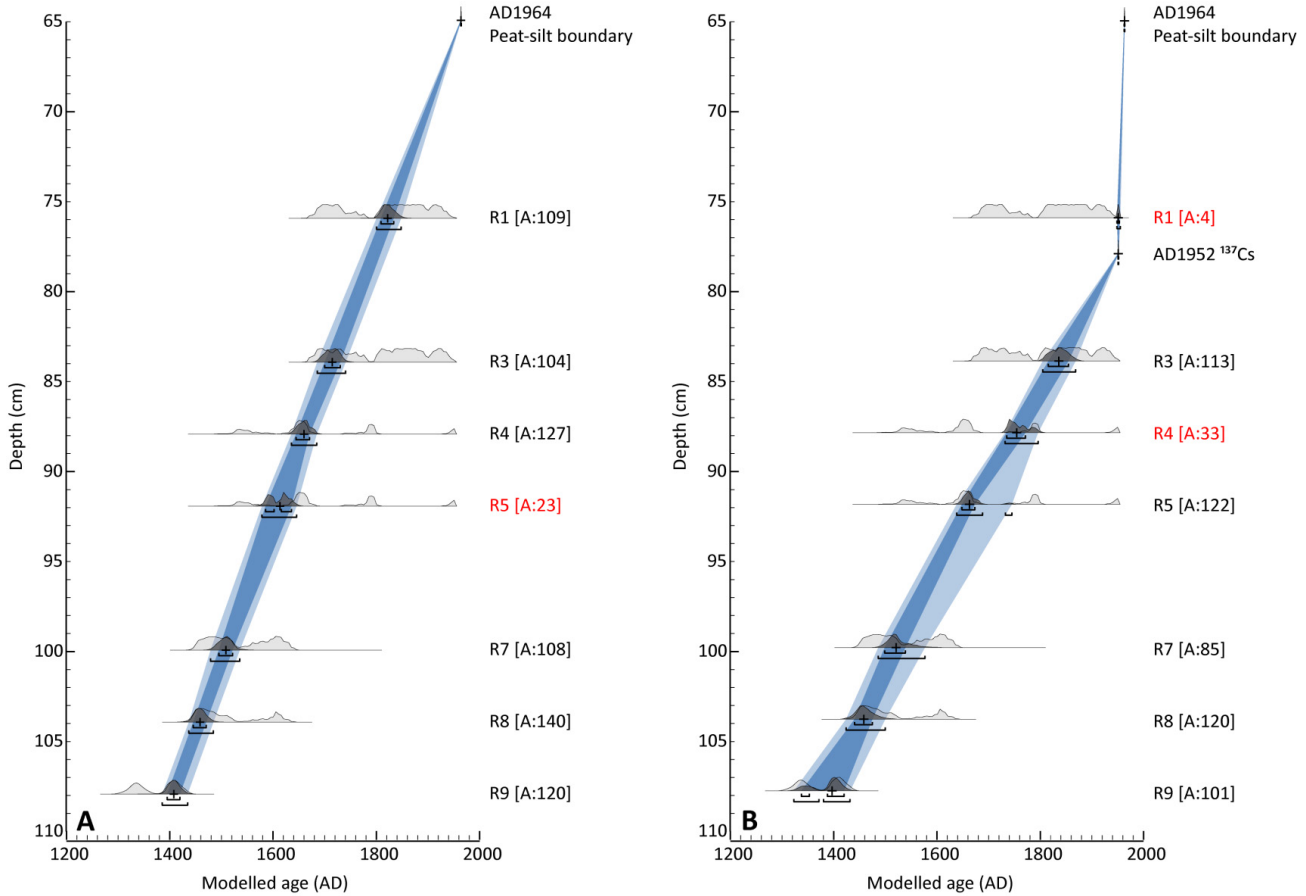

Figure 4.17 - OxCal depositional age models for BP-08-6 radiocarbon dates from upper peat layer (reported in Figure 4.16). Both age models use Bayesian *P_sequence* depositional model, with 5 depositional events per cm (k=500) and IntCal04 calibration curve (Reimer *et al.*, 2004). Model A uses AMS radiocarbon dates and the AD 1964 peat-silt boundary. Model B also includes ^{137}Cs data (Figure 4.14). The interpolation envelope shows 2σ (light blue) and 1σ (dark blue) range. Calibration curves show IntCal04 likelihood and posterior probability distribution. 'A' value in brackets shows agreement index for each radiocarbon date, highlighting in red those that fall below the 60% threshold.

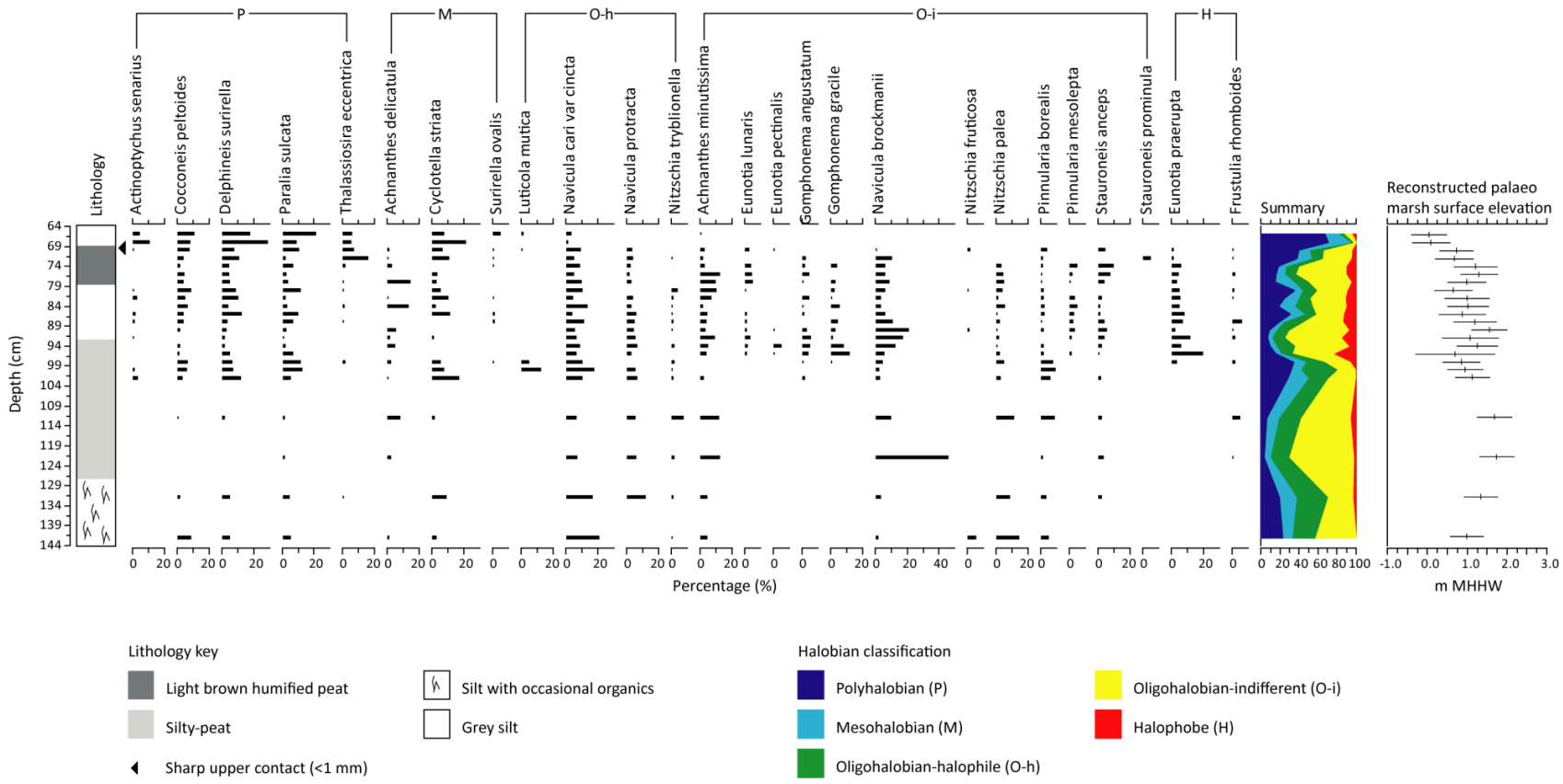

Figure 4.18 - Biostratigraphy of BP-07-3 showing diatoms that account for 5% of total diatom valves counted. Final graph shows reconstructed palaeo marsh surface elevation of each samples relative to m MHHW with errors, using silt with rootlets transfer function for all fossil samples (see sections 4.2.3 and 4.3.2 for details).

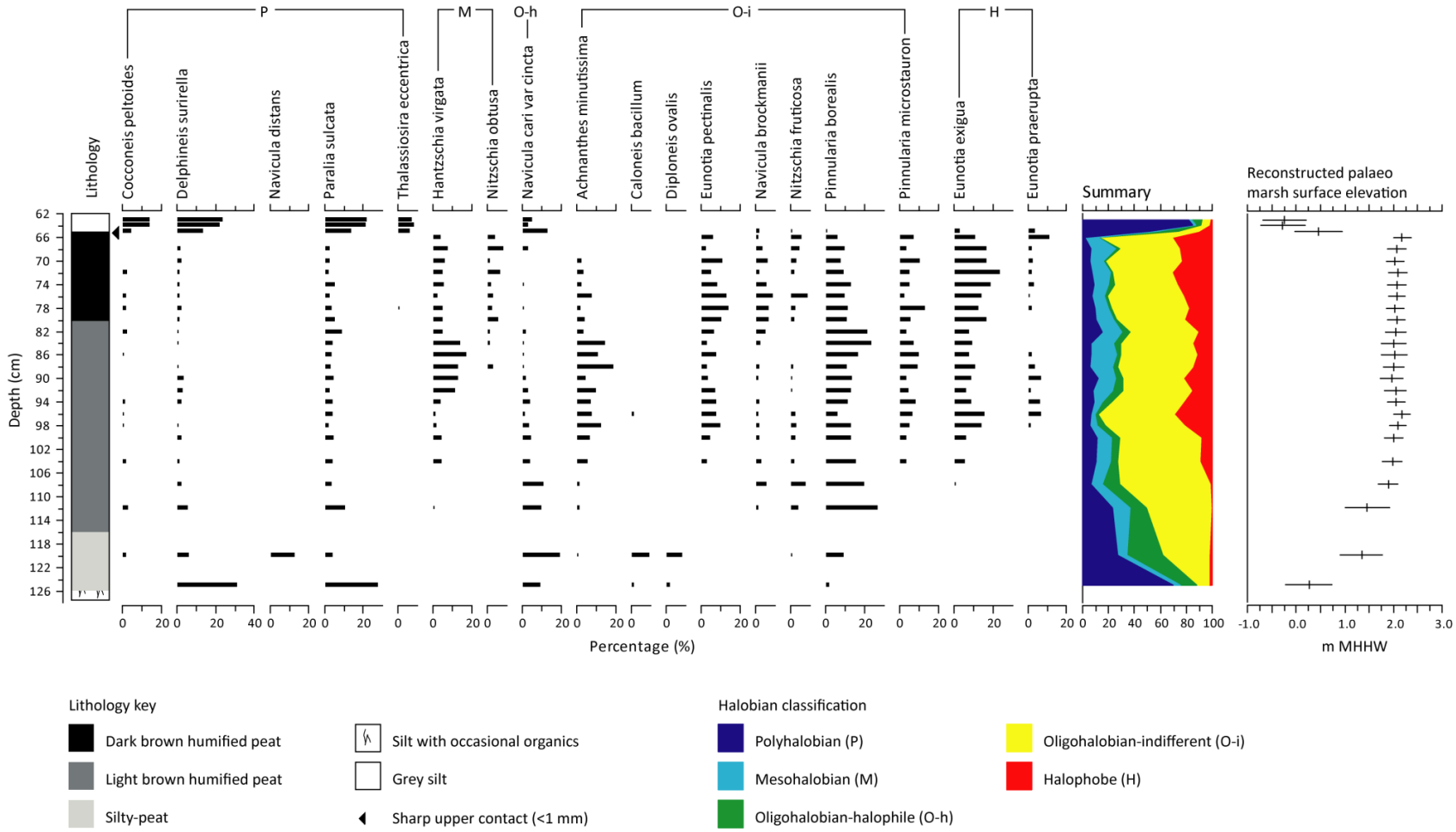

Figure 4.19 - Biostratigraphy of upper most peat-silt couplet at BP-08-6 showing diatoms that account for 7.5% of total diatom valves counted. Final graph shows reconstructed palaeo marsh surface elevation relative to m MHHW with errors, using peat transfer function for samples from fossil peat (112-66 cm) and silt with rootlets transfer function for all other samples.

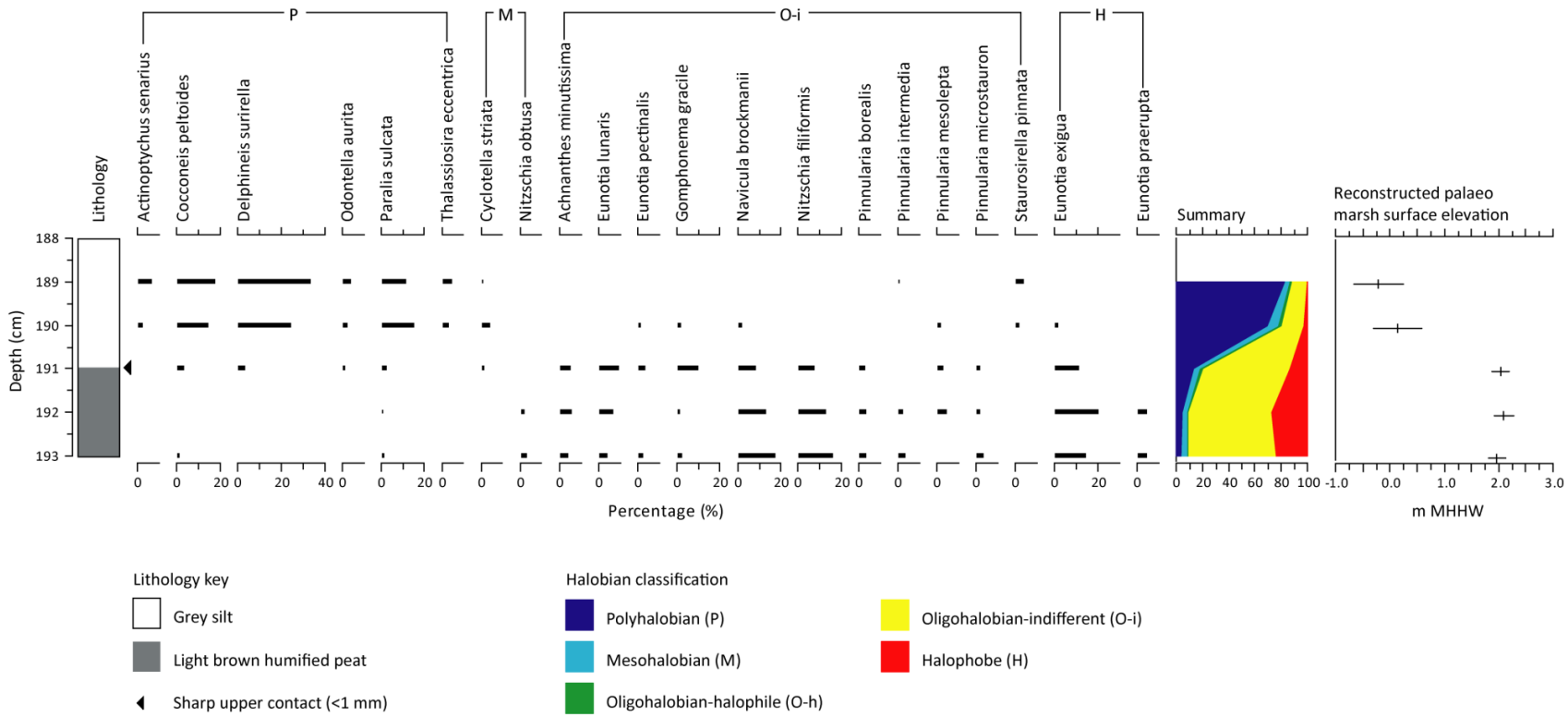

Figure 4.20 - Biostratigraphy of penultimate peat-silt couplet at BP-08-6 showing diatoms that account for 3% of total diatom valves counted. Final graph shows reconstructed palaeo marsh surface elevation for each sample relative to m MHHW with errors, using peat transfer function for samples from fossil peat (191-193 cm) and silt with rootlets transfer function for all other samples..

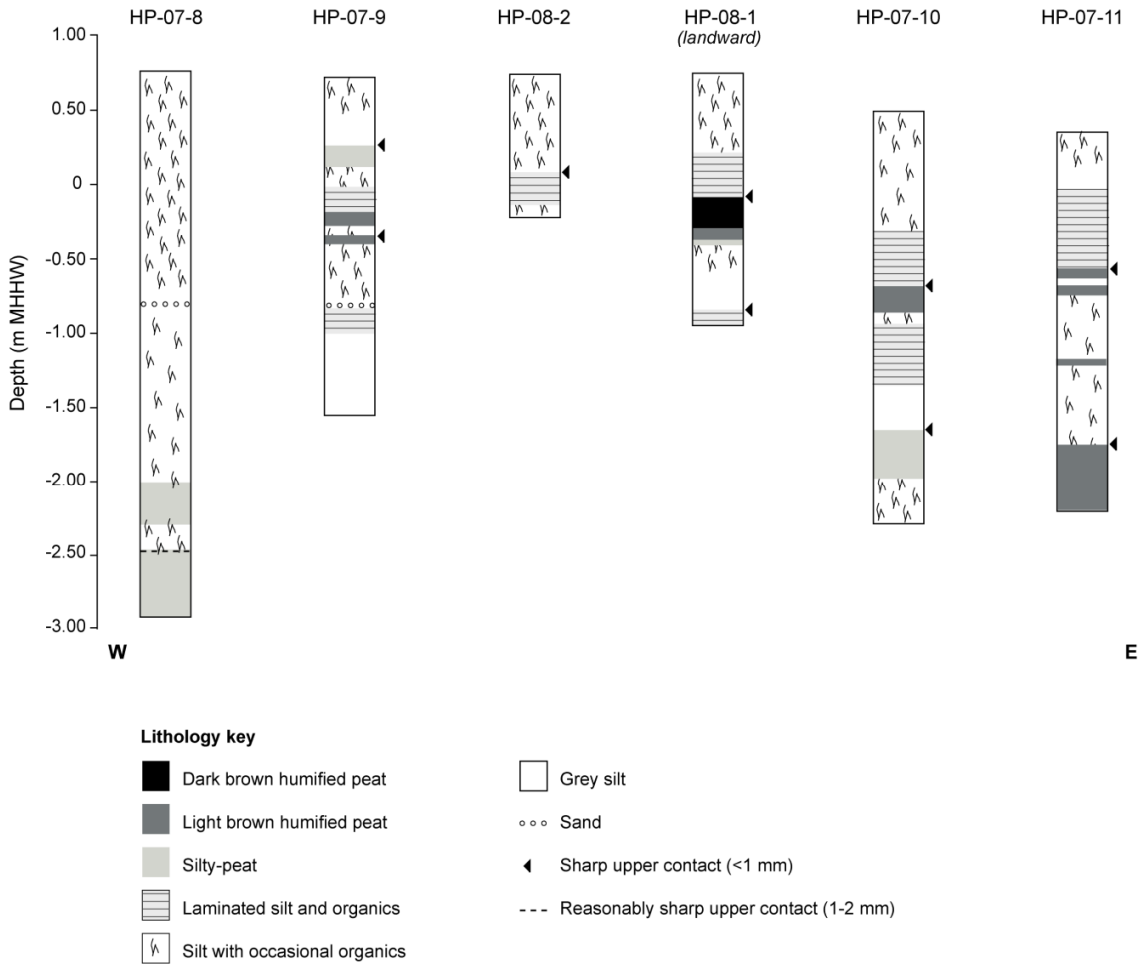

Figure 4.21 - Lithology of cores at Hope to the west of Resurrection Creek.

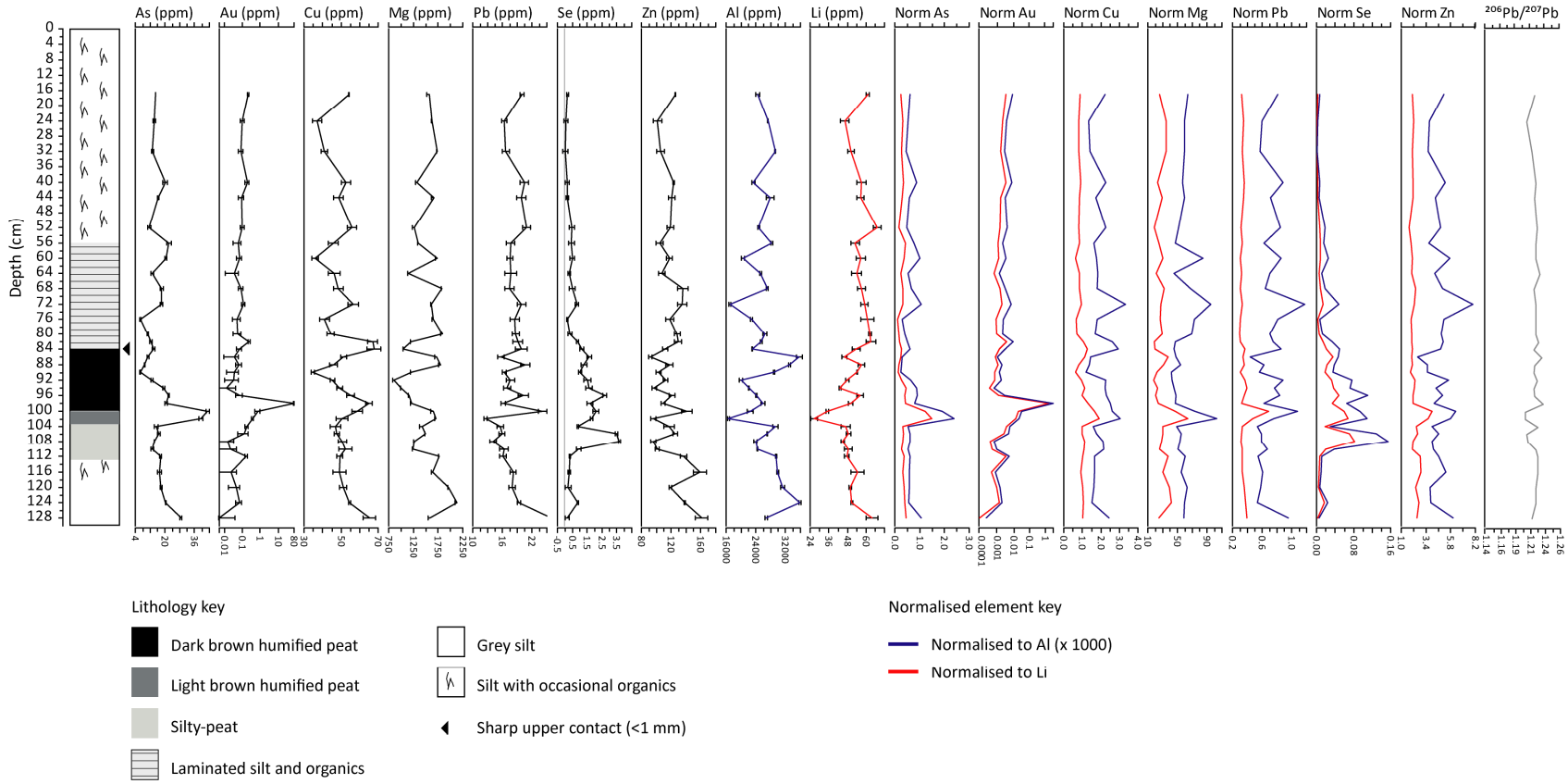

Figure 4.22 - Measured pollutant levels (ppm) through HP-08-1 and ratio of each element to aluminium (blue) and lithium (red) to account for changes in lithology. The ratio of elements to aluminium is multiplied by 1000 to allow plotting on the same axis as the element ratio to lithium. Final graph (in grey) shows ratio of isotopic ^{206}Pb to ^{207}Pb.

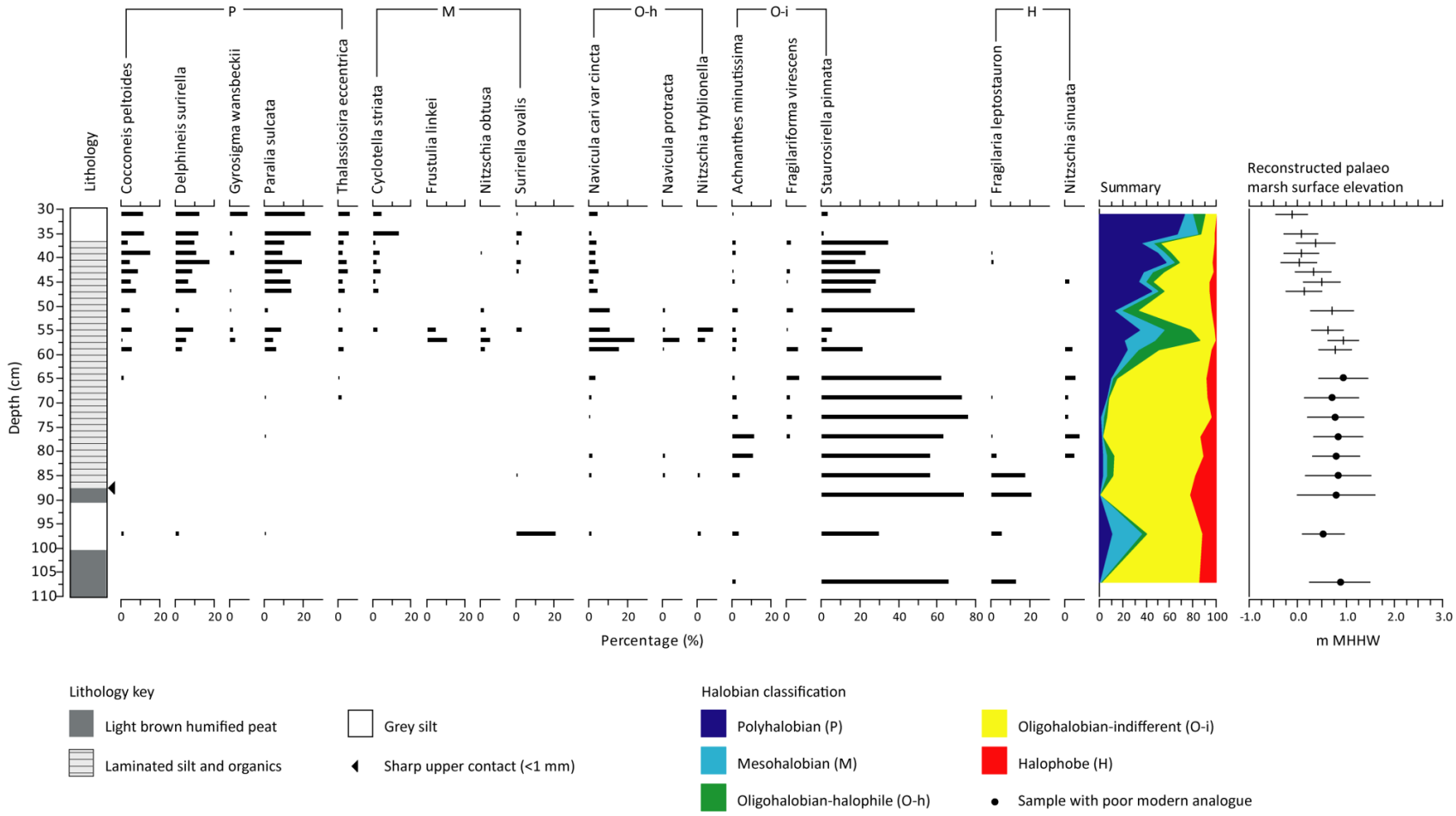

Figure 4.23 - Biostratigraphy of HP-07-11 showing diatoms that account for 5% of total diatom valves counted. Final graph shows reconstructed palaeo marsh surface elevation for each sample relative to m MHHW with errors, using silt with rootlet transfer function for all fossil samples. Those samples considered to have a poor modern analogue shown with circle.

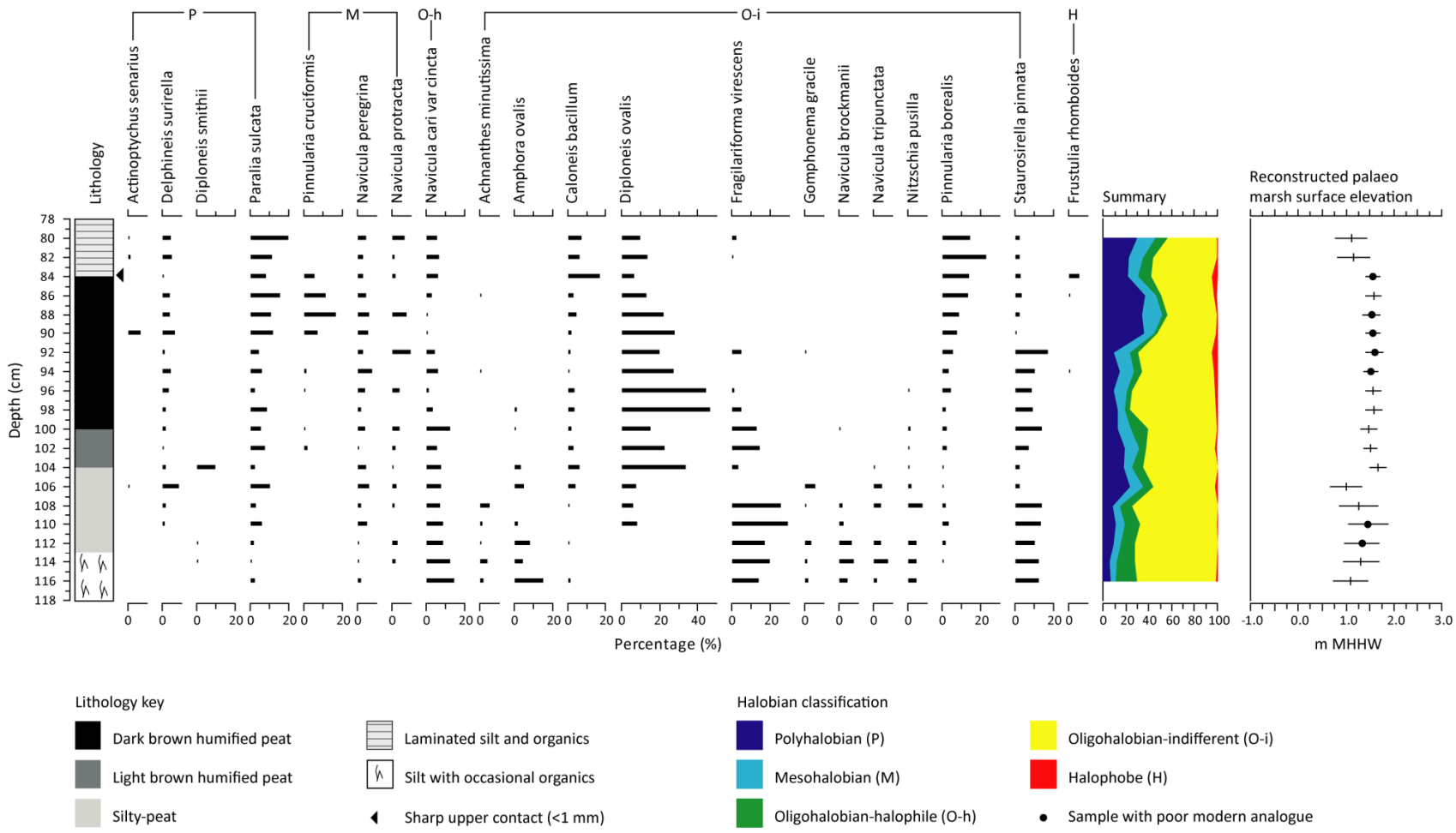

Figure 4.24 - Biostratigraphy of HP-08-1 showing diatoms that account for 5% of total diatom valves counted. Final graph shows reconstructed palaeo marsh surface elevation for each sample relative to m MHHW with errors, using peat transfer function for calibration of fossil peat samples (104-84 cm) and silt with rootlets transfer function for all other fossil samples. Those samples considered to have a poor modern analogue shown with circle.

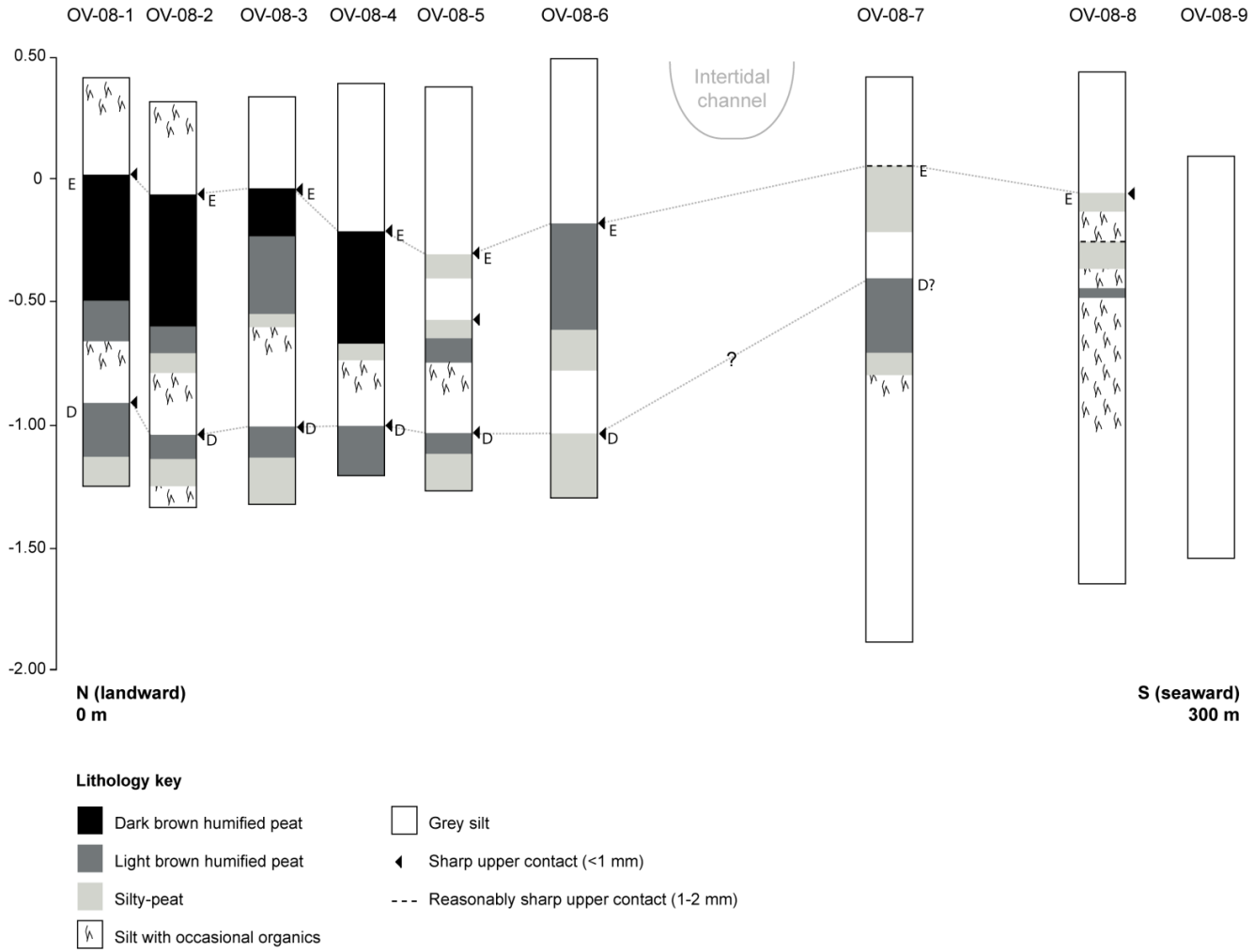

Figure 4.25 - Lithology of cores at Ocean View. Letters suggest correlation with peat layers recorded by Hamilton et al (2005) (Figure 2.17) with peat E being the pre AD 1964 peat layer and peat D the c. 850 yr BP peat.

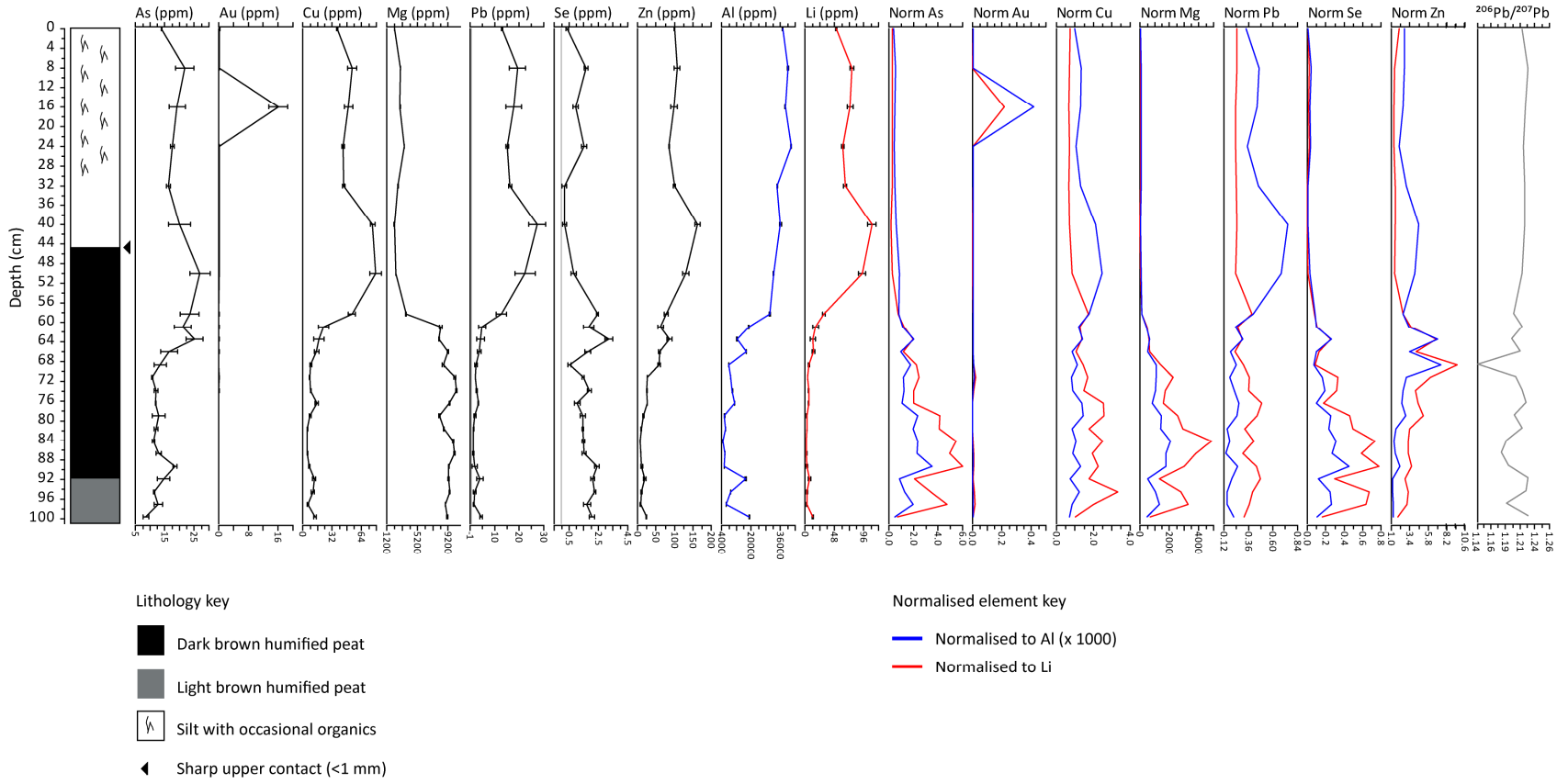

Figure 4.26 - Measured pollutant levels (ppm) through OV-08-2 and ratio of each element to aluminium (blue) and lithium (red) to account for changes in lithology. The ratio of elements to aluminium is multiplied by 1000 to allow plotting on the same axis as the element ratio to lithium. Final graph (in grey) shows ratio of isotopic ^{206}Pb to ^{207}Pb.

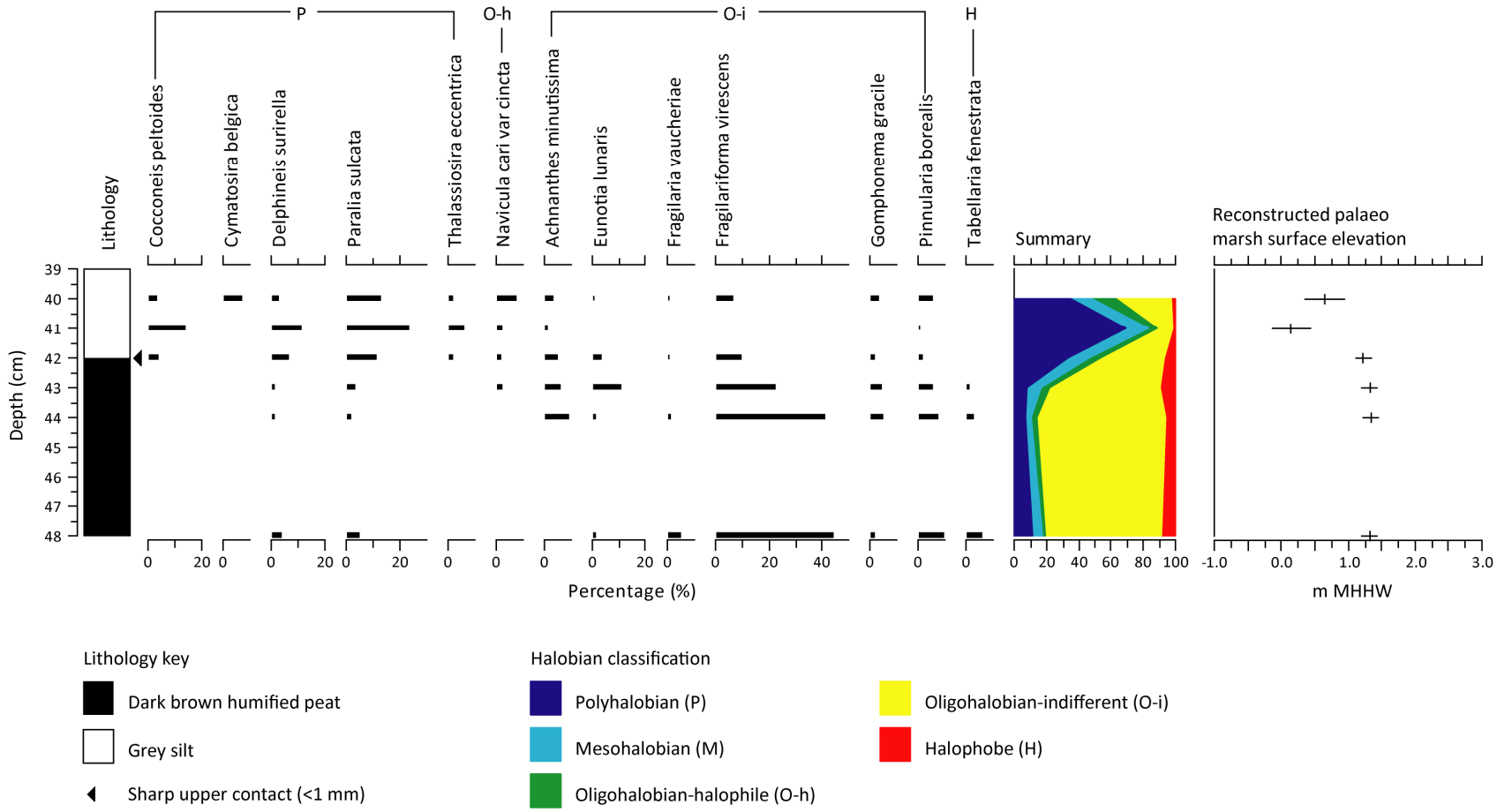

Figure 4.27 - Biostratigraphy of OV-08-2 showing diatoms that account for 5% of total diatom valves counted. Diatoms absent 45-47 cm and below 48 cm. Final graph shows reconstructed palaeo marsh surface elevation for each sample relative to m MHHW with errors, using peat transfer function for fossil samples 48-42 cm and silt with rootlets transfer function for fossil samples 41-40 cm.

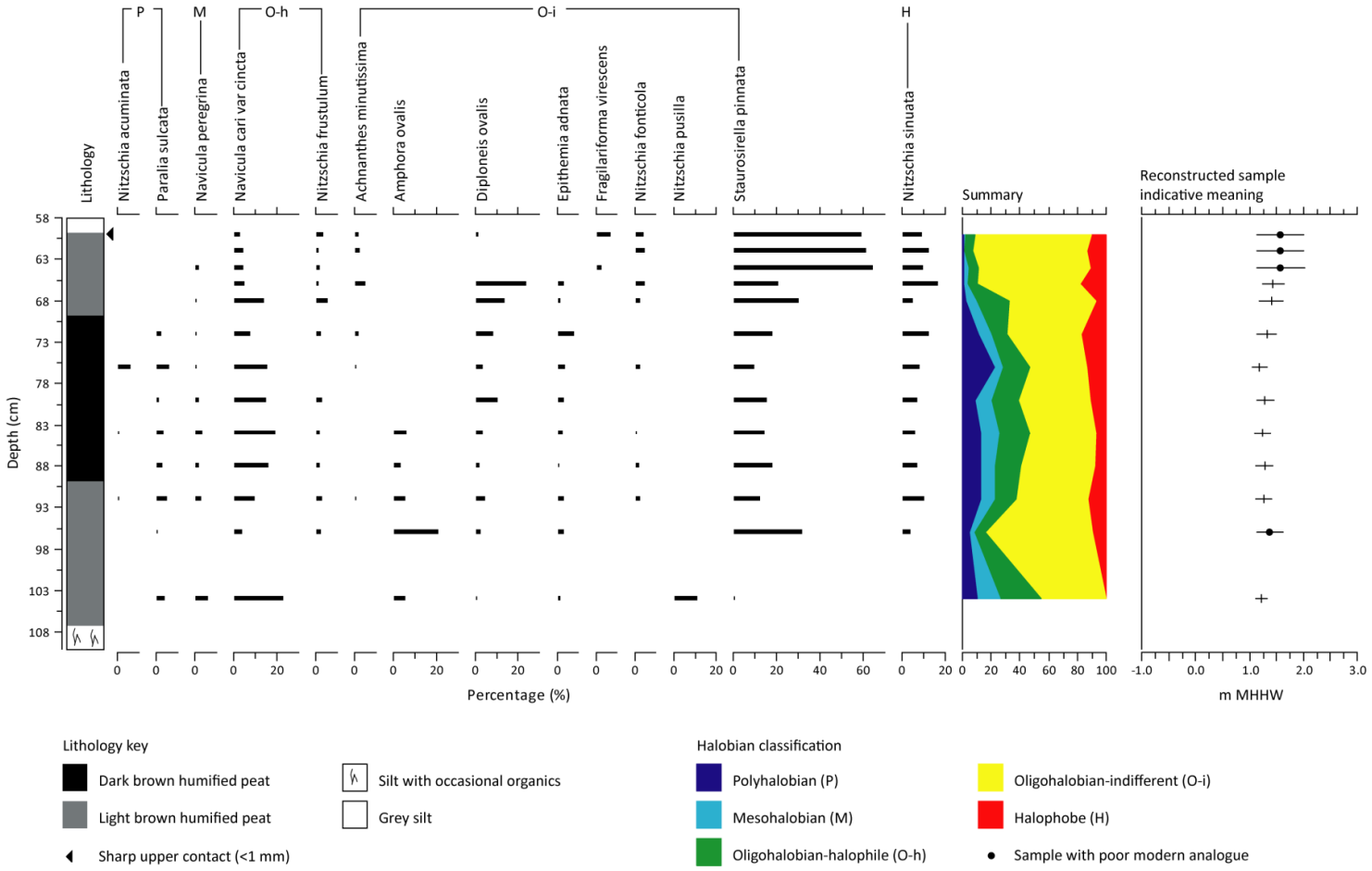

Figure 4.28 - Biostratigraphy of OV-02-4 (Shore Drive transect) showing diatoms that account for 5% of total diatom valves counted. Final graph shows reconstructed palaeo marsh surface elevation for each sample relative to m MHHW with errors, using peat transfer function for all fossil samples. Those samples considered to have a poor modern analogue shown with circle. This core comes from Hamilton *et al.* (2005) Shore Drive transect 1 (see Figure 2.17).

Figure 4.29 - Ponding of water at the foot of the bluff at Shore Drive, Ocean View (January 2006). (Photograph courtesy of Smiley Shields).

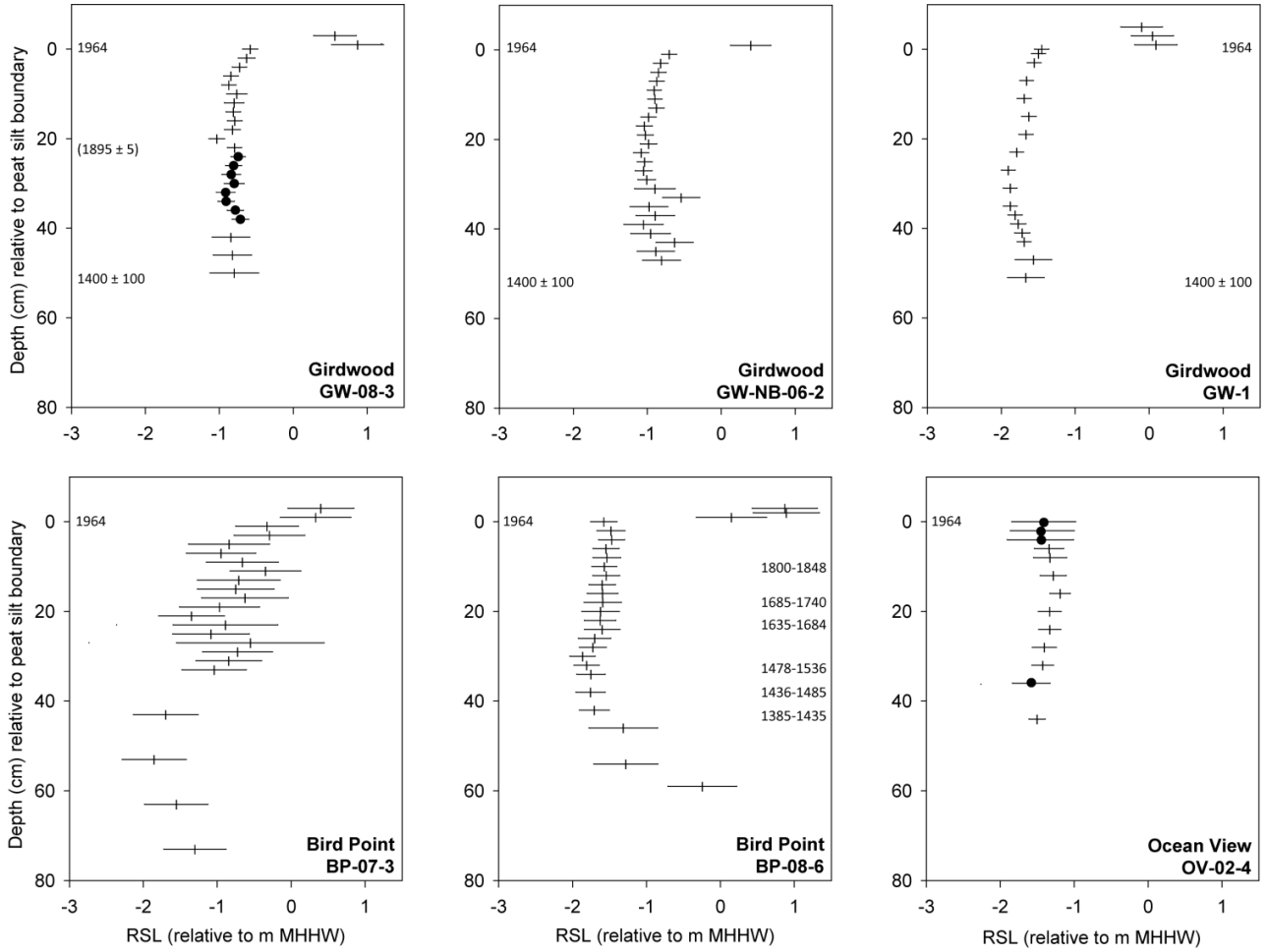

Figure 4.30 - Summary of changes in RSL (relative to MHHW (m)), with depth relative to peat silt boundary, including relevant age models, for six cores from Girdwood, Bird Point and Ocean View. Dates on BP-08-6 are the 2σ range for 6 radiocarbon samples as estimated by the age model (see text for details). Samples with poor modern analogue shown with circle.

Chapter 5 : Figures & Tables

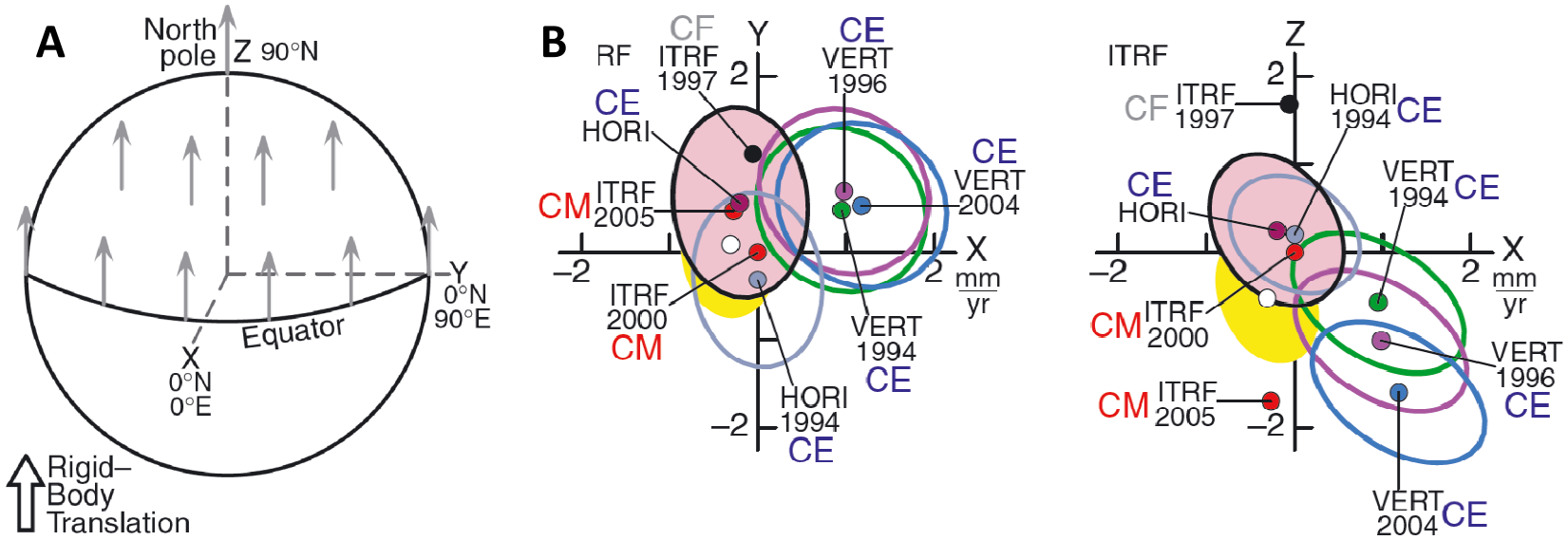

Figure 5.1 – Definition of the Earth's centre. Changing the estimate of the velocity of the Earth's centre in the direction of the South Pole changes all estimates of site velocity by the same amount in the direction of the North Pole (A). The amount by which the vertical (radial) and horizontal (lateral) components of sites velocity change depends on location (A) (Argus *et al.*, 2010 Fig 1). B shows differing velocities between definitions of the Earths centre, relative to the velocity of ITRF2000 at the centre (Argus *et al.*, 2010 Fig 3). Details of each model are given Argus *et al.* (2010) and references therein. Table gives estimates of *Z* velocity of different definitions of Earths centre for reference frames considered/used in this thesis relative to GEODVEL from Argus *et al.* (2010) (white circle in B). The *Z* axis translation for 60°N (south central Alaska) is calculated in the final column.

Earths centre	Model	Velocity *Z* axis (mm yr^{-1})	Velocity *Z* axis for 60°N (mm yr^{-1})
CE	GEODVEL (HORI) (Argus et al., 2010)	0.00	0.00
CM	ITRF2000 (Altamimi et al., 2002)	0.53	0.46
CM	ITRF2005 (Altamimi et al., 2007)	-1.17	-1.01

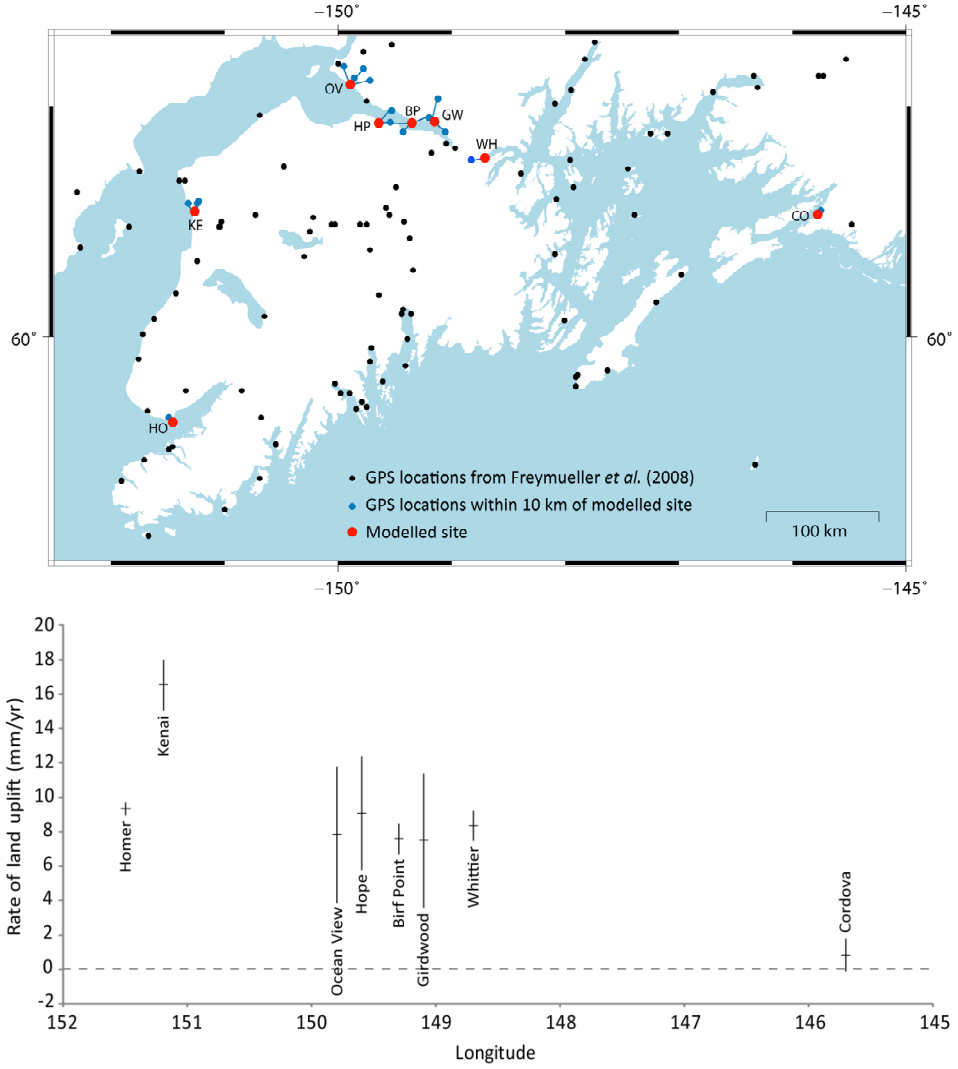

Site	GPS	$z \pm 1\sigma$ (ITRF2000)	$\bar{z} \pm 1\sigma$ (CE)
Homer	HOMA	8.9 ± 0.4	9.4 ± 0.4
Kenai	DIAN	18.6 ± 0.7	16.5 ± 1.5
	H81	8.6 ± 1.6	
	KCGB	24.5 ± 38.2	
	KIRT	12.3 ± 1.3	
Ocean View	VDUS	8.6 ± 1.8	7.8 ± 4.0
	OMAL	-5.6 ± 21.6	
	1000	6.2 ± 1.7	
	HILS	7.5 ± 1.5	
Hope	INDI	12.1 ± 1.3	9.1 ± 3.3
	TURN	7.3 ± 0.8	
Bird Point	TURN	7.3 ± 0.8	7.6 ± 0.9
	PF12	-11.9 ± 16.3	
	S72	6.5 ± 1.9	
Girdwood	S72	6.5 ± 1.9	7.5 ± 3.9
	POOR	9.1 ± 3.3	
	ALAS	6.9 ± 1.9	
Whittier	PRTG	7.9 ± 0.9	8.4 ± 0.9
Cordova	EYAC	0.7 ± 0.5	0.8 ± 1.0
	EYAK	-1.5 ± 1.2	

Figure 5.2 - Vertical velocities ($z \pm 1\sigma$) at GPS sites 10 km from 8 modelled sites relative to ITRF2000 (from Freymueller *et al.* (2008)) (see map), and weighted mean GPS velocities relative to CE ($\bar{z} \pm 1\sigma$) (see graph). Upper weighted mean vertical velocity for each model site used to constrain GIA models.

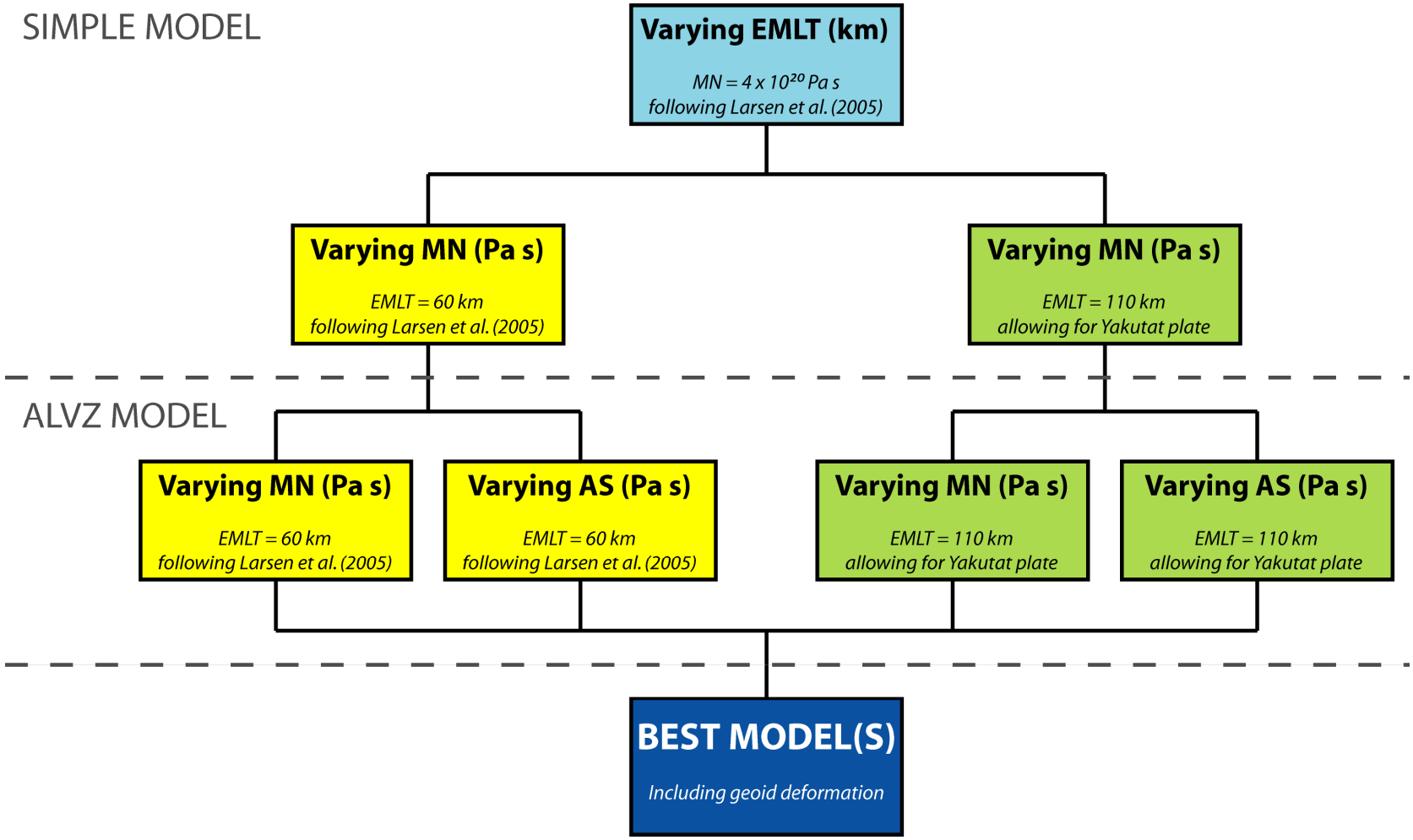

Figure 5.3 - Flow chart of earth model development to test geophysical response to ice load changes through the last earthquake cycle in south central Alaska.

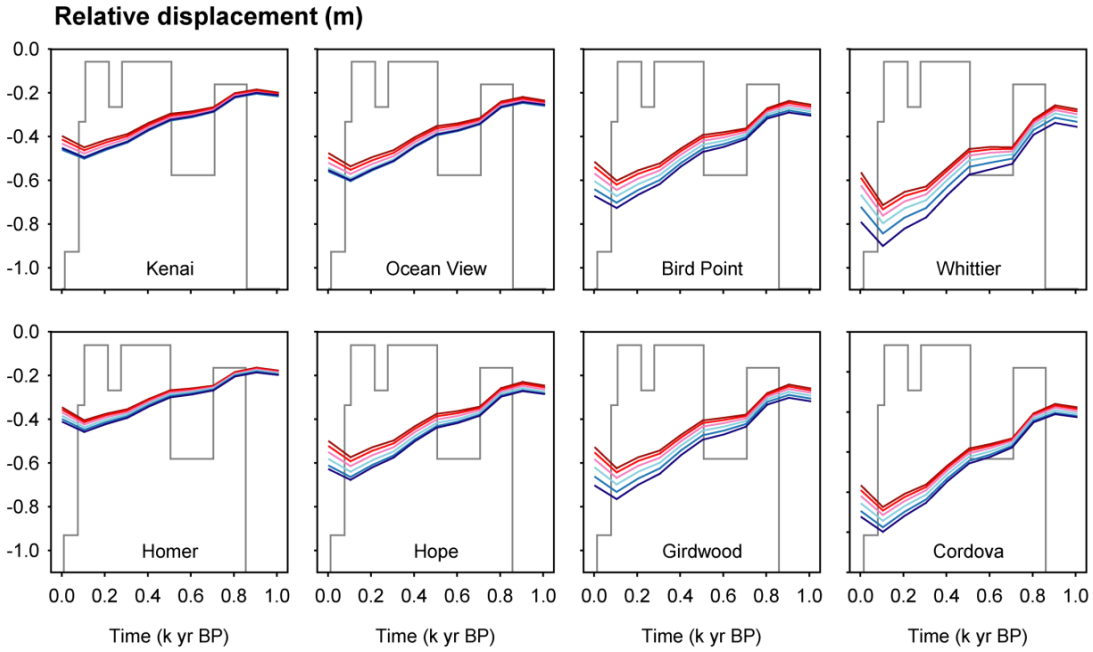

	Input parameters			Modelled rate of present day uplift (mm yr^{-1})							
	EMLT (km)	AS (x 10^{21} Pa s)	MN (x 10^{21} Pa s)	Homer	Kenai	Ocean View	Hope	Bird Point	Girdwood	Whittier	Cordova
	150	-	0.4	1.3	1.2	1.4	1.6	1.8	2.0	3.0	2.4
	130	-	0.4	1.2	1.1	1.3	1.6	1.8	2.0	2.9	2.3
	110	-	0.4	1.2	1.1	1.3	1.5	1.7	2.0	2.9	2.2
	90	-	0.4	1.2	1.1	1.2	1.4	1.6	1.8	2.7	2.1
	70	-	0.4	1.1	1.0	1.2	1.4	1.5	1.7	2.7	2.0
	50	-	0.4	1.1	1.1	1.2	1.3	1.5	1.6	2.5	1.9

Figure 5.4 - Simple earth model results with effective model lithospheric thicknesses (EMLT) from 150-50 km, at 20 km intervals, and a mantle viscosity of 4 x 10^{20} Pa s (following Larsen *et al.*'s (2005) best fit earth model). Graphs show modelled displacement (m) relative to CE (see text, section 5.3 for details) for the last 1000 years for eight selected model sites around south central Alaska. Piecewise ice load model (with arbitrary y-axis) overlain in grey for reference. The table summarises model input parameters (viscosity of asthenosphere (AS) (where applicable) and mantle (MN) expressed as x 10^{21} Pa s), and modelled rates of present day uplift (relative to CE, to one decimal place, mm yr^{-1}) for each site. Those models where upper weighted mean vertical velocities (Figure 5.2) minus modelled GIA present day land uplift is less than zero for sites from Kenai to Whittier, or greater than zero for Cordova, would be shaded in grey and rejected. There is none in this instance.

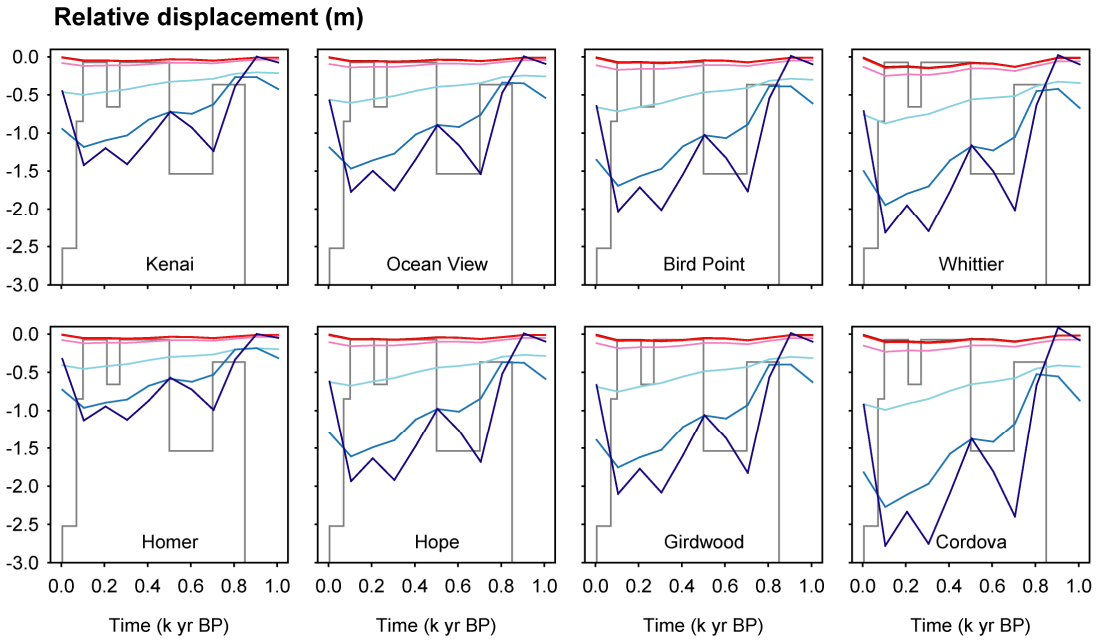

	Input parameters			Modelled rate of present day uplift (mm yr^{-1})							
	EMLT (km)	AS (x 10^{21} Pa s)	MN (x 10^{21} Pa s)	Homer	Kenai	Ocean View	Hope	Bird Point	Girdwood	Whittier	Cordova
	60	-	400	0.8	0.7	0.8	1.0	1.1	1.2	2.1	1.4
	60	-	40	0.8	0.7	0.8	1.0	1.1	1.2	2.1	1.4
	60	-	4	0.8	0.7	0.8	1.0	1.1	1.2	2.1	1.4
	60	-	0.4	1.1	1.0	1.2	1.3	1.5	1.7	2.6	2.0
	60	-	0.04	4.7	5.0	6.0	6.7	7.2	7.6	9.2	9.6
	60	-	0.004	12.3	14.9	18.4	20.2	21.3	22.1	24.8	29.1

Figure 5.5 - Simple earth model results to test varying mantle viscosity, with effective model lithospheric thickness (EMLT) of 60 km. Graphs show modelled displacement (m) relative to CE (see text, section 5.3 for details) for the last 1000 years for eight selected model sites around south central Alaska. Piecewise ice load model (with arbitrary y-axis) overlain in grey for reference. The table summarises model input parameters (viscosity of asthenosphere (AS) (where applicable) and mantle (MN) expressed as x 10^{21} Pa s), and modelled rates of present day uplift (relative to CE, to one decimal place, mm yr^{-1}) for each site. Those models where upper weighted mean vertical velocities (Figure 5.2) minus modelled GIA present day land uplift is less than zero for sites from Kenai to Whittier, or greater than zero for Cordova, are shaded in grey and rejected.

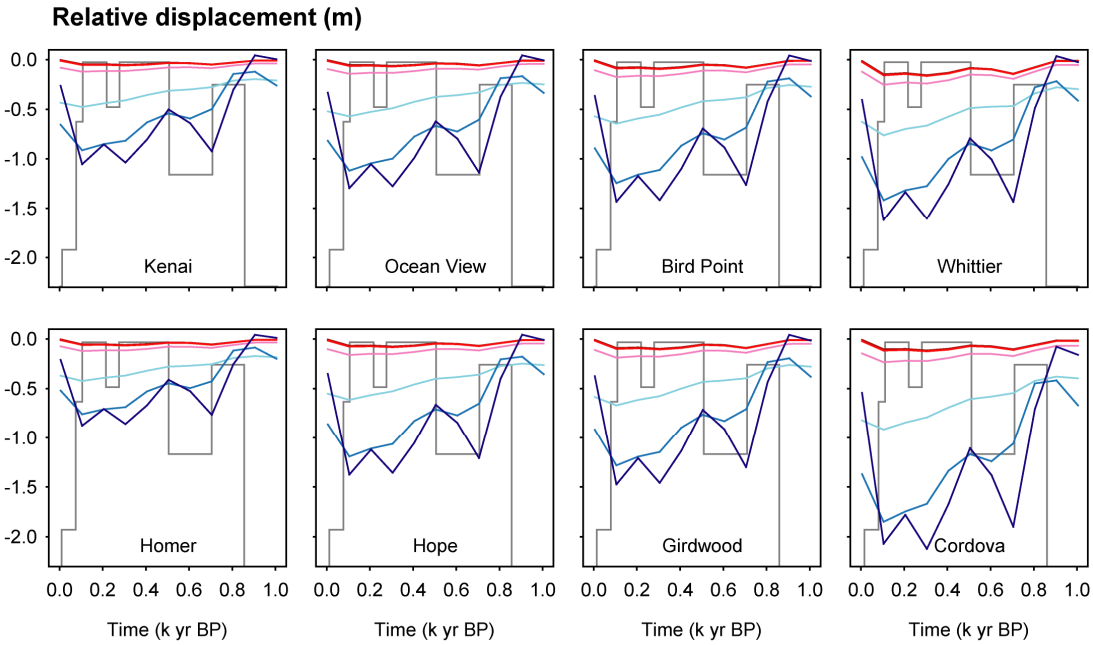

	Input parameters			Modelled rate of present day uplift (mm yr^{-1})							
	EMLT (km)	AS (x 10^{21} Pa s)	MN (x 10^{21} Pa s)	Homer	Kenai	Ocean View	Hope	Bird Point	Girdwood	Whittier	Cordova
	110	-	400	0.9	0.7	0.9	1.1	1.3	1.4	2.4	1.6
	110	-	40	0.9	0.7	0.8	1.1	1.3	1.4	2.4	1.6
	110	-	4	0.9	0.7	0.9	1.1	1.3	1.4	2.4	1.6
	110	-	0.4	1.2	1.1	1.3	1.5	1.7	1.9	2.9	2.2
	110	-	0.04	4.6	5.1	6.0	6.5	6.9	7.2	8.5	9.3
	110	-	0.004	10.2	12.0	14.6	15.5	16.2	16.7	18.6	22.7

Figure 5.6 - Simple earth model to test varying mantle viscosity, with effective model lithospheric thickness (EMLT) of 110 km. Graphs show modelled displacement (m) relative to CE (see text, section 5.3 for details) for the last 1000 years for eight selected model sites around south central Alaska. Piecewise ice load model (with arbitrary y-axis) overlain in grey for reference. The table summarises model input parameters (viscosity of asthenosphere (AS) (where applicable) and mantle (MN) expressed as x 10^{21} Pa s), and modelled rates of present day uplift (relative to CE, to one decimal place, mm yr^{-1}) for each site. Those models where upper weighted mean vertical velocities (Figure 5.2) minus modelled GIA present day land uplift is less than zero for sites from Kenai to Whittier, or greater than zero for Cordova, are shaded in grey and rejected.

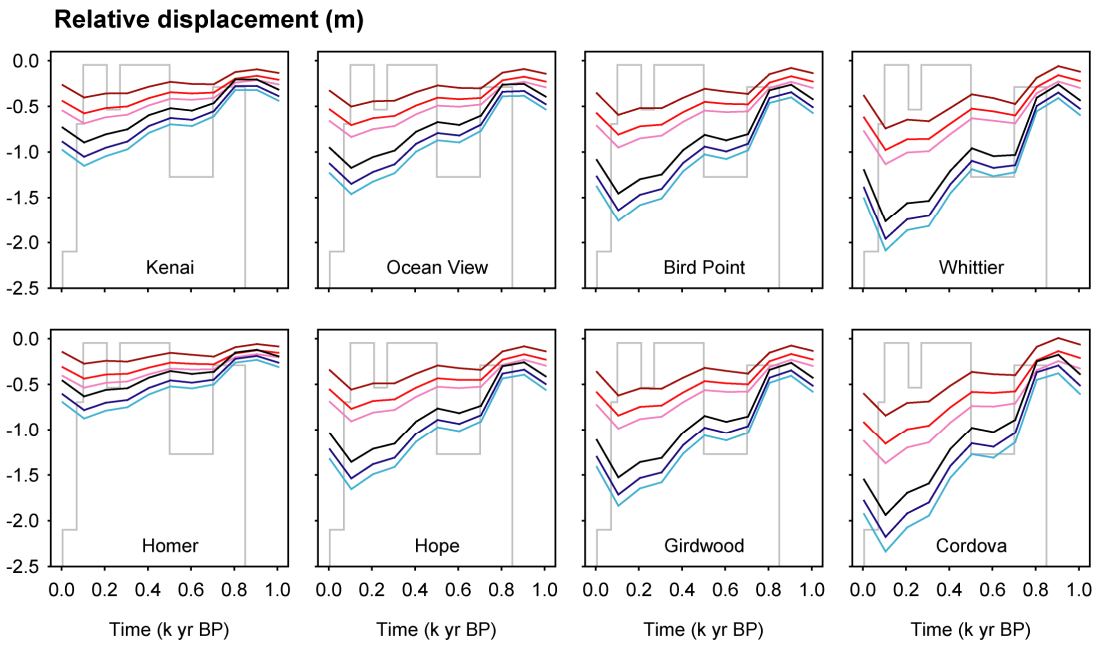

	Input parameters			Modelled rate of present day uplift (mm yr^{-1})							
	EMLT (km)	AS (x 10^{21} Pa s)	MN (x 10^{21} Pa s)	Homer	Kenai	Ocean View	Hope	Bird Point	Girdwood	Whittier	Cordova
	110	0.004	40	2.2	2.4	3.1	2.2	4.1	4.5	6.3	4.8
	110	0.004	0.8	2.3	2.5	3.2	2.3	4.2	4.6	6.4	5.0
	110	0.004	0.4	2.4	2.7	3.3	2.4	4.4	4.8	6.6	5.2
	60	0.004	40	3.4	3.7	4.8	3.4	7.2	7.9	10.5	8.4
	60	0.004	0.8	3.5	3.8	5.0	3.5	7.4	8.1	10.7	8.6
	60	0.004	0.4	3.6	4.0	5.2	3.6	7.7	8.3	10.9	9.0

Figure 5.7 - Asthenospheric low viscosity zone (ALVZ) model results to test varying mantle viscosity, with effective model lithospheric thicknesses (EMLT) of 110 km and 60 km and asthenospheric viscosity of 4 x 10^{18} Pa s (following Larsen *et al.*'s (2005) best fit earth model). Graphs show modelled displacement (m) relative to CE (see text, section 5.3 for details) for the last 1000 years for eight selected model sites around south central Alaska. Piecewise ice load model (with arbitrary y-axis) overlain in grey for reference. The table summarises model input parameters (viscosity of asthenosphere (AS) (where applicable) and mantle (MN) expressed as x 10^{21} Pa s), and modelled rates of present day uplift (relative to CE, to one decimal place, mm yr^{-1}) for each site. Those models where upper weighted mean vertical velocities (Figure 5.2) minus modelled GIA present day land uplift is less than zero for sites from Kenai to Whittier, or greater than zero for Cordova, are shaded in grey and rejected.

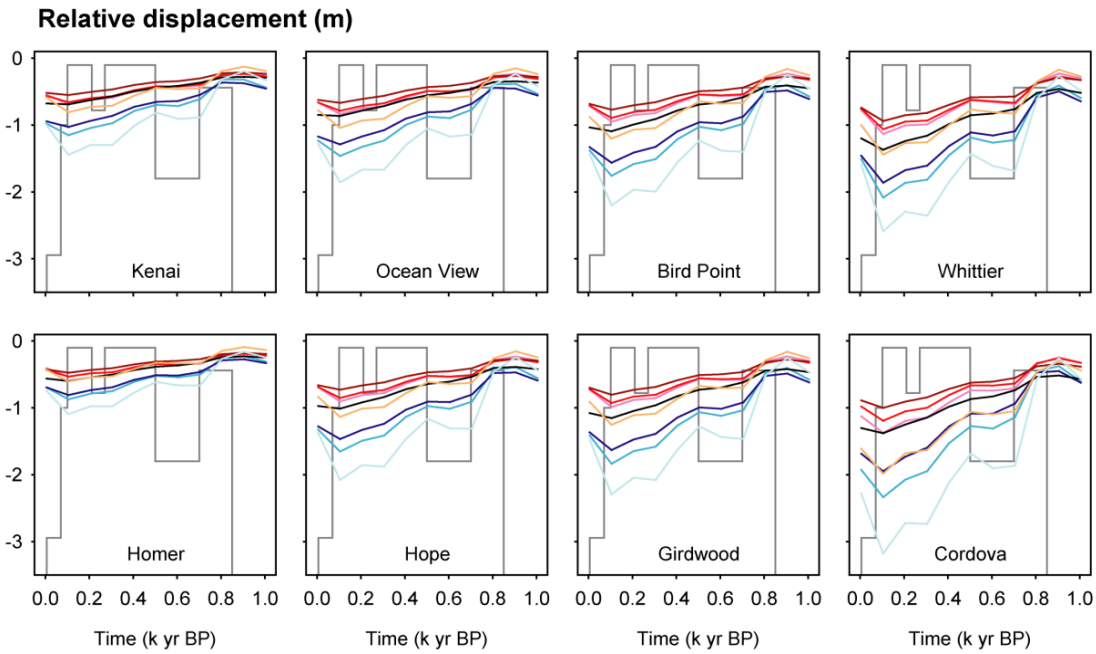

	Input parameters			Modelled rate of present day uplift (mm yr^{-1})							
	EMLT (km)	AS (x 10^{21} Pa s)	MN (x 10^{21} Pa s)	Homer	Kenai	Ocean View	Hope	Bird Point	Girdwood	Whittier	Cordova
	110	0.04	0.4	1.2	1.0	1.3	1.8	2.1	2.5	4.1	2.8
	110	0.008	0.4	2.0	2.1	2.6	3.2	3.7	4.0	5.8	4.5
	110	0.004	0.4	2.4	2.7	3.3	2.4	4.4	4.8	6.6	5.2
	110	0.001	0.4	3.1	4.1	5.1	5.9	6.4	6.8	8.7	9.0
	60	0.04	0.4	1.1	0.8	1.1	1.6	2.0	2.3	4.1	2.6
	60	0.008	0.4	2.6	2.4	3.2	4.5	5.2	5.8	8.2	6.3
	60	0.004	0.4	3.6	4.0	5.2	3.6	7.7	8.3	10.9	9.0
	60	0.001	0.4	6.1	8.0	10.4	12.6	13.8	14.7	17.8	18.5

Figure 5.8 - Asthenospheric low viscosity zone (ALVZ) model results to test varying asthenosphere viscosity, with effective model lithospheric thicknesses (EMLT) of 110 km and 60 km and mantle viscosity of 4 x 10^{20} Pa s (following Larsen *et al.*'s (2005) best fit earth model and Peltier's (2002) VM2 model). Graphs show modelled displacement (m) relative to CE (see text, section 5.3 for details) for the last 1000 years for eight selected model sites around south central Alaska. Piecewise ice load model (with arbitrary y-axis) overlain in grey for reference. The table summarises model input parameters (viscosity of asthenosphere (AS) (where applicable) and mantle (MN) expressed as x 10^{21} Pa s), and modelled rates of present day uplift (relative to CE, to one decimal place, mm yr^{-1}) for each site. Those models where upper weighted mean vertical velocities (Figure 5.2) minus modelled GIA present day land uplift is less than zero for sites from Kenai to Whittier, or greater than zero for Cordova, are shaded in grey and rejected.

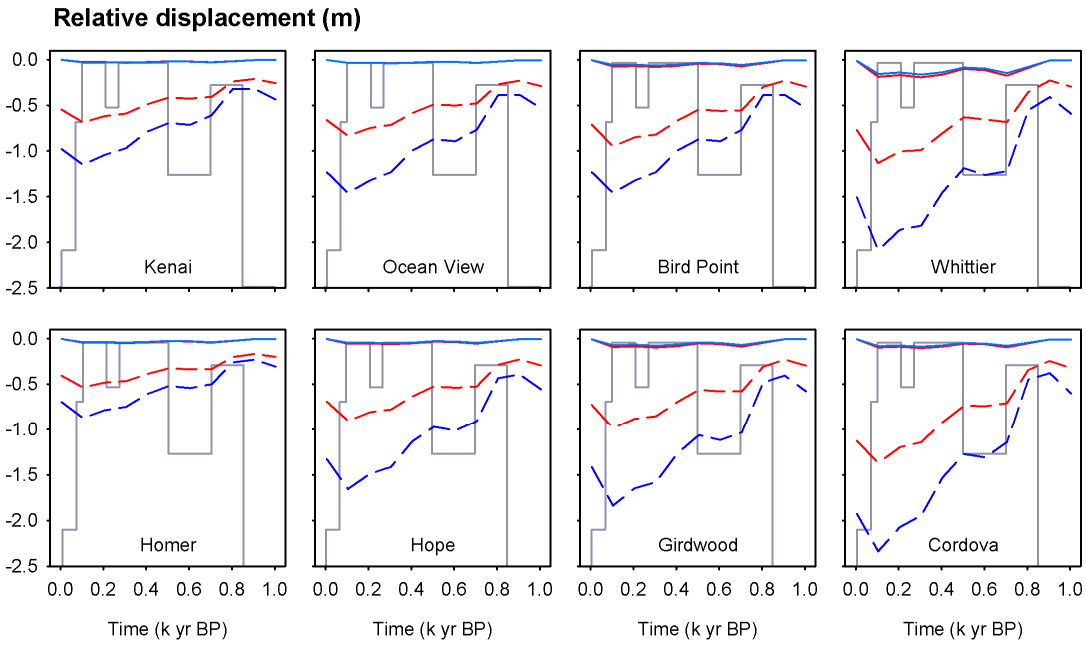

Figure 5.9 - Asthenospheric low viscosity zone (ALVZ) model results to test elastic (solid lines) against viscoelastic (dashed lines) to ice load changes. Earth model uses effective model lithospheric thicknesses (EMLT) of 110 km (red) and 60 km (blue), asthenospheric viscosity 4 x 10^{18} Pa s mantle viscosity of 4 x 10^{20} Pa s (following Larsen *et al.*'s (2005) best fit earth model and Peltier's (2002) VM2 model). Graphs show modelled relative displacement (m) for the last 1000 years for eight selected model sites around south central Alaska. Piecewise ice load model (with arbitrary y-axis) overlain in grey for reference. There is relatively little response from the elastic (lithosphere) component of the Earth's rheology. The difference between the viscoelastic response of the two effective model lithospheric thicknesses show it is the asthenospheric thickness that is the dominant rheological control.

i

	ICE5G(VM2) modelled rate of present day uplift (mm yr^{-1})			
	Seldovia	Nikiski	Anchorage	Cordova
0 k yr BP	-0.28	-0.30	-0.30	-0.19

ii

	Input parameters			Modelled rate of present day uplift (mm yr^{-1})							
	EMLT (km)	AS (x 10^{21} Pa s)	MN (x 10^{21} Pa s)	Homer	Kenai	Ocean View	Hope	Bird Point	Girdwood	Whittier	Cordova
	110	0.004	40	1.1	1.3	1.9	1.1	3.0	3.4	1.2	3.8
	110	0.004	0.8	1.2	1.4	2.0	1.2	3.1	3.5	1.4	4.0
	110	0.004	0.4	1.3	1.6	2.2	1.3	3.3	3.7	1.5	4.3
	60	0.004	40	2.3	2.5	3.7	2.2	6.1	6.8	3.0	7.5
	60	0.004	0.8	2.4	2.7	3.9	2.4	6.3	7.0	3.2	7.7
	60	0.004	0.4	2.6	2.9	4.1	2.5	6.5	7.2	3.4	8.1

iii

	110	0.04	0.4	0.1	-0.1	0.1	0.6	1.0	1.3	-0.5	1.9
	110	0.008	0.4	0.9	0.9	1.5	2.1	2.5	2.9	0.8	3.6
	110	0.004	0.4	1.3	1.6	2.2	1.3	3.3	3.7	1.5	4.3
	110	0.001	0.4	2.0	2.9	3.9	4.7	5.2	5.7	3.2	8.1
	60	0.04	0.4	0.1	-0.3	-0.1	0.4	0.8	1.2	-0.8	1.7
	60	0.008	0.4	1.5	1.3	2.1	3.4	4.1	4.7	1.4	5.4
	60	0.004	0.4	2.6	2.9	4.1	2.5	6.5	7.2	3.4	8.1
	60	0.001	0.4	5.0	6.9	9.3	11.5	12.6	13.5	8.6	17.6

Table 5.1 – Asthenospheric low viscosity zone (ALVZ) modelled rates of present day uplift (relative to CE, to one decimal place, mm yr^{-1}) for each site, from Figure 5.7 (ii) and Figure 5.8 (iii), with addition of long wavelength GIA uplift at 0 k yr BP as estimated by ICE5G(VM2) (Peltier, 2004), for the tide gauge location nearest to each model site (i). Those models where upper weighted mean vertical velocities (Figure 5.2) minus modelled GIA present day land uplift is less than zero for sites from Kenai to Whittier, or greater than zero for Cordova, are shaded in grey and rejected.

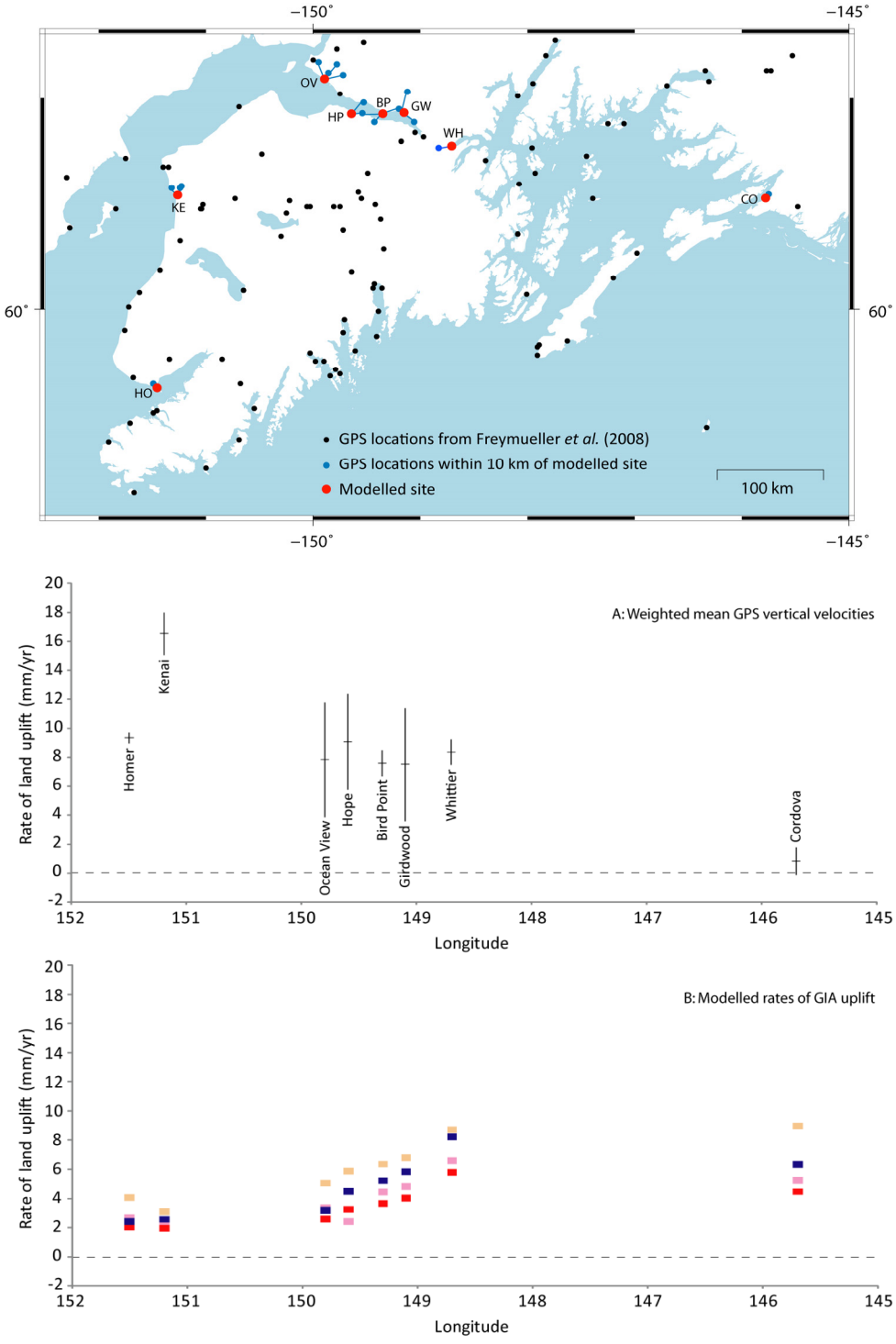

Figure 5.10 - (A) Mean 1992-2007 vertical velocities from GPS (Freymueller *et al.* (2008) and top map) used to constrain valid modelled rates of present day local GIA land uplift (B) for eight modelled sites in south central Alaska. Colours in B correlate to earth models in Figure 5.8. All valid earth models suggest there is some ongoing uplift due to GIA, and therefore the vertical velocities in A must be a combination of AD 1964 post-seismic uplift and GIA. The proportion of the present day uplift that is a result of LIA GIA, relative to ongoing tectonic deformation, is dependent on the selected earth model.

Chapter 6 : Figures & Tables

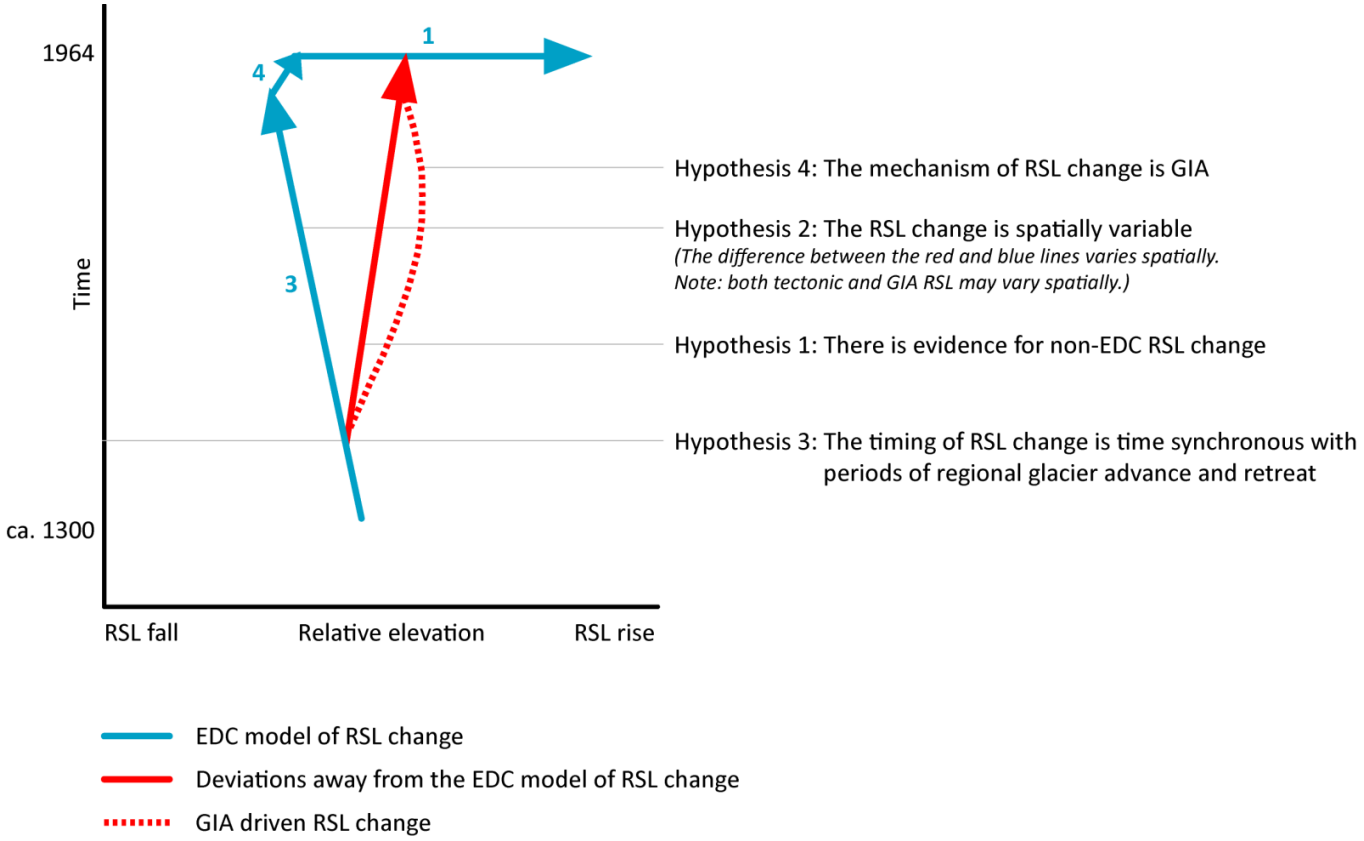

Figure 6.1 - Schematic of hypothesis testing. Blue arrows show expected tectonically driven land level changes under the EDC model (numbers correlation to numbers on Figure 1.3). Red arrows show possible deviation away from the EDC model should there be evidence from non-EDC RSL change in upper Cook Inlet. The discussion in chapter 6 integrates the modelling results and geological data in this thesis to test each hypothesis.

Figure 6.2 - Aerial photos of the Girdwood area of Turnagain Arm from July AD 1957 (left image) and June AD 2006 (right image). Circles provide image reference points. Lithological evidence shows well developed marshes existing in AD 1957 prior to the AD 1964 earthquake. Comparison of the two photos shows the marsh front to be at a similar position prior to the AD 1964 coseismic submergence (left image) relative to the present day (right image). These photographs provide evidence that, though tidal channels migrate seasonally and following the AD 1964 earthquake, the geography of Turnagain Arm has altered little over the last earthquake cycle, suggesting there has been no significant change in tidal regime. Images source: USGS EarthExplorer (http://edcsns17.cr.usgs.gov/EarthExplorer/).

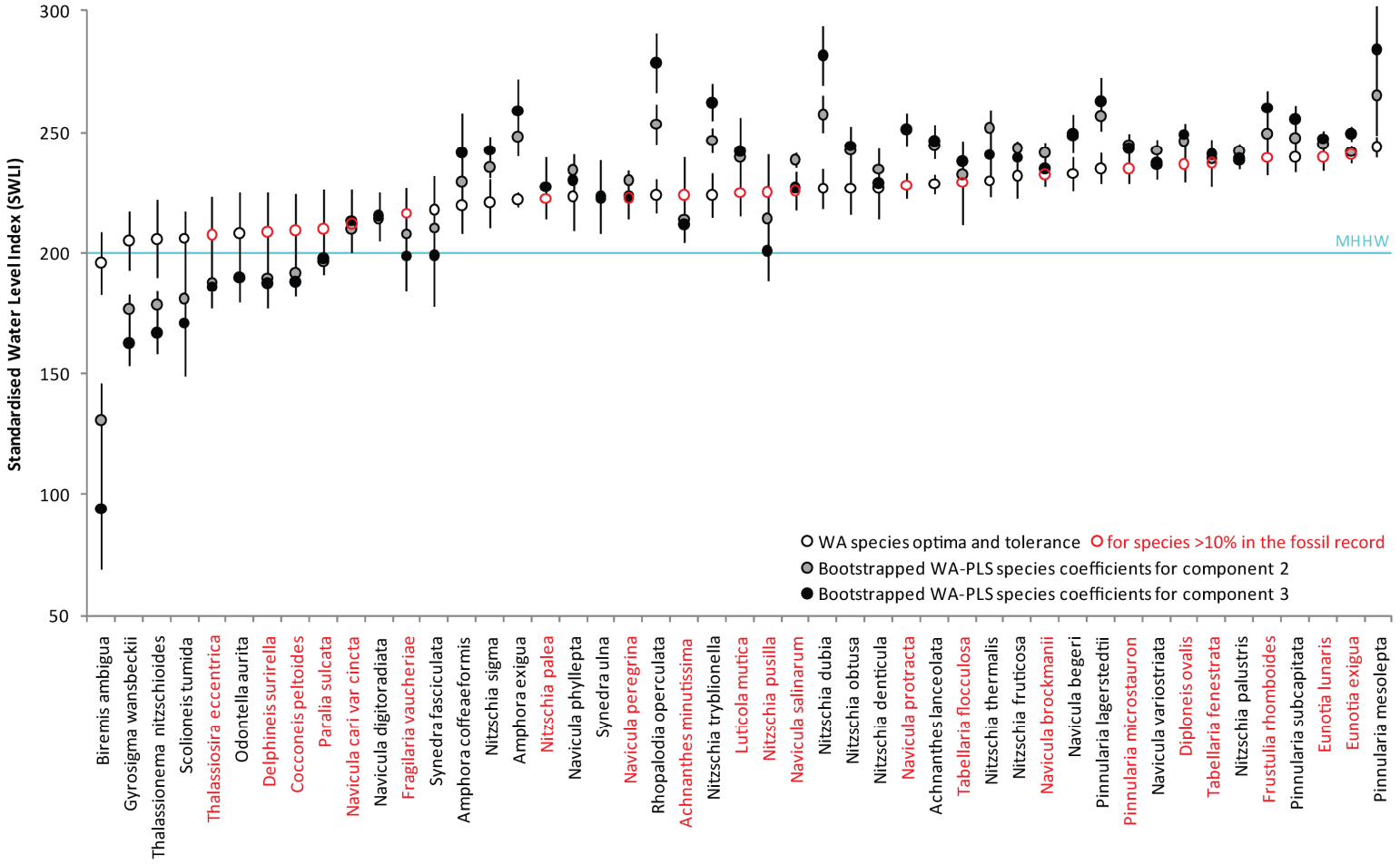

Figure 6.3 – WA estimated optima and tolerances (in SWLI units) of species >10% of total diatom valves counted in the silt with rootlets (samples with SWLI >180) training set, alongside updated species coefficients and bootstrapped estimated errors for the same species by WA-PLS components 2 and 3. Species in red also account for >10% of total diatom valves counted in the fossil samples from Girdwood, Bird Point, Hope and Ocean View.

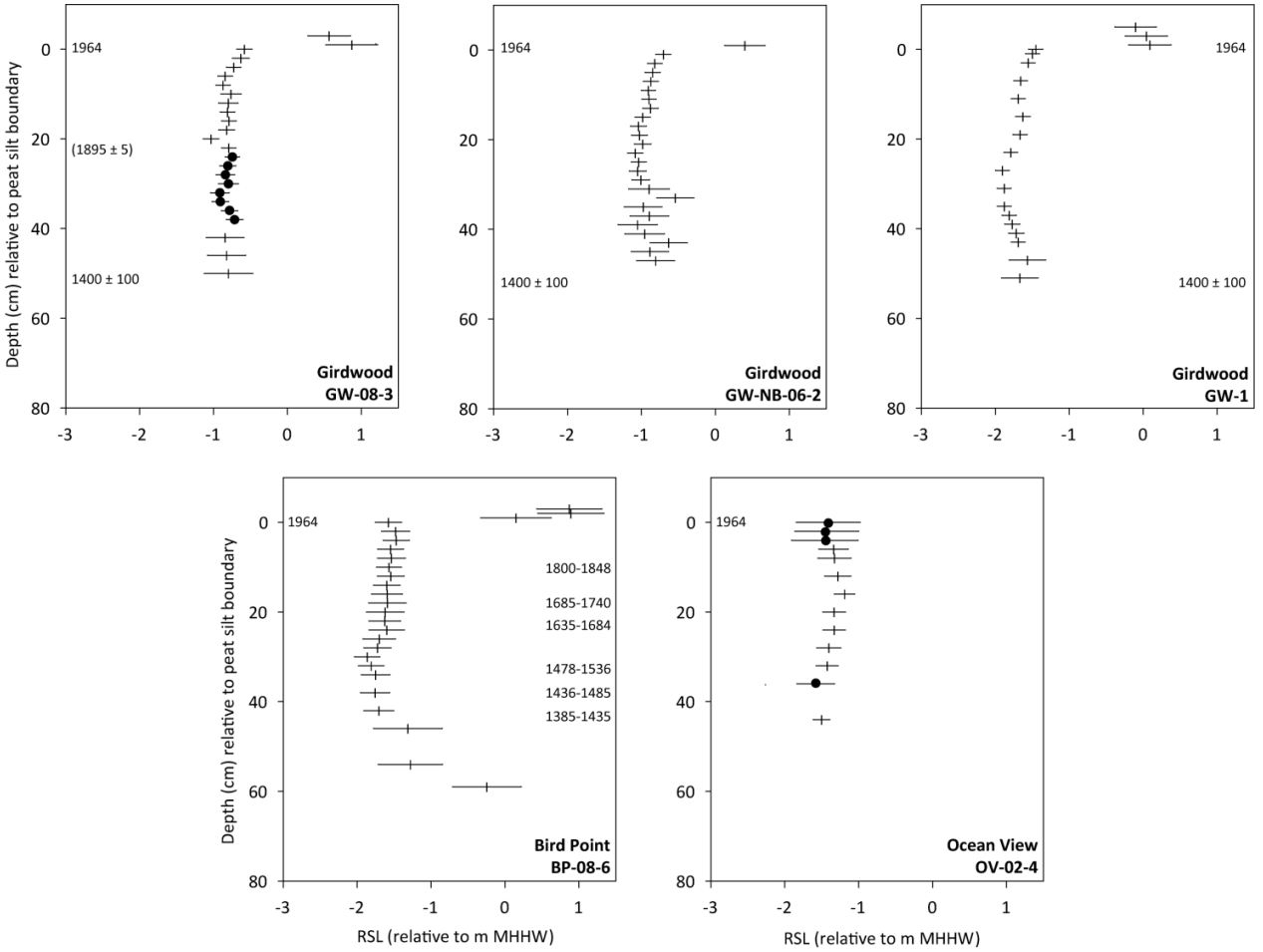

Figure 6.4 - Summary RSL curves estimated by the transfer functions detailed in Chapter 4 for five cores from Girdwood, Bird Point and Ocean View. Dates on BP-08-6 are the 2σ range for 6 radiocarbon samples as estimated by the OxCal Bayesian age model (Figure 4.17A) with additional dates on other cores from lithological, tephra and pollutant markers (see Chapter 4 for details). These RSL changes can be compared against the conceptual model in Figure 6.1 to test the working hypotheses.

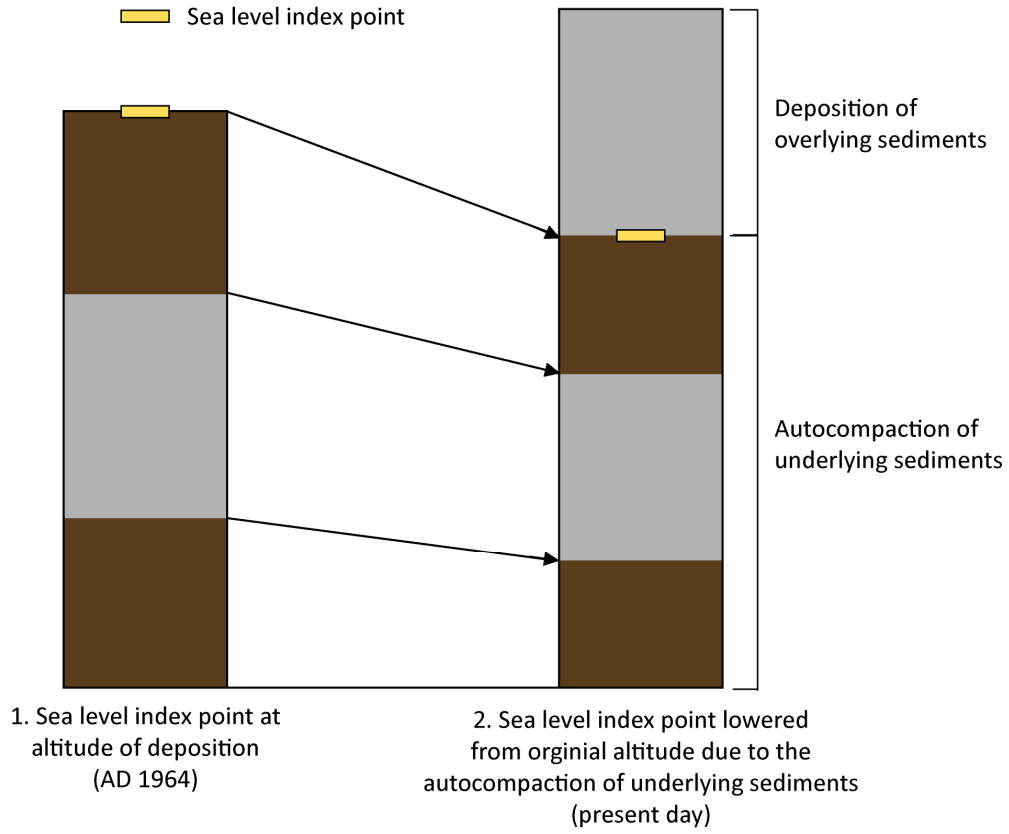

Figure 6.5 - The effect of autocompaction on a sea level index point. The sea level index point is lowered the from the altitude of deposition due to the compaction of underlying sediments by the overburden sediments (modified from Brain (2006) Figure 2.10).

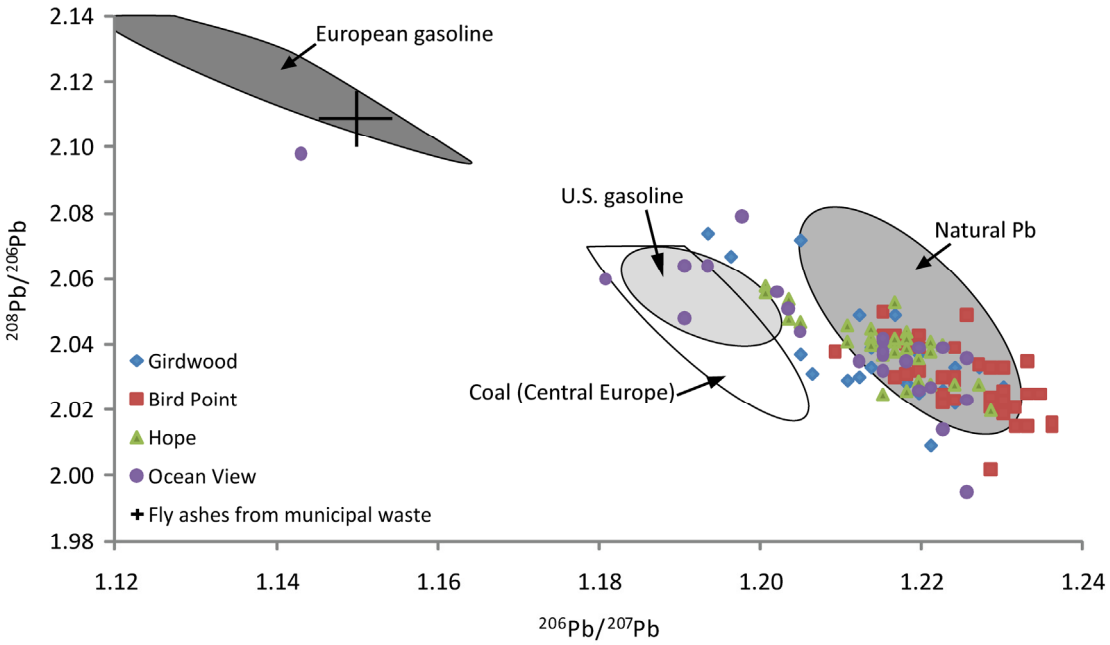

Figure 6.6 - A three isotope plot ($^{206}Pb/^{207}Pb$ v $^{208}Pb/^{206}Pb$) for the fossil stable lead data from Girdwood, Bird Point, Hope and Ocean View, overlaying a schematic (adapted from Komarek *et al.* (2008) Figure 1) showing the isotopic composition of different lead sources.

Reference	Time period	Rate of ESL (mm yr^{-1})	Data source
Church and White (2006)	1870-2000	1.30 ± 0.40	Satellite altimeter data, tide gauge data
Donnelly *et al.* (2004)	1893-1921	2.40	New York, USA tide gauge and New England, USA salt marsh records
Gehrels *et al.* (2005)	19th century	1.60	Nova Scotia, Canada salt marsh records
Gehrels *et al.* (2006)	1800-2000	2.00	Iceland salt marsh records
Jevrejeva *et al.* (2008)	1920-1950	2.50	Modelling
Woodworth (1999)	20th century	1.22 ± 0.25	Liverpool, UK tide gauge
Woodworth (2009)	1901-2006	1.40 ± 0.20	UK tide gauge, geological and geodetic data

Table 6.1 - Estimates of the rate of eustatic sea level (ESL) rise from the 1800's to present from modelling, satellite observation and palaeoenvironmental reconstruction.

Core	$\Delta\xi_{rsl}(\tau)$ (m)	$\Delta\xi_{cos}(\tau)$ (m)	$\Delta\xi_{sed}(\tau)$ (m)	$\xi_{peat}(\tau)$ (m)	$\Delta\xi_{int}(\tau)$ (m)	$\Delta\xi_{int}(\tau)$ (mm yr^{-1})	% AD 1964 coseismic
Minimum $\Delta\xi_{int}(\tau)$ (using minimum $\Delta\xi_{rsl}(\tau)$ of -0.2 mm yr^{-1})							
GW-1	-0.17	1.45	1.10	0.07	0.11	0.13	7
BP-08-6	-0.17	1.72	1.25	0.14	0.16	0.18	9
Maximum $\Delta\xi_{int}(\tau)$ (using maximum $\Delta\xi_{rsl}(\tau)$ of 1.0 mm yr^{-1})							
GW-1	0.86	1.45	1.10	0.07	1.14	1.33	79
BP-08-6	0.86	1.72	1.25	0.14	1.19	1.38	69

Table 6.2 - Minimum and maximum estimates of the rate of interseismic land uplift (mm yr^{-1}) for 860 years from the penultimate great earthquake to AD 1964 using the equation in Hamilton and Shennan (2005a) (see text for details) for Girdwood (GW-1, Hamilton and Shennan, 2005a) and Bird Point (BP-08-6). Minimum and maximum estimates of rate of $\Delta\xi_{rsl}(\tau)$ provide minimum and maximum estimates of $\Delta\xi_{int}(\tau)$ 0.1 and 1.4 mm yr^{-1} respectively for Turnagain Arm.

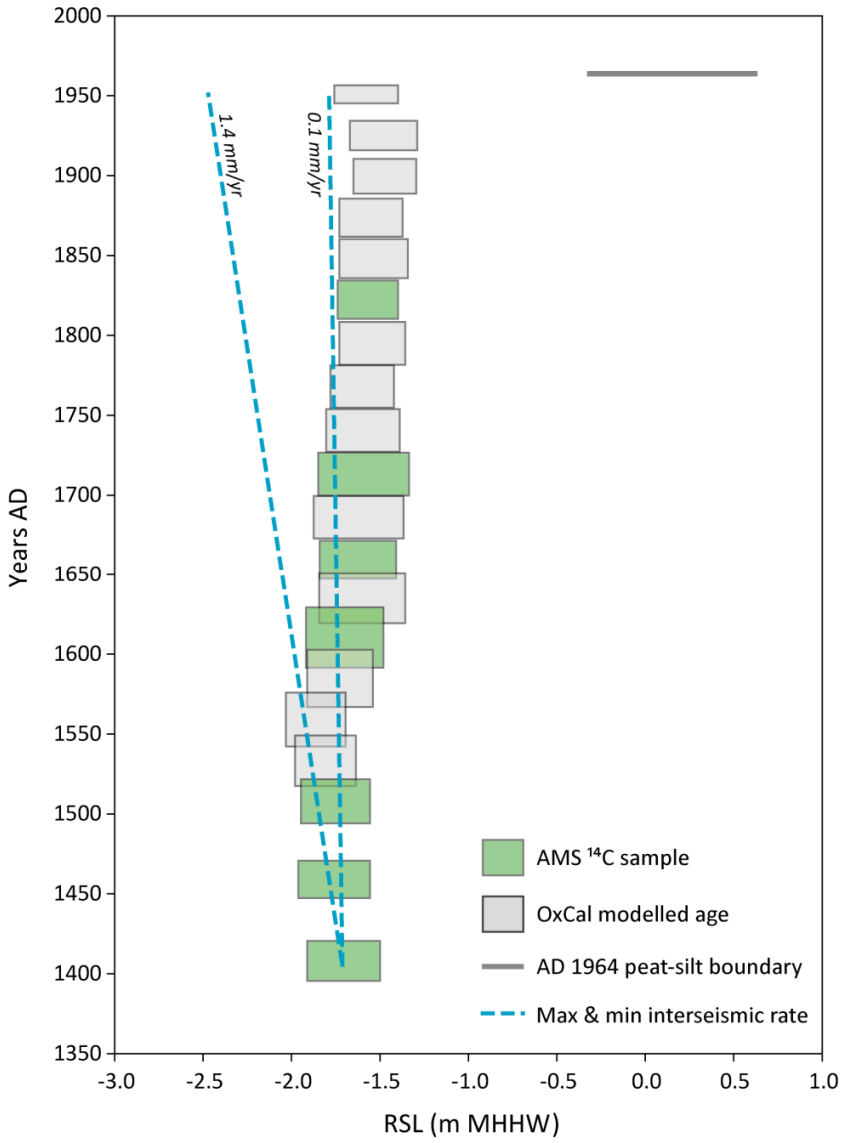

Figure 6.7 - Testing working hypothesis three. Transfer function based reconstruction of RSL at Bird Point (BP-08-6) over the last 600 years, showing the timing of a potential deviation away from the minimum (0.1 mm yr^{-1}) and maximum (1.4 mm yr^{-1}) estimates of the rate of interseismic land uplift. Boxes show sample specific 1σ reconstructed error on the x-axis and 2σ error from OxCal depositional age model on the y-axis using 1 cm thick sediment samples for ^{14}C AMS dating (section 4.3.2).

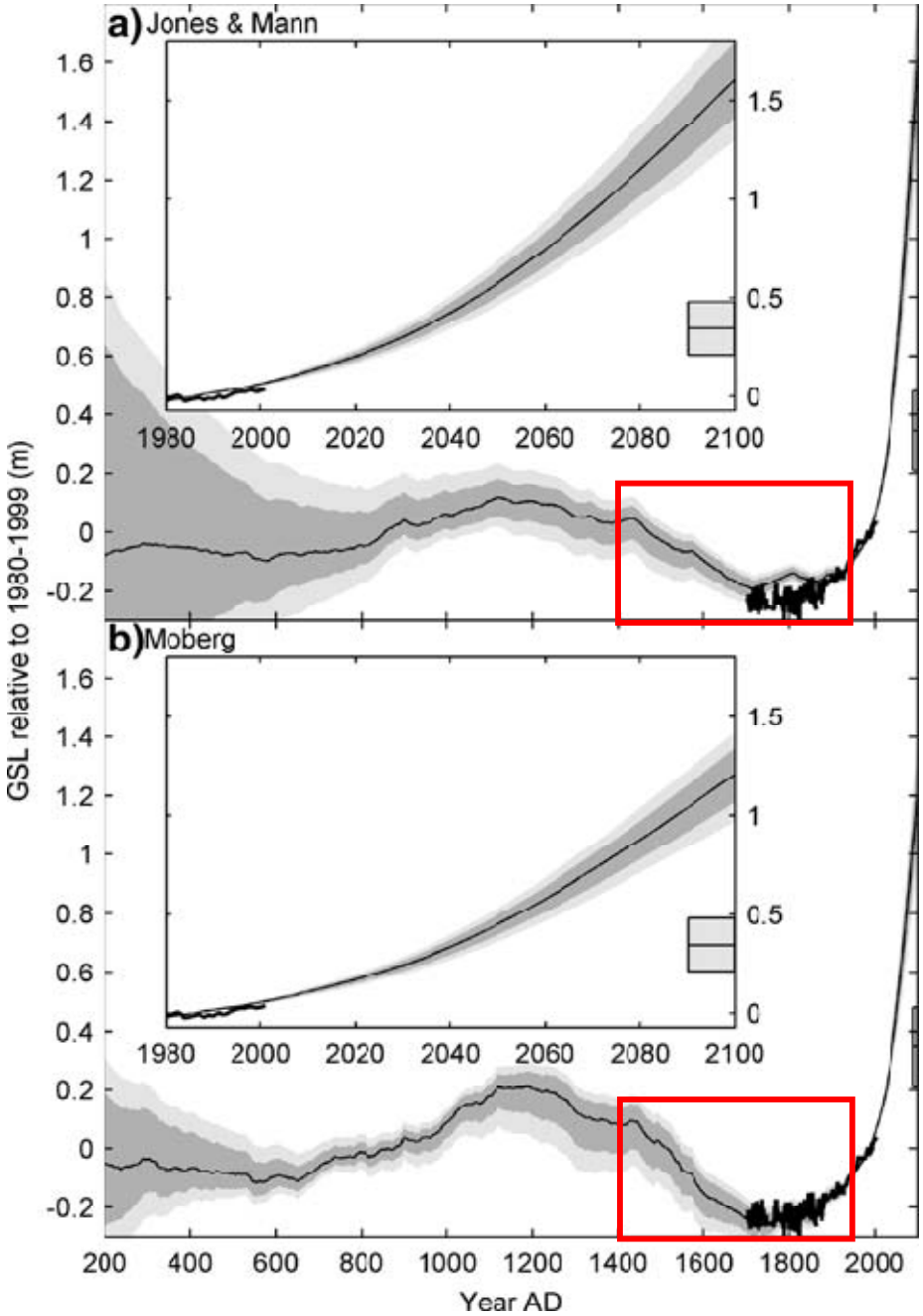

Figure 6.8 - Grinsted *et al.* (2009) projected eustatic sea level (GSL) relative to AD 1980-1999 average (m) based on IPCC scenario A1B using temperature reconstructions of A) Jones and Mann (2004) and B) Moberg *et al.* (2005). Thin black line is median likelihood distribution, dark grey band 1σ and light grey band 5-95 percentiles. The thick black line is reconstructed eustatic sea level extended to AD 1700 using Amsterdam sea level. Box shows IPCC A1B estimate for AD 2090-2100. Inserts show the projections and fits to the eustatic sea level data in greater detail for AD 1980-2100. Red boxes highlights time period of interest for this thesis showing predicted global sea level fall in the 16th-18th centuries (though the projected magnitude varies between the two temperature scenarios), inverse of that recorded in the Turnagain Arm salt marsh sediments (Figure 6.8). Adapted from Grinsted *et al.* (2009) Figure 7.

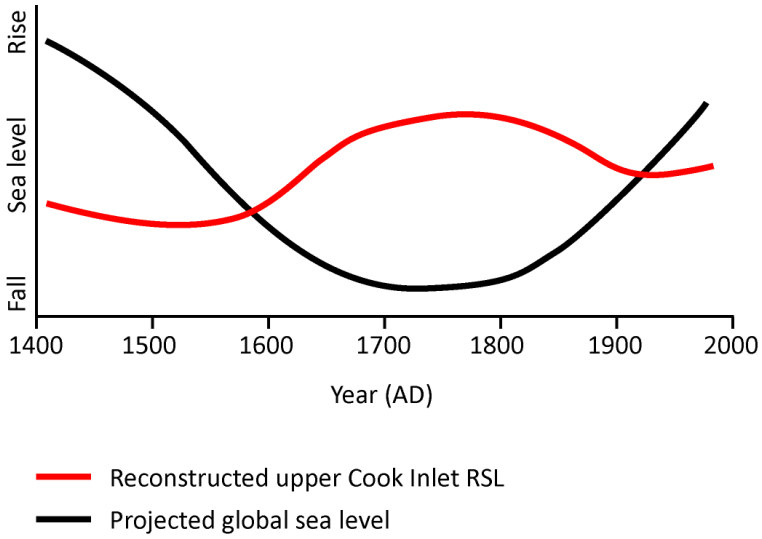

Figure 6.9 - Schematic of projected global sea level by Grinsted *et al.* (2009) against the general pattern of reconstructed RSL in upper Cook Inlet over AD 1400-1964, not taking into account any deviations from a global average (cf. Bindoff *et al.* 2007). Years on x-axis given for guidance only and do not show exact timing of RSL change. The direction of modelled global sea level is the inverse of that reconstructed from salt marsh sediments in upper Cook Inlet, indicating eustasy cannot be the mechanism for the upper Cook Inlet RSL change during AD 1600 – 1900.

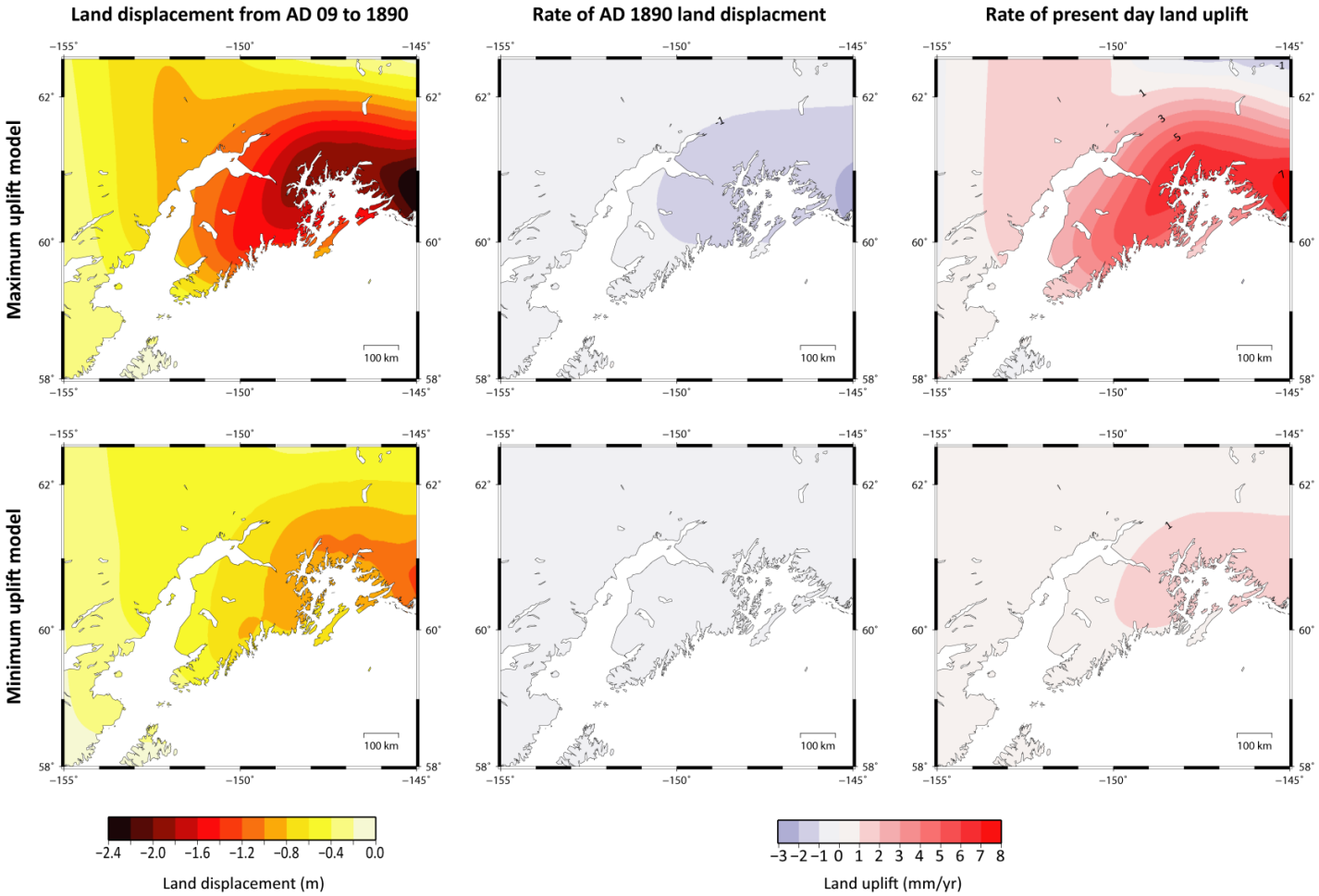

Figure 6.10 - Spatial representation of maximum LIA uplift (LT = 60 km, AS = 4 x 10^{18} Pa s) and minimum LIA uplift (LT = 110 km, AS = 4 x 10^{19} Pa s) regional asthenosphere low viscosity zone (ALVZ) Earth model (see Chapter 5 for details) estimates of AD 09 - 1890 land (radial) displacement (m) and AD 1890 and present (AD 2005) rates of land uplift (mm yr^{-1}) for south central Alaska. Radial displacement relative to CE (see section 5.3 for details).

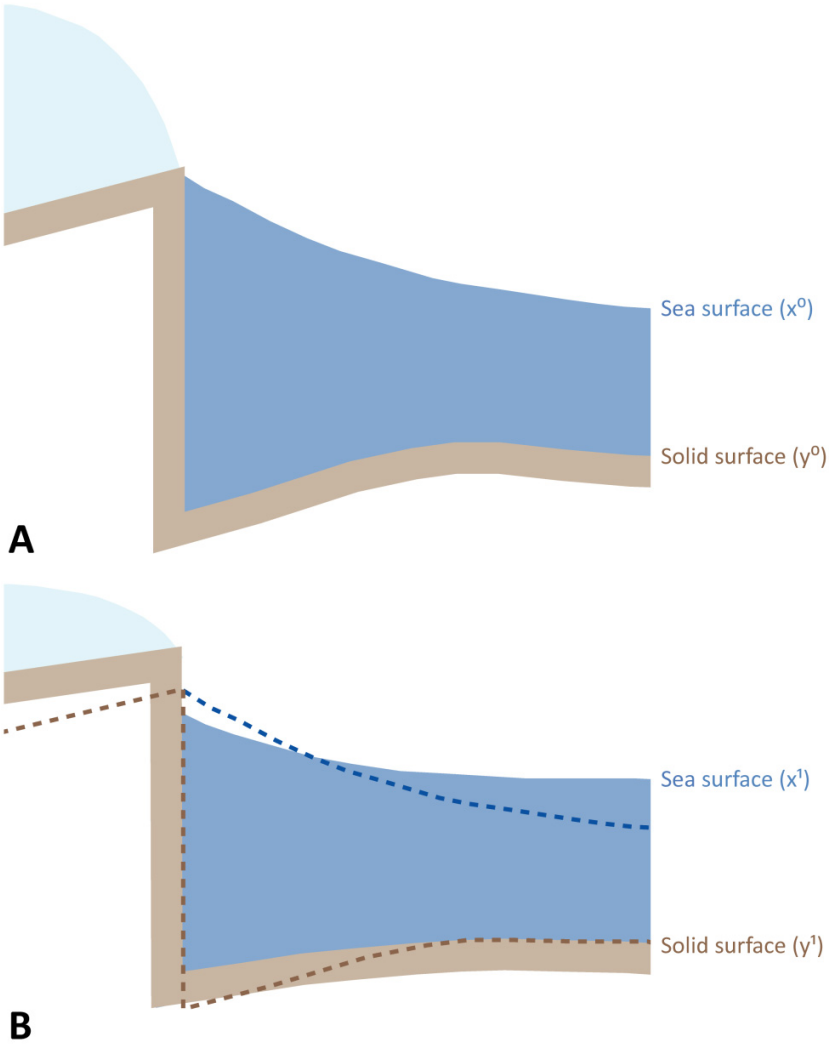

Figure 6.11 - Illustration of the influence of an ablating mountain glacier on the vertical displacement of the solid surface and the ocean geoid height, showing the location of the geoid (sea surface) before (A) and after (B) glacier melting. The relative change in sea level is the change in the sea surface (calculated by subtracting x^o from x^1) minus the change in position of the solid surface (y^o - y^1). The flux of the subsiding solid Earth (B) perturbs the geopotential causing the ocean surface to undergo a net fall near the ice mass and a net rise a greater distance from the ice mass. (Figure adapted from Tamisiea *et al.* (2003) Figure 5).

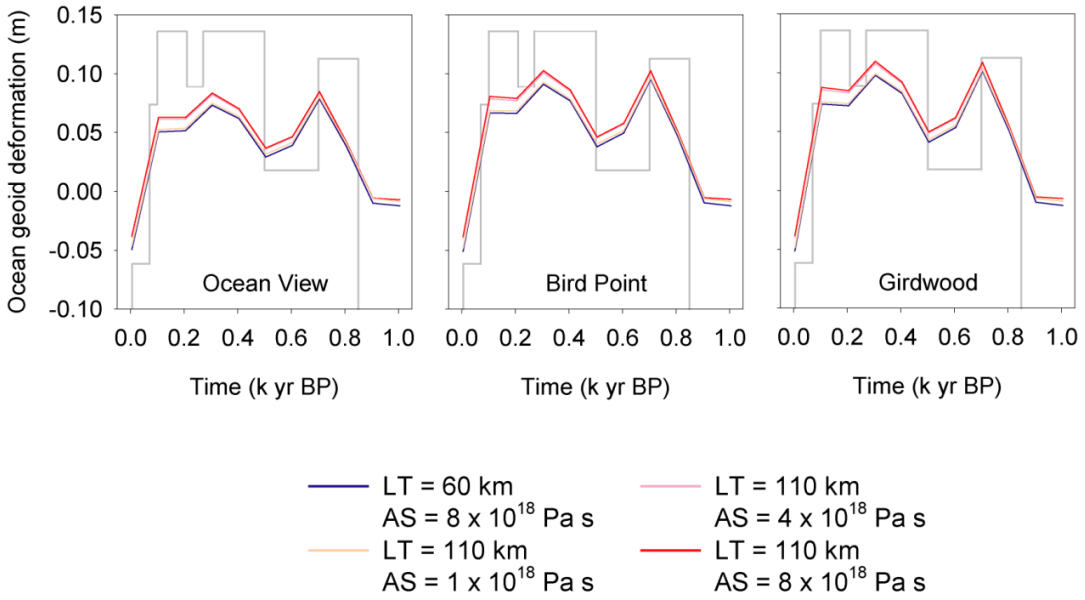

Figure 6.12 - Ocean geoid height deformation (m) at Ocean View, Bird Point and Girdwood over the last 1000 years predicted by asthenospheric low viscosity zone (ALVZ) best Earth models in TABOO (see text, section 5.7) in response to LIA ice thickness changes represented in the Larsen *et al.* (2005) regional ice model. Lithospheric thicknesses and asthenosphere viscosities follow key. Mantle viscosity set at 4 x 10^{20} Pa s (following Larsen *et al.*'s (2005) best fit earth model and Peltier's (2002) VM2 model). Piecewise ice load model (with arbitrary y-axis) overlain in grey for reference.

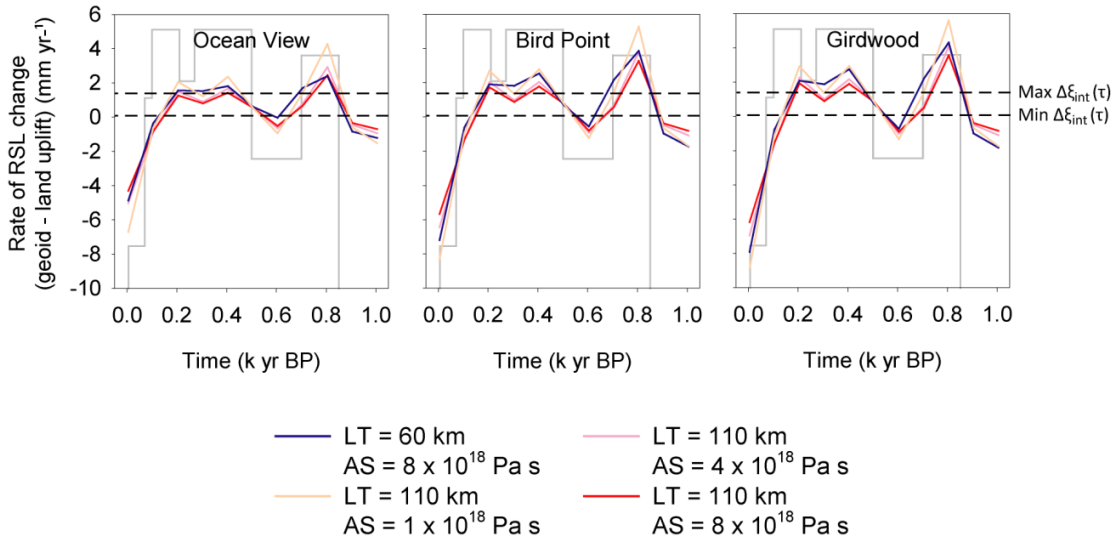

Figure 6.13 - Rate of RSL change (rate of ocean geoid height deformation minus rate of land uplift) at Ocean View, Bird Point and Girdwood over the last 1000 years predicted by asthenospheric low viscosity zone (ALVZ) best Earth models in TABOO (see text, section 5.7) in response to LIA ice thickness changes represented in the Larsen *et al.* (2005) regional ice model. Lithospheric thicknesses and asthenosphere viscosities follow key. Mantle viscosity set at 4 x 10^{20} Pa s (following Larsen *et al.*'s (2005) best fit earth model and Peltier's (2002) VM2 model). Piecewise ice load model (with arbitrary y-axis) overlain in grey for reference. Minimum (0.1 mm yr^{-1}) and maximum (1.4 mm yr^{-1}) estimates of rate of interseismic land uplift ($\Delta\xi_{int}(\tau)$) overlain to test whether the rate of LIA associated RSL change exceeds the rate of interseismic land uplift. In all instances, the model estimated rate of RSL rise exceeds the minimum rate of interseismic land uplift, suggesting there is potential for GIA RSL rise in Turnagain Arm to exceed tectonic land uplift during the middle and late LIA causing net RSL rise.

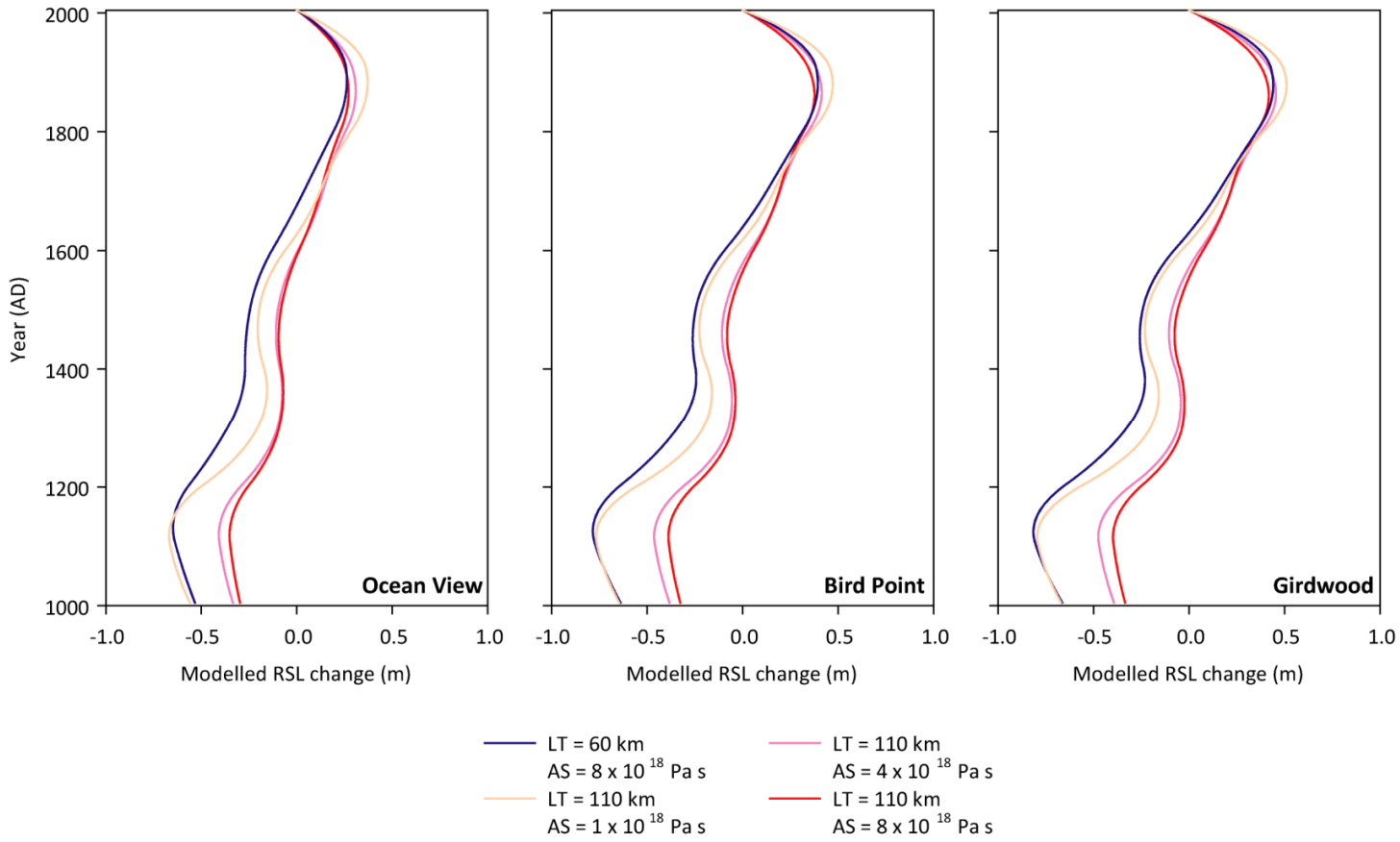

Figure 6.14 - Modelled RSL change (ocean geoid height minus land uplift, relative to CE) at Ocean View, Bird Point and Girdwood over the last 1000 years predicted by asthenospheric low viscosity zone (ALVZ) best Earth models in TABOO in response to LIA ice thickness changes represented in the Larsen *et al.* (2005) regional ice model. Lithospheric thicknesses (LT) and asthenosphere viscosities (AS) follow key. Mantle viscosity set at 4 x 10^{20} Pa s (following Larsen *et al.*'s (2005) best fit earth model and Peltier's (2002) VM2 model).

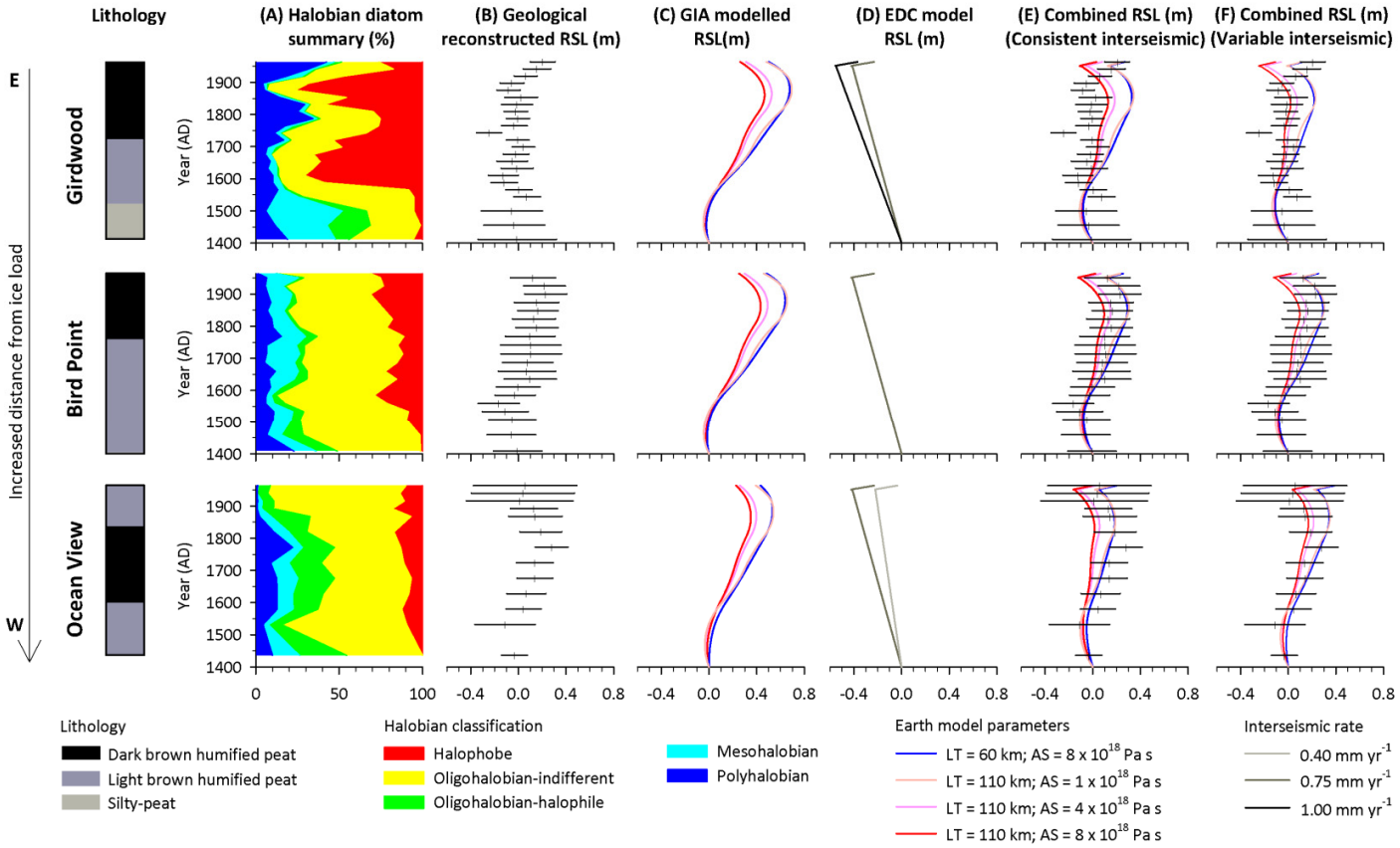

Figure 6.15 - Integration of geological data and geophysical modelling results with estimates of tectonic land level changes to test research hypotheses. All data plotted against age model (detailed in section 6.2.4) and standardised as changes relative to AD 1400. Geological data (A & B) from GW-08-3, BP-08-6 and OV-08-4 (see Chapter 4). Model estimates (C, E & F) use lithospheric thicknesses and asthenosphere viscosities in key, with mantle viscosity set at 4 x 10^{20} Pa s (see Chapter 5). EDC RSL (D) estimated using three interseismic rates (detailed in key and text) from AD 1400-1952 and pre-seismic rate (15.5 mm yr^{-1}) from AD 1952-1964 (detailed in section 6.2.4). Figures E & F overlays the geological data (B) against combined RSL (GIA modelled RSL (C) plus EDC model RSL (D)) for spatially consistent (E) and spatially variable (F) interseismic rates to test working hypothesis four.

Appendix

Appendix 1
A1_1 Girdwood Troels-Smith for cores this thesis

Depth (cm)	Description
GW-NB-06-1	
0 – 62	Grey silt, occasional layers of abundant herbaceous rootlets above 1964 peat layer
62 – 98	Fiberous herbaceous peat (1964), sharp upper contact $Th^2$2 Sh2 Tl^2+ 3,1,2,0,4
98 – 108	Silty herbaceous peat Ag2 $Th^2$1 Sh1 3,0,2,0,0
108 – 125	Silt with abundant herbaceous rootlets. Tephra layer seen at ~ 118cm at base of marsh cliff (though not seen within core sample). Ag2 As1 $Th^2$1 2,0,2,0,0
GW-NB-06-2	
0 – 51	Silt with herbaceous rootlets Ag2 As1 $Th^2$1 2,0,2,0,0
51 – 72	Herbaceous peat (1964), wood at 51-52cm, sharp upper contact $Th^2$2 Sh2 Tl^2+ Dh+ 3,0,2,0,4
72 – 82	Silty herbaceous peat Ag1 $Th^2$2 Sh1 Tl^2+ 31,2,0,0
82 – 110	Silt with abundant herbaceous rootlets. Tephra layer seen at ~ 101cm at base of marsh cliff. Ag2 As1 $Th^2$1 2,0,2,0,0
GW-08-1	
0 – 35	Silt with fresh rootlets Ag3, $Th^0$1 2,0,1,-
35 – 57	Silth with few rootlets Ag4, Th^0+ 2,0,1,0
57 – 71	Dark, well humified peat. Sharp upper contact $Th^2$3, Sh1 4,0,3,4
71 – 94	Light brown humified peat $Th^3$2, Sh2 3,0,3,0
94 – 104	Silt with some organics Ag3, Sh1 2,0,3,0
104 – 115	Silt. Tephra seen at 108cm. Ag4 2,0,3,0
GW-08-2	
0 – 34	Silt with fresh rootlets, some iron staining Ag3, $Th^0$1

	2,0,4,-
34 – 50	Silt with occasional fresh rootlets Ag4, Th^0+ 2,0,3,0
50 – 65	Dark brown humified peat. Sharp upper contact $Th^2$2, Sh2, Ag+ 4,0,3,4
65 – 73	Light brown humified peat Sh2, $Th^2$2, Ag+ 3,0,3,0
73 – 83	Silty peat Ag2, Sh2, Th^2+ 2,0,3,0
83 – 91	Silt, occasional rootlets Ag4, Th^2+ 2,0,3,0
91 – 106	Silt. Tephra seen at 93cm Ag4 2,0,2,0
GW-08-3	
0 – 29	Silt with fresh rootlets Ag3, $Th^0$1 2,0,3,-
29 – 49	Silt with occasional fresh rootlets Ag4, Th^0+ 2,0,3,0
49 – 71	Dark brown humified peat. Sharp upper contact $Th^2$2, Sh2 4,0,2,4
71 – 91	Light brown humified peat Sh3, $Th^2$1 3,0,2,0
91 – 100	Silt, some organics Ag2, Sh2 2,0,2,0
100 – 114	Silt, few organics. Tephra seen at 102cm Ag3, Sh1 2,0,3,0

Appendix 1
A1_2 Bird Point Troels-Smith for cores this thesis

Depth (cm)	Description
BP-07-01	
0 – 22	Silt with fresh rootlets Ag2, $Th^0$2 1,0,3,-
22 – 41	Grey silt with rootlets; with some ferrous material. Ag2, $Th^1$2 2,0,2,0
41 – 64	Dark silt with some organics Ag2, $Th^1$1, Sh1 3,0,2,0
64 – 72	Silt with rootlets and wood fragments. Ag2, $Th^2$1, Dh1 2,0,2,0
72 – 93	Humified organic peat with some silt. Significant presence of wood fragments. Sharp upper contact. Ag1, $Th^2$1, Sh1, Dh1 2,0,3,3
93 – 109	Silt with some organics Ag2, $Th^2$1, Sh1 2,0,3,0
109 – 135	Humified peat with some silt. $Th^2$2, Sh1, Ag1 3,0,3,0
135 – 155	Silt with humified organics Ag2, Sh1, $Th^2$1 2,0,3,0
155 – 176	Silt with occasional rootlets; some presence of sands. Ag3, $Th^2$1, Ga+ 2,0,3,0
176 – 178	Silt with some organics Ag2, $Th^2$1, Sh1 2,0,3,0
178 – 180	Silt with occasional rootlets (with band of sand). Ag2, $Th^2$1, Ga1 2,0,3,0
180 – 219	Very silty peat. Some evidence of sharp upper contact in relation to sand. Ag2, $Th^1$1, Sh1 2,0,3,2
219 – 228	Silt with occasional rootlets Ag3, $Th^3$1 2,0,3,0
228 – 257	Silt with very few rootlets Ag4, Th++ 2,0,3,0
257 – 266	Silty peat. Sharp upper contact. Ag1, $Th^3$2, Sh1 3,0,3,3
BP-07-02	

0 – 111.5	Silt with many fresh rootlets. Some sediment lost at top of core due to saturated material (therefore quite general description). Ag1, $Th^0$2, Sh1 2,0,3,-
111.5 – 123	Silty peat. Sharp upper contact. Ag1, $Th^1$1, Sh1, Dh1 3,0,2,3
123 – 143	Silt with some rootlets Ag2, $Th^2$1, Sh1 2,0,2,0
143 – 151	Band of silty organic material Ag2, $Th^2$2, Sh+ 2,0,2,0
151 – 182	Silty humified peat Ag2, $Th^2$1, Sh1, Dh+ 2,0,3,0
182 – 210	Silty peat with slightly sharp upper contact. Ag2, $Th^2$2, Sh+ 3,0,3,2
210 – 227	Silt with occasional rootlets $Th^2$1, Ag3, Sh+ 2,0,3,0
227 – 233	Silt with bands of sand Ag3, Ga1, Th^2+ 2,0,3,0
233 – 395	Silt with very few rootlets Ag4, Th^2++ 2,0,3,0
BP-07-3	
0 – 23	Loose fresh material lost from the top of the core.
23 – 50	Silt with fresh organic material. Ag2, $Th^0$2 3,0,1,-
50 – 69	Silt with some rootlets Ag3, $Th^1$1 2,0,2,0
69 – 79	Peat with some wood. Sharp upper contact. Ag1, $Th^1$2, Sh1, Dh+ 3,0,3,4
79 – 92	Silt with some organics. Ag2, $Th^1$1, Sh1, Dh+ 2,0,3,0
92 – 127	Humified organics and silt. Ag1, $Th^2$1, Sh1, Dh1 2,0,3,0
127 – 191	Silt with occasional rootlets $Th^2$1, Ag3, Sh+ 2,0,3,0
191 – 201	Silty peat Ag1, Sh1, $Th^2$2 2,0,3,? (Core collapsed at this point. Would suggest sharp upper contact at 191cm with thick organic material starts.)
201 – 224	Very silty peat

	Ag2, $Th^2$1, Sh1 2,0,3,0
224 – 264	Silt with very few rootlets. Some lamination of darker silt. Ag4, Th^2++ 2,2,3,0
BP-07-04	
0 – 63	Silt with fresh rootlets. General description as top part of core lost as very wet.
63 – 80	Peat with sharp upper contact. Ag1, $Th^1$2, Sh1 3,0,2,3
80 – 138	Silty peat. Occasional bands of organic materials. Ag2, $Th^1$1, Sh1 2,1,3,1
138 – 207	Silty peat (1cm band of sand at 150cm). Ag2, $Th^1$1, Sh1 2,0,3,0
207 – 236	Silt with some organic material. Ag3, $Th^1$1, Sh+ 2,0,2,0
236 – 269	Silt with very few rootlets. Some banding of darker material. Ag4, Th^1++ 2,1,3,0
269 – 327	Silt with some organic material $Th^1$1, Ag3 2,0,3,0
327 – 356	Silt with occasional rootlets Ag4, Th++ 2,0,3,0
356 – 373	Silty humified peat Ag1, Sh1, $Th^2$2 3,0,2,? (Unsure of boundary contact due to collapsed sediment at approx 350-355cm)
373 – 389	Silty humified peat Ag2, $Th^2$1, Sh1 2,0,3,0
BP-07-5	
0 – 24	Saturated fresh sediment lost.
24 – 50	Dark silt with fresh organic material. Ag2, $Th^0$2 3,0,2,-
50 – 70	Silt with occasional rootlets Ag3, $Th^1$2 S,0,3,0
70 – 74	Very dark grey humified peat $Th^1$2, Sh1, Ag1 3,0,2,4
74 – 76	Band of sandy silt. Sharp upper contact. $Th^1$1, Ag1, Ga2 2,0,3,3
76 – 124	Silty humified peat. Some fresh rootlets. Sharp upper contact. $Th^1$2, Sh1, Ag1, Dh+ 3,0,3,3

124 – 150	Silty humified peat Ag2, $Th^2$1, Sh1 2,0,3,0
150 – 169	Silt with occasional rootlets Ag3, $Th^2$1 2,0,4,0
169 – 178	Large piece of wood. Possible sharp upper contact. Dh4
178 – 183	Well developed peat. Ag1, $Th^2$2, Sh1, Dh++ 3,0,3,0
183 – 201	Poorly developed silty peat. Ag2, $TH^2$1, Sh1 2,0,3,0
BP-07-06	
0 – 40	Sediment lost
40 – 70	Wet unconsolidated fresh silt and rootlets
70 – 82	Silt with occasional rootlets Ag4, Th^1++ 2,0,2,0
82 – 162	Humified peat. Sharp upper contact. Core very wet; some collapsed. $Th^1$2, Sh1, Dh1, Ag+ 4,0,2,3
162 – 190	Humified peat $Th^1$2, Sh1, Dh1, Ag+ 3,0,1,0
190 – 234	Silt with some organic material Ag2, $Th^2$1, Sh1 2,0,3,0
234 – 253	Silt with occasional rootlets. Wood fragment at 242cm. Ag4, Th^2++ 2,0,3,0
253 – 263	Humified peat. Sharp upper contact. $Th^2$2, Sh1, Ag1 3,0,3,4
263 – 267	Band of silty peat Ag2, $Th^2$1, Sh1 2,0,3,0
267 – 269	Humified peat $Th^2$2, Sh1, Ag2 3,0,3,0
269 – 273	Band of silty peat Ag2, $Th^2$1, Sh1 2,0,3,0
273 – 278	Dark humified peat with wood fragments $Th^2$2, Sh1, Dh1, Ag+ 4,0,2,1
278 – 286	Silty peat Ag2, $Th^2$1, Sh1 2,0,3,0
286 – 298	Humified peat Ag1, Sh1, $Th^3$2 3,0,3,0

BP-07-7	
0 – 50	Sediment lost
50 – 61	Silt with fresh rootlets Ag2, $Th^0$2 2,0,2,-
61 – 88	Silt with occasional rootlets Ag3, $Th^0$1 2,0,3,0
88 – 105	Very wet peat $Th^1$2, Sh1, Ag1 3,0,1,3
105 – 113	Humified peat $Th^2$2, Sh1, Ag++ 4,0,2,0
113 – 130	Silt with occasional rootlets Ag3, $Th^2$1 2,0,3,0
130 – 148	Massive silt AG4, Th+ 2,0,3,0
148 – 165	Well defined humified peat. Sharp upper contact. Sh2, $Th^3$2, Dh+ 4,0,3,4
BP-07-8	
0 – 49	Sediment lost
49 – 65	Silt with fresh rootlets $Th^0$2, Ag2 3,0,2,1
65 – 74	Silt with occasional rootlets Ag3, $Th^1$1
74 – 114	Well developed peat. Sharp upper contact. $Th^1$2, Sh2, Ag+
114 – 135	Silty peat Ag2, $Th^2$1, Sh1 2,0,2,0
135 – 140	Silt with occasional rootlets Ag3, Th1 2,0,2,0
140 – 148	Large wood fragment Dh3, Ag1 3,0,3,0
148 – 177	Massive silt Ag4, Th++ 2,0,2,0
177 – 193	Well defined peat. Sharp upper contact. Sh2, $Th^2$2 4,0,3,4
BP-08-1	
0 – 57	Sediment lost
57 – 75	Grey silt with fresh rootlets Ag2, $Th^0$2 2,0,2,-
75 – 87	Brown silt, some organics $Th^2$1, Sh1, Ag2

	2,0,3,0
87 – 199	Grey silt, some organics Ag2, $Th^2$1, Sh1 2,0,3,0
199 – 219	Grey silt, some organics Ag2, $Th^2$1, Sh1 2,0,2,0
219 – 329	Silt Ag4, Sh+ 2,0,2,0
329 – 344	Silty organics, relatively sharp upper contact Ag2, $Th^2$1, Sh1 3,0,2,2
BP-08-2	
0 – 28	Sediment lost
28 – 37	Grey silt with fresh rootlets Ag3, $Th^0$1 2,0,1,-
37 – 70	Silt, very occasional rootlets Ag4, Th^0+ 2,0,2,0
70 – 79	Peat, some silt. Sharp upper contact $Th^2$2, Sh2, Ag++ 3,0,3,3
79 – 86	Dark brown humified peat $Th^2$2, Sh2 4,0,3,0
86 – 96	Silty peat $Th^2$1, Sh1, Ag2 3,0,3,1
96 – 116	Humified peat $Th^2$1, Sh3 3,0,3,0
116 – 124	Silty peat $Th^2$1, Sh1, Ag2 3,0,3,0
124 – 145	Grey silt Ag4, Sh+ 2,0,3,0
145 – 172	Grey silt Ag4 2,0,2,0
172 – 186	Silty peat. Sharp upper contact $Th^2$1, sh2, Ag1 3,0,3,3
186 – 192	Silt, some organics Ag3, Sh1 2,0,2,0
BP-08-3	
0 – 34	Sediment lost
34 – 53	Silt, with fresh rootlets Ag3, $Th^0$1 2,0,2,-
53 – 75	Silt with very occasional rootlets

	Ag4, Th^0+ 2,0,3,0
75 – 104	Brown, humified peat. Sharp upper contact. $Th^2$2, Sh1, Ag+ 3,0,3,4
104 – 129	Light brown silty peat Sh2, $Th^2$1, Ag1, Dh+ 3,0,3,0
129 – 140	Silt, some organics Ag2, $Th^2$1, sh1 2,0,2,0
140 – 158	Silt, some organics Ag3, Sh1 2,0,2,0
158 – 176	Grey silt Ag4 2,0,2,0
176 – 192	Humified peat. Sharp upper contact. $Th^2$2, Sh2 3,0,3,4
192 – 200	Silty peat Sh2, $Th^2$1, Ag1 2,0,3,0
200 – 215	Silt, some organics Ag3, Sh1 2,0,3,0
215 – 248	Grey silt with very occasional organics Ag4, Th+ 2,0,3,0
BP-08-4	
0 – 100	Grey silt with occasional fresh rootlets. Some sediment lost. Ag3, $Th^0$1 2,0,2,-
100 – 129	Dark brown humified peat. Sharp upper contact. $Th^2$2, Sh2 4,0,3,4
129 – 140	Light brown peat Sh2, $Th^2$1, Ag1 3,0,3,0
140 – 153	Silt, some organics Ag2, $Th^2$1, Sh1 2,0,3,0
153 – 174	Silt, very occasional organics Ag3, Sh+ 2,0,3,0
174 – 208	Humified peat. Sharp upper contact. $Th^2$2, Sh2 3,0,3,4
BP-08-5	
0 – 15	Fresh rootlets with silt Ag2, $Th^0$2 2,0,1,-
15 – 23	Brown silt with some fresh rootlets $Th^1$1, Ag3

	2,0,1,0
23 – 60	Grey silt with some fresh rootlets Ag3, $Th^1$1 2,0,1,0
60 – 90	Silt with very occasional rootlets Ag4, Th+ 2,0,2,0
90 – 104	Dark brown humified peat. Sharp upper contact. $Th^2$2, Sh2 4,0,2,4
104 – 123	Light brown humified peat. $Th^2$2, Sh2, Ag+ 3,0,2,0
123 – 150	Light brown, dry, humified peat $Th^2$2, Sh2 3,0,3,0
BP-08-6	
0 – 14	Sediment lost
14 – 23	Grey silt with some fresh rootlets $Th^0$1, Ag3 2,0,1,-
23 – 47	Dark grey silt, some rootlets Ag3, $Th^2$1 3,0,2,0
47 – 65	Dark grey silt Ag4, Th+ 3,0,3,0
65 – 80	Dark brown peat. Sharp upper contact $Th^2$2, Sh2, Ag+ 4,0,2,4
80 – 116	Light brown herbaceous peat $Th^2$2, Sh2, Ag+ 3,0,3,0
116 – 126	Silty peat Sh1, $Th^2$1, Ag2 2,0,2,0
126 – 143	Silt with occasional rootlets Ag3, $Th^2$1 2,0,2,0
143 – 191	Silt Ag4, Th+ 2,0,2,0
191 – 195	Light brown herbaceous peat. Band of silt at 185cm (1cm thick). Sharp upper contact. Sh2, $Th^2$1, Ag1 3,0,2,3
195 – 212	Silty peat Sh2, Ag2 2,0,2,0
212 – 250	Silt with occasional rootlets Ag3, $Th^2$1 2,0,2,0
250 – 285	Silt, with very few rootlets Ag4, Th+

	2,0,3,0

Appendix 1
A1_3 Hope Troels-Smith for cores this thesis

Some detail is missing due to presence of bears on the marshes at Hope

Depth (cm)	Description
HP-07-01	
0 – 12	Silt with fresh occasional rootlets Ag3, $Th^0$1, Dh+ 2,0,3,-
12 – 32	Silt with occasional rootlets Ag3, $Th^2$1 2,0,3,0
32 – 37	Browny-grey silt with few rootlets Ag3, $Th^2$1 2,0,3,2
37 – 51	Fine grains of sand with some silt Ga3, Ag1 2,0,3,0
HP-07-2	
0 – 27	Massive silt with occasional rootlets Ag3, $Th^0$1 2,0,3,-
27 – 40	Silt with very occasional rootlets Ag4, Th^2+ 2,0,3,0
40 – 53	Silt with some organic material. Some woody fragments Ag2, $Th^2$2, Dh+ 2,0,3,0
53 – 90	Humified browny-grey silty peat Sh2, $Th^2$1, Ag1, Tl+ 3,0,2,2
HP-07-3	
0 – 33	Massive silt with occasional rootlets Ag3, $Th^0$1 2,0,3,-
33 – 48	Humified peat with silt. Sharp upper contact. Sh2, $Th^2$1, Ag1, Dh+ 3,0,2,3
HP-07-4	
0 – 38	Silt with occasional rootlets Ag3, $Th^1$1 2,0,3,-
38 – 122	Massive silt with very few rootlets Ag4, Th^2+ 3,0,3,0
HP-07-5	
0 – 39	Silt with fresh roots Ag2, $Th^0$2 2,0,2,-
39 – 53	Silt with occasional rootlets; some ferrous material. Ag4, Th^3+ 2,0,2,0

53 – 60	Silty peat; some ferrous material. Sharp upper contact. Sh1, $Th^2$1, Ag2 3,0,3,3
60 – 88	Dark silt with occasional rootlets. Ag3, Sh1, Th^3+ 3,0,3,0
88 – 205	Silt with occasional rootlets (At 185cm – 2cm band of ferrous material). Ag4, Th^2+ 3,0,3,0
205 – 231	Silt with occasional rootlets Ag4, Th^2+ 3,0,2,0
231 – 236	Silty sand, with few rootlets Ga2, Ag1, $Th^2$1 3,0,3,1
236 – 239	Silt with occasional rootlets Ag4, Th^3+ 2,0,3,1
239 – 247	Sandy silt (Silty organic deposit at 242-243) Ga2, Ag2, Th^3+ 3,0,3,1
247 – 252	Silt Ag4, Th^3+ 2,0,3,1
HP-07-6	
0 – 6	Silt with fresh roots Ag2, $Th^0$2 2,0,3,-
6 – 42	Silt with occasional rootlets. Ag3, $Th^1$1 2,0,3,0
42 – 49	Humified peat with some silt. Sharp upper contact. Sh2, $Th^2$1, Ag1, Dh+ 3,0,2,4
49 – 53	Silty organics with some sand Ag2, Sh1, $Th^3$1, Ga+ 2,0,3,0
53 – 64	Sandy silt Ag3, Ga1 2,0,2,0
64 – 74	Silty sand and gravel Ag2, Ga1, G_{min}1 2,0,2,0
74 – 97	Sands and gravels with some silt Ga2, Ag1, G_{min}1 3,0,3,1
97 – 116	Silt with some fine sand Ag3, Ga1 2,0,3,0
116 – 122	Gravels and sands with some silt Ga1, G_{min}2, Ag1 2,0,2,0

122 - 137	Silt with some fine sand Ag3, Ga1 2,0,2,0
HP-07-7	
0 – 208	Massive silt Ag4 2,0,2,0
HP-07-8	
0 – 24	Silt with fresh rootlets; some ferrous material Ag2, $Th^0$2 2,0,3,-
24 – 37	Silt with rootlets Ag2, $Th^2$2 2,0,2,0
37 – 100	Dark grey silt with occasional rootlets. Some lamination. Ag3, $Th^2$1 3,1,3,0
100 – 141	Dark grey silt with occasional rootlets Ag3, $Th^2$1 2,0,3,0
141 – 154	Silt with some ferrous material Ag4, Th+ 2,0,3,0
154 – 156	Band of sand Ga4, Ag+ 2,0,3,2
156 – 278	Silt with some rootlets; some ferrous material Ag4, Th+ 2,0,3,2
278 – 303	Silt with humified organics. No visible sharp contact (?) Ag2, Sh2, Th+ 3,0,3,0
303 – 356	Silt with humified organics. Ag2, Sh1, $Th^2$1 2,0,3,0
356 – 368	Silty humified peat Ag2, $Th^2$2, Sh+ 2,0,3,1
HP-07-9	
0 – 17	Silt with fresh rootlets Ag2, $Th^0$2 2,0,2,-
17 – 39	Silt with occasional rootlets Ag2, $Th^1$1, Sh1 3,0,2,0
39 – 46	Silt with large organic deposits Ag2, $Th^1$2, Dh+ 2,0,3,0
46 – 59	Silty peat. Slightly sharp boundary. Ag2, $Th^2$2, Sh+ 2,0,3,1
59 – 75	Silt with occasional rootlets Ag3, $Th^2$1 2,0,3,0

75 – 89	Silt with bands of organics Ag2, $Th^2$1, Sh1 2,0,2,0
89 – 98	Humified peat with silt. Wood fragments at top (unable to determine boundary). $Th^2$2, Sh1, Ag1, Dh+ 3,0,2,?
98 – 106	Silt with occasional rootlets Ag3, Sh1, Th+ 2,0,3,0
106 – 110	Peat with silt. Sharp upper contact. $Th^2$2, Sh1, Ag1, Th+ 2,0,3,3
110 – 154	Silt with occasional rootlets Ag3, $Th^2$1 2,0,2,1
154 – 156	Sandy layer with some peat Ga3, Th1, Ag+ 3,0,3,2
156 – 172	Silt with bands of organics Ag2, $Th^2$1, Sh1 3,0,2,0
172 – 228	Massive silt with very few rootlets Ag4, Th+ 2,0,2,0
HP-07-10	
0 – 16	Fresh rootlets with silt $Th^0$2, Sh1, Ag1 2,0,3,-
16 – 87	Dark silt with occasional rootlets Ag3, $Th^1$1 3,0,3,0
87 – 118	Silt with some peaty organics Ag2, Sh1, $Th^1$1 2,0,3,0
118 – 135	Silty peat. Sharp upper contact. $Th^2$2, Sh1, Ag1 3,0,3,3
135 – 142	Silt with occasional rootlets Ag2, Sh1, $Th^2$1 2,0,3,0
142 – 180	Silt with occasional rootlets/organic material Ag3, Sh1, Th+ 2,0,3,0
180 – 214	Silt with occasional rootlets Ag3, $Th^2$1 2,0,3,0
214 – 246	Silty peat. Sharp upper contact $Th^2$2, Sh1, Ag1 3,0,2,3
246 – 278	Silt with occasional rootlets Ag2, $Th^2$1, Sh1 2,0,3,0
HP-07-11	

0 – 13	Sediment lost due to compression
13 – 36	Silt with very few rootlets Ag4, Th++ 2,0,2,-
36 – 47	Peat with some sand and silt. Sharp upper boundary $Th^2$2, Sh1, Ag+
47 – 49	Silt Ag4
49 – 52	Peat, with a band of silt (0.5cm) $Th^2$2, Sh1, Ag1
52 – 58	Silt with some organics AG3, $Th^2$2, Sh++
58 – 60	Peat with some silt bands $Th^2$2, SH1, Ag1
60 – 64	Silt with some organics Ag3, $Th^2$2, Sh++
64 – 70	Well humified peat $Th^2$2, Sh2, Ag+
70 – 72	Silty peat Ag2, $Th^2$2, Sh1
72 – 75	Peat with some silt Sh2, $Th^2$1, Ag1
75 – 88	Silt with some organics Ag2, $Th^2$1, Sh1
88 – 91	Well developed humified peat, sharp upper contact $Th^2$2, Sh2
91 – 101	Silt with very few rootlets Ag4, Th++
101 – 121	Peat with some silt (reasonably sharp upper contact) $Th^2$1, Sh2, Ag1
121 – 133	Silt with some rootlets Ag3, $Th^3$1
133 – 180	Silt with v few rootlets, with band of organics at 149 – 151 (well humified peat $Th^2$2, Sh2) Ag4, Th++
180 – 208	Massive silt. (Large wood fragments at 201-206 which broke core). Ag4, Th++ 3+,0,2,0
208 – 252	Humified peat with some silt $Th^1$2, Sh1, Ag1 2,0,3,3
HP-08-1	
17 – 56	Silt with some fresh rootlets. Some ferrous material. Ag3, $Th^0$1 2,0,2,-
56 – 84	Silt with abundant organic material and rootlets Ag2, $Th^1$1, Sh1 2,0,2,0
84 – 100	Humified dark brown peat. Sharp upper contact. $Th^2$2, Sh2, Ag++ 4,0,3,4
100 – 104	Humified peat with wood fragments $Th^2$1, Sh1, Dl2, Ag++ 4,0,3,1

104 – 113	Silty peat Ag2, Sh1, $Th^{2}1$ 3,0,3,0
113 – 116	Silt with organics Ag2, $Th^{1}2$ 2,0,3,0
116 – 130	Silt with very few organics Ag3, Sh1 2,0,2,0
HP-08-2	
Full Troels-Smith not recorded due to presence of bears on the marsh	
0 – 65	Silt with rootlets
65 – 85	Laminated peats and silt
85 – 95	Silt with rootlets

Appendix 1
A1_4 Ocean View Troels-Smith for cores this thesis

Cores along new Coral Lane Transect

Depth (cm)	Description
OV-08-01	
0 – 17	Silt with fresh rootlets Ag2, $Th^0$2, 2,0,2,-
17 – 39	Silt with few rootlets Ag3, $Th^1$1 3,0,3,0
39 – 90	Very saturated peat. Sharp upper contact $Th^2$2, Sh2 4,0,0,4
90 – 106	Light brown, very saturated humified peat $Th^2$2, Sh2 3,0,0,0
106 – 118	Silt with some organics Ag2, Sh2 2,0,1,0
118 – 132	Silt Ag4 2,0,2,0
132 – 153	Humified peat. Sharp upper contact $Th^3$2, Sh2, Dh+ 3,0,2,3
153 – 165	Silty peat. Ag2, $Th^3$1, Sh1 2,0,3,0
OV-08-2	
0 – 32	Light grey silt with few fresh rootlets Ag3, $Th^0$1, 1,0,3,-
32 – 34	Silt Ag4 3,0,3,0
34 – 38	Wood, some organics Dh3, $Th^1$1 3,0,3,4
38 – 92	Peat $Th^2$2, Sh2 4,0,0,0
92 – 102	Light humified saturated peat Sh3, $Th^3$1 3,0,0,0
102 – 110	Silty peat Sh2, Ag2 3,0,3,0
110 – 123	Silt with few rootlets Ag4, Sh++ 2,0,3,0

123 – 136	Silt Ag4 2,0,3,0
136 – 145	Light brown peat. Sharp upper contact $Th^3$1, Sh3 3,0,3,4
145 –156	Silty peat Ag2, Sh2 3,0,3,0
156 –165	Silt with some organics Ag3, Sh1 2,0,2,0
OV-08-3	
0 – 37	Light grey silt Ag4 1,0,0,3
37 – 57	Dark brown peat. Sharp upper contact $Th^3$1, Sh2, Dh1 4,0,2,4
57 – 89	Light brown humified peat Sh3, Dh1, Th++ 3,0,0,0
89 – 94	Silty peat Sh2, Ag2 2,0,2,0
94 – 104	Silt with some organics Ag3, Sh1 2,0,2,0
104 – 135	Silt Ag4 2,0,3,0
135 – 147	Peat. Sharp upper contact Sh3, $Th^3$1 3,0,3,4
147 – 166	Silty peat Ag2, Sh1, $Th^3$1 2,0,3,0
OV-08-4	
0 – 60	Silt Ag4 2,0,2,-
60 – 106	Peat. Sharp upper contact Sh2, $Th^2$1, Dh1 4,0,2,4
106 – 112	Silty peat Ag2, Sh2, Dh at 112cm 2,0,3,0
112 – 124	Silt with some organics Ag4, Sh++ 2,0,3,0
124 – 139	Silt Ag4 2,0,3,0
139 – 159	Peat. Sharp upper contact

	Sh2, Th^{3}1, Dh1, Ag+ 3,0,3,4
OV-08-5	
0 – 38	Light grey silt Ag4 1,0,3,-
38 – 69	Silt Ag4 3,0,3,0
69 – 79	Silty peat. Sharp upper contact Th^{3}1, Sh1, Ag2 3,0,3,4
79 – 83	Silt Ag4 3,0,3,0
83 – 89	Light grey silt Ag4 1,0,3,0
89 – 95	Silt Ag4 3,0,3,0
95 – 103	Silty peat Th^{3}1, Sh2, Ag1 4,0,3,4
103 – 112	Very light brown humified peat Sh2, Th^{3}1, Ag1 2,0,3,0
112 – 125	Silt with some organics Ag3, Sh1 2,0,3,0
125 –141	Silt Ag4 2,0,3,0
141 –149	Silty peat. Sharp upper contact Ag1, Sh2, Th^{2}1 3,0,3,4
149 –164	Silty peat Ag2, Sh1, Th^{3}1 2,0,2,0
OV-08-6	
0 – 68	Silt Ag4 2,0,3,-
68 – 112	Peat. Sharp upper contact Sh2, Th^{3}2 4,0,3,4
112 – 127	Silty peat Ag2, Sh2, Dh from 116 -120 2,0,3,0
127 – 153	Silt Ag4 2,0,3,0
153 – 178	Silty peat. Sharp upper contact Th^{3}1, Sh1, Ag2

	3,0,3,4
OV-08-7	
0 – 37	Silt Ag4 2,0,3,-
37 – 64	Silty peat Ag2, Th[1]1, Sh1, Dh+ 3,0,3,1
64 – 82	Silt Ag4, Sh+ 2,0,3,0
82 – 113	Peat Sh2, Th[2]2,, Ag+ 3,0,3,0
113 – 122	Silty peat Ag2, Sh2 2,0,2,0
122 – 130	Silt with some organics Ag4, Sh++ 2,0,2,0
130 – 231	Silt Ag4 2,0,2,0
OV-08-8	
0 – 51	Silt Ag4 2,0,2,0
51 – 57	Silty peat Sh2, Ag2 3,0,3,3
57 – 70	Silt with some organics Ag3, Sh1 2,0,4,0
70 – 79	Silty peat Ag2, Sh1, Dh1 2,0,3,1
79 – 86	Silt with some organics Ag3, Sh1 2,0,3,0
86 – 90	Peat with some silt Ag1, Sh1, Th[3]1, Dh1 3,0,2,0
90 – 113	Very wet silt with organics Ag2, Sh2, Th[3]1, Dh+ 2,0,0,0
113 – 141	Silt with some organics Ag2, Sh2 2,0,3,0
141 – 208	Silt Ag4 2,0,3,0
OV-08-9	
0 – 163	Silt. Some Fe at 107cm Ag4

	2,0,2,-

Appendix 2
A2_3 Names and codes of upper Cook Inlet diatoms

Code	Name
Ab	Achnanthes brevipes
Ac	Achnanthes conspicua
Ad	Achnanthes delicatula
Ae	Achnanthes exigua
Ah	Achnanthes hungarica
Al	Achnanthes lanceolata
Am	Achnanthes minutissima
As	Actinoptychus senarius
AA	Amphiprora alata
Ap	Amphora coffeaeformis
Ax	Amphora exigua
Ao	Amphora ovalis
aV	Amphora veneta
AR	Arachnoidiscus sp.
Mg	Aulacoseira granulata
ac	Auliscus sculptus
Br	Berkeleya rutilans
BX	Biremis ambigua
Cd	Caloneis amphisbaena
Cb	Caloneis bacillum
CB	Caloneis brevis
Cc	Caloneis clevei
Cn	Caloneis ventricosa
cw	Caloneis westii
Ca	Ceratoneis arcus
Co	Cocconeis pediculus
Cp	Cocconeis peltoides
Cl	Cocconeis placentula
Cs	Cocconeis scutellum
Cm	Coscinodiscus sp.
cM	Cyclotella meneghiniana
Ct	Cyclotella striata
Ce	Cymatopleura elliptica
Cg	Cymatosira belgica
CK	Cymbella affinis
Cu	Cymbella angustata
Cr	Cymbella aspera
Ci	Cymbella cistula
Cy	Cymbella cymbiformis
CN	Cymbella naviculiformis

CF	Cymbella turgida
Cv	Cymbella ventricosa
Ds	Delphineis surirella
Du	Denticula subtilis
De	Diatoma elongatum
Dh	Diatoma hiemale
Dh	Diatoma hyemale
Dg	Didymosphenia geminata
Di	Diploneis interrupta
Do	Diploneis ovalis
Dm	Diploneis smithii
Ez	Epithemia adnata
Et	Epithemia turgida
Ee	Eunotia exigua
Eg	Eunotia germainii
El	Eunotia lunaris
Ep	Eunotia pectinalis
Ea	Eunotia praerupta
Eu	Eunotia triodon
V8	Fallacia pygmaea
Oi	Fallacia vitrea
Fc	Fragilaria construens
Fl	Fragilaria leptostauron
Fe	Fragilaria vaucheriae
FC	Fragilariforma constricta
Ff	Fragilariforma virescens
Fi	Frustulia linkei
Fr	Frustulia rhomboides
Fv	Frustulia vulgaris
Go	Gomphoneis olivaceum
Gc	Gomphonema acuminatum
Gm	Gomphonema angustatum
Gg	Gomphonema gracile
Gp	Gomphonema parvulum
Gv	Gomphonema vibrio var bohemicum
Gi	Gomphonema vibrio var vibrio
Ga	Gyrosigma acuminatum
Gw	Gyrosigma wansbeckii
Ha	Hantzschia amphioxys
Hv	Hantzschia virgata
Lm	Luticola mutica
Om	Martyana martyi
ms	Mastoglia smithii
Me	Mastogloia exigua

ms	Mastogloia smithii
Mc	Meridion circulare
Y1	Navicula begeri
Y2	Navicula brockmanii
nG	Navicula capitata
X1	Navicula cari var cincta
Y3	Navicula clementis
nE	Navicula crucicula
X2	Navicula cryptocephala
U1	Navicula dicephala
V1	Navicula digitoradiata
U2	Navicula distans
V2	Navicula elegans
Y4	Navicula exigua
U3	Navicula flanatica
V3	Navicula forcipata
Y0	Navicula galikii
Y5	Navicula graciloides
V4	Navicula halophila
X3	Navicula heufleri
N£	Navicula laevissima
Ol	Navicula levanderi
V5	Navicula peregrina
V6	Navicula phyllepta
V7	Navicula protracta
Y6	Navicula pupula
Y7	Navicula pusilla
Y8	Navicula radiosa
OR	Navicula ramosissima
Y9	Navicula rhynchocephala
V9	Navicula salinarum
n3	Navicula species 1
W1	Navicula tripunctata
W2	Navicula variostriata
W3	Navicula viridula
#b	Neidium bisulcatum
Ni	Neidium iridis
na	Nitzschia acuminata
NP	Nitzschia apiculata
n2	Nitzschia commutata
ND	Nitzschia debilis
Ny	Nitzschia denticula
Na	Nitzschia dissipata
Nd	Nitzschia dubia

nf	Nitzschia filiformis
Nz	Nitzschia fonticola
Nr	Nitzschia frustulum
Nf	Nitzschia fruticosa
Ng	Nitzschia gracilis
Nh	Nitzschia hantzschiana
nh	Nitzschia hungarica
u1	Nitzschia hustedtiana
Nw	Nitzschia ignorata
Nc	Nitzschia linearis
Nl	Nitzschia linkei
No	Nitzschia obtusa
Ne	Nitzschia palea
Nb	Nitzschia palustris
Nn	Nitzschia pseudofonticola
Nu	Nitzschia punctata
Np	Nitzschia pusilla
Nk	Nitzschia scalaris
Ns	Nitzschia sigma
Nx	Nitzschia sinuata
Nj	Nitzschia socialis
Nq	Nitzschia terrestris
Nm	Nitzschia thermalis
Nt	Nitzschia tryblionella
Nv	Nitzschia vitrea
Oa	Odontella aurita
OM	Opephora marina
OP	Opephora pacifica
Ps	Paralia sulcata
Pa	Pinnularia abaujensis
Pe	Pinnularia acrosphaeria
Pb	Pinnularia borealis
PO	Pinnularia brebissonii
Pr	Pinnularia brevicostata
Z9	Pinnularia cruciformis
Pg	Pinnularia gentilis
Pi	Pinnularia intermedia
Pl	Pinnularia lagerstedtii
Pf	Pinnularia mesolepta
Pm	Pinnularia microstauron
Po	Pinnularia molaris
Pt	Pinnularia stomatophora
Pu	Pinnularia subcapitata
Pd	Pinnularia subsolaris

Pv	Pinnularia viridis
U1	Placoneis elginensis
Ph	Plagiogramma vanheurckii
TL	Plagiotropis lepidoptera
Fb	Pseudostaurosira brevistriata
CQ	Reimeria sinuata
Rp	Rhaphoneis psammicola
Rg	Rhopalodia gibba
Ro	Rhopalodia operculata
st	Scolioneis tumida
Sa	Stauroneis anceps
Sg	Stauroneis gregorii
St	Stauroneis phoenicentron
Sp	Stauroneis prominula
Fp	Staurosirella pinnata
sF	Surirella fastuosa
sg	Surirella gemma
So	Surirella ovalis
sV	Surirella ovata
SS	Surirella smithii
sS	Surirella striatula
Sb	Synedra acus
Sf	Synedra fasciculata
Su	Synedra ulna
Ta	Tabellaria fenestrata
Tf	Tabellaria flocculosa
Tn	Thalassionema nitzschioides
Te	Thalassiosira eccentrica
Tr	Trachyneis aspera

Appendix 3
Example of TABOO Task#3 input file

For details of what each element means see: Spada (2003) TABOO User Guide

```
Active

Harmonic_Degrees
2 1024
1
0
0

Make_Model
2
7 (user defined PREM averaged Earth model)
110
1
0.4
0.04

Ad_Hoc
AK5.xyz (user defined file)

Local_Study
2
1 1 1 1 1 1
GPSagain.dat (user defined file)
0.005 1.005 0.1
0
```

Appendix 3_2
TABOO verification exercise

To verify TABOO's suitability as a postglacial rebound calculator and ability to calculate rates of uplift taking into account the model assumptions, I initially model rates of present day uplift for Fennoscandia in response to LGM ice loading, as briefly discussed in section 5.2. This is a relatively tectonically stable region with a well-established glacial chronology and rates of uplift observed by tide gauge and GPS (Ekman, 2009; Lidberg *et al.*, 2009). The exercise is useful at the initial stage of analysis, although it is recognised that the Fennoscandinavia ice sheet was considerably larger than the smaller ice fields and glaciers that are the target for modelling in Alaska.

TABOO includes the ICE-3G deglaciation model (Tushingham and Peltier, 1991) built with 808 spherically symmetrical disk ice elements (Spada *et al.*, 2003) similar to those in the Larsen *et al.* (2005) Alaska regional Neoglacial ice model. Present day uplift is modelled for 193 tide gauge locations in Fennoscandia using an Earth model with a 120 km thick lithosphere and upper mantle of 10^{21} Pa s, in line with Bergstrand *et al.*'s (2005) best Earth model estimates for this region, combined with a 100 kyr linear loading phase,. The model output shows a radial uplift pattern, with maximum uplift of >8 mm yr^{-1} in the north Baltic Sea (Figure A), and the results compare favourably to the postglacial land uplift model NKG2005LU (Svensson *et al.*, 2006) (Figure D). The modelled region of maximum lift is slightly offset from the geodetic measured uplift, likely an artefact of the resolution of the ice model. Rates of uplift are highly dependent on rheology and by decreasing the upper mantle viscosity to 7 x 10^{20} Pa s, below the 10^{21} Pa s threshold suggested by Bergstrand *et al.* (2005), the modelled rate of uplift changes (Figure B). Figure C summarises sensitivity of the input parameters in achieving a best-fit model. Sold Earth response to the Laurentide load is mainly long wavelength due to the size of the load and the viscosity of the upper and lower mantle. Response to smaller loads, particularly in areas with a low upper mantle/asthenosphere viscosity is expected to be of a much shorter wavelength.

This verification exercise provides confidence in the application of TABOO to reconstruct vertical land motions associated with large ice loads in Fennoscandinavia and demonstrates the sensitivity of model outputs to south central Alaska, where ice and Earth models differ significantly compared to with the relatively simple conditions of Fennoscandinavia. Larsen *et al.* (2005) demonstrates the successful application of TABOO when quantifying the RSL changes during the Neoglacial in south east Alaska.

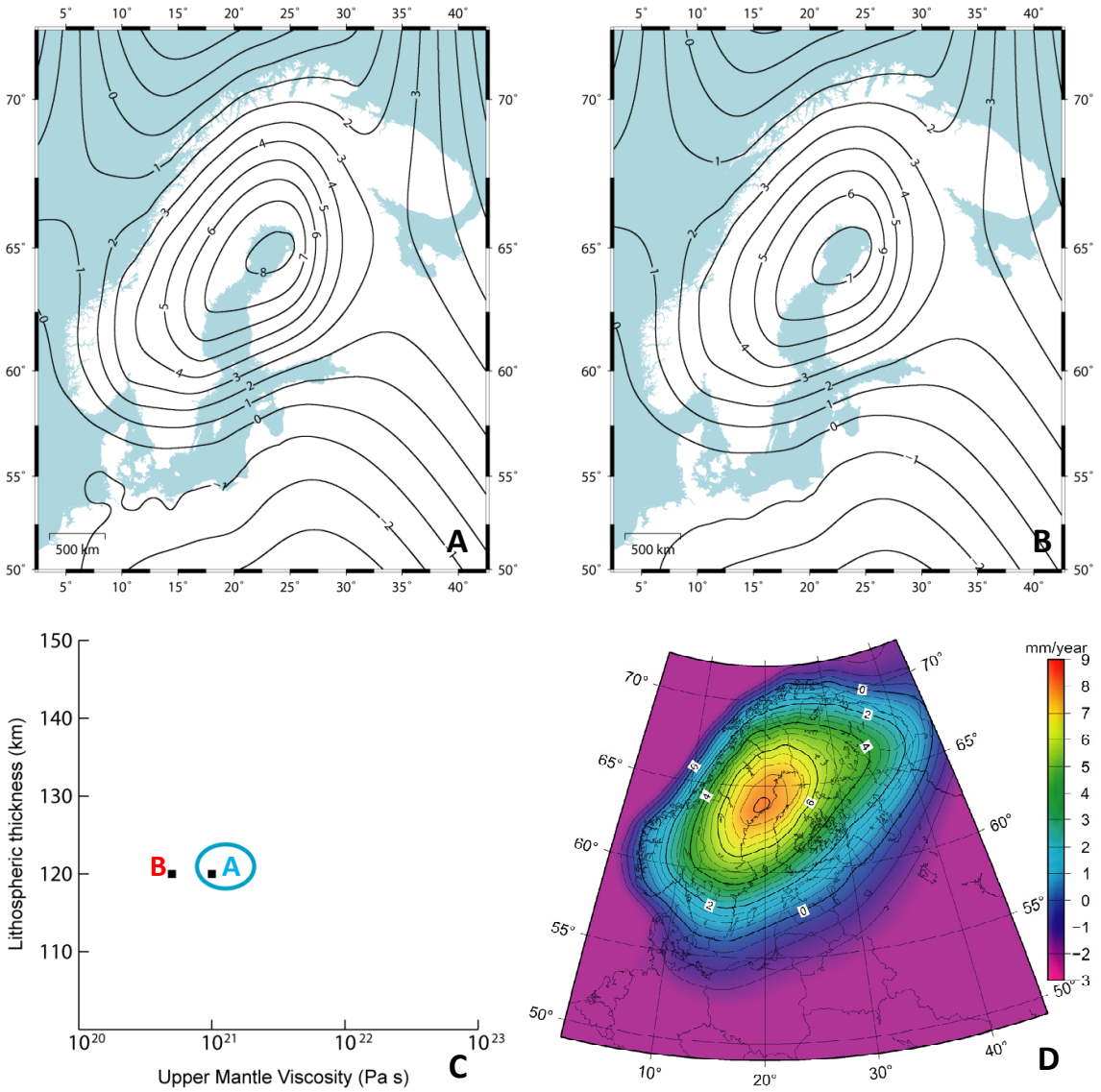

Modelling present day Fennoscandian uplift to verify TABOO's suitability as a postglacial rebound calculator. A: present day uplift (mm yr^{-1}) modelled using ICE-3G (Tushingham and Peltier, 1991) ice model and best earth model from Bergstrand *et al.* (2005) with 120 km thick lithosphere and upper mantle of 10^{21} Pa s; B: present day uplift (mm yr^{-1}) modelled using ICE-3G and earth model with reduced mantle viscosity of 7 x 10^{20} Pa s; C: graph summarising the sensitivity of the earth model input parameters to achieving a best fit model; D: NKG2005LU postglacial land present day rates of uplift reference model for Fennoscandiava (Svensson *et al.*, 2006) to compare to the TABOO model outputs.

RADIOCARBON ANALYTICAL REPORT

Allocation No.: 1339.1008 **Submitter:** I Shennan, University of Durham

Project Title: Quantifying crustal response during the Little Ice Age in south-central Alaska.

Sampling location: Bird Point, Turnagain Arm, upper Cook Inlet, Alaska, USA

Sample composition: Above ground plant macrofossils.

Pre-treatment of raw samples: Samples were digested in 1M HCl (80^{o}C, 8 hours), washed free from mineral acid with deionised water then dried and homogenised. The total carbon in a known weight of the pre-treated sample was recovered as CO_2 by heating with CuO in a sealed quartz tube. The gas was converted to graphite by Fe/Zn reduction.

Results:

Publication Code	Sample Identifier	^{14}C Enrichment (% Modern ±1σ)	Conventional Radiocarbon Age (years BP ± 1σ)	Carbon content (% by wt.)	$\delta^{13}C_{VPDB}$‰ ± 0.1
SUERC-22662	BP086R1 76 cm	98.64 +/- 0.45	110+/- 37	48	-28.0
SUERC-22663	BP086R2 80 cm	104.14 +/- 0.48	modern	48	-29.8
SUERC-22666	BP086R3 84 cm	98.45 +/- 0.45	125+/- 37	48	-28.6
SUERC-22667	BP086R4 88 cm	96.94 +/- 0.45	250+/- 37	45	-28.2
SUERC-22668	BP086R5 92 cm	96.95 +/- 0.44	248+/- 37	60	-28.0
SUERC-22669	BP086R7 100 cm	95.53 +/- 0.42	368+/- 35	50	-28.1
SUERC-22670	BP086R8 104 cm	95.15 +/- 0.44	399+/- 37	55	-27.9
SUERC-22671	BP086R9 108 cm	93.39 +/- 0.43	549+/- 37	47	-28.0
SUERC-22672	BP086R10 112 cm	115.50 +/- 0.50	modern	44	-27.7
SUERC-22673	BP086R11 191cm	88.40 +/- 0.39	991+/- 35	45	-28.6
SUERC-22676	BP086R12 191 cm	87.64 +/- 0.40	1060+/- 37	42	-28.5

Notes:

- Sample BP086R6 96 cm failed because the graphitisation reaction did not reach the necessary minimum yield of 95%. There was no back-up material to repeat the sample combustion.
- Samples noted as modern contain radiocarbon emitted during the period of nuclear weapons testing (early 1950s onwards).

Dr Charlotte Bryant
25th March 2009